

DISSERTATION

On-board Processing for an Infrared Observatory

ausgeführt zum Zwecke der Erlangung des akademischen Grades eines
Doktors der technischen Wissenschaften unter der Leitung von

Univ. Prof. Dr. Horst Bischof
183/2
Institute for Computer Graphics and Vision
Technische Universität Graz

eingereicht an der Technischen Universität Wien
Fakultät für Informatik

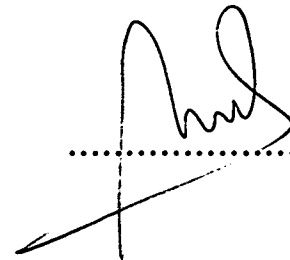
von

Dipl.-Ing. Ahmed Nabil Belbachir

Matr.Nr. 9926842

1200 Wien, Brigittenauer Lände 164-168/Stg.3/Top 29

Wien, am 9. Dezember 2004



.....

To *Fadila, Hana* and *Jasmina*.

Kurzfassung

Diese Dissertation ist eine interdisziplinäre Zusammenarbeit zwischen dem Forschungsfeld der Astronomie und der digitalen Bildverarbeitung, die neue Perspektiven in beiden dieser Gebiete eröffnet. Einerseits profitieren die Astronomen von den neuen Verarbeitungsprozessen und Analysemethoden, der verbesserten Leistungsfähigkeit sowie der Qualität der Ergebnisse, andererseits erschließt sich den Technikern ein neuer Forschungs- und Anwendungsbereich. Ein Beispiel hierfür ist die digitale Bildverarbeitung, die durch ein Weltraumprogramm initiiert wurde, ja sogar die Bildkompression hatte ihren Ursprung in einer Weltraumanwendung.

Das Ziel dieser Arbeit ist die Erkennung und die Entwicklung neuer Methoden und Software-Werkzeuge für Weltraum-Observatorien, um Kompressionsstandards in der Weltraumastronomie einzuführen. Für die Validierung der Ergebnisse wurde der Fall von Infrarotastronomie besonders analysiert. Die verwendeten Weltraumtechnologien haben grundsätzlich einen besonderen technologischen Aufbau und sind mannigfaltigen äußeren Einflüssen ausgesetzt. Vor allem Infrarotdetektoren unterscheiden sich von herkömmlichen bildgebenden Instrumenten durch ihre höhere Ausleserate, was einen sehr viel höheren Datenstrom bedingt.

Diese Arbeit stellt eine Lösung für die Infrarotastronomie dar, wobei das Konzept "On-Board Verarbeitung" (OBP) für optimale Nützung der Telemetriebandbreite und der limitiert On-Board Ressourcen eingeführt ist. JPEG 2000 könnte eine intuitive Lösung sein um die Telemetrie-Anforderungen zu erfüllen. Eine große wissenschaftliche und wirtschaftliche Gesellschaft beschäftigt sich mit der Entwicklung und der Verbesserung dieser Bildkompressionsstandards. Jedoch zeigen wir mit einem einfachen Beispiel in Kapitel 4.4, daß JPEG 2000 nicht für Infrarotastronomie geeignet ist, während OBP die optimale Lösung liefert. Thermische Infrarot Sensordaten enthalten das "Source" Signal und den Ungewünschte "Background", der tausend mal grösser als das Signal ist. Deswegen kann die generische Quantisierung (z.b. Fall von JPEG 2000) relevante Informationsverluste zur Folge haben, während OBP unter Einbeziehung von Sensoren "Know-How", die einzige Lösung für optimale Leistung ist.

Die Vorgehensweise besteht aus der Kodierung der Daten, wodurch die Redundanz in den Infrarotbildern über den Gebrauch eines Dictionarys ausgenutzt wird. Die Daten werden dann mit einem neuartigen Kompressionsalgorithmus reduziert. Die Beurteilung der Leistung der Algorithmen erfolgt unter der Rücksichtnahme von Kompressionsverhältnis, Qualität des Resultats und Komplexität des Algorithmus. Die Auswirkung auf die Zukunft der Informationstechnologie soll die Entwicklung von Datenübermittlungssystemen sein, wobei die Kommunikationsbandbreite, die Qualität der Ergebnisse, und die Datenarchivierung berücksichtigt werden. Die OBP Lösung hat ein verbessertes Kompressionsverhältnis und qualitativ hochwertigere Ergebnisse im Vergleich zu "state-of-the art" Kompressionsalgorithmen, was eine weitere Reduzierung des Datentransfers beim Infrarot Weltraumsatelliten-downlink zur Folge hat.

Abstract

During the past two decades, image compression has developed from a mostly academic **Rate-Distortion (R-D)** field [130], into a highly commercial business [144]. Various lossless and lossy image coding techniques have been developed [109].

This thesis represents an interdisciplinary work between the field of astronomy and digital image processing and brings new aspects into both of the fields. In fact, image compression had its beginning in an American space program for efficient data storage. The goal of this research work is to recognize and develop new methods for space observatories and software tools to incorporate compression in space astronomy standards. While the astronomers benefit from new objective processing and analysis methods and improved efficiency and quality, for technicians a new field of application and research is opened. For validation of the processing results, the case of **InfraRed (IR)** astronomy has been specifically analyzed.

This work presents a solution for infrared astronomy, where the concept of **On-Board Processing (OBP)** is introduced for efficient exploitation of the telemetry bandwidth and the budget-limited space observatories. Indeed, IR astronomy, most commonly, requires space observatories because the Universe cannot be accessed from ground in the full IR range as Earth's atmosphere blocks most IR wavelengths. Thus, IR astronomy is a good candidate to support our investigation. Furthermore, IR imaging with dedicated observations requires specific techniques with a complex semiconductors technology. Thus, the resulting data is very sensitive to noise, which make the feasibility of our approach challenging.

IR detectors consist, as a rule, of fewer pixels than those for the visual range, but the design of multi-sensor instruments for space applications with special technologies and a harsh radiation environment require high readout rates leading again to larger data volumes. Therefore, although many applications exist, which generate or manipulate astronomical data (including wavelet-based methods), transmitting image information still faces a bottleneck such that the proposed techniques are often ad-hoc and sometimes inconsistent. One intuitional solution can be the JPEG 2000 standard to achieve the telemetry requirements. Indeed, a large scientific and commercial community is contributing for the development and the improvement of the JPEG 2000 compression codec. We demonstrate with a simple example in Section 4.4 the limitation of this compression method (JPEG 2000), concerning this astronomical application while OBP outperforms this generic compression codec. Indeed, thermal IR detector raw data (at wavelengths $> 5\mu\text{m}$) consist of two constituent contributions: the source signal, and the unwanted background. The background is generally higher than the source signal in the order of several thousands. Therefore, generic quantization (e.g. case of JPEG 2000) may lead to drop away the relevant information, while a dedicated compression technique using infrared detector knowledge is the only way to optimal performance.

The performance of this solution (OBP) is being measured by considering the compression ratio, result quality and algorithmic complexity. A new complexity analysis and measure is

developed for Digital Signal Processor (DSP) architecture. The OBP complexity is evaluated for the *Analog Device* processor ADSP 21020. The impact of this research on the future of information technology is to develop data delivery systems where communication bandwidth and quality are at a premium and archival storage is a costly endeavor. This new framework has an improved compression ratio and result quality over the best-known pre-existing compression algorithms, which will lead to a reduction of the data traffic for infrared observatories.

Résumé

L'avancement rapide dans le domaine "compression d'image", d'un aspect académique taux-distorsion [130] jusqu'aux applications commerciales [144], a vu le développement de plusieurs techniques de codages durant ces deux dernières décennies.

Cette thèse représente un travail interdisciplinaire entre le traitement numérique des images et l'astronomie qui contribue par de nouveaux aspects dans les deux domaines. En effet, la compression d'image a vu le jour dans un programme spatial américain dans les années 50. le but de ce travail consiste en la reconnaissance et le développement de nouvelles méthodes pour les observatoires spatiaux et de les incorporer dans les standards de compression pour l'astronomie spatiale. Tandis que les astronomes bénéficient de nouvelles méthodes objectives de traitement et d'analyse et d'une qualité meilleure de résultats, les techniciens profitent d'un nouveau domaine de recherche et d'application. Pour valider ce traitement, le cas d'astronomie en **InfraRouge** (IR) est spécialement analysé.

Dans cette thèse, une solution est mise en oeuvre pour l'astronomie en IR et le concept traitement à bord (OBP) est introduit pour l'exploitation efficace du canal de transmission pour les observatoires spatiaux à ressources limitées. En effet, l'astronomie en IR nécessite des observatoires spatiaux, comme l'univers ne peut pas être accédé de la terre sur l'ensemble longueurs d'onde IR à cause de l'atmosphère qui bloque la majorité des radiations IR. En plus, l'acquisition d'image IR exige des techniques spécifiques avec une technologie complexe. Ainsi, le signal résultant est sensible au bruit ce qui rend la faisabilité de notre approche très critique.

JPEG 2000 est une solution intuitive pour le problème de compression d'image. En effet, une grande communauté scientifique et commerciale contribue pour le développement et l'amélioration de ce standard de compression d'image. On démontre avec un exemple très simple dans le paragraphe 4.4, la limitation de la méthode générique JPEG 2000, tandis que notre solution proposée (OBP) est mieux adaptée aux images astronomiques IR. En effet, les données sources des détecteurs IR consistent en deux contribution: le signal source (désiré) et le signal du télescope (bruit non- désiré). Le signal du télescope est généralement milliers de fois plus grand que l'information nécessaire (signal source). De ce fait, la quantification générique (l'exemple de JPEG 2000) cause une perte de l'information, tandis que la compression dédiée pour l'astronomie IR en utilisant la connaissance des caractéristiques des détecteurs est le seul moyen pour aboutir à la solution optimale.

Les performances de cette solution (OBP) sont mesurées en tenant compte du taux de compression, qualité des résultats et la complexité algorithmique. Une nouvelle méthode d'analyse et de mesure de complexité est développée pour les processeurs de signaux. La complexité de OBP est évaluée pour le processeur ADSP 21020 d'*Analog Device*. L'impact de cette recherche sur le futur de la technologie de l'information est le développement de système de codage de

données pour une exploitation optimale des canaux de transmission et de capacité de stockage. La nouvelle méthode développée présente de meilleurs résultats (taux de compression, qualité, complexité) comparés à ceux de l'état de l'art, ce qui réduit le trafic pour les observatoires spatiales.

ملخص

شهدت السنوات الأخيرة تطورا ملحوظا في مجال تقريص الصور من المجال النظري إلى الميدان التجاري الاستثماري. نجب عن هذا التقدم ظهور عدة تقنيات لتشفير الصور. أشهرها JPEG 2000 التي يشارك في نصيبتها العديد من الباحثين و المؤسسات. نبرهن في هذه الرسالة بمثال بسيط عن محدودية هذه التقنية في حل مشكلة المراصد الفضائية في الموجات تحت الحمراء لإرسال المعلومات.

الهدف الرئيسي لهذه الرسالة هو حل هذه المشكلة بالتعرف على الطريقة المثلى لتقريص صور المراصد الفضائية في الموجات تحت الحمراء لإرسالها إلى الأرض.

Acknowledgments

This is the most critical part of the thesis. It took me a long time to write this section. It is not an easy task to justly deal with all contributions and to quantify them into few words. This work could never have been achieved without contributions and discussions with many people. I apologize if I forgot names.

Horst Bischof: This work could never be successful without the contribution of Horst, my thesis advisor. He adopted my employment within the Austrian contribution to the Herschel-mission and demonstrated me what scientific work means. He showed me the way to deal with the thesis topic. He always was **present** supporting me to surpass obstacles. His worthwhile ideas and criticism influenced with a large extent the successful completion of this thesis work. Thanks for everything!

Franz Kerschbaum: He is the co-investigator of the Herschel-PACS project and the reviewer for this thesis. He also adopted me within the PACS team and supported my thesis work. This work could never be achieved without his support, comments and recommendations. He did the hard job to secure the funding for PACS contribution and thus, the achievement of this thesis. Thanks for everything !

I would like to thank also all my colleagues at PRIP for the exciting environment for doing scientific work.

Robert Sablatnig: Thanks to Robert for reading part of my thesis as science project. I thank him for the scientific support and the proof-reading of my work, which significantly improved the dissertation organization.

Walter Kropatsch: I should not forget Prof. Kropatsch, the head of PRIP for his valuable comments and efforts to the success of this work. I understand his constructive criticism for the qualitative contribution of my thesis into the scientific community (Shaking for Waking). Thank you for giving me the opportunity for doing this work.

Peter Goebel: Thanks to Peter for the intense discussion regarding the thesis contribution. Thanks also for his valuable support of my work.

Ernestine Zolda and Paul Kammerer: Many thanks for supporting me during my work.

Norbert Braendle: Thank you for the thesis template and for supporting my work.

All PRIP Colleagues: Thanks for Allan Hanbury, Georg Langs, Martin Kampel and all PRIP members for offering a nice and enjoyable environment for doing research in a familiar atmosphere

Many thanks also all my colleagues at the Institute for Astronomy (IfA) at the university of Vienna for the support of this work.

Roland Ottensamer: This work could not be achieved without Roland's contribution. Thanks for everything. (Wir werden alle in die Hoelle gehen, deswegen müssen wir schnell auf eine Religion einigen)

Christian Reimers: Thanks for your contribution to this work

Peter Reegen: Thanks for discussion within the PACS project.

I want also to thank the PACS project team for the valuable discussions and especially **Helmut Feuchtgruber, Mathias Rumitz, Bernhard Schulz, Babar Ali, Diego Cesarsky, Albrecht Poglitsch** and many others...

Thanks also to the former PRIP colleagues and my friends **Roman Pflugfelder, Roland Glantz** and **Christian Wolf** for their support and the funny time at PRIP.

I can never forget my previous advisor **Mohamed Faouzi Belbachir** for his valuable advices for the progress of this work.

Thanks also to my friends at USTO **Nawal Benmoussat, Hafida Senoussi, Lila Siga** and many others...

I am also grateful to several foundations to a direct or indirect financial support for my studies: Austrian Ministry for Transport, Innovation and Technology, the Austrian Space Agency and the Austrian Research Society.

Thanks to everybody!

Contents

1	Introduction and Overview	1
1.1	Motivation	1
1.2	The Contribution of this Work	5
1.3	Outline	7
2	Astronomical Aspects	8
2.1	Photometric Definitions	8
2.2	Discovery of the Infrared	9
2.3	Infrared Signal Detection with Photodetectors	9
2.3.1	Infrared Detector Technology	12
2.3.2	Individual Detectors	12
2.3.3	Detector Arrays	19
2.3.4	Efficiency of a System	23
2.3.5	Seeing in the Infrared	24
2.3.6	Some Representative Instruments	26
2.3.7	Observing and Data Reduction	28
2.4	Aspects of Infrared Astronomy	31
3	Preliminary Notions and State of the Art Data Compression	34
3.1	Noise Generalities	34
3.1.1	Thermal or Johnson Noise	35
3.1.2	Flicker and 1/f Noise	36
3.1.3	Poisson Noise	36
3.1.4	Gaussian and Poisson Noise	37
3.1.5	Other Types of Noise	38
3.2	Definition of Data Compression	38
3.3	The Reconstruction Error	40
3.4	Compression Challenges	41
3.4.1	Compression Ratio vs. Reconstruction Error	42
3.4.2	The Algorithmic Complexity of the Method	43
3.4.3	Additional Aspects	43
3.5	Rate-Distortion Principle	44
3.6	State-of-the Art Compression	47
3.6.1	Transform Coding Methods	47
3.6.2	Entropy Coding Methods	53

3.7	Astronomical Compression Methods	56
4	On-Board Processing	58
4.1	Classical Processing for Space Observatories	58
4.2	Integrated Processing for Space Observatories	60
4.3	On-Board Processing	62
4.3.1	Detector Selection	63
4.3.2	Preprocessing	63
4.3.3	Glitch detection	63
4.3.4	Oversampling Reduction	68
4.3.5	Integration	72
4.3.6	Redundancy Reduction	72
4.3.7	Entropy Encoding	75
4.3.8	Raw Data Selection	78
4.4	Application of the On-Board Processing for Astronomical Infrared Images . . .	79
5	Complexity Related Aspects	84
5.1	Complexity Definition and Measures	84
5.1.1	Qualitative Complexity	85
5.1.2	Quantitative Complexity	85
5.2	Software Complexity	86
5.3	Implementation Complexity	86
5.4	State-of-the art Complexity Measurements and Optimizations	87
5.5	Measuring the Complexity	88
5.5.1	Arithmetic Complexity	89
5.5.2	Memory Complexity	95
5.5.3	The combination: Arithmetic and Memory Complexity	97
5.6	Complexity Calculation of the On-Board Processing	98
5.6.1	Flowchart for the Raw Data Selection Module	99
5.6.2	Flowchart for the Detector Selection Module	100
5.6.3	Flowchart for the Preprocessing Module	100
5.6.4	Flowchart for the Glitch Detection Module	102
5.6.5	Flowchart for the Oversampling Reduction Module	102
5.6.6	Flowchart for the Integration Module	103
5.6.7	Flowchart for the Redundancy Reduction Module	104
5.6.8	Entropy Encoding Module	104
6	Case Study: HERSCHEL-PACS Infrared Camera	107
6.1	The Herschel Mission	107
6.2	The PACS Instrument Description	109
6.2.1	Design Concept	111
6.2.2	The PACS Instrument Units	119
6.3	PACS Constraints	122
6.3.1	PACS Signal Description	122
6.3.2	PACS Signal-to-Noise Ratio	123

6.3.3	PACS Telemetry Rates	125
6.3.4	Summary of PACS Constraints for Data Processing	125
6.4	Illustration of PACS Data	126
6.5	PACS Data Analysis	128
6.5.1	PACS Input Data	129
6.5.2	Ramp Morphology	130
6.5.3	Ramp Types	130
6.5.4	Analytical Ramp Model	132
6.6	Tests and Evaluation of the On-board Processing	133
6.6.1	Oversampling Reduction Results	134
6.6.2	Compression Results	134
7	Conclusion and Perspectives	139
7.1	Summary	139
7.2	Main Achievements	142
7.3	Future Work	143
	Bibliography	144

Abbreviations and Acronyms

AGB	Asymptotic Giant Branch stars
ASW	Application SoftWare
BIB	Blocked Impurity Band
BLUE	Best Linear Unbiased Estimator
CCD	Charged Coupled Device
CCSDS	Consultative Committee for Space Data Systems
CPU	Central Processing Unit
CR	Compression Ratio
CRE	Cryogenic Readout Electronic
CTT	ConTourlet Transform
CVT	CurVelet Transform
DC	Direct Current
DCT	Discrete Cosine Transform
DEC/MEC	DEtector Controller /MEchanical Controller
DPU	Digital Processing Unit
DSP	Digital Signal Processor
DWT	Discrete Wavelet Transform
EBCOT	Embedded Block Coding with Optimized Truncation
EPWIC	Embedded Predictive Wavelet Image Coder
ESA	European Space Agency
FCVT	Fast CurVelet Transform
FFT	Fast Fourier Transform
FWHM	Full Width at Half Maximum
Ge:Ga	Germanium :Gallium
HST	Hubble Space Telescope
ICVT	Integer CurVelet Transform
IR	InfraRed
IRAS	InfraRed Astronomical Satellite
ISO	Infrared Space Observatory
ISOCAM	Infrared Space Observatory CAMera
JPEG	Joint Photographic Expert Group
KL	Kullback Leibler
KLT	Karhunen Loève Transform
MAE	Mean Absolute Error

MSE	Mean Square Error
NEP	Noise Equivalent Power
OBP	On-Board Processing
PACS	Photodetector Array Camera and Spectrometer
PDF	Probability Density Function
PIL	Potential Information Loss
PMF	Probability Mass Function
PMT	Pyramidal Median Transform
PRIP	Pattern Recognition and Image Processing group
PSF	Point Spread Function
PSNR	Peak Signal to Noise Ratio
QE	Quantum Efficiency
RANSAC	RANdom SAMple Consensus
R-D	Rate-Distortion
RDT	RaDon Transform
RGT	RidGelet Transform
RMSE	Root Mean Square Error
SAR	Synthetic Aperture Radar
SDDM	Slope Deviation Detection Method
SDE	Slope Deviation Error
SIRTF	Space InfraRed Telescope Facility
SNR	Signal to Noise Ratio
SPU	Signal Processing Unit
SST	Spitzer Space Telescope
SWS	Short Wavelength Spectrometer
WVT	WaVelet Transform

Chapter 1

Introduction and Overview

1.1 Motivation

During the past few decades, InfraRed (IR) imaging has become a major tool in astronomy due to the rapid advances in IR detector technology [43]. Our eyes are detectors, which are designed to detect visible light waves (or visible radiation). Visible light is one of the few types of radiation that can penetrate our atmosphere and be detected on the Earth's surface.

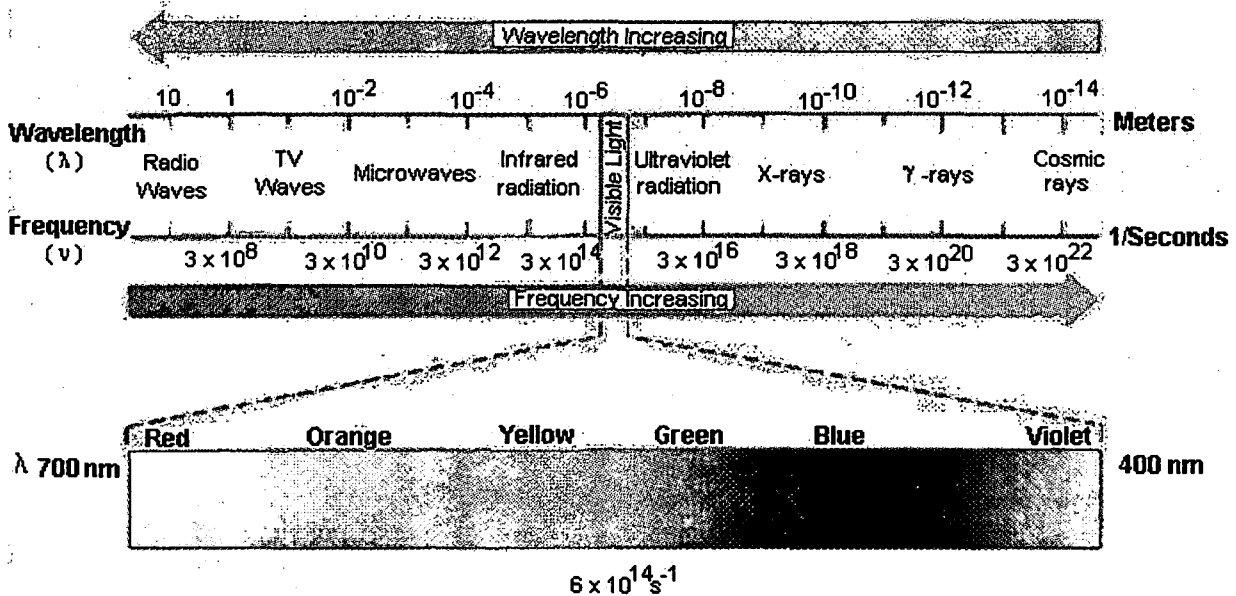


Figure 1.1: The electromagnetic spectrum

The full electromagnetic spectrum includes gamma rays, X-rays, ultraviolet, visible, IR, microwaves, and radio waves. These different forms of radiation all travel at the speed of light (c). They differ, however, in their frequencies and wavelengths. The product of the frequency (ν) times the wavelength λ of electromagnetic radiation is always equal to the speed of light.

$$c = \nu \cdot \lambda \quad (1.1)$$

Figure 1.1 depicts the above-listed regions of the electromagnetic spectrum respective to wavelengths and frequencies. IR radiation lies between the visible and microwave portions of the electromagnetic spectrum [107]. The wavelength range of IR radiation is broken into three categories: near, mid and far IR. Near IR ($0.7 \mu\text{m} - 5 \mu\text{m}$) refers to the part of the IR spectrum that is closest to visible light and far IR ($30 \mu\text{m} - 1\,000 \mu\text{m}$) refers to the part that is closer to the microwave region. Mid IR ($5 \mu\text{m} - 30 \mu\text{m}$) is the region between these two (near and far IR) [43, 107].

IR radiation is invisible for the human eye [43]. Even objects that we think of as being very cold, such as an ice cube, emit IR radiation. For this reason, IR telescopes can observe astronomical objects that remain hidden for optical telescopes, such as cool objects that are unable to emit in visible light. For this reason also, IR instruments need to be cooled down to temperatures below 3 degrees Kelvin, otherwise their own IR emission would spoil the observations. Opaque objects, those surrounded by clouds of dust, are another specialty for IR telescopes: the longer IR wavelengths can penetrate the dust, allowing us to see deeper into such clouds [43].

Indeed, IR astronomers can detect/observe a much wider part of objects of the Universe. Many of the Universe's constituent parts (such as stars) are found in dusty environments or (such as galaxies) include a huge amount of dust features. IR detectors enable us to peer into the obscured cocoons of star formations and into the heart of dusty galaxies [43, 54]. Furthermore, many interesting astrophysical phenomena are relatively cool (planets, interstellar gas and dust), and hence radiate primarily at IR wavelengths [50]. On the other hand, several objects are best studied in the IR. These include cool stars which are too faint to be detected in visible light (e.g. brown dwarfs), star forming regions which are embedded in thick dust and cannot be seen in visible light, star-burst galaxies, our galactic center, planets, asteroids, light from the distant Universe, which has been red-shifted [43] into the IR, and the dust between the stars [50]. However, the Earth's atmosphere acts as an umbrella for most IR wavelengths, preventing them from reaching the ground, such that the water vapor at the Earth's atmosphere absorbs most of the IR radiations [43, 143]. Almost none of the IR portion of the electromagnetic spectrum can reach the surface of the Earth, although some portions can be observed by high-altitude aircrafts (such as the Kuiper Observatory [155]) or telescopes on high mountaintops (such as the peak of Mauna Kea in Hawaii). Therefore, a space observatory (equipped with an IR-telescope) is required to detect this kind of radiation invisible to the human eye, and to study the entire IR range.

Nowadays, astronomical data collected on-board space observatories impose enormous storage and bandwidth requirements for downlink, regarding the continuous observation and the high readout rates [122]. IR detectors consist, as a rule, of fewer pixels than those for visual

range, but the design of multi-sensor instruments leads to even higher data volumes. If multiple detectors are operated in parallel to support multi-spectral or even hyper-spectral imaging, then the data volumes multiply. Furthermore, small spacecrafts are usually used for deep space missions. They are characterized by being restricted to low budget and consequently to low data rate. Therefore, although many applications exist, which generate or manipulate astronomical data [15, 95, 107, 134], transmitting image information still face a bottleneck such that this constraint has stimulated advances in compression techniques for astronomy [24, 72]. However, the proposed techniques are often ad-hoc and sometimes not appropriate for IR data. For example, in [72], the listed methods involve filtering of information, which is not considered relevant, by making use of object recognition methods that face the background estimation problem to guarantee not to destroy relevant information. Furthermore, this lessens the interpretability of the results and limits the extension of the method to non-image data structures.

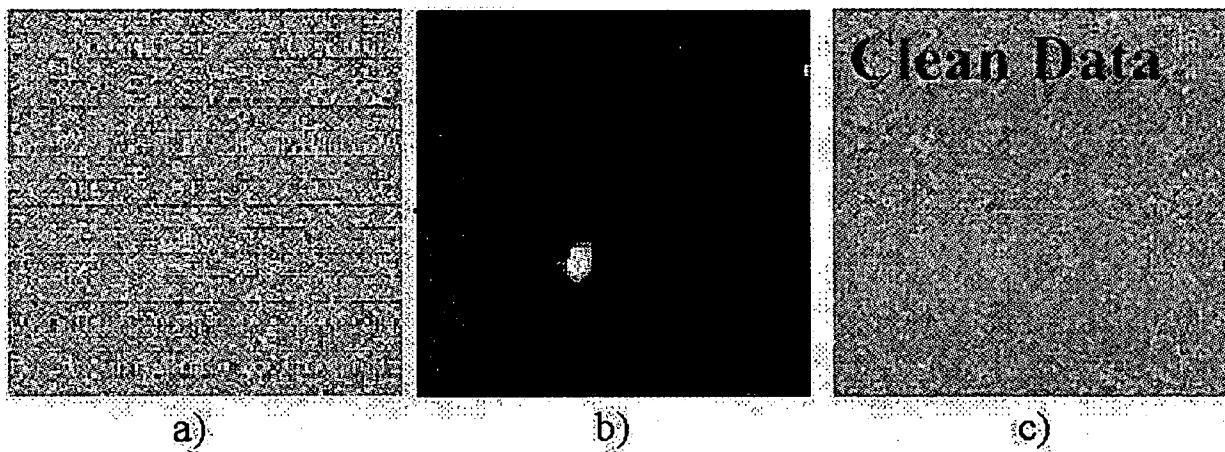


Figure 1.2. Example of an infrared image. a) Raw image at 1500 s integration time. b) One interesting object in the image 'Galaxy SBS-0335-05210'. c) Resulting Image after denoising (Noise from the electronic)

Indeed, thermal IR (mid and far IR) imaging is a measure of heat. To capture this energy, a complex instrumentation is used such that the detectors are cooled down to few kelvins, to not spoil the target signal. Therefore, the detector measures a composite signal: source + background. The source is considered as the object heat (observed target). The background is the environment heat (telescope signal) whose amplitude is usually, for performance reason, far too high than that of the observed target. To capture the IR image of the wished target, one has to integrate several images over time (usually hours, depending on the wavelength), that is called, integration time. Other observation techniques are also used to capture IR images of an object including chopping and wavelength switching [13]. Therefore, the IR image acquired at time t usually has no object structure, which make the compression task challenging, such that it has to ensure that the relevant signal (observed source) is not lost while compression. Furthermore,

IR image acquisition is susceptible to heavy particles (glitches) that might on one side disturb the signal accuracy, changing the electronic characteristics (e.g. responsivity), and on the other side, it might increase the signal entropy that may decrease the compression efficiency. Figure 1.2 depicts an example of an image from the IR telescope GEMINI [121]. Figure 1.2 a) shows the raw image at 1500 sec integration time. One interesting object (Galaxy) in the image after a post processing can be found in Figure 1.2 b). Figure 1.2 c) shows the relevant image for the astronomy expert after removing the noise and the stripping artifact due to the instrument electronic. The challenge of data compression is to preserve as much information as possible from the image such that the relevant image structure (e.g. Figure 1.2 b)) can be reconstructed.

Although data compression is still a major topic of research, the industry has already come up with several compression standards, like ZIP, JPEG and JPEG2000 [109, 144, 145]. All compression techniques exploit the fact that the data are highly redundant. This redundancy allows us to reconstruct a signal (e.g. image or video) from compressed information that is only a small fraction of the original data, in size. Of course, using compressed data implies that the consuming application must first reconstruct the signal information. Thus, we are in fact compensating for inadequate network bandwidth with processor-power. While technologies evolve, constraints on data quality grow with the challenging consumer demands and the algorithms for compressing and decompressing visual information are becoming increasingly complex [23, 97]. Therefore, a significant research effort has also been invested in analyzing the performance of compression algorithms in terms of quality and complexity. Such an analysis forms the basis for optimizing the algorithms, and also for determining whether a given algorithm is appropriate for the application at hand. To my knowledge, no real study has been performed for astronomical IR data compression apart the use of wavelet-based compression techniques [24, 72]. The IR data per definition contain high entropy due to the influence of noise [43, 90]. Therefore, advanced compression techniques have to be used in order to satisfy the quality requirements within a typical processing environment.

This thesis is concerned with integrating new data compression and caching techniques for improving the efficiency of bandwidth-limited transmission channels in case of IR space astronomy. Generally, IR data are collected on-board of an observatory (satellite) that can overload downlink bandwidths and on-board memory resources rapidly. This discrepancy is a common phenomenon for deep space applications with very limited telemetry rates as well as for Earth observation missions where admissible payload masses and energy budgets allow the assembly of high-rate payloads. Hence, an efficient data compression method with knowledge on IR detector characteristics is required for optimal performance.

The Institute of Computer-Aided Automation, Pattern Recognition and Image Processing group together with the Institute for Astronomy of the University of Vienna have been involved in the Herschel project [149] from the European Space Agency (ESA). They have developed and implemented data compression algorithms for the IR Photo-detector Array Camera and Spectrometer (PACS) [4, 12]. The compression method has been developed for the Ge:Ga photo-conductor arrays [103, 138] and silicon bolometer arrays [83]. Due to the difference in signal characteristics, the compression algorithms used depend on the detectors activated.

The PACS compression scheme is part of the contribution of this thesis. Furthermore, an accurate investigation of the IR astronomical signal is performed to recognize a generalized compression method for different types of IR detectors. We propose goal-driven compression with new algorithms, which address both aspects of distortion/rate and complexity. Distortion/rate theory is generally used to assess the merits and performances of a compression method. It makes use of a quantitative measure of a distortion by mean of the calculation of the reconstruction error versus the compression ratio achieved. On the other hand, the complexity of the algorithm is relevant because it defines the feasibility of the method. Therefore, the implementation of the method has to be part of the method design.

Although we will specifically consider only data compression algorithms for IR astronomy, the techniques developed here may be used to analyze any signal-processing algorithm. Our approach integrates the two basic ideas of compression and caching into a single mechanism, i.e. data are automatically cached whenever possible, avoiding retransmission altogether, and if data have to be transmitted, they are compressed in a very efficient way, which surpasses the performance of compression algorithms which are widely used at this time. Therefore, we develop an optimized model for data compression that adapts the environment characteristics and exploits the available resources better. The compression algorithms developed within this thesis can be also used to utilize archival storage effectively.

The evaluation of the investigated methods are performed according to several metrics supported by experts in IR astronomy. Based on its simplicity, pixel-based Root Mean Square Error (RMSE) or its derivatives Signal-to-Noise-Ratio (SNR), Peak Signal-to-Noise-Ratio (PSNR) are dominant metrics in practice. However, RMSE does not take the spatial property of human's visual perception into account that is the reason why it fails under many circumstances. In this thesis, we use the Potential Information Loss (PIL) metric and the support of astronomers for the assessment of the compression quality on images. PIL is a derivative of the Kullback-Leibler (KL) information gain, which consider astronomical object profile as Gaussian curve. Data from the InfraRed Astronomical Satellite (IRAS) [148], the Infrared Space Observatory (ISO) [147] and the Herschel Space Observatory (HSO) [149] are used for test and evaluation of the developed methods.

Astronomers' community will profit from this investigation such that they will benefit from new objective processing and analysis methods and improved efficiency and quality. The impact of the research on the future of information technology will be the development of data delivery systems for situations in which communication bandwidth and result quality are at a premium and archival storage is an exponentially costly endeavor.

1.2 The Contribution of this Work

The work presented in this thesis contributes to further development of science (signal/image processing) and enhancement of the understanding of the field "compression for infrared astronomy". This work presents a solution for infrared astronomy by the recognition of an efficient

data transmission for infrared space astronomy for:

- a better exploitation of the telemetry bandwidth by means of a study of:
 - signal characteristics for infrared instruments and
 - the light detection mechanism with infrared sensors
- and a better exploitation of the available processing resources by means of:
 - quantitative measure of complexity
 - assessment of the software and implementation complexity and its optimization for embedded applications

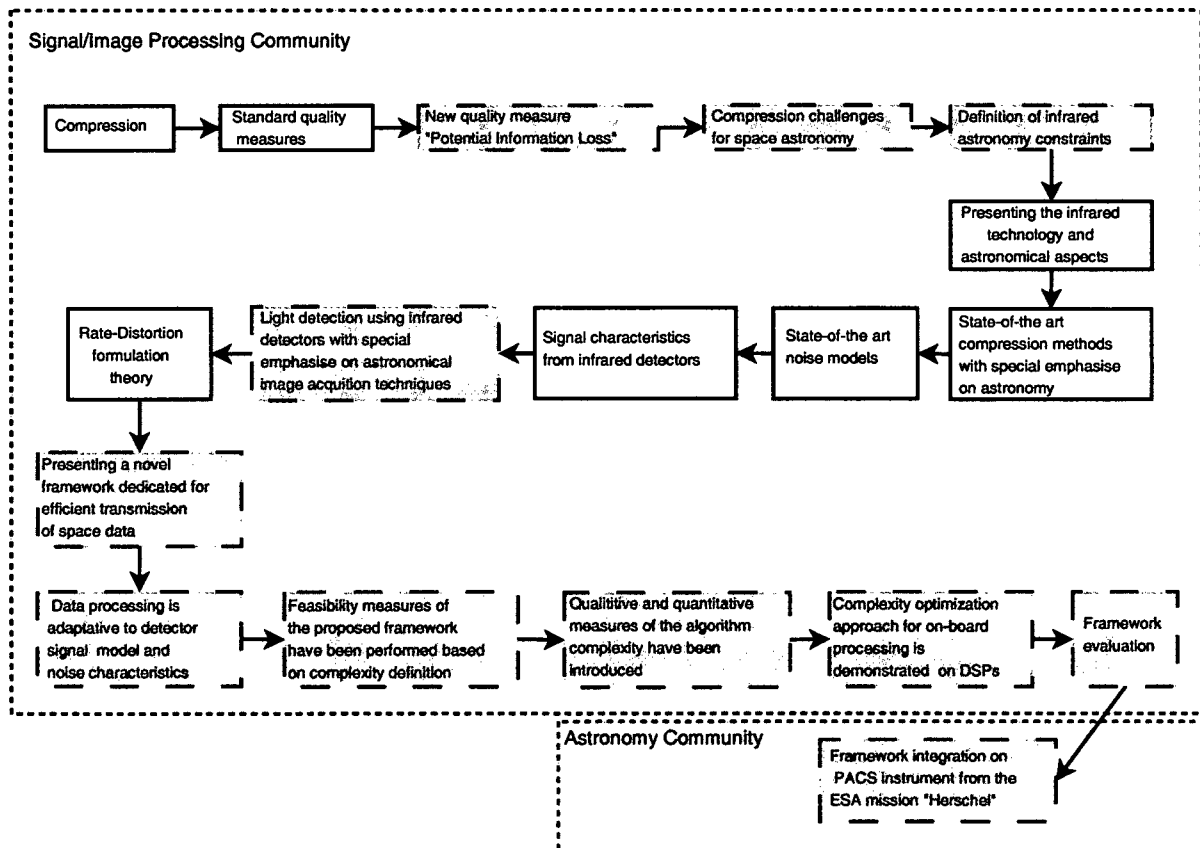


Figure 1.3. Main contributions of this work for further development of signal/image processing. The novelty is displayed with boxes of discontinuous lines and dark (green color) background

Figure 1.3 illustrates a summary of the scientific contribution of the thesis in both fields signal/image processing and astronomy. The boxes with dashed lines and dark (green color) background are the novelty of the thesis into science.

1.3 Outline

The thesis can be subdivided into two main parts, the one dealing with the analysis of the infrared detectors signal for compression and the second part dealing with the compression performance assessment in term of result quality and algorithmic complexity. The Herschel-PACS camera has been used for the evaluation of the analysis results and for the proposed on-board processing solution.

In Chapter 2, important aspects from infrared astronomy are presented. In the first part, the astronomical signal characteristics from infrared detectors and their mathematical formulation are given including the light detection mechanism, the detector technology and the readout modes. In the last part, typical images from infrared astronomy are illustrated and the astronomical efficiency of the system is given.

Chapter 3 introduces preliminary notions on data compression. The formal definition of data compression and conventional assessment criteria for compression algorithms are given. Furthermore, the existing noise models, relevant for astronomy applications, are introduced. It also presents state-of-the art compression methods for both signal and image processing applications. Dedicated methods for astronomical applications are also summarized in this chapter.

In Chapter 4, the main contribution of this work to the scientific research is presented. An on-board processing framework has been proposed for infrared observatories constrained with limited telemetry, processing resources and large data volume. All on-board processing modules have been detailed and illustrated with examples. Finally, a demonstration of this framework performance has been made on images from ISO. It is shown that the proposed solution outperforms the generic image compression standard JPEG2000 for infrared astronomy.

In Chapter 5, an investigation on the algorithmic complexity of the proposed processing method for IR astronomy is performed. In the first part, a dedicated methodology for complexity analysis and measure of any compression algorithm is given. In the second part, the resulting approach is used to measure the on-board processing complexity on the Analog Device digital signal processor ADSP 21020. It was shown that final complexity is the sum of the contribution of all processing modules, that fit to the resource limitation.

Chapter 6 presents experimental results of the proposed processing concept on the Herschel-PACS camera [149]. The PACS specific constraints have been detailed. An analysis of PACS spectroscopy data (ramps) has been performed and observed models are included in an Atlas with five ramp morphologies. The performance of the proposed on-board processing are evaluated on PACS data according to this Atlas using the introduced four metrics (Chapter 3) and the compression ratio.

In the last Chapter, a summary of the thesis is given. Furthermore, possible extensions for this investigation are proposed.

Chapter 2

Astronomical Aspects

Before we start, important photometric definitions are introduced in the first section. In the second part, historical aspects of IR discovery are given. The signal characteristics of IR sensors are detailed in the third part including the light detection mechanism, the detector technology and types and the readout modes. In the last part, examples of astronomical images and object classification are presented for illustration.

2.1 Photometric Definitions

The total outward flow radiation from a body is called its luminosity "L" measured in Watts. If divided into spectral intervals, this quantity becomes its monochromatic luminosity L_ν , measured in units of Watts Hz^{-1} , or L_λ , measured in units of Watts μm^{-1} , where λ is the wavelength. The power emitted from unit area of a source into unit solid angle is called the intensity "I" and it is measured in Watts $\text{sterad}^{-1}\text{m}^{-2}$. The same quantity, when divided into spectral intervals, is called the specific intensity I_ν . Similarly for I_λ .

The received radiation, F_ν or F_λ per unit of frequency or wavelength, is measured in $\text{W m}^{-2}\text{Hz}^{-1}$ or $\text{W m}^{-2}\mu\text{m}^{-1}$. This quantity is known as the monochromatic flux density or simply the monochromatic flux in astronomical parlance. The monochromatic flux density is also called the spectral irradiance and this is the astronomical signal of interest as it represents the science product. Flux densities in frequency units can be converted into wavelength units and vice versa. The flux density in unit frequency interval is F_ν . Since Equation 1.1 we have

$$d\lambda = -\frac{c}{\nu^2}d\nu = -\frac{\lambda^2}{c}d\nu \quad (2.1)$$

If we put $d\lambda = 1$, $d\nu$ becomes the frequency interval corresponding to unit wavelength interval and it is seen that

$$F_\lambda = 2.998 \times 10^8 F_\nu / \lambda^2 \quad (2.2)$$

if expressed in the SI-system (Système Internationales d'unités). It is also interesting to

note that

$$\nu F_\nu = \lambda F_\lambda \quad (2.3)$$

In discussing the overall energy distribution of the radiation from an astronomical object, $\log \nu F_\nu$ or $\log \lambda F_\lambda$ is often graphed against $\log \nu$ or $\log \lambda$ to show in what frequency or wavelength regime it emits the most power per decade.

If I is the intensity of a ray of original intensity I_0 which has passed through a layer of absorbing material, then the optical depth τ of the material is given by

$$I = I_0 e^{-\tau} \quad (2.4)$$

For $\tau = 1$, the ray energizes at $e^{-1} \simeq 0.368$ times its original strength. More specifically, we can write

$$I_\lambda = I_{\lambda_0} e^{-\tau_\lambda} \quad (2.5)$$

2.2 Discovery of the Infrared

The both musician and astronomer Sir Frederick William Herschel (1738-1822) [16] has discovered the IR radiation in the year 1800. Herschel (see Figure 2.1) is perhaps most famous for his discovery of the planet Uranus in 1781, the first new planet found since antiquity.

He was interested in learning how much heat passed through the different colored filters he used to observe the Sun and noticed that filters of different colors seemed to pass different levels of heat. He discovered the IR radiation while measuring the temperature of each color from a directed sunlight through a glass prism by measuring the temperature just beyond the red portion of the spectrum in a region apparently devoid of sunlight. To his surprise, he found that this region had the highest temperature of all. Herschel's experiment was important not only because it led to the discovery of infrared, but also because it was the first time that someone showed that there were forms of light that cannot be seen with human eyes. Herschel's original prism and mirror are on display at the National Museum of Science and Industry in London, England.

Today, infrared technology has many exciting and useful applications. In the field of infrared astronomy, new and fascinating discoveries are being made about the Universe. Medical infrared imaging is a very useful diagnostic tool. Infrared cameras are used for police and security work as well as in fire fighting and in the military. Infrared imaging is used to detect heat loss in buildings and in testing electronic systems. Infrared satellites have been used to monitor the Earth's weather, to study vegetation patterns, and to study geology and ocean temperatures.

2.3 Infrared Signal Detection with Photodetectors

The simplest light-detection method possible with photodetectors is incoherent or direct detection, in which the signal involves the photocurrent itself (directly proportional to the power of



Figure 2.1: Sir William Herschel

incident light), or the difference in photocurrent between two separate exposures of the detector to light. In the following we consider the sensitivity of incoherent detection, asking the question: what is the smallest power that can be detected in a given amount of time, given the parameters of detector and instrument?

The basic incoherent-detection setup is shown schematically in Figure 2.2. Besides the detector, it is assumed to include:

- some optical elements that can add significant amounts of light to the beam, in addition to that provided by the signal power from a celestial source. The simplest example of the addition of such background light is thermal (blackbody) emission from the optical elements themselves, which is commonly the dominant background source at IR wave-

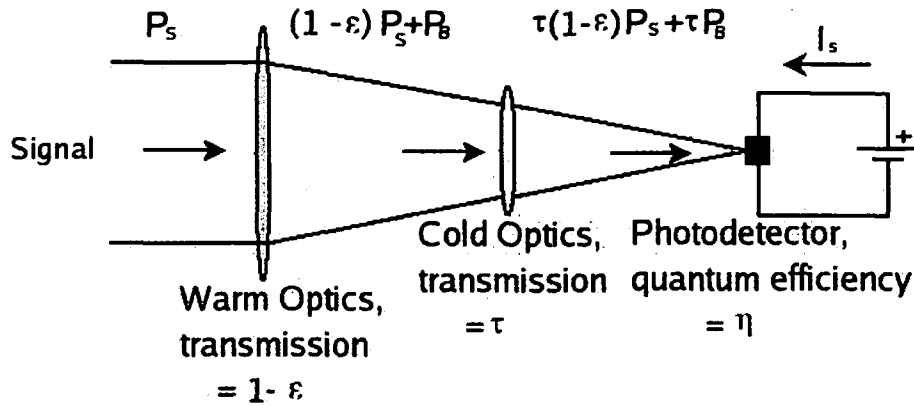


Figure 2.2: Light detection with photodetectors

lengths and longer ($\geq 2 \mu\text{m}$) for room-temperature optics. If the transmission of these optics is represented by $1 - \epsilon$, then the signal is reduced by that factor, that is, an incident power P_S is reduced to $(1 - \epsilon)P_S$, and ϵ , the effective emissivity of the optics, gives rise to thermal radiation in the amount

$$P_B = \epsilon B_\nu(T) \Delta\nu A\Omega = \epsilon \frac{2h\nu^3}{c^2} \frac{1}{e^{h\nu/kT} - 1} \Delta\nu A\Omega, \quad (2.6)$$

where T is the temperature of these optics, $\Delta\nu$ is the bandwidth of light which we are concerned (assumed $\ll \nu$), and $A\Omega$ is the area-solid angle product of the beam (assumed $\ll 4\pi A$). We will refer to any such optical elements as warm. At visible and shorter wavelengths, blackbody emission from optics at normal room temperature is negligibly small, so such optics can be considered cold in this wavelength range. However, other sources of background not easily described as thermal emitters can come into play, such as twilight, air-glow, and scattered streetlights in the case of a ground-based telescope. If the atmosphere above an earth-bound telescope has non-unit transmission, it can be considered among the warm optical elements. Most atmospheric absorption would be from the lower layers of the air, which we presume safely to be at the same temperature as the telescope.

- optical elements that do not add significant background, and by analogy to those discussed above can be called cold optical elements. This class of optical elements includes the filters (usually several filter elements) that determine the Full Width at Half Maximum (FWHM) bandwidth $\Delta\nu$ and center frequency ν of light transmitted to the detector, with peak transmission ($\nu < 1$) at the center frequency. Usually, "cold" for these optics means cryogenic temperatures, especially for IR wavelengths and longer. But detectors usually need to operate at cryogenic temperatures for best performance at $\lambda \geq 1 \mu\text{m}$, astronomical detectors are usually cooled to $T_{det} < 30 \text{ K}$ by use of liquid helium (boiling point 4.2 K at 1 atmosphere pressure), so filters are often made cold by placing them in the cryostat with the detectors.

Using IR and longer wavelengths as our example, just because there is a simple expression for the background emission in this range, the power incident through the warm and cold optics on the detector (one typical detector, if an array is used) is

$$P = \tau(1 - \epsilon)P_S + \tau P_B, \quad (2.7)$$

(see Figure 2.2), where P_B is given by Equation 2.6. We are trying to measure P_S , which is the power from the celestial source, within the wavelength band determined by the filters, and within the solid angle Ω . What would keep us from measuring arbitrarily small signal power in a given time is noise in the photocurrent. Usually, it is possible to design the readout circuitry so that Johnson noise is negligible compared to photocurrent shot noise, so it is this process we must consider.

2.3.1 Infrared Detector Technology

Infrared detector technology continues to advance at a rapid rate in astronomy [54]. Early infrared astronomers used thermocouples and thermopiles (a sequence of thermocouples combined in one cell) [43]. In the 1950's astronomers started to use Lead-sulphide (PbS) detectors to study infrared radiation in the 1 to 4 micron range [43]. When infrared radiation in this range falls on a PbS cell it changes the resistance of the cell. This change in resistance can be measured and is related to the amount of infrared radiation, which falls upon the cell. To increase the sensitivity of the PbS cell it was cooled to a temperature of 77 degrees Kelvin by placing it in a flask filled with liquid nitrogen. Astronomers now use InSb (Indium Antimonide), HgCdTe (Mercury Cadmium Telluride) and Ge:Ga (Germanium Gallium) detectors [103, 143]. These operate in a way similar to the Lead-sulphide detectors but use materials, which are much more sensitive to the infrared. The development of infrared array detectors in the 1980's caused another giant leap in the sensitivity of infrared observations [43]. Basically a detector array is a combination of several single detectors. These arrays allow astronomers to produce images containing tens of thousands of pixels at the same time. Infrared arrays have been used on several infrared satellite missions. In 1983 the IRAS mission used an array of 62 detectors. Astronomers now typically use 256x256 arrays (that is 65,536 detectors) [13, 43, 54]. Due to these breakthroughs in infrared technology, infrared astronomy has developed more rapidly than any other field of astronomy and continues to bring exciting new views of the universe [147, 148, 153, 154].

2.3.2 Individual Detectors

As mentioned in Chapter 1, IR starts to be considered different from the visible on technical grounds at a wavelength of $1.1\mu\text{m}$. This represented the limit at which individual photons could be detected, at least until recently. Typical detectors are classified as photovoltaic or photoconductive, according to whether they register photons by generating a current of electrons or merely by changing their resistance.

Detectors are made of semiconductors and rely on the excitation of electrons from an energy band in which they are immobile to the conduction band, where they are free to move about.

The difference in energy levels determines the minimum energy required of the incident photon if it is to have the desired effect. Materials that have suitable natural band structure are called intrinsic and those which are doped to provide suitable levels or bands are called extrinsic. The maximum wavelength that can be detected is given by the formula

$$\lambda_{cutoff}(\mu m) = 1.24E_{excit} \quad (2.8)$$

where " E_{excit} " is the excitation energy in electron-Volts.

The characteristics of a few common detector materials are given in the table 2.1 [43].

Material	Temperature (K)	λ_{cutoff} (microns)
Si	295	1.11
Ge	295	1.85
InSb	77	5.4
HgCdTe [152]	77	2.5
Si:As	5	23
Si:As [116]	5	30
Si:Sb	5	36
Si:Sb [116]	5	40
Si:Ga [76]	10	17.5
Ge:Ga	...	115
Ge:Ga(stressed) [150]	...	200

Table 2.1: Maximum usable wavelengths for several common detector materials

The smaller the band-gap, the more likely electrons are to enter the conduction band unwanted, by thermal excitation. It is therefore necessary to cool these longer-Wavelength detectors more than the shorter wavelength ones.

Detectors are characterized by their quantum efficiency, linearity, response time and dark current. The quantum efficiency is the fraction of the incident photons that produce collectible conduction electrons in the detector. The linearity of a detector must be checked, for example by observing standard stars of widely different magnitudes. Compensation must be applied if non-linear behavior is found. The response time of a detector to a change in photon flux is also an important characteristic, affecting readout speed and frequency response. The dark current is a source of noise. It consists of spurious conduction electrons arising from sources other than photon detections, such as thermal excitation and electrical leakage within the array. The readout noise is usually expressed as the error in determining the number of electrons collected during the period of exposure. It is more a property of the readout electronics than of the detector itself. For example, if an array has a readout noise of 30 electrons, it would be exceeded by the Poisson statistical fluctuations in the detected signal only if $\sqrt{n_e}$ exceeds 30, where " n_e " is the number of conduction electrons. Recent developments in detectors have included a solid-state photomultiplier which offers single-electron detection in the near- to mid-

IR. The principles of these devices were discussed in [100].

Photoconductors

A photoconductor, as its name implies, is a material which increases its conductivity when illuminated. From a noise point of view, it suffers the disadvantage that a current must be passed through it to detect the change in resistance produced. A common effect of this is noise with a power spectrum that varies according to $1/f$ (flicker noise), where f is the measuring frequency. Its extent is kept small by careful choice of contact type and bonding technique. It appears to arise where surfaces contact each other, for example between the very small crystals that make up a chemically-deposited PbS detector.

Photoconductors are usually made of doped Si or Ge. The dopant is chosen to provide impurity levels or bands at a level below the conduction band suitable for a particular range of IR photon energies. Detectors of this kind are favored for wavelengths beyond $5\mu\text{m}$. The choice of dopant also depends on the absorptivity of the compound at the wavelength of interest and the thermal dark current generated.

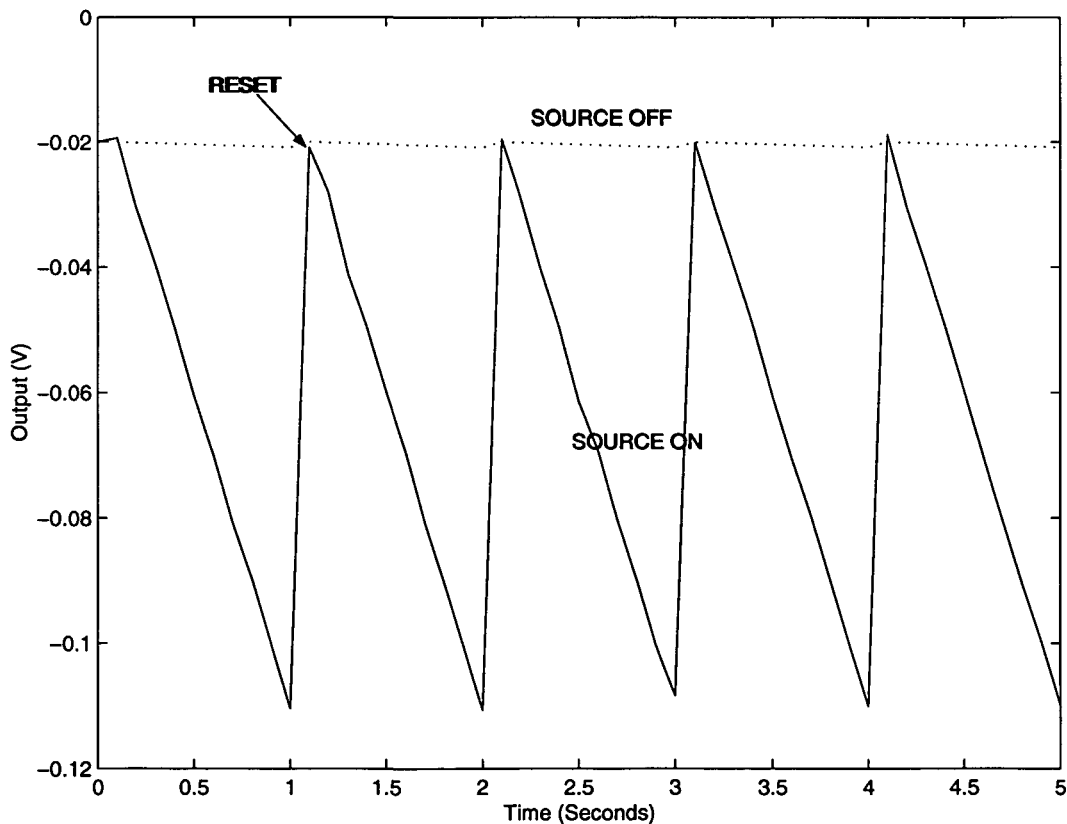


Figure 2.3: Typical photoconductor output signal

Photoconductive gain relates the number of electrons collected at the output of the device to the number of photons giving rise to conduction electrons. It is typically less than 1 due to loss of electrons to recombination before they are collected. However, in some devices, such as the solid-state photo-multiplier and some **B**locked **I**mpurity **B**and (BIB) detectors, gains in excess of 1 may be obtained, though often with the introduction of extra noise.

Figure 2.3 shows typical photoconductor signal using the Cryogenic Readout Electronic [81] with linear ramps. The bias was set to 100mV for the source flux of approximately 106 photons/s. The integration time (reset time) of this data is 1s. Difference between the integration ramps for the source on/off states is clearly seen.

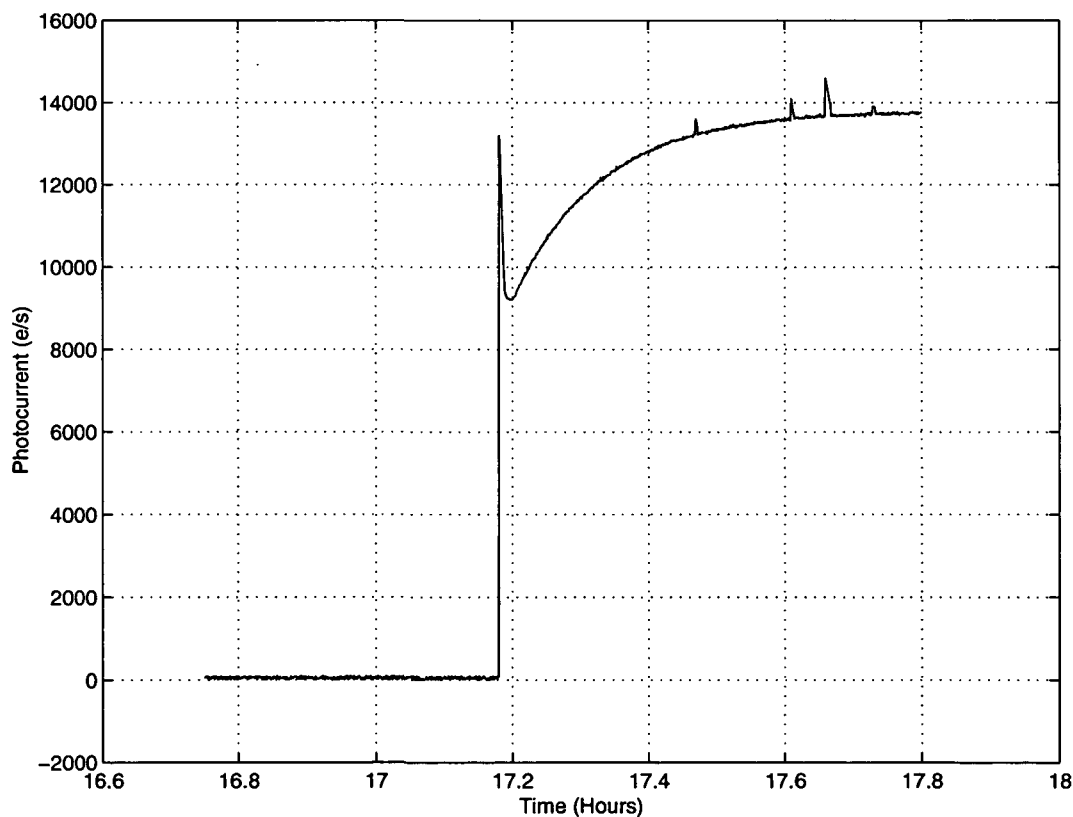


Figure 2.4: Ge:Ga response to step illumination change

Figure 2.4 depicts an example of the photoconductor signal behavior (Photocurrent) for the **M**ultiband **I**maging **P**hotometer for **S**pitzer (MIPS) instrument from the **S**pitzer **S**pace **T**elescope (SST) [154] (formerly SIRTf, the **S**pace **I**nfrared **T**elescope **F**acility). This space observatory has been launched last year and is already sending IR images from the Universe. This figure shows the response of a Ge:Ga detector to a step change in illumination. The detector shows a prompt response which is followed by a drop in photocurrent (the "hook") and

finally a slow increase to an equilibrium level (due to dielectric relaxation) [46]. Note that under the very low backgrounds for a space observatory, the dielectric relaxation time constant can be measured in hours. These non-ideal detector responses have posed significant problems in the calibration of photoconductor data, especially since the photocurrent as a function of time can depend on the illumination history in a complicated manner [110].

Photodiodes

Photodiodes (photo-voltaic devices) generate a current proportional to the number of incident photons. They are operated where possible at zero voltage, in a feedback circuit, to avoid $1/f$ noise. Generally, single-element detectors are limited by the input noise characteristics of the field-effect transistors that amplify their signals. Much better noise performance is usually obtained from modern array detectors than from single-element devices, essentially because the individual elements are physically small and so have small electrical capacity, making for a higher output voltage per electron, which overcomes the readout noise.

Figure 2.5 represents a typical output of a photodiode when reverse-biased, which is extremely linear with respect to the illuminance applied to the photodiode junction [56].

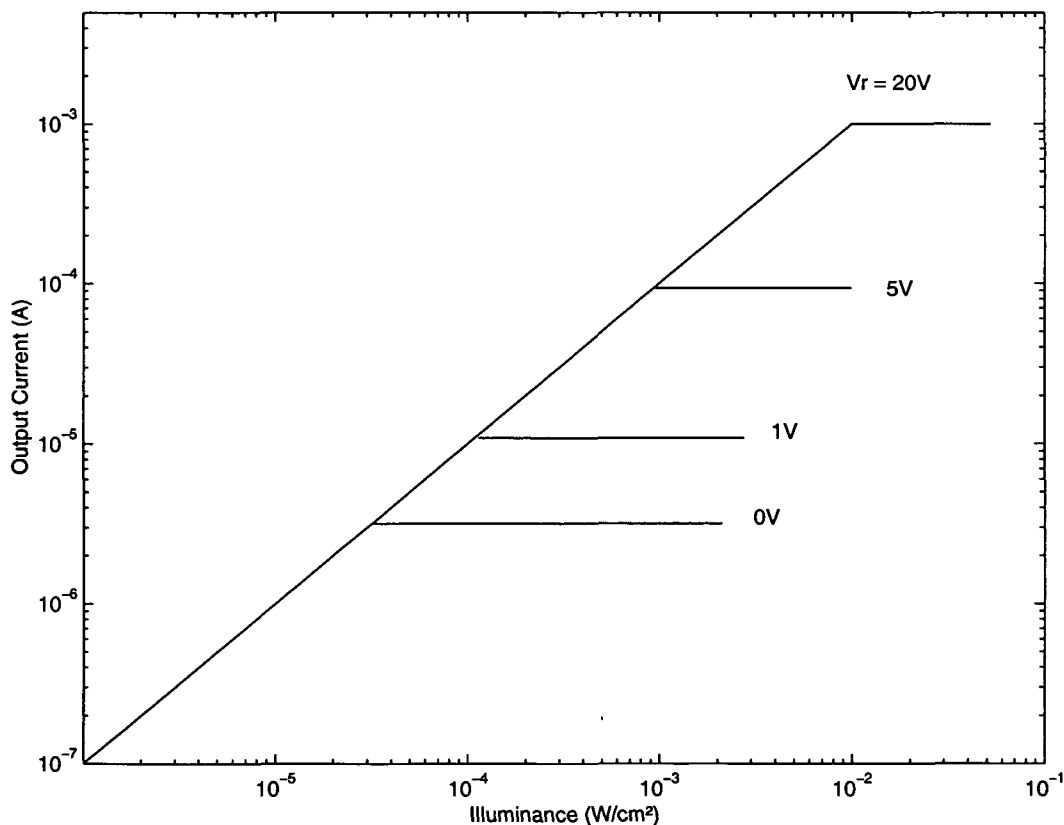


Figure 2.5: Linear photodiode output for reverse bias V_r

In many design applications, the designer needs to know the minimum detectable light (power) of the photodiode. The minimum incident power required on a photodiode to generate a photocurrent equal to the total photodiode noise current is defined as the Noise Equivalent Power (NEP).

$$NEP = \frac{\text{noise current}(A)}{\text{responsivity}(A/W)} \quad (2.9)$$

The NEP is dependent on the measuring system bandwidth. Since a photodiode light power to current conversion depends on the radiation wavelength, the NEP power is quoted at a particular wavelength. The NEP is non-linear over the wavelength range, as it is the responsivity.

Blocked Impurity Band (BIB) Detectors

When it is attempted to make heavily-doped extrinsic photoconductors (in order to obtain high quantum efficiency), it is found that the resistivity of the material becomes too low for the construction of a low-noise detector in the normal way. For this reason, an insulating layer of pure undoped material is introduced between the detector layer and the metallic contacts on the back of the device which are used to connect it electrically to its readout circuit. Such a layer allows the movement of charges promoted into the conduction band but blocks charge migration in the impurity band. (The other connection of each detector is made to an optically thin buried conducting layer on the input side.)

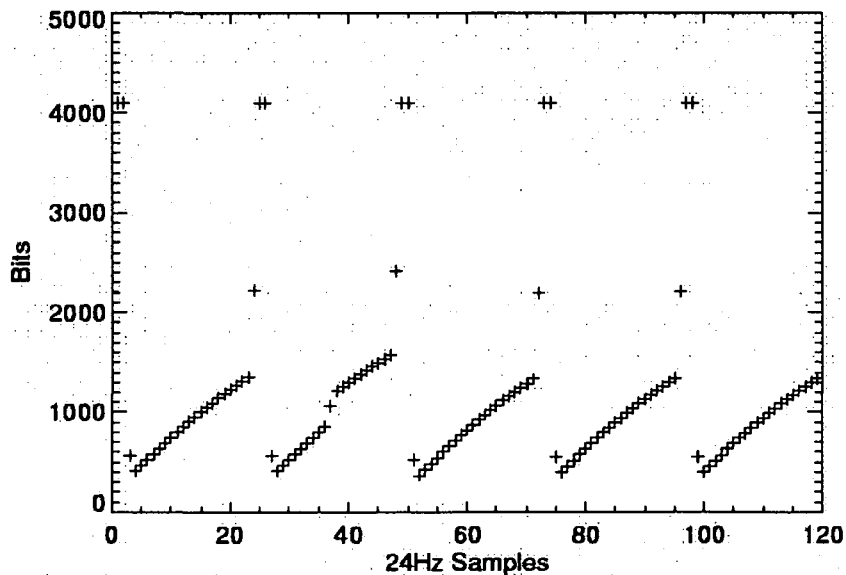


Figure 2.6. Example readouts, from part of an SWS observation. Note the glitch approximately half-way through the second slope, where the output suddenly increases. Also note the curvature in the slopes, caused by the AC filter

The same principle applies in the case of Impurity Band Conduction (IBC) detectors. The names BIB and IBC are used by Boeing (formerly Rockwell) and Raytheon (formerly Santa Barbara Research Center) for detectors constructed according to the same principle. Figure 2.6 gives a data example from the Short Wavelength Spectrometer (SWS) [65] Si:As BIB detectors from the ISO mission [147] in which the individual datapoints from the non-destructive readouts and reset pulses can be seen. The plot starts with a reset pulse, where the capacitor is short-circuited causing the bit readout to spike high. The system stabilizes after about four readouts, and as light falls on the detector, the charge on the integrating capacitor slowly increases. Careful analysis shows the system to require more than four readouts to stabilize.

Bolometers

An ideal bolometer, by definition, is a device that detects all the radiation falling on it. Although various forms of bolometers have existed for 100 years or more, astronomical interest is restricted to their modern form, in particular the Ga-doped Ge bolometer developed by Low (1961) [73] and doped Si devices operating on similar principles. These devices are neither photoconductors nor photodiodes.

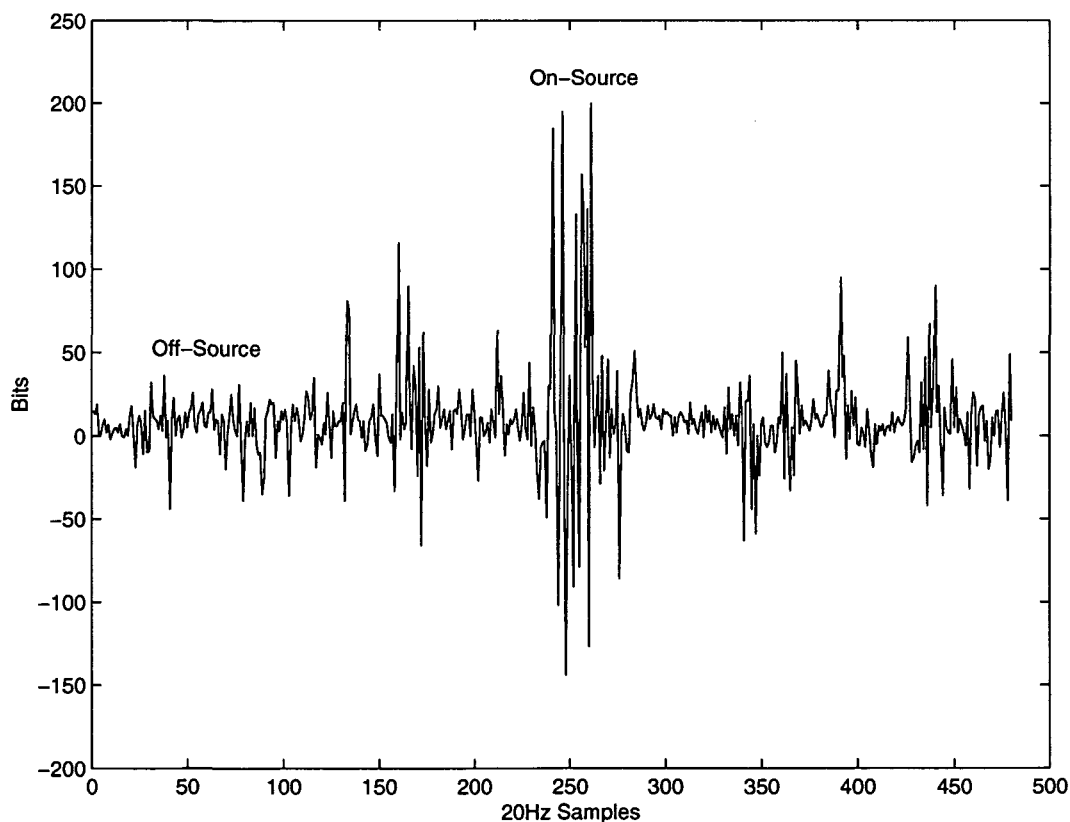


Figure 2.7: Example readouts from a PACS bolometer test

A typical detector consists of a small chip of the doped material supported by very thin wires, which act as electrical conductors for the measurement of its resistance and at the same time connect it to a heat sink with a certain thermal resistance, which has to be chosen in advance according to the background level of radiation that is expected to strike it. The doping level of the material is chosen to provide an optimum sensitivity of resistance to temperature at around its operating temperature, which is typically 1-2K. The surface of the detector is blackened with a suitable absorptive paint. The sensitivity of the device is wavelength independent, so long as the paint is absorptive and so long as the dimensions of the detector are larger than the wavelength of the radiation.

The coefficient of change of resistance with temperature of a Ga-doped Ge bolometer is dependent on its operating temperature, which means that it also depends on the background flux striking it. Since this may vary according to the filters in use, as well as ambient conditions, care must be taken to establish its sensitivity with sufficient frequency and for each waveband.

Figure 2.7 gives a data example from PACS [150] silicon bolometers operating at a temperature of 0.3K for wavelength range 60-210 μm . It is noted the signal difference between the off-source and on-source observation.

2.3.3 Detector Arrays

A multi-element array consists of a large number of picture-elements or pixels arranged in rows and columns. Whereas efficient visible arrays can be made on silicon and so are able to take advantage of mature manufacturing technology, the same is not quite true for the infrared. Infrared arrays are usually made at present as two-layered devices. The upper layer consists of a suitable infrared-sensitive material formed into photoconductors or photodiodes. The read-out of the array is done through the bottom layer, called the multiplexer, which is constructed using conventional Si-based techniques. The performance of the multiplexer is in many ways as critical to the success of the array as that of the IR-sensitive layer. The two parts are joined electrically with one connection for each pixel. The interconnection is achieved through the use of small indium pillars called "bumps". It is the ideal material for this purpose because of its malleability and low melting point. During manufacture, the two layers are aligned under an IR-viewing microscope and the bumps are welded by pressing them together. The layers of an IR array inevitably have different thermal expansion properties and repeated cooling cycles may lead to difficulties such as detachment of the bump bonds [43].

Each individual photodiode and its associated electronics (located on the silicon part of the device) possesses a certain electrical capacitance C . Normally the voltage V across this capacitor is set to a particular value (in the "reverse" or non-conducting direction of the diode) when the pixel is "reset" at the beginning of an exposure. Electrons released as a result of incoming photons discharge the capacitor according to the usual relation

$$\Delta V = \frac{\Delta Q}{C} = \frac{n_e e}{C} \quad (2.10)$$

where " n_e " is the number of electrons and " e " is the charge on an individual electron ($1.6 \times$

10^{-19} Coulomb).

Unfortunately, the capacitance of a diode is dependent on the voltage across it, so that the relationship between voltage and the number of photons is to some extent non-linear, requiring compensation during image processing. A discussion of this problem for the NICMOS 3 array is given in [77].

The lower the capacitance, the higher is the voltage developed for each photon and the easier it is to overcome the inevitable electronic background noise. However, the capacitance can only accept a certain number of electrons before it is fully discharged and, under conditions of high background, it is desirable that this quantity, known as the well depth should be as large as possible in order to permit reasonably long times between readouts. Thus the requirements for high and low-background conditions differ. The design of the multiplexer electronics for long-wavelength detectors is very much related to the background conditions that are expected. Different systems are used when the background is low, such as in space-borne cryogenic telescopes. Ground-based broad-band cameras have high backgrounds whereas ground-based spectrometers represent an intermediate case.

The duration of the exposure in an infrared camera is not controlled by a shutter because it would have to be cold to avoid radiating and also because it would usually have to be rapid-acting. Instead, the exposure time of a pixel is effectively the time between reset and readout. One position of the (cold) filter wheel is usually made opaque to enable measurements of the array to be made with no radiation falling upon it.

Readout Electronics

The readout of most IR arrays is called direct, because the voltage levels of the pixels are read out directly, one-by-one, unlike in a visible-region Charged Coupled Device (CCD), where the charge is first fed to a resettable integrating circuit. In a direct array, a pixel to be read out is "addressed" by its x and y coordinates, and the voltage on the pixel, buffered by its private source follower, is connected directly to the output bus of the chip. Each pixel also has a mosfet switch, which can be used to connect it to the reset bus, if resetting is desired [43].

To avoid the problem of non-linearity caused by storing charge within the detector, a variant on the standard readout circuitry has been developed, incorporating a Capacitive Trans-Impedance Amplifier (CTIA). Each detector is connected to a high-gain DC amplifier with capacitive feedback. The photocurrent is collected in the feedback capacitor C until it is discharged by a MOSFET switch. The output voltage of the stage is given by $V = n_e / C$. The potential across the detector is automatically kept constant and near zero by this type of circuit. In addition, the well depth can be made arbitrarily large by choice of the value of C. A discussion of amplifier performance was given in [60]. Most present-day multiplexers use on-chip shift registers to generate the pixel x and y addresses sequentially, rather than individual address lines or address decoders.

Readout Modes

Every measurement of the number of electrons collected on a pixel has noise associated with it. If the number of electrons is n_e , the noise from Poissonian statistics alone is $\sqrt{n_e}$. However, when the number of electrons detected is small, the Poissonian noise may often be smaller than the RMS readout noise associated with the read-out process of the array itself. This latter type of noise, as for a single detector, is usually expressed in terms of equivalent numbers of electrons. In what follows, it will be seen that noise may be minimized by attention to the employed readout procedure [43].

A. Noise Reduction: Because a direct readout array can be read many times without affecting the charges accumulated on the individual detectors, an improvement in the random readout noise can often be obtained by making multiple measurements and averaging them. If the Poissonian noise of the collected electrons should be dominant, naturally no improvement will occur. In arrays that show glow from their output amplifiers, multiple readouts may actually increase the Poissonian noise by increasing the background.

B. Simple Readout: In this mode, an exposure is made by simply resetting each pixel, exposing, and reading the voltage developed at the end of the exposure time. Unfortunately, this method is very noisy due to uncertainty in the voltage level at the start of the exposure, arising from a fundamental limit to the accuracy of the reset process called *kTC Noise*. This noise associated with the gate capacitor of a Field-Effect Transistor (FET) and can be non-negligible. The output RMS value of this noise voltage is given by:

$$kTC \text{ Noise}(Voltage) = \sqrt{\frac{kT}{C}} \quad (2.11)$$

where C is the FET gate switch capacitance, k is Boltzmann's constant, and T is the absolute temperature of the CCD chip measured in Kelvin.

C. Correlated Double Sampling: Correlated double sampling involves making two measurements: one directly before a change being measured and the other directly afterward. By taking the difference, the effects of

- the uncertainty in the initial voltage level and
- the long-term (i.e. low-frequency) drifts

are reduced. This technique is used very effectively in reading out the charge packets from CCDs such as visible-region arrays and some early IR. Correlated double sampling may be used with direct readout arrays by making the first measurement at the time a reset is performed or directly afterward. The second measurement is made at the end of the exposure, just before the next reset.

D. Reset-Read-Read: In this improved version of correlated double sampling, all pixels of the array are reset in sequence before the beginning of an exposure, without reading the output voltages (e.g. [38]). The completed reset is followed by the first readout sequence. The array is read out again at the end of the exposure time. The desired signal is the

difference between the two reads. This is the basic procedure in use at the present time (e.g. [13]).

E. Multiple Fowler Sampling: By reading the whole array " n " times each at the beginning and end of the exposure, and averaging before subtraction, the noise may be reduced by a factor of order " \sqrt{n} ". It is important to note that each pixel must be addressed freshly each time it is read. The noise reduction does not occur if the signal is merely digitized " n " times. The source of the noise is related to the addressing of the pixel, though its cause is not well understood. The signal-to-noise ratio produced by multiple sampling has been examined by Fowler and Gatley [38] and Garnett and Forrest [42]. They show that in the read-noise limited case, optimal results are obtained by sampling continuously for the first and last thirds of the exposure but omitting the middle third.

F. Continuous Readout: It is still possible to optimize the readout further by the technique of continuous readout, where the readout process begins at the start of the exposure and continues (without reset) until its completion. The output voltage is closely proportional to the integration time and the slope of its value vs time becomes the measured quantity. Each measurement effectively reduces the error in slope, so that the readout noise experienced in ordinary correlated double sampling is again reduced.

In [42], it is also shown, again for the read-noise limited case, that this line-fitting process is slightly superior to optimal multiple Fowler sampling.

Array Controllers

The controller is an electronic box which provides a variety of well-stabilized fixed voltage levels and pulsed waveforms suitable for driving the x-y addressing elements and reset circuitry of the array. In addition it controls the operation of one or more sampling voltmeters used to measure the output signals. The latter depend on analogue-to-digital converters, which usually have a resolution of 16 binary bits (65536 discrete levels). The speed with which the converters can function, determines the time taken to read out the array, together with the bandwidth of the multiplexer electronics and the transfer characteristics of the signal train. It is always desirable to keep these as short as possible in the interests of efficiency, but it becomes essential when the background is high and array has to be read out many times per second.

Handling of Arrays

Infrared array detectors are exceedingly expensive even when compared to visible CCDs, thanks to their experimental nature and the small numbers of them that are produced. They are also very liable to damage through static electrical discharge and have to be handled very cautiously with this in mind. Some arrays are imperfectly "passivated", i.e. they are liable to change their behavior if exposed to ordinary levels of atmospheric water vapor. The degradation produced in this way is, however, generally reversible by baking the array at moderate temperatures under high vacuum.

2.3.4 Efficiency of a System

The design of an infrared astronomical instrument is governed by the need to maximize the signal-to-noise ratio (Equation 3.10) of its output. Clearly, it is necessary to keep the throughput of photons as high as possible and to minimize the extraneous background [43].

Throughput

In an instrument such as a camera, spectrograph or photometer, the throughput will be the product of factors listed in Table 2.2

Considerations
Atmospheric Transmission
Reflectivity of Mirrors
Telescope Secondary Mirror Obscuration
Dewar Window Transmission
Lenses Transmission
Filter Transmission
Efficiency of Diffraction Grating
Detector QE

Table 2.2: Summary of efficiency considerations [43]

Choice of Pixel Size

The individual picture-elements of an array are called pixels. For optimum accuracy and sensitivity, the focal plane scale of the telescope must be matched to the pixel size. For example, if the seeing is about one arcsec FWHM, the pixel scale should correspond to about 2-3 pixels per arcsec to ensure good sampling for accurate photometry. On the other hand, if adaptive optics are used, a much larger number of pixels per arcsec may be appropriate, since the images themselves will be smaller.

In general, it is undesirable to over-sample an image because the readout noise will increase according to the number of pixels involved in each stellar image. Many camera designs incorporate focal reducers of different ratios so that an appropriate choice can be made according to the prevailing seeing. As the numbers of pixels in an array increase, the demands on the optical designs of focal reducers become more severe. The wavelength range coverable by e.g. an InSb detector may require that two focal reducer lenses are used so that their designs can be optimized for particular wavelength ranges [43].

The Unwanted Background

For ground-based instruments, the background against which the faint astronomical sources must be detected arises from the sources listed in Table 2.3. The noise from these sources is equal to the square root of the number of photons emitted per second.

Background Elements
Atmospheric Emissivity
Emission of Telescope Mirrors
Emission of Telescope Structure in Beam
Emissivity of Warm Windows
Emissivity of Surfaces within the Cryogenic Vessel
Scattered Light within Instrument

Table 2.3: The unwanted background [43]

If the background seen by a detector arises entirely from objects at ambient temperature, then in the near-IR, a change of temperature can make a considerable difference to its level because of the rapid rise of the blackbody curve at its short-wavelength end.

Low-temperature telescopes and detector surroundings remain essential if the full advantages of space-borne instrumentation are to be realized. It becomes possible to cool the telescope itself to very low temperatures without fear of condensation of atmospheric gases, and very low backgrounds may be obtained [43].

2.3.5 Seeing in the Infrared

Atmospheric Turbulence

The angular resolution of all but the smallest telescopes is limited by the turbulence of the Earth's atmosphere, which gives rise to the blurring of images called seeing. Ideally, the image of a point-like source in the focal plane of a telescope should be a classical diffraction pattern with its strong central peak. In practice, the time-averaged image of such a source resembles a two-dimensional Gaussian distribution. The usual measure of seeing quality is FWHM of the distribution. The quality of the image produced by an optical system may also be described by its Strehl ratio, which is the ratio of its intensity on-axis to that, which would be produced if there were no aberrations [43].

Seeing in the infrared is somewhat better than in the visible. Provided the intrinsic minimum given by the diffraction limit of the telescope does not come into account, it is found that

$$Image\ Size \propto \lambda^{-0.2} \quad (2.12)$$

Thus at $16\mu\text{m}$ the images should have half the extension that they have at $0.5\ \mu\text{m}$.

Seeing Compensation

By means of adaptive optics, a way for compensating the aberrations introduced by atmospheric turbulence within the telescope, the seeing quality can be improved. The possibilities offered by this technique are much more easily realized at IR wavelengths than in the visible. The wavefronts of the light from a star as they enter a large telescope are bent and distorted from their passage through the Earth's atmosphere, so that as the light strikes the mirror it is in phase over only small regions of the pupil, causing the instantaneous image of a point source to appear as a series of "speckles". The scale length over which phase coherence is preserved, is called the Fried parameter, r_0 [43]. It is a function of wavelength λ and zenith angle ζ :

$$r_0(\lambda, \zeta) \propto \lambda^{6/5} f(\zeta) \quad (2.13)$$

In the near IR, the image formed by a 2m or similar-sized telescope in good seeing is dominated by a single large speckle moving about in the focal plane [43].

Isoplanatic Angle

An important concept in seeing compensation is the isoplanatic angle, namely a radius of a circle in the sky over which the atmospheric wavefront disturbances can be considered identical. It is thus a measure of the size of the region over which diffraction-limited images might be obtained with ideal adaptive optics.

The timescale of image motion is proportional to the Fried parameter, so that the reaction time needed in the adaptive optics can be longer in the IR than at shorter wavelengths [43].

Guide Stars

The operation of adaptive optics depends on having a suitably bright guide star from which the corrections to the wavefront may be determined. Thus only fields within the isoplanatic angle of such guide stars can be observed in this way. Although the requirements ease with increasing wavelength, the usable regions are quite limited.

The use of artificial guide stars generated by lasers has been demonstrated [43].

Some account of military work in this field has been also given in [41]. Lloyd-Hart et al. [71] present some astronomical images which have been sharpened using this technique.

Tip-Tilt and Software Seeing Compensation

The lowest order distortion produced by the atmosphere amounts to a linear shift of the image in the focal plane of the telescope. This term is a large fraction of the image degradation produced and it is relatively easy to design equipment to compensate for it [22]. The isoplanatic field that applies to translational motion of the image is larger than that for full (diffraction-limited) correction. The response time of the compensation system may be longer and guide stars from a larger area of sky may be used. Close and McCarthy [22] describe an adaptive tip-tilt secondary system and camera called FASTTRAC, attached to the 2.3m telescope at Steward Observatory. They report a factor of two improvement in the Strehl ratio in the H-band, using a guide camera

operating at K.

Tip-tilt compensation can also be applied in software when the readout rate of an array is sufficiently rapid. The displacement of a bright star in the field of an individual exposure can be measured and used to counter-shift the digital data before co-adding.

2.3.6 Some Representative Instruments

In the following sections some simple, representative instruments are discussed. The infrared accessories for the 8-10m telescopes completed or near completion are similar in principle to those described, but differ in terms of size, versatility and engineering complexity [43].

Photometer

Simple single-channel photometers still offer the best method for obtaining high-precision photometry of moderately bright uncrowded objects. Traditionally, star-sky chopping was accomplished by a rotating multi-bladed mirror and a fixed mirror in the focal plane, but this arrangement led to extra noise at longer wavelengths (from diffraction of the moving mirror edges and imperfect matching of the pupil in the two positions) and defocusing of the image. Chopping is normally now accomplished by means of a stepwise oscillating secondary mirror within the telescope, which effectively creates two positions on the sky, or beams, viewed alternately by the detector. It is passed to a phase-sensitive detector (lock-in amplifier) which automatically subtracts the signal in one sky patch from that in the other, synchronously with the chopping action. The difference is integrated and recorded. By moving the telescope periodically, say every 20 seconds, so that the objects is placed first in one beam and then in other, residual "second-order" background can be subtracted. (This background arises from the fact that the detector captures slightly different parts of telescope structure in the two positions of the chopping secondary.)

Camera

The essential parts of an IR camera can be found in [43]. The field lens lies in the focal plane of the telescope and forms an image of the exit pupil on a cold stop, close to whichever re-imaging lens is in use. Re-imaging allows for magnifications of 1:1 and 1:0.5, to allow for different seeing conditions or fields of view. Baffles are employed to reduce the effect of stray light. Larger arrays mainly differ by having more elaborate optical components. For example, fast doublet re-imaging lenses distort too much when used with larger arrays and better focusing of the telescope exit pupil on the cold stop is achieved with an achromatic field lens.

- Array Camera Sensitivity

The sensitivity of an IR camera operating under background-limited conditions can be estimated from the following formula, based on Poissonian statistics, for the SNR in combination

with a known value on some particular telescope with the same thermal and night-sky background per arcsec²:

$$S/N \propto D \left(\frac{t\eta}{N_{arcsec^2}} \right)^{1/2} \quad (2.14)$$

where D is the diameter of the telescope, t is the integration (exposure) time, η is the quantum efficiency of the detector and $N_{arcsec^2}^2$ is the number of arcsec² over which the image is spread. The last factor, $N_{arcsec^2}^2$, enters because the level of the background is proportional to the area covered by the image [43].

Spectrometers

In a spectrometer, the area of the sky to be measured is defined by a cold slit or aperture. The next component in the optical path is a collimator, which renders the rays parallel before they strike a diffraction grating at the image of the telescope exit pupil. The diffracted rays are then focused by a "camera" onto the detector array.

There are many alternatives on this simple theme. A high-dispersion spectrograph can be constructed by having an echelon grating and an order-separating prism, so that a long spectrum can be placed in parallel segments onto a detector array. A grism (grating-prism combination in a single optical element) can be used in a camera to give spectroscopic coverage of a whole field. The prism component deflects the spectrum at mid-range to compensate for the deflection of the grating, so that the combination acts as an in-line disperser. Examples of such an instrument are the NICMOS camera [152] of the Hubble Space Telescope (HST) [151] and the IRIS camera of the Anglo-Australian Observatory (AAO) [2].

Efficient baffling is even more important in a spectrometer than in other IR instruments, because each pixel of a camera is receiving a very small fraction of the desired spectrum. Astronomical spectrometers for the 8-m and other large telescopes have been described in the literature. Their optical layout is usually complicated by the need for versatility (many dispersions and wavelength ranges) and compactness, which involves "folding" the long beam paths with plane mirrors.

In practice, sensitivity can be calculated as for a camera but allowing for the inefficiency of the extra optical components, especially the grating. The entrance slit may also be undersized for good resolution, at the expense of the amount of light entering the spectrometer, and the response pattern at a particular wavelength may be spread over many pixels.

- Fourier Transform Spectrometers (FTS)

Fourier transform spectrometers, based on the Michelson principle [20], offer very high resolution but are confined to the examination of bright objects. They are uncompetitive for faint ones because they use one or two detectors which receive the photon noise of all wavelengths (within the range selected by cold pre-filters), whereas more modern spectrometers are based

on arrays and each detector receives only the flux associated with its wavelength interval. The achievements of FTS have been summarized by Ridgway and Brault [99].

2.3.7 Observing and Data Reduction

Before planning an observing program, it is necessary to understand the procedures involved in data reduction. A typical exposure contains, besides the desired image, background contributions from telescope and atmospheric radiation. In addition, the sensitivity (quantum efficiency) will vary across the array and there will be numbers of bad pixels, which may be dead (insensitive) or have excessive dark current (and hence noise).

The typical night might include flat field exposures for each band in use, telescope focus exposures, standard stars, program objects and comparison fields. The well-known data reduction packages such as IRAF (Kitt Peak National Observatory), MIDAS (ESO), FIGARO (AAO), STARLINK (Rutherford-Appleton Laboratory) and ISO contain routines, which can be used for infrared image reduction. Amongst these is the important facility to mosaic a group of small-area images into a large final product.

Some on-line reduction facilities should be available for checking each image immediately after acquisition, in case a repeated exposure should be necessary. For example, it is possible to subtract a previous frame, taken with the same filter and exposure time, to get a rough image. Some stellar images can be examined rapidly by a Gaussian fit to check the focus, the seeing and the image quality before moving on to the next exposure [43].

Array Problems

The on-chip output amplifiers of many arrays have the undesirable property that they glow in the infrared, causing pixels in their neighborhood to show high background levels. This effect can be mitigated by operating the output circuitry at the lowest possible current levels for proper operation and by switching it off during exposures.

Arrays frequently suffer from other problems such as memory effects, which cause images from previous exposures to re-appear as ghosts on later ones, especially when the electron storage capacity of the array has been saturated by exposure to excessively bright sources. This problem can sometimes be reduced or eliminated by multiple "pre-wipes" to read out the charge very thoroughly.

Long-wavelength arrays on satellites often change their characteristics due to bombardment with charged particles, such as are encountered when passing through the van Allen Belts, and some form of annealing, such as a partial warming-up, may be necessary after each such occasion [43]. The behavior of the NICMOS camera and arrays on HST, and the cameras on ISO have been investigated in detail and several papers have been devoted to them (see [151] and [147] for more details).

Linearizing

As mentioned in previous sections, the data from infrared arrays may need to be linearized before further processing. The linearizing consists of fitting the signal to the theoretical model (expected detector output) in order to reduce the noise (electronics, readouts).

Removal of Instrumental and Sky Background

In principle, for a well-behaved detector and atmosphere, a frame can be cleaned of extraneous background by subtracting a sky frame of equal exposure time, made at a nearby position that does not contain astronomical objects. For large-format detectors, suitable patches of blank sky may be impossible to find.

At long wavelengths, very short exposures may be made in synchronism with chopping. The individual exposures may be added to, or subtracted from, an image accumulator according to the position of the chopper. In this way, the first-order background is reduced. The telescope may also be moved periodically, and a second subtraction is performed, to eliminate residual effects caused by differences in the thermal radiation seen by the detector in the two positions of the chopper [43].

Dithering: Dealing with Bad Pixels

Dithering refers to a technique where several exposures are made with the position of the telescope slightly displaced each time, relative to the field center. The displacements may be larger or smaller than the pixel spacing, according to the type of problem to be overcome [43].

A. Overcoming Background Variations: If dithering is used to overcome background variations, exposures may be made with shifts greater than the size of a stellar image, so that the median averaging process works properly. Of course, if the field is very crowded, chance coincidences of images on the shifted frames may lead to median averages which do not represent the true background.

B. Isolated Bad Pixels: When there are many isolated bad pixels, a set of exposures with the telescope displaced successively by one pixel width may be obtained. During data processing, the numerical images may be counter-displaced. A perfect final image is then formed by median-averaging the re-centered images pixel-by-pixel. Isolated anomalous pixels are eliminated in this way. Alternatively, bad pixels may be mapped and "bridged over" by replacing them with the average value of surrounding good pixels, though this is not to be recommended.

C. Undersampling of Images: When a stellar image is undersampled, i.e., there are too few pixels per image, it can be profitable to make multiple images with sub-pixel displacements of the field. This ensures better photometry by reducing effects due to non-uniform sensitivity across pixels or dead spaces between them.

Sky Frame from Median Averaging

The median average of a set of measurements is the value, which has equal quantities of individual measurements above and below it. For large samples with a Poissonian distribution, it approaches the mean value.

As mentioned, a sky frame without stars is often impossible to obtain. An "empty" sky frame may be generated by median averaging a number of frames of different fields, obtained with the same exposure time and filter etc. The stellar images are eliminated by this process if the fields are reasonably sparsely populated. However, before median averaging can take place, it is usually necessary to adjust each pixel of the frame by a uniform amount for variations in the background level, so that the mode (most frequently obtained pixel value) of each is the same.

In survey work, determination of the sky level by median averaging saves time by removing the necessity of taking equal numbers of empty frames. The subtraction of a sky frame will, of course, increase the random background noise of the reduced data. However, by taking a large number of background frames and median averaging them, this source of additional noise can be made negligible [43].

A. Flat Fielding: The sensitivity of the detector can be normalized by dividing it by a flat field frame. Such a frame is constructed by observing the uniform source, for example a screen or a featureless piece of sky, and subtracting a dark frame of equal duration. In the case of a screen, a flat field free of telescope background and scattered light can be obtained by subtracting an exposure with the illumination off, from one with illumination on. This process can be repeated a sufficient number of times and the results averaged to make the flat field essentially noise-free.

B. Standardization: For accurate work, measurements of standard stars should be undertaken with sufficient frequency. These stars should be as near as possible in zenith angle to the measured object to reduce errors due to imperfectly known extinction coefficients. Ideally, they should be of similar color to the objects of interest in the infrared. On-line reduction is valuable in assessing the photometric quality of the night and hence the frequency with which standards must be observed.

C. Extraction of Photometric Information: The positions and intensities of stellar images may be extracted efficiently and automatically by using a program (see [147, 148] for more information). Such a program makes optimum fits to the images to reduce the contribution of pixels with insignificant data to the noise. Calibration must be done separately, for example by using "aperture photometry" on the images and comparing the results with the standard values. Corrections for extinction as a function of airmass must be applied when standardizing the photometry.

2.4 Aspects of Infrared Astronomy

Infrared astronomy includes the detection and study of the IR radiation (heat energy) emitted from objects in the universe. Every object that has a temperature radiates in the IR. Much of the information sent by the universe, in the form of electromagnetic radiation (or light), is in the IR, which cannot be seen with visible light telescopes. Only a small amount of this IR information reaches the Earth's surface, yet by studying this small range of wavelengths, astronomers have uncovered a wealth of new information. Only since the early 1980's we have been able to send IR telescopes into orbit around the Earth, above the atmosphere, which hides most of the universe's light from us. The new discoveries made by these IR satellite missions have been astounding. The first of these satellites - IRAS [148]- detected about 350,000 IR sources, increasing the number of cataloged astronomical sources by about 70 %.

Many objects in the universe, which are much too cool and faint to be detected in visible light, can be detected in the IR. These include cool stars, IR galaxies, and clouds of particles around stars, nebulae, interstellar molecules, brown dwarfs and planets. For example, the visible light from a planet is hidden by the brightness of the star that it orbits. In the IR, where planets have their peak brightness, the brightness of the star is reduced, making it possible to detect a planet in the IR [43]. Many of the most interesting IR objects are associated with star formation. Stars form from collapsing clouds of gas and dust. As the cloud collapses, its density and temperature increase.

We often think of the vast areas of space between the stars as being completely empty. However, this is not really true. Much of the space between the stars is filled with gas (primarily hydrogen and helium) and tiny pieces of solid particles or dust (composed mainly of carbon, silicon and oxygen) [43]. In some places, this interstellar material is very dense, forming nebulae. Figure 2.8 shows an IR view of the gas and dust along the plane of our galaxy 'Milky Way' with areas of dense gas and dust as well as areas, which are nearly empty.

Typical object structures in IR astronomy can be summarized under the following categories [43, 88]:

- **Point sources** (e.g. field stars): mainly young and late-type stars are embedded in a diffuse circumstellar medium that reduces the contrast between the objects and their surroundings.
- **Diffuse sources** (e.g. nebulae): some nebulae show filamentary structures and/or knots with irregular edges.
- **Sources of different morphological types** (e.g. galaxies): some galaxies show extended structures like spiral arms, in which the IR emitting dust is concentrated

Figure 2.9 shows examples of astronomical objects observed at infrared wavelengths with ISOCAM [13, 147]. Figures 2.9.A-G are images for different types of objects already reduced for cosmic particles while Figure 2.9.H depicts ISOCAM raw images in 5.04 sec integration time with cosmic particles influence from the solar flare. Figure 2.9.A and 2.9.B present a mosaic of an array of 32x32 pixels, at several positions, for galaxies observed by ISOCAM. Figure 2.9.E depicts galaxies at larger distance. Figure 2.9.C and 2.9.F show unresolved sources

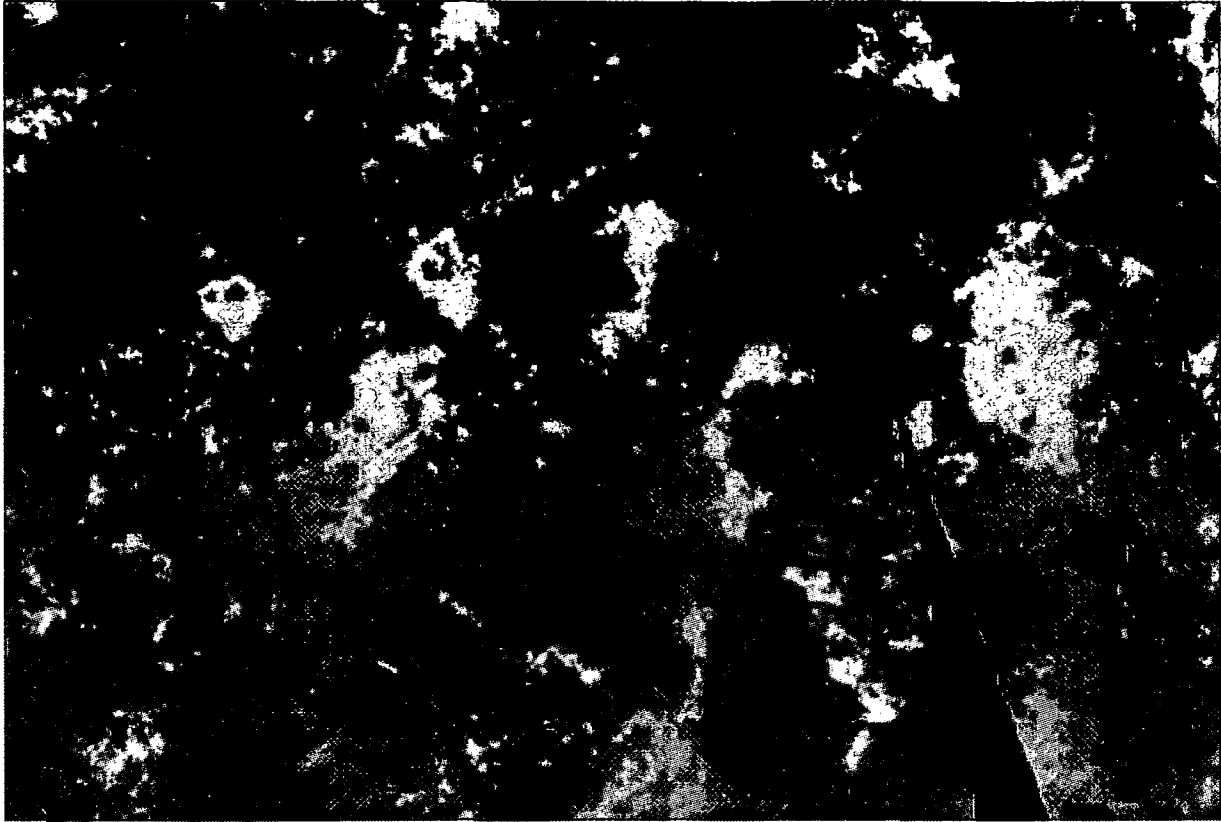


Figure 2.8: Milky Way galaxy seen by IRAS

where the objects of interests are blue dots (Figure 2.9.C) and white dots (Figure 2.9.F) with size of a few pixels. Figure 2.9.D and 2.9.G are respectively resolved circumstellar shell and resolved bright object (Jupiter) observed with ISOCAM.

The images shown in Figure 2.9.A-G are already reduced, freed from cosmic rays and the background problem. Works for the reduction of the raw data related to these images can be found in the papers [55, 108, 124, 132]. The simplest objects are blobs brighter than the background, which may either have a Gaussian-like spatial distribution of pixels or a relatively simple internal structure like 1 or 2 highlights of the blob. More complex objects are formed by constellations of simple objects with a particular structure like a spiral. The existence of a correlation, anticorrelation or non-correlation has important consequences for the interpretation and compression of these observable quantities, which emerge from a combination of physical quantities [39]. Relations between images are generally analyzed with the pixel-to-pixel correlation function. However, this method gives little information in the case of an anticorrelation on the scale of spiral arms, like in M51 (Figure 2.9.A), or when the diffuse emission on larger scales has no counterpart in the other image (e.g. polarized IR emission) [74]. One alternative is to use the multiscale analysis for these images to detect the dominant scales in this galaxy and also to see if the decomposition can be useful to determine the statistical characteristics for given scales in the maps. These characteristics can be exploited for the compression purpose.

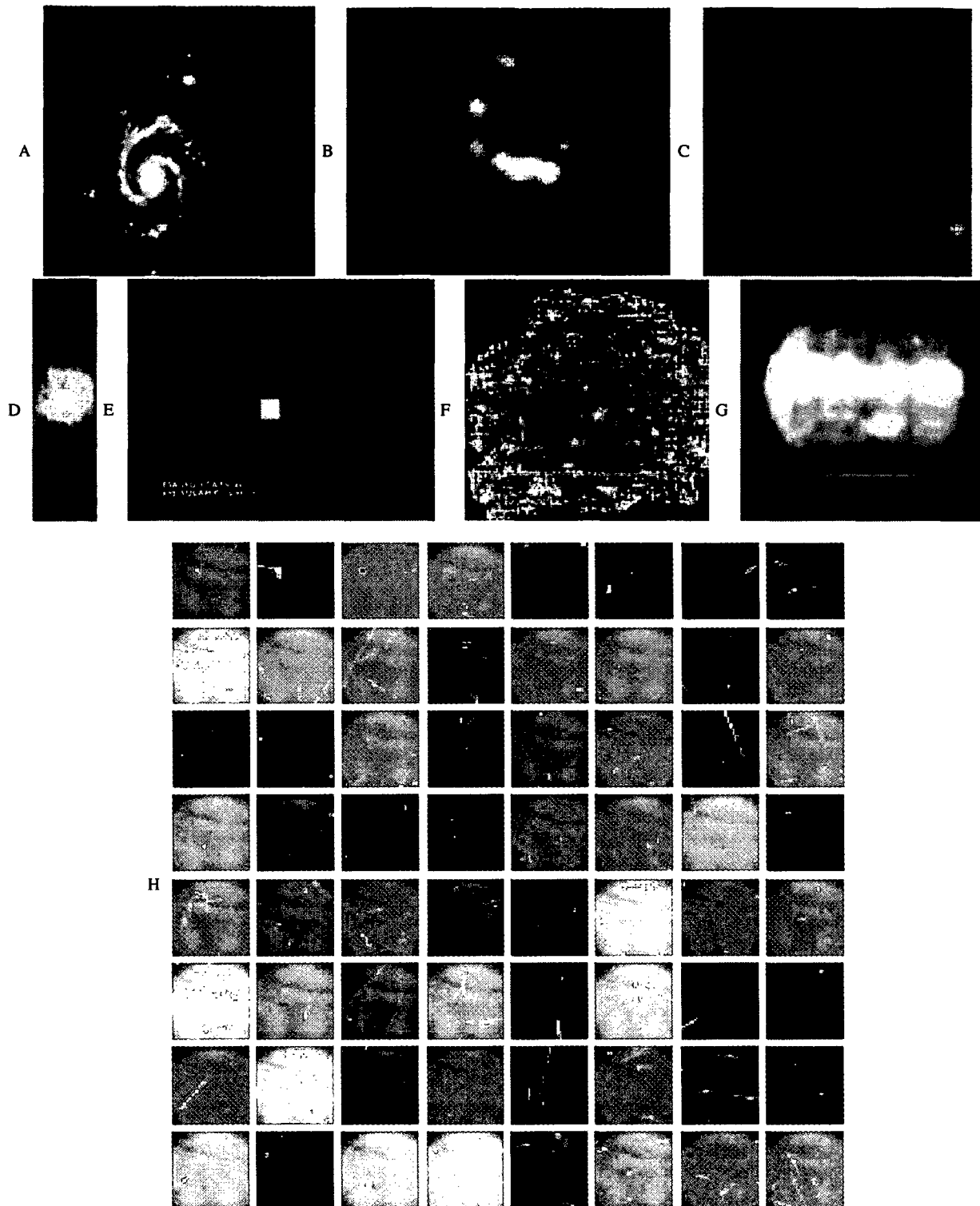


Figure 2.9. Examples of astronomical objects observed by ISO at infrared wavelengths. A: Grand Design Spiral M51. B: Interacting Galaxy Pair "Antennae Galaxies". C: Quasar (Unresolved Source). D: Resolved Circumstellar Shell. E: Interacting Pair ARP220 at Larger Distance. F: Very Deep Integration in the Hubble Deep Field. G: Resolved Bright Object "Jupiter". H: Cosmic Particles Influence in ISOCAM Raw Images

Chapter 3

Preliminary Notions and State of the Art Data Compression

First, the existing noise models, relevant for astronomy applications, are introduced. Then, the formal definition of data compression is presented and the typical data compression concept is depicted. Furthermore, state-of-the-art assessment criteria for compression methods are listed. Then, the research status of the area "data compression" relevant for the dissertation goals are presented. In Section 3.6, a list of methods used for compression is given in a chronological form starting from DCT [109] up to the multiscale approach [117]. Recent multiresolution methods like the CurVeleT (CVT) [17] and the ConTourleT (CTT) transforms [28] that are susceptible to be used for image compression are also presented in Section 3.6. Moreover, relevant approaches for linear approximation of detector measurements, which can be exploited by the compression method are presented. Then, state-of-the-art entropy coders are given. Section 3.7 lists the state-of-the-art compression methods used for space applications, which include HCOMPRESS [134], FITSPRESS [95] and the Pyramidal Median Transform (PMT) [117].

3.1 Noise Generalities

Data and images generally contain noise. In most applications, it is necessary to know if a data element is due to signal (i.e. it is significant) or to noise. Generally, noise in astronomical data follows a Gaussian or a Poisson distribution, or a combination of both [117]. The noise in IR astronomy has several origins: the detectors noise, the amplifier noise, the electric cross-talk noise, the photon-shot noise or the pick-up noise [117]. Furthermore, astronomical data suffer from cosmic ray impacts (glitches) and the transient behavior of the detectors, which may cause potentially scientific data loss in case of integration over several samples for compression purpose. Therefore, a deep investigation has to be made in order to prevent this noise before data compression, because IR space observatories are frequently confronted with this type of noise. In the following, the existing noise models are summarized.

3.1.1 Thermal or Johnson Noise

Johnson and Nyquist in the 1920s studied the noise resulting from the thermal agitation. This thermally generated noise produces a spectrum that has about the same energy for each cycle of bandwidth. This equal-power per cycle noise is termed "Gaussian" or "white noise". Equation 3.1 from [102] gives the mathematical formulation of the Johnson noise V_n in voltage.

$$V_n = 2\sqrt{kTRB} \quad (3.1)$$

where:

- V_n is the noise voltage (V/\sqrt{Hz})
- k is Boltzmann's constant ($1.38 \times 10^{-23} J/K$)
- T is the temperature in degrees Kelvin (K)
- R is the resistance in ohms (W)
- B is the bandwidth in hertz (Hz)

On the other hand, it can have shot of Gaussian noise if the electric current (change flow) does not flow in a uniform, well-behaved manner. Shot noise is often termed "Rain on the Roof" noise or the photon noise when applied to the photodetectors. Suppose a simple circuit, shown in Figure 3.1, has a very small but steady Direct Current (DC) current "I" running through it, and that this can be measured by counting the charge carriers (electrons) as they pass some point A. Because the electrons can collide with each other and with the charged metal ions in the wire, they pass point A at completely random intervals. They also have a finite charge, $q = 1.6022 \times 10^{-19}$ coulombs or 4.803×10^{-10} esu (electric charge unit), so although after counting the electrons for many intervals of length Δt , it would result an average number \bar{N} of

$$\bar{N} = \frac{I\Delta t}{q} \quad (3.2)$$

during a period Δt , the number for any given Δt would be different; sometimes a few more, sometimes a few less. Thus, what is the probability that exactly N (no bar) show up during a time interval Δt ?

To answer this question, the exposure time Δt is first divided up into a very large number n of equal segments of time. The average number arriving in a segment is \bar{N}/n , and if n is very large, $\bar{N}/n \ll 1$. Let us use that limit. Since it cannot have less than one electron arrive, what this means is that the probability that an electron arrives during one given segment is \bar{N}/n , where the probability is simply the number of times something is likely to occur per time it is tried; if something is sure to happen, its probability is 1. It is also seen from this limit that the probability of an electron not arriving during the given segment is $1 - \bar{N}/n$, since there is a total probability of 1 that an electron will either show up or not show up, and that the probability of two electrons showing up during the same segment is $(\bar{N}/n)^2$ so much rarer than single-electron arrivals that multiple-electron events are henceforth neglected. The probability of the arrival of electrons within N segments is therefore $(\bar{N}/n)^n$, and the probability of no electrons arriving

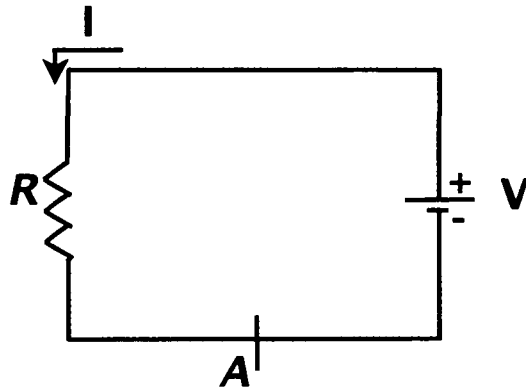


Figure 3.1: Current with shot noise

within the remaining $n-N$ segments is $1-(\bar{N}/n)^{n-N}$.

As described above, this noise is usually quantified using the probability and statistics. This noise follows the Gaussian distribution with zero-mean and standard deviation σ . There are different ways to estimate the standard deviation of Gaussian noise in an image [70]. Olsen [9] made an evaluation of six methods and showed that the average method was best, and this is also the simplest method. This method consists of filtering the image "Im" with the average filter and subtracting the filtered image from "Im". Then a measure of the noise at each pixel is computed.

3.1.2 Flicker and 1/f Noise

In addition to the fundamental Johnson noise, many devices exhibit a second noise phenomenon caused by the flow of electric current. Electron or charge flow (current) is not continuous, well-behaved process. There is a randomness that produces an alternating current (random AC) on the top of the main direct current flow. This noise is difficult to quantify and to measure. This noise, in general, has a $1/f$ spectrum and is termed "pink noise". Pink noise has equal power per octave of frequency (log2 scale). An empirical description of the $1/f$ noise according to Hooge [52, 53] is a spectrum with

$$C_{1/f} = \frac{\alpha}{N_{tot}} \cdot \frac{1}{f} \quad (3.3)$$

Where N_{tot} means the total number of moving charges in the device and f is the frequency. The Hooge-Parameter α is a material characteristic.

3.1.3 Poisson Noise

In addition to the mean and variance, we can also discuss noise in terms of the shape of the distribution for each data element. One common distribution for the values of each element is

determined by the nature of light itself. Light isn't a continuous quantity, but occurs in discrete photons. These photons don't arrive in a steady stream, but sometimes vary over time. Think of it like a flow of cars on a road—sometimes they bunch together, sometimes they spread out, but in general there's an overall average flow. Discrete arrivals over a period of time are modeled statistically by a Poisson distribution. If the noise in the data "s" is Poisson, the Anscombe transform [117]

$$t(s(x)) = 2\sqrt{s(x) + \frac{3}{8}} \quad (3.4)$$

acts as if the data arose from a Gaussian white noise model (Anscombe, 1948), with $\sigma=1$, under the assumption that the mean value of "s" is large.

A Poisson distribution [45] is described by Equation 3.5

$$P(i) = \frac{m^i}{i!} \exp(-m) \quad (3.5)$$

where m is the mean and $i!=1 \times 2 \times 3 \times \dots \times i$.

In Poisson distribution the mean=variance. It is similar to a Gaussian distribution with the following exceptions/properties [117]:

- A Poisson distribution is for discrete values, not continuous ones.
- A Poisson distribution applies only to non-negative quantities—one counts arrivals, not departures.
- A Poisson distribution has the property that its variance is equal to its mean.

3.1.4 Gaussian and Poisson Noise

For small Poisson parameter values, the Anscombe transformation loses control over the bias [117]. Small numbers of detector counts will most likely be associated with the image background .i.e. errors related to small values carry the risk of removing real objects, but not of amplifying noise, because at increasingly low values, the pixel value is increasingly underestimated. Therefore, an extension of the Anscombe transformation has been performed by Bijaoui [11] to cope with the Poisson model limitation by taking the combined noise into account.

The arrival of photons, and their expression by electron counts, on CCD detectors may be modeled by a Poisson distribution. In addition, there is an additive Gaussian readout noise. Consider the signal $s(x)$, as a sum of a Gaussian Variable, γ , of mean g and standard deviation σ ; and a Poisson variable, n , of mean m_0 . Let us set $s(x)=\gamma + \alpha n$. where α is the gain.

The generalization of the variance stabilizing Anscombe formula can be written as:

$$t = \frac{2}{\alpha} \sqrt{\alpha s(x) + \frac{3}{8}\alpha^2 + \sigma^2 - \alpha g} \quad (3.6)$$

With appropriate values of α , σ and g , this reduces to Anscombe transformation (Equation 3.4).

3.1.5 Other Types of Noise

The types of noise considered so far correspond to the general consideration in astronomical imagery [117] for uniform noise distribution. However, not all IR detectors might have identical characteristics and equivalent readout electronic. Let us describe now briefly methods, which can be used for non-uniform and multiplicative noise.

- **Additive non-uniform noise:** If the noise is additive but non-uniform, the standard deviation cannot be estimated for the whole data. However, it can often be assumed that the noise is locally Gaussian and, then, a local standard deviation of the noise for every data element can be computed. In this way, a standard deviation map of the noise is obtained $s_\sigma(x)$ and can be used for detector indexing or further processing.
- **Multiplicative noise:** If the noise is multiplicative, the data can be transformed to a logarithmic scale, if isotropy is fulfilled. In the transformation space, the noise is additive, and a hypothesis of Gaussian noise can be used in order to find the detection level at each scale.
- **Multiplicative non-uniform noise:** In this case, the logarithm of the data is taken, and the resulting signal is processed as for additive non-uniform noise above.
- **Unknown noise:** If the noise does not follow any known distribution, sigma-kappa clipping method [114] can be used for the reduction of the noise in the data.

3.2 Definition of Data Compression

Data compression consists of finding and removing most, if not all, the redundancy from the data for an efficient data transmission or storage (Figure 3.2). The degree of data reduction obtained as a result of the compression process is known as the **Compression Ratio (CR)**. This ratio measures the quantity of compressed data in comparison with the quantity of original data [49].

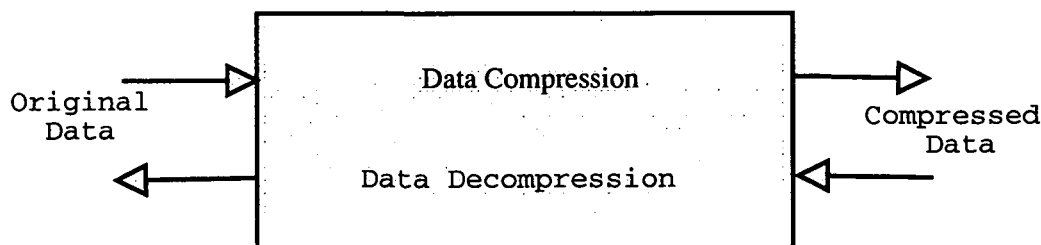


Figure 3.2: Basic data compression block diagram

$$CR = \frac{\text{length of original data string}}{\text{length of compressed data string}} \quad (3.7)$$

Compression techniques can be classified into one of two general categories or methods - Lossless or Lossy- [49].

- Lossless compression techniques are fully reproducible and are primarily restricted to data operations. Data are compressed such their decompression should result in the exact reconstruction of the original data. Other common terms used to reference lossless compression include 'reversible' and non-destructive compression.
- Lossy compression techniques may not be fully reproducible and are primarily restricted to operations on images, video, or audio. The data are reduced by permanently eliminating certain information. Therefore, the use of the lossy compression techniques depends on the application, respectively the data, at hand. Since the obtainable CR by the use of lossy compression can significantly exceed the CR obtainable from lossless compression, the primary trade-off concerns the need for reproducibility versus the storage and transmission requirements.

The general block diagram for data compression/decompression is depicted in Figure 3.3 [49]. The original data are shown in the top-left whereas the reconstructed data are represented in the bottom-right side of the figure. The upper boxes show the data compression stage in two steps: lossy and lossless. The lossy compression part consists of a decorrelation stage (usually DCT, Wavelet..etc) [109, 135] and a quantization stage. Lossless data compression consists of lossless entropy coding (e.g. Huffman, Lempel-Ziv, arithmetic coding...etc) [49]. The boxes shown in the bottom of Figure 2 represent the decompression stage. It consists of reconstructing the original data by decoding and demultiplexing the compressed data stream. The bandwidth-limited transmission channel that links the two stages is depicted on top-right and bottom-left of the figure. Constraints related to data compression are described in the following subsections.

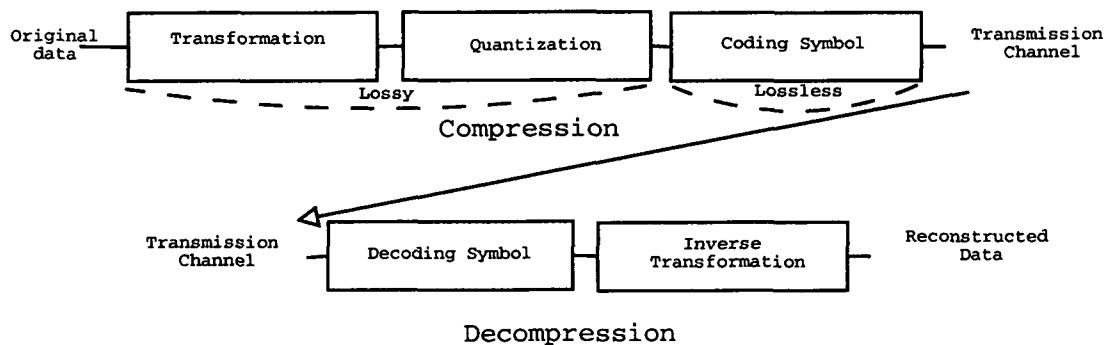


Figure 3.3: General block diagram for data compression/decompression

3.3 The Reconstruction Error

The reconstruction error is a parameter used to assess the performance of a compression method. It is applied to quantify the data distortion by means of the difference between the original and the reconstructed data. There are several quantitative measures for this distortion. These measures includes **Mean Absolute Error (MAE)**, *RMSE*, *SNR*, *PSNR* and *KL* information gain; that is, the distortion measure often used in R-D (Rate-Distortion) optimization. In the following, the definitions of the measures listed above are given.

- *MAE*: This is the simplest measure. If S is the original data and S_R is the reconstructed data, then the mean absolute error for N samples with index x is defined as follows:

$$MAE(S, S_R) = \frac{1}{N} \sum_{x=1}^N |S(x) - S_R(x)| \quad (3.8)$$

- *RMSE*: In contrast to *MAE*, the *RMSE* averages the squares of the differences and then the square root of the result is taken. The *RMSE* is an area weighted statistics. It is calculated as the standard deviation of all reconstructed data set relative to the original data. It is defined as follows:

$$RMSE(S, S_R) = \sqrt{\frac{1}{N} \sum_{x=1}^N (S(x) - S_R(x))^2} \quad (3.9)$$

- *SNR*: The *SNR* attempts to improve the *RMSE* equation by taking into account the intensity of the reference. This is done by dividing the total reference power by the total error power. Taking the logarithm is one way of reducing the range of values, and the 10 in front is the convenience factor.

$$SNR(S, S_R) = 10 \log_{10} \frac{\sum_{x=1}^N S(x)^2}{\sum_{x=1}^N (S(x) - S_R(x))^2} \quad (3.10)$$

Notice that this measure is inversely proportional to the previous two.

- *PSNR*: This criterion is widely used for the evaluation of compression methods. The reason is that *PSNR* is mathematically repeatable and is highly susceptible to different intensities.

$$PSNR(S, S_R) = 10 \log_{10} \frac{(\max(S(x)) - \min(S(x)))^2}{\frac{1}{N} \sum_{x=1}^N (S(x) - S_R(x))^2} \quad (3.11)$$

- *KL gain*: This measure, also known as a relative entropy, makes use of the probability distribution of the data. For instance, the original data S has a 'true' probability distribution Q and an estimated distribution E . The *KL* information gain (DG_{KL}) could be calculated as follows [33]:

$$DG_{KL}(Q, E) = a \sum_x p(x/S) \log_2 \frac{p(x/S)}{p(x/S_R)} \quad (3.12)$$

where:

- $a \geq 0$ constant,
- $p(x/S)$ is the probability of occurrence of the element x in the original data S and
- $p(x/S_R)$ is the probability of occurrence of the element x in the reconstructed data S_R .

The KL information gain may be applied to quantify the distortion by means of the difference between the original data and the data reconstructed after compression.

- *PIL*: This is a new ease-of-use metric served for the evaluation of quality of the reconstructed image. This metric uses the assumption that an astronomical object in an image has a profile which is closer to a Gaussian curve [117]. Therefore, the peak of the curve is used as reference for the evaluation of the information loss

$$PIL = 1 - \frac{PDF(S_R(x))}{PDF(S(x))} \quad (3.13)$$

where PDF is the **Probability Density Function**.

The histogram of the original and reconstructed images are used for the calculation of *PIL* by means of the difference between both histograms i.e. by computing the sum of the relative differences between all graylevel counts. In addition to its simplicity, *PIL* metric seems to provide realistic results for compression evaluation [98].

The above listed metrics aim to measure the quality loss resulted from the applied data compression methods. However, it is not obvious to have a single metric that fit to the human interpretation (Human visual inspection). Our goal is to trace the curve (compression ratio vs. reconstruction error) resulting from the processing of selected data, combining the listed metrics, for an objective measure of the compression performance. Furthermore, at least 5 astronomers are solicited to support the evaluation of the compression method for a set of IR astronomical images.

3.4 Compression Challenges

The major concern of a compression method is to recognize and remove all redundancy in the data in order to reduce the traffic over the transmission channel. A redundancy may be investigated in the 1-D detector signal depending on the sensors characteristics, by modeling the sensor reaction (function) to the IR rays. A parametrized model can be used for the representation of the 1-D detectors signals by a set of parameters and thus reducing the data volume. However, cosmic particles (outliers) would disturb the detector output signal which makes the modeling challenging. Further compression can be achieved by exploiting the source signal (signal of the observed target) redundancy using e.g. multiresolution approach [121]. However, this latter alternative usually presents high algorithmic complexity that makes the feasibility of these approaches challenging on the limited resources environment of IR astronomy. The quality vs.CR

vs. algorithmic complexity trade-off has to be further investigated and analyzed.

The aim of this thesis is to concentrate on the exploitation of the redundancy from the sensor to achieve the highest possible CR and to analyze the noise effect on the CR and algorithmic complexity. The performance of a data compression method can be evaluated using the following relevant parameters:

- The compression ratio vs. the **Reconstruction Error (RE)**
- The algorithmic complexity of the method

3.4.1 Compression Ratio vs. Reconstruction Error

The first criterion generally used to assess the performances of a compression method is the achieved **CR**. It points out to the capability of the method to find and remove the redundancy in the data. The more redundancy is removed the greater CR is achieved.

RE defines the quality of the data after reconstruction. The results quality criterion, which can be retained for estimating the merits and performances of a compression method, in case of astronomy, falls under these headings:

- * Visual Aspect,
- * Signal to Noise Ratio,
- * Detection of real and faint objects,
- * Object morphology,
- * Astrometry and
- * Photometry.

As an experience from former joint projects [5, 12, 57, 93], it is necessary to work close together with astronomers to find out a realistic solution for number of problems like:

- Transfer of astronomical aspects into computer terms,
- Reduction of problems into small sub problems that can be handled by the computer and
- Evaluation and verification of the results.

that can only be solved by a cooperative team of technicians and astronomers. Therefore, the validation of the assessment is supported by astronomers, which is mandatory to validate the reconstruction results and to support the quantitative error measures proposed in Section 3.3. The main challenge is to trace the curve (CR vs. RE) resulting from the processing of different data models, with support from astronomers, for an objective measure of the compression performance

3.4.2 The Algorithmic Complexity of the Method

Although the above-mentioned criteria are very important to design a compression method [130], the complexity of the algorithm is of bigger importance because it defines the feasibility of the method. This criterion should not be performed at latest stage of the design, but it has to be taken into consideration to assess a compression method. Therefore, the implementation of the method has to be part of the design of the method. Especially, for IR astronomy applications where astronomers are interested for a compression method that have to fit the limited-resources space observatories.

Usually, the execution time is used to assess the algorithmic complexity of a compression method. Indeed, algorithmic complexity and execution time are highly correlated but not identical. The execution time mainly depends on the algorithm implementation and on the machine where it is running. Starting from its complexity, one can deduce the execution time of a given compression algorithm if the way the method is implemented and the hardware description are known.

The complexity of an algorithm can be analyzed in two ways. One way involves only an intuitive understanding of the complexity. Such techniques are classified as qualitative analysis techniques. With qualitative analysis it is not possible to measure or quantify the gain when the algorithm is optimized. The other approach to complexity analysis involves building a model of the complexity. This allows objective comparison of different algorithms.

In this thesis, both kinds of complexity analysis techniques are addressed. First, data compression algorithms are optimized based on qualitative analysis. Then, a new methodology to measure the complexity is investigated (and used). The proposed measure takes into account arithmetic operations, tests (or branches) and memory operations. The measure works in two steps, one depending on the algorithm, and the other, on the architecture on which the algorithm is implemented. The complexity of the algorithm is then expressed by a weighted sum of the algorithm-dependent counters, where the weights are determined by the architecture-dependent step. However, even with this well-defined methodology, analysis of the complexity analysis is still a long and difficult process. One way to simplify the problem is to use the fact that most algorithms can be divided into a succession of small tasks (or blocks). This is especially true for image compression algorithms. Therefore, the complexities of the most common processing blocks for image compression are studied separately. The complexity analysis of a new algorithm then becomes the sum of the complexity of each one of its building blocks.

3.4.3 Additional Aspects

Compression is mandatory for IR space missions as the readout rate generally exceeds the available telemetry bandwidth. Usually, lossy compression is required in order to fulfill the high compression requirements in term of compression rate. Therefore, the method to be used, should take into consideration the relevance in the data information as stated in Table 2.2. However, the compression method is faced with the noise, that is by definition incompressible, which

is mainly originated from the unwanted background (Table 2.3), the cosmic particles and the detector relaxation after the (cosmic hits) event.

As described in Figure 3.3, data compression consists of two steps: lossy and lossless. Generally, lossless compression leads to low data compression factor (up to 5 in case of astronomy), especially for noisy data with higher entropy. Therefore, lossy compression is mandatory for several applications (radar, space applications, telecommunications) [135] to achieve additional CR. Although certain operational applications (e.g. CCD images of deployment of solar panels or position of landing gear) allow a high amount of quality loss, noisy data has to be compressed with care such that real objects (e.g. faint objects) are not lost while compression.

One of the most common methods for lossy compression (Figure 3.3) is transform coding e.g. Discrete Cosine Transform (DCT) [109], WaVeLeTs (WVT) [21], RidGeLeTs (RGT) [30]...etc. The objective is to minimize statistical dependence between the output values of the transform. Desirable characteristics are decorrelation, energy concentration, and computational efficiency. All these transforms assume that the original data is free of noise or that noise is a part of significant data elements. In addition to the quality loss due to artifacts (blockiness) problem [49, 117, 135] which limits the capabilities of these transforms, significant data (e.g. faint objects in images) may not be reconstructed which leads to information loss. This is because some information with equivalent amplitude to the noise has been neglected.

However, compression is more challenging for IR astronomy applications as the source target amplitude is much lower than the background amplitude which makes the simultaneous decorrelation critical. Therefore, more noise models have to be considered before compression in order to preserve as much as possible data quality. Rate-Distortion (R-D) principle is introduced in the next section. Then, state-of-the-art compression methods are presented afterward, in addition to dedicated methods for astronomy applications.

3.5 Rate-Distortion Principle

In this Section, the trade-off between the compression rate and the image quality is exposed (R-D). Effect of the noise on an adequate R-D trade-off is also given. Furthermore, discussion about the adaptivity of the compression model to the R-D trade-off is made. Lossy compression is a typical engineering trade-off: lower data quality for higher transmission rate. If the rate decreases a large amount for a small decrease in data quality, then lossy compression is usually considered desirable. For this reason, lossy compression is often evaluated with reference to a rate-distortion curve.

The relationship between the rate and the distortion in a signal is depicted in Figure 3.4. Note that R (entropy) is in bits/sample while the D (distortion) represents the reconstruction error 3.3.

It is shown that a lower bit rate R allows some acceptable distortion D in the signal. In Figure 3.4(b) and (c), the equivalent constrained optimization problems, often unwieldy, are given. Minimization of one parameter (R or D) is only done for a given reference (D or R).

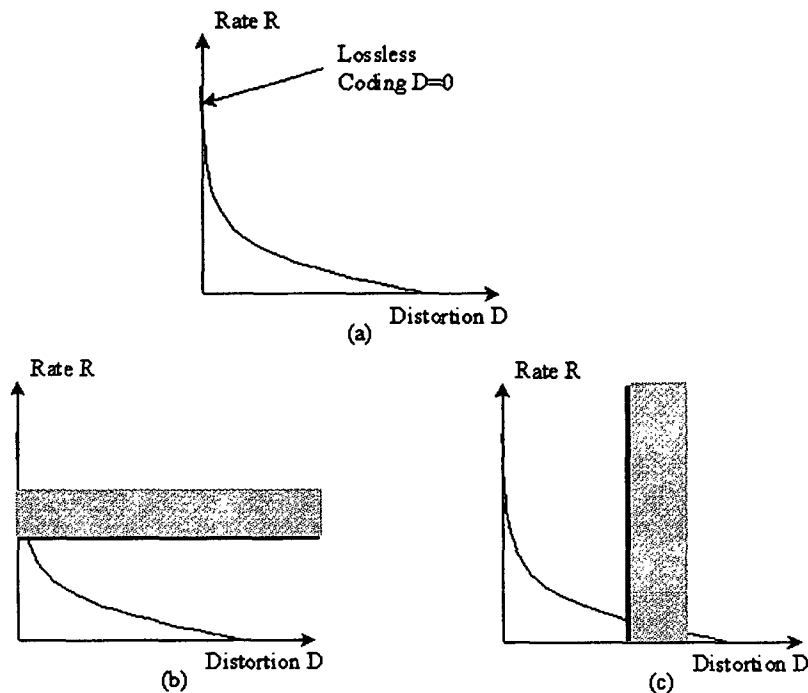


Figure 3.4. (a) Compression rate and distortion trade off. (b) and (c) Equivalent constrained optimization problems giving a maximum rate or distortion

There exist several formulations of the R-D problem for instance:

- A. Shannon Source Coding Theorem and Converse [112]:** For a given maximum average distortion D , the rate-distortion function $R(D)$ is the achievable lower bound for the transmission bit-rate. $R(D)$ is continuous, monotonically decreasing for $R > 0$ and convex. Equivalently, the distortion-rate function $D(R)$ can be used.
- B. The Lagrangian Formulation [130]:** Instead of the cost function D , with constrained R , or R , with constrained D , the unconstrained Lagrangian cost function is used for a convex R-D function and non-increasing, for $D > 0$, subject to minimize

$$J = D + \lambda R$$

- C. The Blahut's Algorithm [130]:** This algorithm intends to solve the Lagrangian-formulation of the R-D problem. It is used to compute the R-D bound or the optimality testing by applying it to the tentative testing solution.

For fixed Probability Mass Function (PMF) $q(y|x)$, optimal PMF $q(y)$ is:

$$q(y) = \sum_{x \in X} q(y|x)p(x) = q(y) \cdot f(y) \tag{3.14}$$

where $p(x)$ is the PDF of x . For fixed $q(y)$, optimal $q(y|x)$ is:

$$q(y|x) = \frac{q(y)e^{-d(x,z)}}{\sum_{z \in Y} q(z)e^{-d(x,z)}} \quad (3.15)$$

where $p(y)$ is PDF of y and $d(x, z)$ is the distortion parameter for (x, z) .

D. The Kuhn-Tucker Optimality Conditions [130]: The Kuhn-Tucker condition for optimum $q(y)$:

$$f(y) = 1 \text{ if } q(y) > 0 \quad f(y) \leq 1 \text{ if } q(y) = 0 \quad (3.16)$$

This method sets several constraints on R and D in order to investigate on the problem of optimality of the solution.

Those methods listed above contribute to solving the mathematical problem R-D in order to find the best compromise for rate/quality. Indeed, the signal considered is the signal of interest which is noise-free. The question is how would the distortion behave while performing compression on astronomical signal by removing the noise. Optimally, it will result in higher compression rate for zero-distortion if the reconstructed signal represents the signal of interest. However, compression using noise-removal is hardly achievable for IR astronomy applications as the noise itself can not be mathematically defined and modeled due to the different noise sources. Furthermore, even if the noise model is well-known, which is not the usual case, the realization of such a compression for space applications is computationally prohibitive due to the limited resources. Therefore, a compromise between compression performance (CR, complexity) and data quality is investigated in the next sections.

3.6 State-of-the Art Compression

The data compression process deals with the removal of the redundancies in the data representing the signal. The redundancy of data is mainly caused by the source information and its quality (noisy or not), the sampling rate and the number of quantization levels. In the following subsections, the research status of state-of-the-art lossy and lossless compression are presented.

3.6.1 Transform Coding Methods

The data compression also consists of a decorrelation stage using a signal transformation e.g. DCT [109], WVT [21, 25, 113, 145], RGT [18] and CVT [17]. One of the basic image characteristics we profit from is that the correlation among the neighboring samples is leading to a reduced number of relevant transform coefficients if the transform acts as a decorrelating procedure. These fewer transform coefficients can be then quantized and coded efficiently [49]. For the image data compressor module most often the JPEG algorithm is employed. It uses for the decorrelation stage the DCT for the space-frequency transformation on small blocks or subsets of the image. It has however the adverse property of showing a block structure in the reconstructed image, the so-called blockiness, the higher compression ratio the worse it becomes. An alternative is the use of the multiscale transforms which does not require blocking the input image. In case of WVT that are performed repeatedly (typically up to about 5 decomposition levels), the corresponding coefficients of the different decomposition levels are correlated and show a characteristic trend. This residual correlation is indicative of a further compression potential. Figure 3.5 shows an illustration of 2-D WVT using the Mallat decomposition [79].

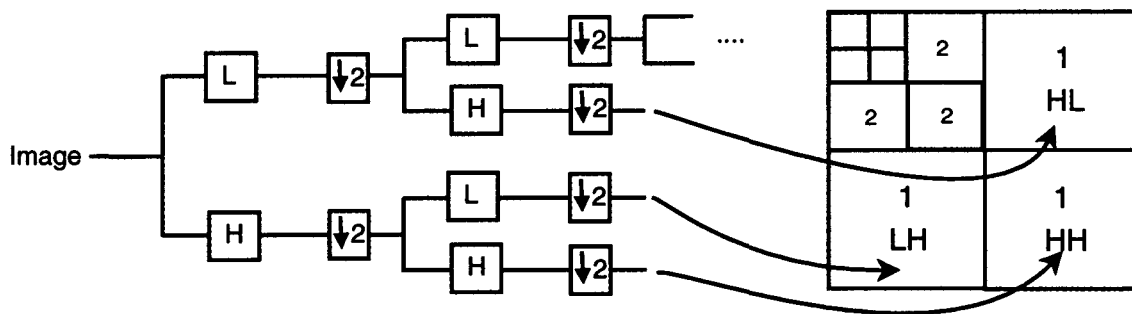


Figure 3.5. Illustration of 2-D wavelet decomposition using the Mallat transform. The numbers correspond to the decomposition steps that have been applied to produce the subbands. The two letters indicate if the subband was passed through a high-pass (H) or a low-pass filter (L) along the horizontal and vertical direction. The subband containing low-pass information in both directions is situated on the upper-left part of the image. $\downarrow 2$: represents subsampling the subband by a factor 2

Standard compression methods (e.g. JPEG2000 [145]) get profits from this potential, especially when considering sets of transform coefficients as feature specific compounds. However,

for image compression, the WVT has a problem with the orientation selectivity because it provides local frequency representation of image regions over a range of spatial scales, and therefore, it does not represent two-dimensional singularities effectively [120, 121]. Furthermore, wavelet reconstruction contains many disturbing artifacts along edges because of the reduced number of the maintained coefficients. In other words, WVT of images exhibits large coefficients even at fine scale, all along the image edges. In a map of the large wavelet coefficients one sees the edges of the images repeated at scale after scale. While this effect is visually interesting, it means that many wavelet coefficients are required to reconstruct the edges in an image properly. Reducing this number of coefficients for compression purpose, will introduce then artifacts on the edges of the reconstructed image.

RGT [18] was developed over several years in an attempt to break an inherent limit plaguing wavelet denoising of images. This limit arises from the well-known and frequently depicted fact that the 2- Dimensional (2-D) WVT of images exhibits large wavelet coefficients to represent the image edges. A basic tool for calculating ridgelet coefficients is to view ridgelet analysis as a form of wavelet analysis in the Radon domain. The ridgelet coefficients $R_f(a, b, q)$ of an object f are given by analysis of the **RaDon Transform (RDT)** via

$$R_f(a, b, q) = Rf(\theta, t)a^{-1/2}\psi((t - b)/a)dt \quad (3.17)$$

where:

- $Rf(\theta, t)$ is the RDT of an object f for the orientation parameter q and instant t .
- $a > 0$ is a scale parameter and b is a location scalar parameter
- ψ is a wavelet.

Hence, RGT is precisely the application of 1-D WVT to the slices of the RDT where the angular variable q is constant and t varying. Figure 3.6 shows an illustration of RGT on a 2-D signal. It has been shown in [30] that ridgelet representation solve the problem of sparse approximation of smooth objects with straight edges. However, in image processing, edges are typically curved rather than straight and ridgelets alone cannot yield efficient representation. However, at sufficiently fine scales, a curved edge is almost straight, and so to capture curved edges, one ought to be able to deploy ridgelets in a localized manner, at sufficiently fine scales.

Therefore, curvelets [17] have been introduced. They are based on multiscale ridgelets combined with a spatial bandpass filtering operation to isolate different scales. The curvelet decomposition of an image consists of the following steps (see also Figure 3.7):

- **Subband Decomposition:** The object f is decomposed into subbands using 2D WVT.
- **Smooth Partitioning:** Each subband is smoothly windowed into "squares" of an appropriate scale.
- **Ridgelet Analysis:** Each square is analyzed via the discrete RGT, which consists of RDT and 1-D WVT.

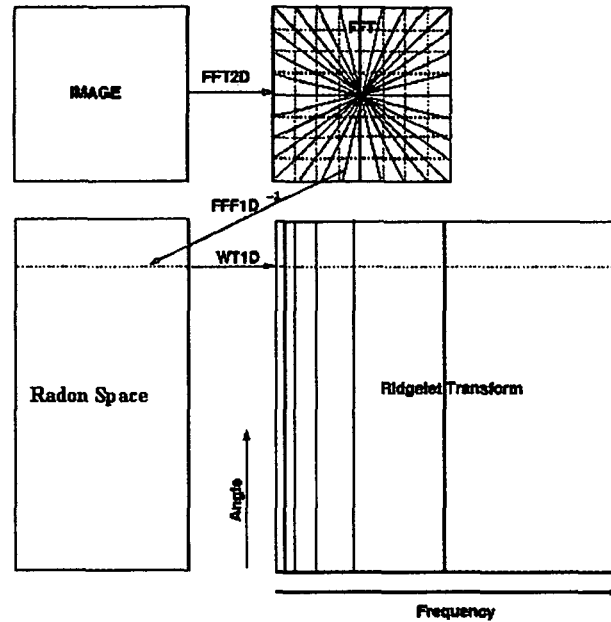


Figure 3.6: Illustration of the ridgelet transform

CVT [17] was initially developed in the continuous-domain via multiscale filtering and then applying a block RGT [18] on each bandpass image. Later, the authors proposed the second-generation CVT [19] that was defined directly via frequency partitioning without using RGT. Both curvelet constructions require a rotation operation for the frequency decomposition, which makes the construction possible in the continuous-domain but causes the implementation of the CVT for discrete images – sampled on a rectangular grid – very challenging. In particular, approaching critical sampling seems very difficult in such discretized constructions [28, 120].

Another approach starts with a discrete-domain transform and then investigates its convergence to an expansion in the continuous-domain, which is named the contourlet transform [28]. A discrete-domain multiresolution and multidirectional expansion using non-separable filter banks is constructed, in the same way that wavelets are derived from filter banks. This construction results in a flexible multiresolution, local, and directional image expansion using contour segments due to the fast-iterated filter bank algorithm. CTT has however the adverse property of showing other types of artifacts due to the discrete approach.

The performance of the data compression scheme (Figure 3.3) is dominated by the efficiency of the signal transform in the decorrelation of the original data and therefore to facilitate the compaction of the information. For an efficient data compression process, the transformation should be:

- Orthogonal series expansions as it provides series of coefficients which are uncorrelated
- Unitary as it preserves the signal energy and pack most of the information into a smallest number of them

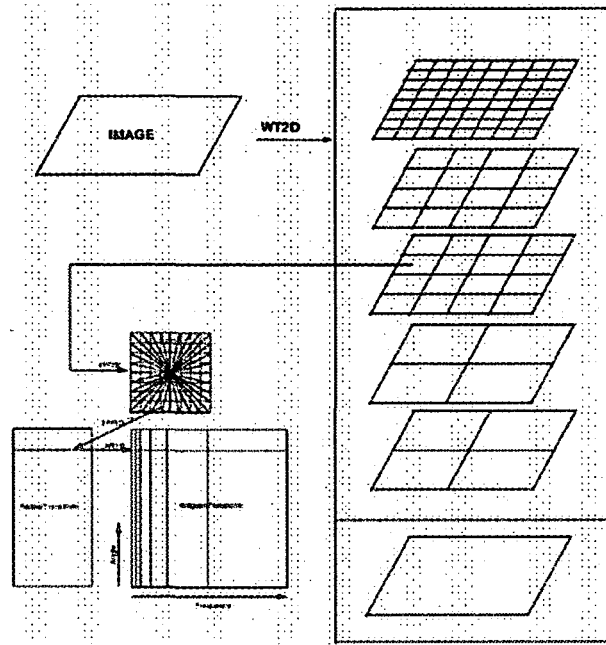


Figure 3.7: Illustration of the curvelet transform

- Linear as it offers a fast computation algorithm

An objective measure of the efficiency of the orthogonal transform is the coding gain G

$$G = \frac{1}{N} \sum_{x=1}^N \sigma_i^2 \left(\prod_{x=1}^N \sigma_i^2 \right)^{-\frac{1}{N}} \quad (3.18)$$

where σ_i^2 is the variance of the output of the i^{th} analysis filter and N is the number of original data samples. G indicates the factor by which the **Mean Square Error (MSE)** of the reconstruction is reduced when applying an optimal separate quantizer to each transform component. The transformation that maximizes G is the **Karhunen-Loeve Transform (KLT)** [64]. The KLT is signal dependent and extremely computationally complex comparing to DCT and WVT.

Shapiro [113] introduced the embedded image coding based on WVT, where all encoding of the same image at low bit rates is embedded at the beginning of the bit stream. Therefore, the quality of the reconstructed image depends on the given target bit rate. A wavelet coefficient x_n^m for a position (m, n) is said to be insignificant with respect to a threshold T if $|x_n^m| < T$. This construction is based on the observation that if a wavelet coefficient at a coarse scale is insignificant, then all coefficients in the same spatial location at finer scales are likely to be insignificant. This leads to the definition of the **Best Linear Unbiased Estimator (BLUE)** for a given u and v such that $u = (x_n^m)^2$ and $v = (x_n^{m-1})^2$

$$u_{BLUE} = E[u] - \rho \frac{\sigma_u}{\sigma_v} \cdot (E[v] - v), \quad (3.19)$$

where ρ is the correlation coefficient of u and v , $E[.]$ represents the expectation operator. Thus, in addition to the decorrelation property of the WVT, the prediction of the insignificance across scales provides a substantial coding gain. The Shapiro algorithm uses successive approximations quantization enabling the progressive transmission and adaptive arithmetic coding. Similar methods, but with advantages both in compression rate and speed are presented in [106].

In [15], a full joint statistical model is developed. It describes the interaction between pairs of wavelet coefficients at adjacent spatial locations, orientations and scales. The wavelet coefficients at one scale are considered decorrelated and distributed according to a generalized Gaussian probability density function.

The stochastic model is used for bit prediction resulting in an Embedded Predictive Wavelet Image Coder (EPWIC), with superior efficiency compared to [113, 106]. As can be seen, the compression behavior is dependent on the signal statistics. A high compression rate is obtained for smooth signals, for which many of the WVT coefficients are zero or almost identical.

Up to here, only the statistics of the WVT coefficients were analyzed. No attempt was made to model the signal to be compressed. Any observed image is affected by noise, which, from the point of view of data compression, is reducing the data rate. Thus, a pre-processing step, i.e. image separation from observation noise, is expected to lead to higher CR.

Donoho [31] introduced a simple denoising algorithm applied in the WVT domain. The signal, we wish to estimate is defined on the interval $[0,1]$.

$$Y = x + \sigma.z, \tag{3.20}$$

where x is the original signal (noiseless), z is a white Gaussian noise of zero mean and unit variance, and σ is the noise level. The denoising algorithm minimizes the MSE, $E[x - x']$, subject to the constraint: "with high probability, x' is at least as smooth as x ". The algorithm has 3 steps:

1. Obtain the empirical wavelet coefficients using the interval-adapted pyramidal filtering.
2. Apply the soft thresholding non linearity where t is a threshold depending on the noise level σ :

$$N_t(x) = \text{sgn}(x)(|x| - t) \tag{3.21}$$

3. Invert the pyramid filter recovering the estimated signal x' .

In [86], it was observed that denoising could be encapsulated in the quantization process of a WVT data compression algorithm, thus increasing the probability of longer zero streams.

The algorithm was applied for the simultaneous cross-section estimation and data compression of Synthetic Aperture Radar (SAR) images.

In [121], CVT has been used for astronomical image representation. It has been shown that curvelet reconstruction does not contain disturbing artifacts along edges that one sees in wavelet reconstructions. Although the results obtained by simply thresholding the curvelet expansion are encouraging, there is still need for further improvement and especially in the realization of the method with low complexity. Furthermore, CVT are well adapted for anisotropic features but astronomical images also contain many isotropic features that can badly represented by only CVT.

The methods listed so far consider the data of interest as an image. However, the 2-D signal in IR astronomy is also a result of concatenated measurements from joined IR detectors. Each detector may be read out several time for a dedicated astronomical efficiency. In this case, the compression can be considered as an approximation of the detector measurements that best fit to the sensor readings.

A mathematical procedure for finding the best-fitting curve to this given set of points is the least squares method [63]. It minimizes the sum of the squares of the offsets (the residuals) of the points from the curve. The sum of the squares of the offsets is used instead of the offset absolute values because this allows the residuals to be treated as a continuous differentiable quantity. This approach is optimal with respect to the Gaussian noise process. However, because squares of the offsets are used, outlying points can have a disproportionate effect on the fit, a property that may not be desirable.

The **RAN**dom **SA**mple **C**onsensus method (RANSAC) [37] is another alternative for linear fit. RANSAC is an analytic procedure for fitting a straight line out of set of measurements using the following steps (see also Fig. 3.8):

1. Take randomly two samples and calculate the line which passes exactly through these samples.
2. All samples that are within a pre-specified distance Θ to the line are put into the support set.
3. Repeat this process many times.
4. Select the line with the largest support set (if there is more than one take the one with the smallest residual error).

For the case where dealing with just few samples per line (4), all possible lines (6) can be calculated. If dealing with lines containing more samples, the complexity of the solution exponentially increases with the number of measurements. However, a subset of points can be taken to speed up the processing. It has been shown that RANSAC obtains the theoretically optimal breakdown point of 50%, i.e. it still can fit a line if not more than 50% of the measurements are outliers.

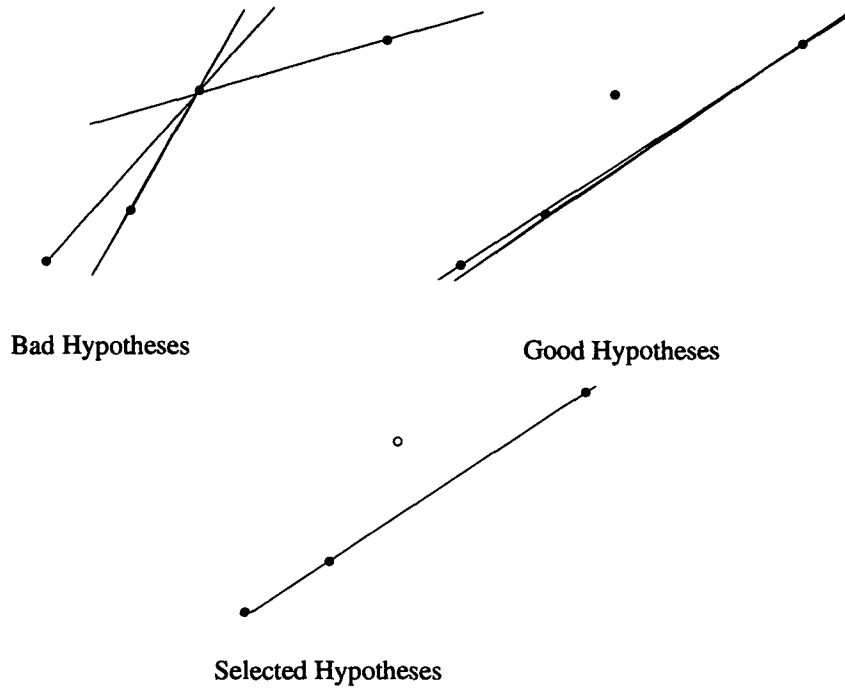


Figure 3.8: Illustration of RANSAC.

3.6.2 Entropy Coding Methods

So far, the status of research concerning the lossy part of data compression methods have been listed. Indeed, several algorithms have been used in astronomy as backend lossless compression. They consist of character-oriented compression techniques (e.g. run-length encoding [109], half-byte packing [49]...etc), statistical encoding techniques (e.g. Huffman coding [109], arithmetic coding [49]...etc) or dictionary-based compression techniques (e.g. Lempel-Ziv...etc) [49]. These algorithms differ in performance and complexity. Therefore, the choice of one of these algorithms depends on the entropy in the data and on the available resources (CPU power, memory). Evaluation of these algorithms for astronomy can be found in [23, 59].

In the following subsections, the run-length and arithmetic encoding are particularly detailed as they are interesting for the dissertation research goals for their attractive characteristics e.g. efficiency vs. complexity.

Run-Length Encoding:

Run-length encoding is a fast data compression method that physically reduces any type of repeating character sequence, once the sequence of characters reaches a predefined level of occurrence. For the special case where the null character is the repeated character, run-length compression can be viewed as a superset of null suppression. In this case, it simply ignores nulls by encoding non-zero symbols and their relative position in the original sequence. In other words, it encodes the number of nulls between the symbol and the one that was encoded before.

This is an example for encoding null character in sequence of symbols.

A	0	B	0	0	0	0	0	0	0	C	0	0	0	A	{SOURCE}
A	0	B	1	C	7	A	3								{DEST}

The first symbol's position information is always 0.

Note that that a symbol sequence, which does not at least contain as many nulls as other symbols, is not compressed but expanded.

Arithmetic Coding:

One of the limitations associated with the other statistical encoding methods like Huffman and Shannon-Fano coding is the fact that these methods are optimal only when the probabilities associated with each symbol are integral powers of $1/2$, which is usually not a good representation of reality [49]. For example, let us assume that the probability of a symbol is $1/3$. Then, $-\log_2(1/3)$, i.e. $\log_2 3$ or approximately 1.59 bits would be required to represent the symbol. When Huffman or Shannon-Fano is used, two or more bits would be assigned to the symbol. Then, each time the symbol is compressed, the encoding technique would result in the addition of approximately 0.4 or more bits over the symbol's entropy. As the probability of symbols in a set increases, the coding variance between the entropy of the symbol and the number of bits required to encode it using the Huffman or Shannon-Fano technique increases. Therefore, arithmetic coding [49] has been developed, which does not require symbol probabilities to be integral powers of $1/2$ to obtain an optimum efficiency.

Arithmetic Coding [62] is a technique in which each symbol in a symbol set is assigned an interval between 0 and 1 based upon its probability of occurrence. As astronomical data are formed by the concatenation of separate symbols, those symbols are used to define smaller and smaller intervals between 0 and 1, resulting in a set being represented by a floating number. Thus, arithmetic coding results in the replacement of individual character codes used by Huffman and Shannon-Fano coding by the use of a single code for an entire symbols sequence.

The algorithm for encoding data using arithmetic coding works conceptually as follows:

- The encoding process begins with a current interval $[L; H[$ initialized to $[0; 1[$.
- For each symbol in the data, two steps are performed:
 - o The current interval is divided into subintervals, one for each possible alphabet symbol. The size of a symbol's subinterval is proportional to the estimated probability that the symbol will be the next symbol in the data, according to the model of the input.
 - o The subinterval corresponding to the symbol that actually occurs next in the data stream is selected as the new current interval.

- Enough bits are output to distinguish the final current interval from all other possible final intervals.

The length of the final subinterval is clearly equal to the product of the probabilities of the individual symbols, which is the probability p of the particular sequence of symbols in the data. The final step uses almost exactly $-\log_2 p$ bits to distinguish the data. An additional mechanism is needed to indicate the end of the data, either a special end-of-data symbol coded just once, or some external indication of the data's length.

In the second step, it is required to compute only the subinterval corresponding to the symbol that actually occurs. To do this, two cumulative probabilities are defined,

$$Pc_i = \sum_{k=1}^{i-1} p_k \text{ (the cumulative probability)} \tag{3.22}$$

and

$$Pn_i = \sum_{k=1}^i p_k \text{ (the next cumulative probability)} \tag{3.23}$$

The new subinterval is $[L + Pci(H - L), L + Pni(H - L)]$. The need to maintain and supply cumulative probabilities requires the model to have a complicated data structure.

Example: a non-adaptive code, encoding the stream "bbb" using arbitrary fixed probability estimates $pa = 0.4$, $pb = 0.5$, and $pEOF = 0.1$. Encoding proceeds as shown in Table 3.1.

Current Interval	Action	Subinterval a	Subinterval b	Subinterval EOF	Input
[0.0000;1.000[subdivide	[0.000;0.400[[0.400;0.9000[[0.9000;1.000[b
[0.4000;0.900[subdivide	[0.400;0.500[[0.600;0.8500[[0.8500;0.900[b
[0.6000;0.850[subdivide	[0.600;0.700[[0.700;0.8250[[0.8250;0.850[b
[0.7000;0.825[subdivide	[0.700;0.750[[0.750;0.8125[[0.8125;0.825[EOF
[0.8125;0.825[subdivide				

Table 3.1: The basic arithmetic coding process

The final interval is $[0.8125, 0.8250[$, which in binary is approximately $[0.11010\ 00000, 0.11010\ 01100[$.

This interval is uniquely identified by putting out 11010 00. According to the fixed model, the probability p of this particular file is $(0.5)^3 (0.1) = 0.0125$ (exactly the size of the final interval) and the code length (in bits) should be $-\log_2 \approx 6.322$. In practice, 7 bits are needed to represent 24 bits data which results on a CR of 3.42, excluding the probability table size.

3.7 Astronomical Compression Methods

In this section, dedicated methods for astronomical data compression are listed. Compression methods used in astronomy include HCOMPRESS [134], FITSPRESS [95] and Pyramidal Median Transform (PMT) [117]. The first two methods are based on linear transforms, which in principle help to reduce the redundancy of the pixel values in a block and to decorrelate spatial frequencies or scale. PMT is similar to mathematical morphology method [111] in the sense that both try to understand what is represented in the image. In the following, the 3 methods are briefly described:

1. **HCOMPRESS** was developed at Space Telescope Science Institute. It consists of the Haar wavelet transform [123], linear quantization of the wavelet coefficients and Huffman backend coder. This method suffers from the introduction of visible artifacts in the sky background, and error in the detected position of sources, caused by the transform. Iterative reconstruction allows them to be suppressed but in this case the reconstruction takes time [72].
2. **FITSPRESS** was developed at the center for Astrophysics in Harvard. It is wavelet-based compression method for FITS images [95]. It uses a threshold on very bright pixels and applies a linear wavelet transform. The wavelet coefficients are thresholded according to a noise threshold, quantized linearly and run-length encoded. This method leads to cross-like artifacts in the residual image, a loss of faint objects and a decrease in objects brightness [72].
3. **PMT** compresses in the image what is considered as significant (objects) in the image. It selects the object to be kept by using the pyramidal median transform, and codes this information without any loss [117]. Thus, the first phase searches for the minimum set of quantized multiresolution coefficients that produce an image of high quality (quality means there is no visual artifacts in the decompressed image and the residual does not contain any structure). Using this method, the non-selected information is lost and can not be recovered. It is also not well-suited for infrared images as the objects are hidden in the high-amplitude noise [13].

In another context, a multiresolution transform (similar to PMT) based on mathematical morphology, has been used by Appleton [3] for cirrus (due to intergalactic dust phenomena) filtering in infrared images. This method has been used for the post-processing of the astronomical images after decompression, knowing the object structure.

The methods listed above seem to be either generic compression methods that are used to reduce the data volume using a dedicated quantization of WVT coefficients or model-based compression methods that directly extract the object of interest from raw images. However, these methods are not adequate for IR astronomy applications, as there is no object structure in the raw images. Long integration time over several images, generally hours (depending on the wavelength), is required to detect objects in IR range. Furthermore, to my knowledge, there is no real study on the modelization of the IR astronomical signal and no accurate investigation of the compression efficiency and performance for such a signal. Therefore, we are concerned in

this thesis to recognize the best compression that adapt the IR astronomy needs to the available resources.

Chapter 4

On-Board Processing

This chapter presents the main contribution of this work into science. First, the classical data processing concept for space-borne missions is presented. Furthermore, optimal processing concept for IR space observatory is motivated by the needs of high compression rate for the particular IR detection system characteristics, which are mainly the high entropy. Then, an "Integrated Processing" concept for IR observatories is proposed including an on-board processing approach, which consists of moving part of the processing into the remote side using the detection system know-how for optimal compression performance. Afterwards, the on-board processing steps are presented and the involved processing modules are detailed. Finally, on-board processing performance is demonstrated on infrared images from ISO [147] and the compression results are compared with those using the generic compression framework JPEG2000.

4.1 Classical Processing for Space Observatories

The classical concept for data transmission and processing from space-borne missions is reported in Figure 4.1-a. This concept consists of two main parts: remote and local processing parts.

1. Remote side

It is subdivided into two steps:

- **Acquisition:** As described in Section 2.3, acquisition systems transform radiant energy (astronomical signal) into an electrical signal from which an image can be reconstructed using dedicated readout and sampling modes. Images are formed by the optical system that projects radiation into a photodetector in the image plane. The photodetector converts the radiation into a latent image as an electric signal that is amplified, sampled and quantized for digital transmission.
- **Compression:** This part consists of the entropy coding of the acquired image for the reduction of the data traffic on the transmission channel. The efficiency of this lossless compression depends on the entropy in the data, and thus, on how much redundancy are present in the image.

2. Local side (user)

It is subdivided into two steps:

- **Exploitation:** Usually, the downlinked data are first decompressed, then calibrated using normalized parameters. This step is performed to restore the data by predicting the negative effect of the tasks of acquisition and compression. In other words, the science images/signals are reconstructed using dedicated processing tools and made available for usage.
- **Application:** During this step, the reconstructed images can be used for the purpose they were intended for e.g. for scientific purpose (astronomy) or for operational purpose (meteorology, geodesy, ecology...etc).

Such a scheme is inadequate for IR observatories, where the information rate largely exceeds channel capacity and high compression rate is mandatory to fulfill the transmission requirements. In addition to that, IR detectors are continuously exposed to high energy cosmic particles inducing a disturbance (glitches) of the detector signal and transient behavior, which may increase the signal entropy and hence the capability to achieve the required CR even with the most powerful compression algorithms.

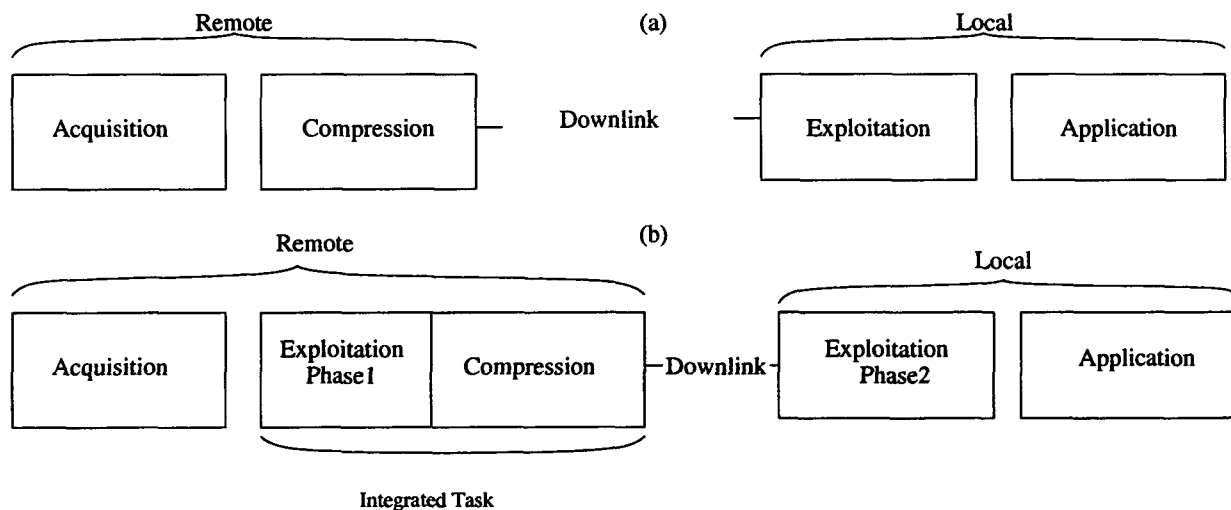


Figure 4.1. a.) Classical data compression b.) Data compression model using distributed data exploitation –Integrated Processing–.

Therefore, it is more convenient that some processing is performed on-board i.e. to move a part of data processing from the user side to the remote side. In other words, the alternative to efficient data transmission is to make the on-board sensor intelligent, and hence capable for interpreting the collected data. In the scientific literature several data compression algorithms exist, which are nearly optimal for a wide class of data. They make use of information extraction

methods in order to reduce the original data, by keeping the relevant information (parameters). On the other hand, it turns out that techniques for information extraction strongly depend on the kind of information or pattern to be sought and recognized. Those methods cannot be used for IR astronomy, especially for mid and far-IR as the features of the object of interest cannot be recognized at higher scale and lower integration period (see figure 1.2-a).

The global aim of this thesis is to recognize the optimal processing for space observatories' IR data for efficient transmission. For this purpose, a new compression concept is proposed by integrating part of the processing in the remote side, that is **On-Board Processing (OBP)**.

4.2 Integrated Processing for Space Observatories

The integrated processing is presented in Figure 4.1-b). It consists of two main part: OBP at the remote side and on-ground processing at the user side (local). A distributed processing (exploitation) on the remote and the user sides is used, so imposing to resort to data reduction (lossy compression), with potentially negative effect to the applicative tasks to be run at the ground station. This work is mainly focusing on the OBP part whereas the on-ground processing can be another topic of research, though both steps are highly dependant.

The OBP concept uses the IR detection systems know-how for optimal processing by adapting the methods to the signal characteristics. A model-based approach is used at the remote side in order to reduce the data according to the IR signal models. Besides allowing for qualitative data reduction at the airborne segment by means of a simple detection algorithm, this would also yield a strongly reduced computational burden, and the capability of performing a refined detection stage at the ground station on the decompressed data. Furthermore, knowing the data model leads to a very high compression efficiency (CR).

The scheme in Figure 4.1-b) differs from the classical data compression concept by integrating part of the the processing on-board the space observatory (Exploitation Phase 1).

1. Remote side: OBP

It is subdivided into three steps:

- Acquisition: It is identical to that in the classical concept.
- Exploitation Phase1: Figure 4.2 shows roughly the steps performed within this phase. The basic idea is to perform on-board integration in order to achieve a high CR. Thus, this reduction uses preliminary knowledge about the expected detector signal for low information loss. However, the resulting signal is usually contaminated by outliers due to the cosmic particles hit (glitches). Therefore, care is taken to not integrate over invalid detector readings by including glitch detection and removal before the integration.

The glitch event is also a sort of noise, which has to be reduced for efficient entropy encoding. However, it has to be to ensured that the noise reduction does not lead

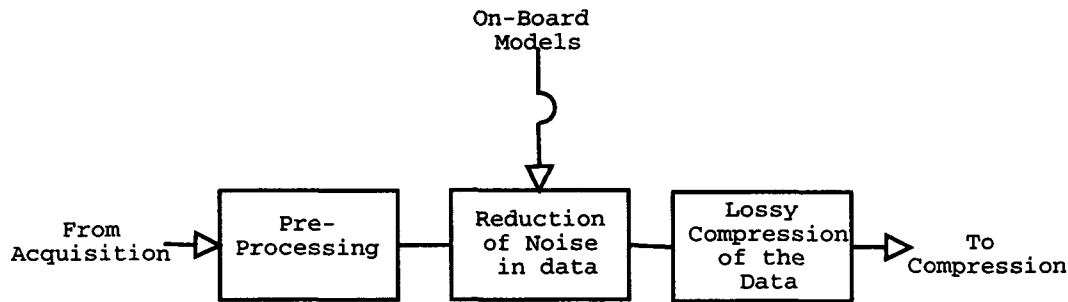


Figure 4.2: On board data reduction – Exploitation Phase1 –

to relevant information loss. Therefore, the glitch detection has to be adapted to the noise model using an adequate algorithm. Thus, this concept foresees to transmit a fraction of the data in raw such that the noise model can be computed and monitored at the user level for the update of the on-board glitch detection algorithm. Hence, the noise (considered as non-relevant information) is lowered from the data before the reduction using this adequate estimation of the noise. It can also be noticed that the reconstruction error mainly depends on the robustness of the modeling and the glitch removal.

- **Compression:** The lossless compression is adapted to the resulting signal from the previous step for optimal efficiency. For this purpose, dedicated sorting algorithm and entropy coders are proposed in this work, which are adapted to the IR detector signal.

2. Local side (user): on-ground processing

It is subdivided into two steps:

- **Exploitation Phase 2:** This is the counterpart of the OBP. It is performed to restore the data and make it available for usage, by predicting the negative effect of the tasks of exploitation phase 1. Indeed, the accuracy of the on-board modeling of the noise is relevant for image reconstruction. The multiscale filtering method [117] based on WVT might be used for the extraction of the information of interest. Indeed, multiscale analysis is useful, especially for faint sources, such that one can reduce the influence of noise by eliminating less important details in lower-resolution versions of the image. Furthermore, it finds regions of interest for plan-guided analysis at low cost in low resolution images, ignoring irrelevant details.
- **Application:** It is identical to that in the classical concept.

In the following sections, OBP concept is detailed and the individual processing steps are described. Though, this concept can be adapted to any detector type, the presented algorithms illustrate the case of the photoconductors. As mentioned before, on-ground processing that is another research subject, which is correlated with the dissertation goals, is not considered in this thesis. Although, decompression scheme has also been developed for the OBP concept in order to validate the feasibility of this proposed approach.

4.3 On-Board Processing

It is clear that IR space astronomy imposes specific requirements, which consist of fulfilling the bandwidth limited downlink requirement for a minimal data loss by means of limited on-board resources (memory and CPU power) due to the high cost of space-qualified devices. Therefore, improvement of the transmission reliability is possible while exploiting the signal model of the used detection system, in order to adapt the compression ratio to the available bandwidth, and by defining optimal schemes for coding information for different telemetry rates.

The On Board Processing (OBP) concept is then proposed to exploit this detection system know-how for efficient transmission of IR data from space observatories. IR astronomy data have high entropy due to the influence of noise [13, 43]. There are several sources of noise: detector noise, amplifier noise, electric cross talk, and pick-up noise and glitches [43].

The main challenging noise source for the OBP approach is the glitches since on-board integration is used. Therefore, glitch detection is a critical task that can only be efficient if including the user interaction for defining appropriate noise parameters for dedicated glitch detection algorithms.

The individual relevant processing steps used by the OBP approach is depicted in Figure 4.3. The following subsections describe these individual modules in detail, with special emphasise on the glitch detection, the oversampling reduction and the integration parts.

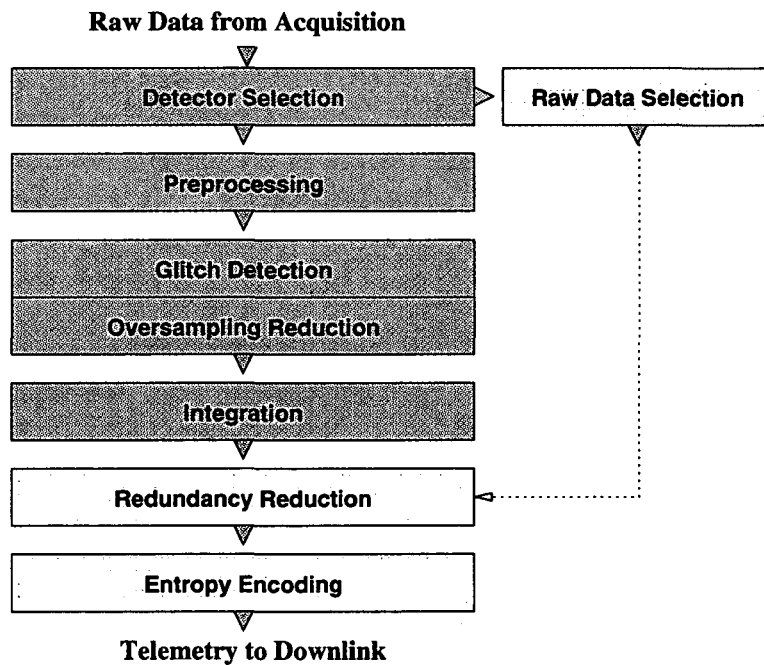


Figure 4.3. A schematic diagram outlining the OBP concept. (Dark Grey color for the modules where data are lossy compressed)

4.3.1 Detector Selection

In this step data selection according to a specific detectors status map is performed. The detectors selection makes use of on-board stored tables in order to discard non-relevant pixel's data from the downlink. As noted in Section 2.3.7, several detectors might be damaged in-flight such that their output signal is irrelevant for the scientific purpose. Therefore, it is necessary to isolate and remove them from the downlink for efficient exploitation of the telemetry bandwidth. Furthermore, in many cases, it is not necessary to use the whole detector array for an observation especially, if the object can be encapsulated in few pixels and the position of the object in the array is known. Therefore, depending on the object structure, pixels that represent the object of interest are selected and data from the other ones are discarded, whenever the point source is localized within the detector array.

4.3.2 Preprocessing

This step is dedicated to compensate the detector performance (i.e. the resulting signal is different from the mathematical model) by fitting the output data to the an expected model. The received signal is transformed to the appropriate form (e.g. linearizing as shown in Section 2.3.7) whenever the detector output model is known. Indeed, on-board signal correction (shape, linearity) is useful for efficient compression in terms of rate and complexity. In fact, this is used to reduce the noise (pick up and cross talk noise) in the data. It uses the characteristic of infrared detectors where blind pixels (not exposed to the light) are used as reference for the correlated pick up noise. A correlation matrix between the blind pixels on the reference lines and the actual pixels is used to remove the correlated noise.

4.3.3 Glitch detection

This is a critical step in the OBP scheme as the result quality of the compression depends on the glitch detection efficiency. Since on-board integration is performed, it has to be ensured to not integrate over invalid sensor readings (i.e. glitches). The detection of such events will be performed in the glitch detection module. The glitch detection will be done at the individual readouts level "Intrinsic Deglitching" as well as at integration level "Extrinsic Deglitching" and by considering subsequent integrated signals.

Intrinsic Deglitching: The idea is the use of a sigma-kappa clipping method for the detection of outliers at readout level. This is a simple method that can be adapted to any signal model respectively to any detector type. For illustration, let us consider the case of photoconductors where the detector output is in the form of ramps. The intrinsic deglitching makes use of the Slope Deviation Detection Method (SDDM), that is, the second derivative of the 1-D detector signal.

let us consider the case of 1-D detector signal " $X(i)$ " with 3 glitch occurrences as shown in Figure 4.4-A. SDDM performs the following steps:

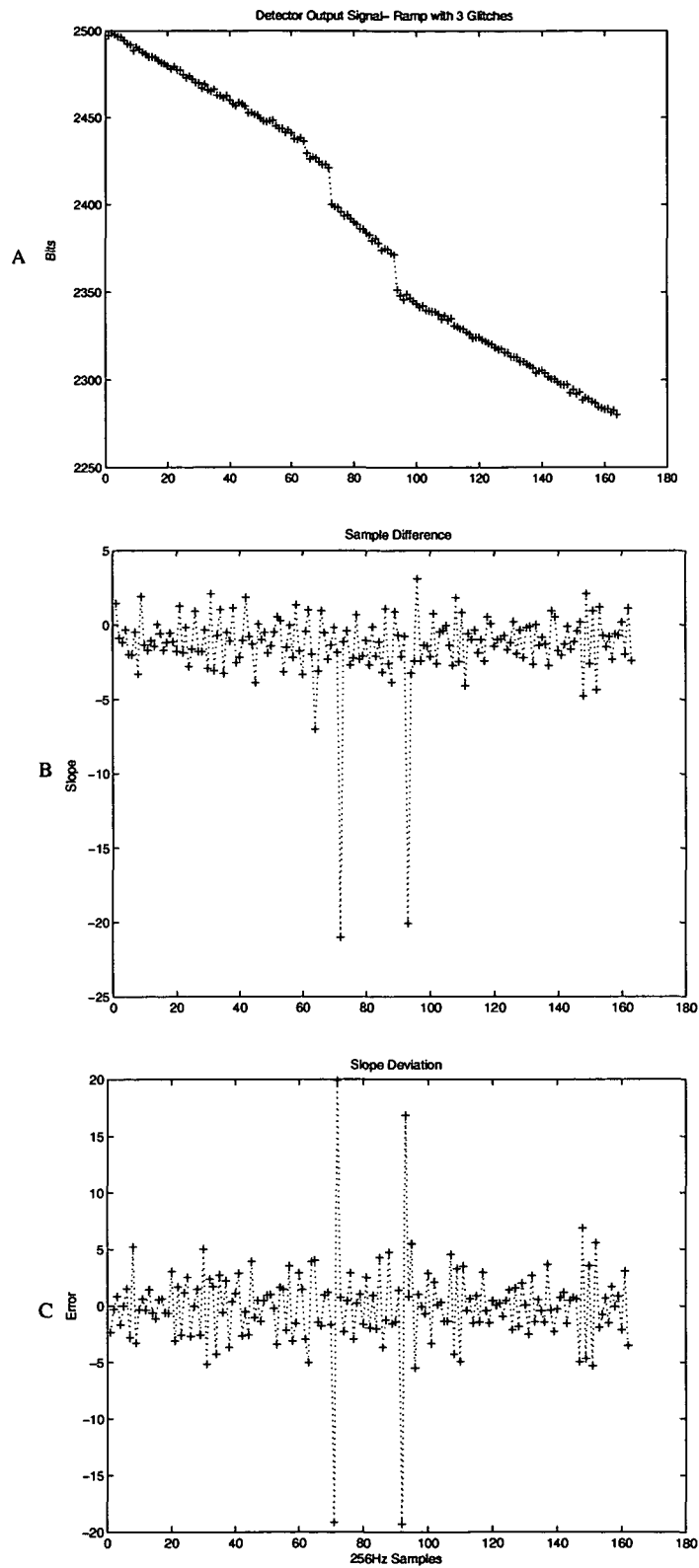


Figure 4.4. Illustration of intrinsic deglitching. A- 1-D detector raw signal. B- 1st step of SDDM (first derivative). C- 2nd step of SDDM (second derivative)

- Calculate the differences between all successive readouts in a ramp. As the readout interval usually is equidistant, the differences represent the slopes of the 1st derivative functions using two successive readouts (see Figure 4.4-B).

$$D(i) = X(i + 1) - X(i) \quad (4.1)$$

- Calculate the deviation of these slopes. It is the difference of the differences of successive samples. In other words, it represents the second derivative of the raw signal $X(i)$ (see Figure 4.4-C).

$$Dev(i) = D(i + 1) - D(i) \quad (4.2)$$

If no glitches occur for a linear ramp, the output would be zero.

- Remove all deviations that are above 3σ , where the σ represents the slope precision i.e. the non-linearity threshold.
- Perform the median averaging in order to reconstruct the removed samples and to make them available for the oversampling reduction.

Using this method, all detector outliers according to the σ level are discarded. It has the following advantages:

- Robust as all readouts are tested
- Fast as it only calculates samples differences. For N readouts ($2N-2$) operations are required.
- Well-suited for IR space astronomy as each readout is equivalent to the number of photons/time. For equidistant readout interval, this number is constant or near a constant in the ideal case. The amplitude might changes for a glitch event, which can be easily detected and rejected.

However, this method can be computationally expensive for limited processing resources as OBP consists of several processing steps. Therefore, this intrinsic deglitching can be further computationally improved as it solicits each readout twice for the difference calculation. An improvement of this method is made by involving each sample once for the difference calculation using different combinations. Indeed, the glitch event likely occurs on more than one measurement, depending on the detector type, the hit energy amplitude and the electronics efficiency. Therefore, the difference calculation between a subset of measurement is an alternative to speed-up the processing. The improved version of SDDM is named Slope Deviation Error (SDE).

Six cases are considered and represented in Figure 4.5.

- SDE_REG_APP1: This is the SDE regular approach1 that is equivalent to SDDM where several readouts are two times solicited for the calculation of the subslopes (the difference between subsequent samples). Then, the slope deviation is calculated between all successive subslopes. For N readouts, there are $2N-2$ operations.

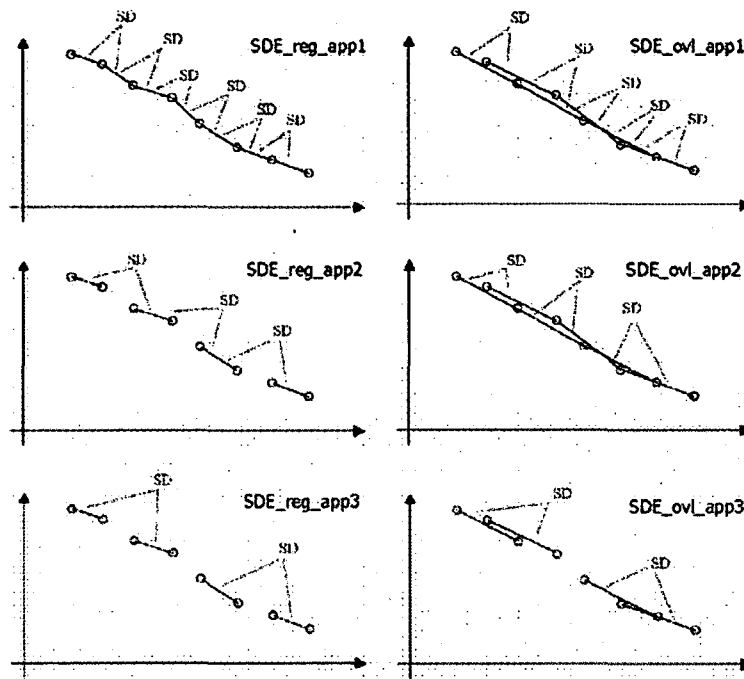


Figure 4.5: A schematic diagram for different approaches to slope deviation error

- **SDE_REG_APP2:** This is the SDE regular approach2 where all readouts are solicited one time for the calculation of the subslopes. Then, the slope deviation is calculated between all successive subslopes. For N readouts, there are N-2 operations.
- **SDE_REG_APP3:** This is the SDE regular approach3 where all readouts are solicited one time for the calculation of the subslopes. Then, the slope deviation is sequentially calculated for each pair of subslopes. For N readouts, there are $(3N/4) - 2$ operations.
- **SDE_OVL_APP1:** This is the SDE approach1 with overlapping where subslopes are calculated for readouts at odd index or even index positions. For example:

subslope1= readout3-readout1,

subslope2= readout4-readout2,

subslope3= readout5-readout3

.... etc.

Then, the slope deviation is calculated between all successive subslopes. For N readouts, there are 2N-2 operations.

- SDE_OVL_APP2: This is the SDE approach2 with overlapping where subslopes are calculated as for SDE_OVL_APP1. Then, the slope deviation is calculated sequentially for each pair of subslopes. For N readouts, there are N-2 operations.
- SDE_OVL_APP3: This is the SDE approach3 with overlapping where subslopes are calculated as for SDE_OVL_APP1 but solicited only one time. Then, the slope deviation is sequentially calculated for each pair of subslopes. For N readouts, there are $(3N/4)-2$ operations.

Regular cases are noted (REG) while approaches with overlapping are noted (OVL).

For a compromise between efficient glitch detection and fast computation, the case of SDE_REG_APP2 or SDE_OVL_APP2 are sufficient for detecting the glitch using an appropriate σ . However, SDE_REG_APP1 or SDE_OVL_APP1 are mandatory for short integration ramps because resetting the detector signal for a new exposure can release part of the glitch energy, which make the detection of the invalid measurements challenging.

Furthermore, the intrinsic deglitching cannot efficiently detect the transient behavior of detectors if a long relaxation time is needed to discharge the cosmic hit energy. Therefore, extrinsic deglitching is used to complement the glitch detection process.

Extrinsic Deglitching: In this case, the difference between integrated readouts is taken into account in order to detect for glitches. The same approach used at readout level (SDDM) is applied at integration level. If two subsequent integrations differ more than 2σ , there is an indication of a glitch.

For short time constant, the indication of a glitch leads to the removal of the whole integration. The reconstruction of such data may be performed on-ground either by using the median averaging of the subsequent integrations or by replacing it with the average value of surrounding good integrations, although it is not recommended.

Indeed, the detection of glitch tails after the cosmic hit relaxation is a critical issue. Since the behavior of the detector might change for some time after it has been hit by a glitch, this is a critical issue. Indeed, for short time constant, the hit samples shall be discarded, otherwise the user support is required for long duration observation in order to automatically detect this transient behavior using an appropriate σ .

The next thing to consider is the potential loss of scientific data. Of course, the glitch detection will not be 100% correct. Therefore, the potential loss of scientifically valid data can be quantified by the glitch detection rate and the number of ramps that will be integrated. Assuming a glitch rate of every 10s/pixel, with a glitch tail of 0.5s, there is a probability of $p_{glitch} = 1/20$ that a ramp is effected by a glitch. Then, the potential loss of scientific data p_{loss} can be calculated as follows:

$$p_{loss} = 1 - (1 - p_{glitch}(1 - p_{det}))^n \quad (4.3)$$

where n is the number of integrated ramps and p_{det} is the glitch detection efficiency.

Table 4.1 lists the potential data loss for various numbers of integrations for different glitch detection rates.

# ramps	no glitch detection	50%	90%	99%
2	9.75%	4.94%	0.99%	0.1%
4	18.55%	9.63%	1.99%	0.19%
8	33.66%	18.33%	3.93%	0.39%
14	51.23%	29.84%	6.77%	0.67%

Table 4.1: Potential loss of scientific data

A glitch detection rate of more than 95% seems feasible, therefore the potential data loss will be around 1%-3%. In fact, it will be lower because in the above calculations it was assumed for simplicity that a glitch and its tail are independent events, which is not true. In fact, if the glitch is detected its tail can be also tracked. In addition, it was assumed that when a glitch is not detected, all integrated measurements will be lost. In fact, if a small glitch is missed and integration over it is performed, this just decreases the signal to noise ratio. Another thing not considered is a false negative rate, i.e. to discard a ramp even if it is not affected by a glitch, this will of course also lead to a loss of scientific data. But this can be directly estimated. In addition, this has no effect on the other data. From these considerations, it can be noticed that the glitch detection efficiency is a driving factor for high CR with minimal loss of scientifically valuable data.

4.3.4 Oversampling Reduction

The oversampling reduction is one of the crucial steps of the proposed data reduction concept. For quantum efficiency purpose, the detectors readouts are oversampled at the multiplexer stage. For the different oversampling techniques, see Section 2.3.3. The oversampling reduction method depends on the sensor used. It represents ramp-fitting in case of photoconductors, while it is curve-fitting in case of photodiodes or bolometers (Section 2.3.2). For illustration reason, the case of the photoconductors is considered. Extension to other detector types can be easily made as far as the data model of the detector output is known.

In the case of photoconductors, ramps represent the detector output model. There are two kind of ramps: linear and non linear. Let us focus first on linear ramps. The ramps are fitted to the sensor readings in order to obtain the flux. Let us consider the samples belonging to a ramp given by a vector $\mathbf{x} = [x_1, \dots, x_n]^T$. A linear ramp is given by

$$\mathbf{x} = \mathbf{st} + \mathbf{o} + \boldsymbol{\eta} \quad (4.4)$$

where s is the unknown slope, \mathbf{t} are the known instants of sampling, \mathbf{o} is the unknown offset and $\boldsymbol{\eta}$ is a vector of random variables with distribution of every element assumed to be $N(0, \sigma)$,

characterizing the noise process.

In order to obtain the parameters of interest this equation has to be solved in a robust manner. Therefore, particular considerations on the detector measurements have to be taken into account.

1. Gaussian Noise:

For pure Gaussian noise, the contribution of each individual measurement to the ramp fit is unique. By considering a ramp consisting of n data points, the statistical weight of each sample is $1/n$. In this case the least squares solution is the optimal one.

2. Poisson Noise: For pure Poisson noise, all information relevant for the ramp fit is contained in the last measurement. By considering a ramp consisting of n data points, the statistical weight of the n^{th} sample is 1, and the statistical weight of all other samples is 0. In this case, the last measurement is the result of the ramp fit. Because of the simplicity of this solution, this case will not be discussed in the following subsections.

3. Combined Noise Sources: For combined noise sources, an intermediate solution is expected. By considering a ramp consisting of n data points, the statistical weight of each sample increases with index k , $k = 1, \dots, n$. In this case, a combination approach is required for the best ramp fit result.

In the following subsections, the ramp fitting options [12] for the oversampling reduction are detailed and its feasibility respective to the glitch detection efficiency is discussed.

Least squares solution: The least squares solution can be easily calculated in analytic form, and is optimal with respect to the Gaussian noise process. However, in case of extreme outliers (i.e. glitches) it performs very poor. Fig. 4.6(a) shows an example where least squares is performing very well. Whereas Fig. 4.6(b) shows the least squares solution on the same data as in Fig. 4.6(a) where one sample is an outlier. One can clearly see that the obtained ramp is far from being perfect. Therefore, in case the extreme outliers are not detected/removed by the glitch detection module, the least square fit will not provide the expected signal.

Robust solution: Since the solution has to be found in a robust manner, a robust fitting procedure has to be used. There have been many proposals how to obtain a solution to the Equation 4.4 in the presence of outliers (e.g. see [48, 104]). RANSAC is one of these proposals. As mentioned in Section 3.6.1, RANSAC obtains the theoretically optimal breakdown point of 50%, i.e. it still can fit ramps if not more than 50% of the points are outliers. Fig. 4.7(a) shows the same example like in Fig. 4.6(b) but fitted using RANSAC. One can clearly see that in this case the outlier is ignored and we obtain a perfect fit. Fig. 4.7(b) demonstrates the drawback of RANSAC, namely its low efficiency in removing Gaussian noise. Since the RANSAC solution is based only on two points there is no possibility of reducing the Gaussian noise. To alleviate this problem, the robustness of RANSAC with the optimality of the Least squares method can be combined.

RANSAC and Least Squares: The idea is very simple. First RANSAC is performed on the ramp, then all points in the support set are taken to calculate the least squares solution.

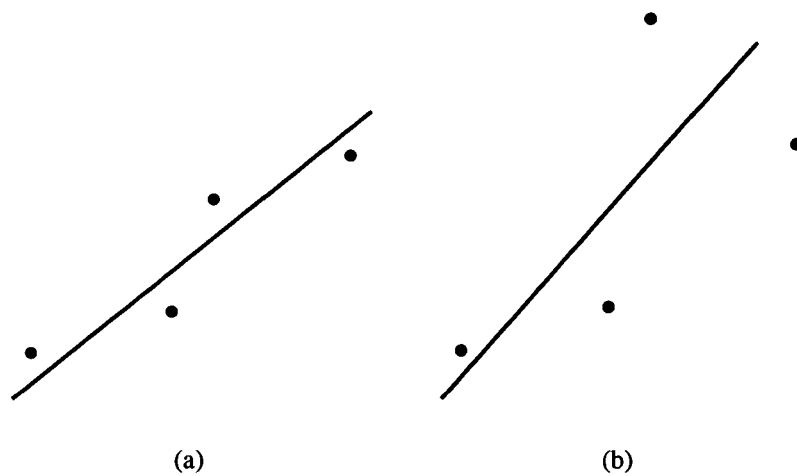


Figure 4.6: Least squares fitting.

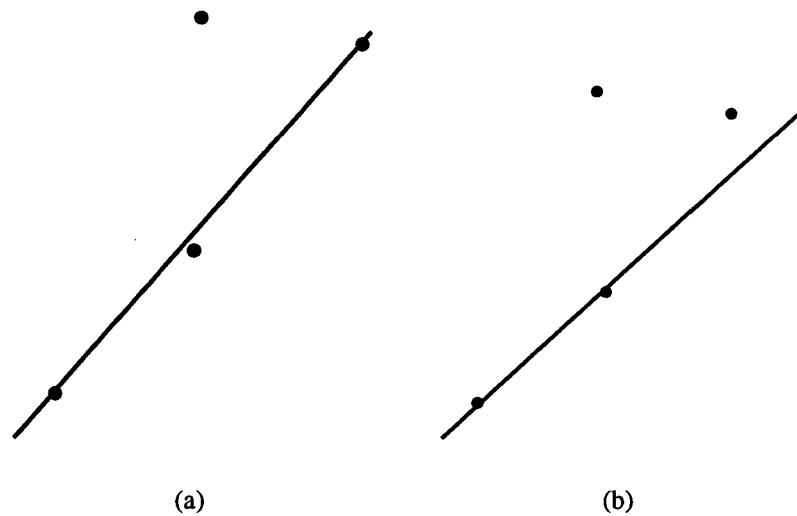


Figure 4.7: RANSAC Fitting.

Thereby, we have the robustness of RANSAC and in addition the efficiency of the least squares solution. Fig. 4.8 demonstrates this on the example of Fig. 4.7(b). One can clearly see that the solution obtained ignores the outlier and smooths the Gaussian noise.

The result of the ramp fitting are the slope and the offset of the ramps, and for each sample on the ramp we have a flag if it is an outlier or not. If it is not an outlier we have in addition a residual value. Therefore, if the glitch detection performs well, then the least square will be sufficient to reduce the Gaussian noise while fitting the sensor reading. Otherwise, the combined approach is mandatory for robustness against outliers at the price of additional processing time.

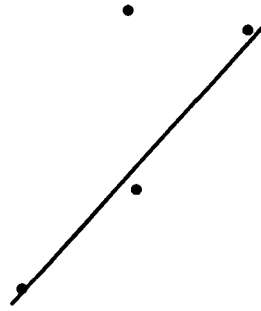


Figure 4.8: Illustration of RANSAC and Least squares.

It can be shown that an extension to the non-linear ramps could be easily done whenever an analytic model of the ramp is available. Furthermore, the fitting can be performed over a small part of ramps (subramps), typically 4 samples, such that non linear ramps are also considered to be linear in short time constant, if non linearity is above the 4 samples scale. Figure 4.9 illustrates an example of sub-ramp fitting for non linear ramps. The flux can be computed, then, as a weighted mean of sub-slopes.

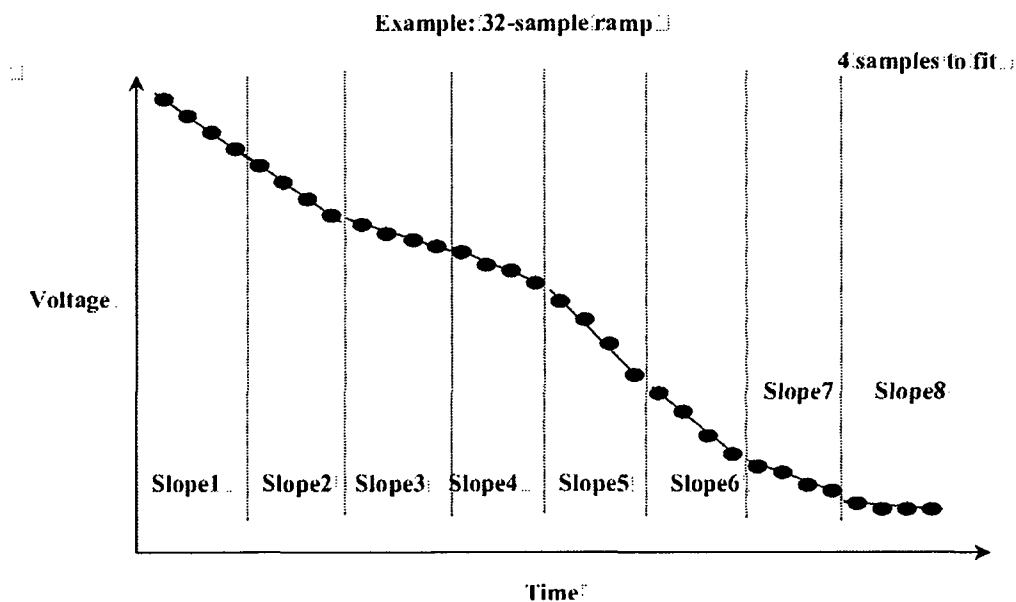


Figure 4.9: Non-linear fitting: Least squares fitting of sub-ramps.

4.3.5 Integration

This module will perform on-board integration of the sensor readings in order to achieve the desired compression ratio. This is the lossy compression part of the approach. Special emphasis has to be paid in order to guarantee integration over the right readings – synchronized with the positions of the chopper and the telescope pointing – and not to integrate over exposures affected by glitches. Thus, the integration process first determines whether to discard all data of an integration block if there is a lack of confidence in at least some of the samples. Then successive integrations of a number of successive exposures within the same chopper and pointing positions will be added, if they are free of glitches.

4.3.6 Redundancy Reduction

The previous modules represent the lossy, i.e. reduction, part of the data reduction/compression system. The further modules constitute the lossless, i.e. compression, part. To achieve the high required ratio, many iterated compression steps should be applied. After the integration, there is a sequence of arrays we call frames with dimension $M \times N$ (i.e., A^t , where $A \in \mathbb{R}^{M \times N}$ is an array of integrations at time t). Since temporarily and spatially adjacent measurements will be similar, one can use this fact for further data reduction.

Another alternative for efficient lossless compression is to perform a proper sorting respective to the detector knowledge before the redundancy reduction. The aim of the data-sorting step is to increase the local redundancy between successive samples in memory for fast and efficient entropy coding. For example, in case of photoconductors, the method applied in this step makes use of the detector knowledge under the assumption that the detector response to incident light does not significantly change from ramp to ramp (excluding the glitch) at detector level i.e. the first sample in the second ramp of one detector output is assumed to not deviate too much from the first sample of the first ramp of the same detector. Under this assumption, the data-sorting is first applied, according to the sample index in a ramp, for increasing the redundancy before the redundancy reduction and entropy coding steps.

Ramp Samples Sorting: Figure 4.10 depicts an example of photoconductor's data for 16-sample ramps.

In case of 512 detectors and 'N' ramps, data might be organized in a buffer as follows:

detector1[ramp1...rampN] detector2[ramp1...rampN]... detector512[ramp1...rampN]

where the number of ramps (rampN) is equal to:

number of frames / number of samples per ramp (16 in our example).

By making use of this knowledge, the sorting can be performed as follows:

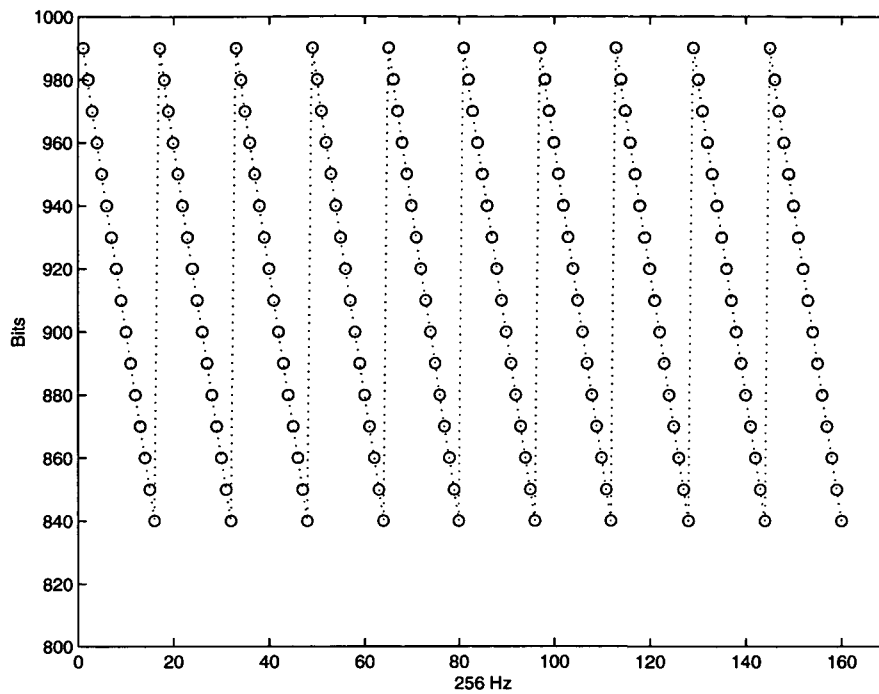


Figure 4.10: Examples of a sequence of 16-sample ramps

1st sample of 1st ramp of 1st detector

1st sample of 2nd ramp of 1st detector

...

1st sample of Nth ramp of 1st detector

1st sample of 1st ramp of 2nd detector

...

1st sample of Nth ramp of 2nd detector

...

1st sample of Nth ramp of 512th detector

2nd sample of 1st ramp

...

16th sample of 1st ramp of 512th detector

16th sample of 2nd ramp of 512th detector

...

16th sample of Nth ramp of 512th detector.

Figure 4.11 illustrates the sorting result of the data illustrated on Figure 4.10. Using this method, efficient redundancy reduction can be performed by sequentially looking in memory for duplicated symbol at smaller distance (represented by plateaus in Figure 4.11).

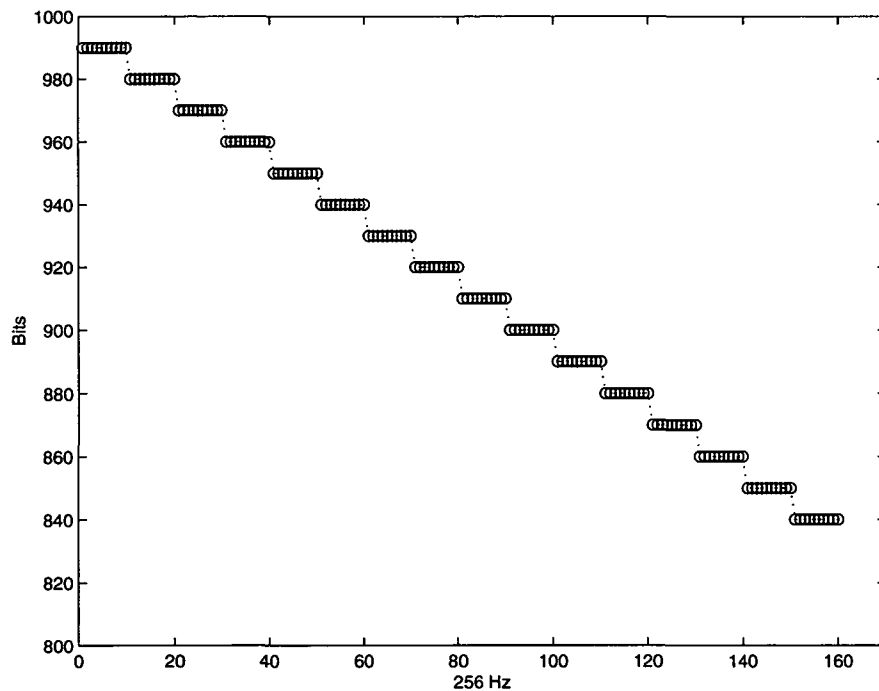


Figure 4.11: Sorting result of the 16-sample ramps sequence

Temporal Redundancy Reduction: Let us calculate:

$$\Delta^{t+1} = A^t - A^{t+1} \dots \Delta^{t+n} = A^t - A^{t+n} \quad (4.5)$$

If subsequent frames are similar, then,

$$|\Delta^{t+i}| \ll |A^{t+i}|, 1 \leq i \leq n \quad (4.6)$$

Therefore, It will result from this reduction:

$$A^t \text{ and } \Delta^{t+i}, 1 \leq i \leq n \quad (4.7)$$

Spatial Redundancy Reduction: After the temporal redundancy reduction, spatially neighboring values in Δ^{t+i} should be similar (in the ideal case they are zero), therefore, additional compression gain could be achieved by encoding the difference of neighboring pixels.

4.3.7 Entropy Encoding

Redundancy reduction as outlined above, should have reduced the magnitude of pixels values as much as possible. This fact makes it possible to make assumptions about the distribution of the data, what is a prerequisite for efficient lossless coding. Generally, the astronomical images have uniform background stray-light "Dark Current". Therefore, the data packet related will contain many identical sample values. The redundancy reduction is suitable to optimize the data packet size. A combination between the RZIP [93] and arithmetic encoding [49] algorithms is performed for further compression. The RZIP algorithm which is a variety of run-length encoding was especially developed for PACS [150] data entropy coding, but can be adapted for other detector data encoding using a proper sorting. Indeed, the RZIP entropy coder, like other coding algorithm, finds its efficiency using a proper data sorting. The data sorting depends on the instruments and detectors proper responsivity, that differs between detectors. Below, you find the formal descriptions of the RZIP algorithm.

RZIP Algorithm: *RZip* is a character-oriented compression technique that was initially developed for PACS Header compression [93]. It is also intended for compression of any other data, whenever the contexts are known. The emphasis was on writing an algorithm that runs *fast* on the DSP and compresses data as efficient as possible.

The strategy of *RZip* for searching redundancies in the input buffer is closely related to the data granularity. Let us consider an example of words with 32-bit wide. Therefore, a symbol size of 32 bit ensures a good chance in finding recurring equal symbols. Another important factor to consider is the word size of the CPU or – e.g. the DSP –. Most DSP instruction sets only support 32-bit granularity.

So, *RZip* focuses on 32-bit words. Given an arbitrary 32-bit symbol of a data buffer, a logical question can be asked, "Does it recur, or not?" If so, "where in the buffer or how often does it repeat?"

Basically, *RZip* takes a symbol and looks ahead for recurrence within a certain index range. The index difference of the two occurrences is encoded taking already coded indices into account. After that, the next occurrence of the symbol is sought if the end of the buffer is not encountered. In case there are no more occurrences, the source buffer is investigated for the next candidate symbol.

The distances can be encoded in different ways. One way is to use the maximum distance as an indicator for no more recurrences. For example, a binary flag after a symbol in the encoded data stream indicates either that an offset will follow or that there are no more occurrences for the current symbol.

Two parameters determine the performance of the algorithm:

- The size of a symbol quantifies the number of bits per symbol. In our case, this is fixed at 32 bit per symbol.
- Δ sets the width of the range to look ahead for recurring symbols. For instance, a Δ of 4 means that $2^4 = 16$ indexes will be checked.

For illustration of the method, an explanatory example run is given:

RZIP Example:

Let SOURCE be the data buffer to be compressed. Let DEST be the destination buffer where the compressed data will be put.

Δ is the parameter that determines the number of bits to use for encoding ranges. In the following example, 2 is chosen, therefore the effective offset counter δ will be 0..3 ($= 2^2 - 1$). The size of a symbol shall be 32 bit.

The SOURCE (symbol buffer) may look like:

A A B C A A C C B B {SOURCE}

There is also need for a workbuffer WORK. At the beginning of the algorithm, it has to be cleared.

0 0 0 0 0 0 0 0 0 0 {WORK}

a) Select the first unused (workbuffer = 0) symbol and the workbuffer to 1.

A A B C A A C C B B {SOURCE}
 1 0 0 0 0 0 0 0 0 0 {WORK}

b) Look ahead if the symbol recurs within δ . If yes, code 1 within 1 bit and δ within Δ bits. Set the proper position of the found symbol in the workbuffer to 1. Reset the δ to 0 and continue until no further occurrences are found, then code 0 in 1 bit.

c) Go back to a) until the end of the buffer.

First, all As are coded.

```
A A B C A A C C B B {SOURCE}
1 1 0 0 1 1 0 0 0 0 {WORK}
A  y0 . . y2y0 n     {DEST}
```

The next symbol to code is B.

```
A A B C A A C C B B {SOURCE}
1 1 1 0 1 1 0 0 0 0 {WORK}
Ay0y2y0n B n       {DEST}
```

Next one is C.

```
A A B C A A C C B B      {SOURCE}
1 1 1 1 1 1 1 1 0 0    {WORK}
Ay0y2y0nBn C . . y0y0 n {DEST}
```

And finally, B again.

```
A A B C A A C C B B      {SOURCE}
1 1 1 1 1 1 1 1 1 1    {WORK}
Ay0y2y0nBnC y0y0n B y0 n {DEST}
```

In this example, 10 symbols of 32 bit size are encoded to 4 symbols plus 10 flags plus 6 ranges $\Delta = 2$ bit. So, the input stream was 320 bit and the output stream is 150 bit. Therefore, the achieved CR in this case is 2.13.

Note that the difference between A A will be encoded 0 (0 symbols are between them). The difference between A X X A will be encoded 2 if the X have not been coded before

and if a range of 2 is allowed due to the set Δ (this should be the case). In case all As have been already encoded, the difference between the Bs in $B \ A \ C \ B$ will be encoded as 1 (the As are already invisible due to the mask in the workbuffer).

Once a buffer has been compressed with a set of parameters, it can be encoded another time with different parameters. For example, PACS header compression works best with $\Delta = 6$ applied *twice*. Using more than three iterations did not yield any more compression in most cases.

Arithmetic Coding: The resulting data from RZIP are further compressed by the arithmetic coder in order to reduce the statistical redundancy.

4.3.8 Raw Data Selection

This step is responsible for transmitting selected data that are lossless compressed using the redundancy reduction and entropy coding modules. The main reason for this module is to check the performance of the on-board data processing and the signal models, on ground, for further algorithms adaptation and improvement. This is an important module, which allows the user to access part of the raw data in order to monitor the OBP and interact with the individual processing steps for the improvement of the processing performance.

4.4 Application of the On-Board Processing for Astronomical Infrared Images

In this section, a demonstration of the OBP performance is made on astronomical IR images and compared with those from the compression standards mainly JPEG2000. Further evaluation of the OBP approach on a large database from PACS detector data is given in Chapter 6. State-of-the-art generic compression methods are applied on Mid-IR images from the ISO camera [147] in order to present their performances for evaluation. Images from the starburst galaxy NGC 1808 [115], taken with ISOCAM [13] on January 1998 at the wavelength of $6.7 \mu\text{m}$, are used to compare the performance of JPEG 2000 [126], ZIP [157] and RAR [156] with the proposed framework "OBP".

To fix ideas, the NGC 1808 is a barred spiral galaxy similar to the milky-way galaxy (our galaxy). It is undergoing so much star formation it has been deemed a starburst galaxy. This makes its study interesting in the IR range as it allows to peer into the dust. However, it is worth to show the impressive NGC 1808 image (Figure 4.12) in the visual range, taken by Hubble Space Telescope (HST) [151] on March 1998. The blue glow depicts regions with active star formation. As filaments of dark dust are obscuring even more activity, it is interesting to further analyze these activities in IR range.

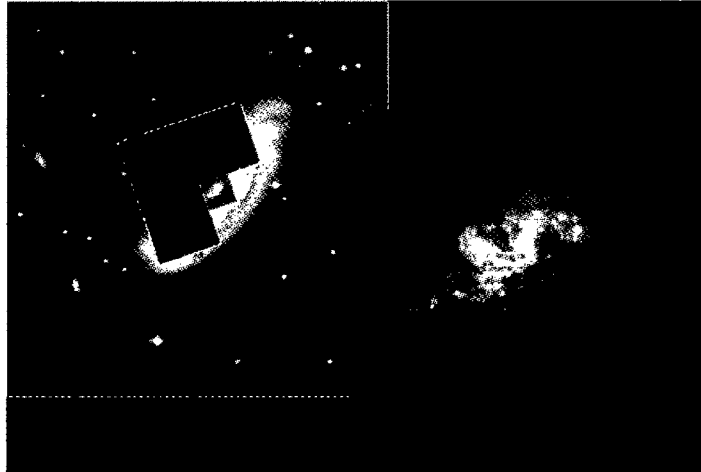


Figure 4.12. Starburst galaxy NGC 1808 taken by the Hubble Space Telescope using the instrument "Wide Field Planetary Camera 2"

The science infrared image of NGC 1808 is depicted in Figure 4.13, as taken by ISOCAM at $6.7 \mu\text{m}$ for the detector array of 32×32 pixels Charge Injection Device (CID), with 16-bit. This image is a result of 19 minutes observation, after post-processing of 1032 raw images with 2.1 seconds exposure duration on each image. At the beginning of this selected exposure time,

the pixels were reset to a constant charge and read out, after which the detector was exposed to incoming radiation for the exposure time and read again. The quantum of measurement consists, therefore, of a pair of RESET and End-Of-Integration (EOI) frames. Figure 4.14 depicts a sequence of 30 selected raw images of NGC 1808. Images with odd index represent the constant charge readout while images with even index represent the EOI frame. The white vertical line represents the column 24 with dead pixels, detectors that were lost during the mission. Some images show white dots and curves, which represent the cosmic particle hits (glitches), that influence the EOI raw images calibration. No on board reduction was needed for this observation as the readout rate fits into the telemetry rate of about 4 Kbits/s. Otherwise, several images was averaged on-board to fit the telemetry whenever a shorter exposure time was used. However, most of the processing has been performed on-ground offline the observation.

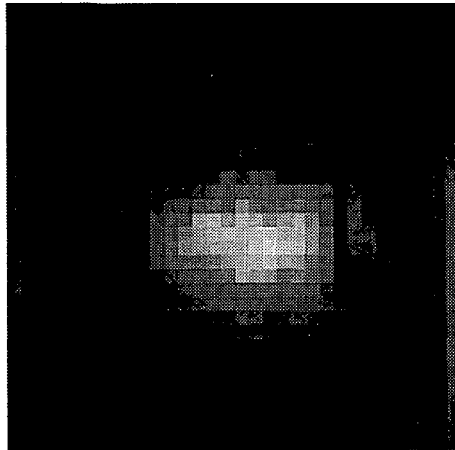


Figure 4.13: Starburst galaxy NGC 1808 taken by ISOCAM at $6.7\mu\text{m}$

On the other hand, OBP is mandatory for larger detector arrays and, thus, higher data volume as the data rate exceeds the available telemetry bandwidth. What is, then, the best and adequate method to fit the telemetry?

As a first step, JPEG 2000 [126], ZIP [157] and RAR [156] methods are applied to these NGC 1808 raw images (1032 frames) for performance evaluation. Figure 4.16 depicts the resulting image from OBP for a compression ratio of 15. Figure 4.15 depicts the resulting image after JPEG 2000 compression of individual raw images for a compression ratio of 6. This JPEG2000 implementation [128] (Kakadu software) uses EBCOT algorithm (Embedded Block CODing with Optimized Truncation) [127] for the quantization of the wavelet coefficients and the binary arithmetic coder as backend entropy codec. The quality loss compared to the original image (Figure 4.13) can be observed, which is due to the performed quantization by means of the EBCOT algorithm. For better error display, both reconstructed images are plot as a 1-Dimensional signal in Figure 4.17. On the X-axis, the pixel indices (1-1024) are represented

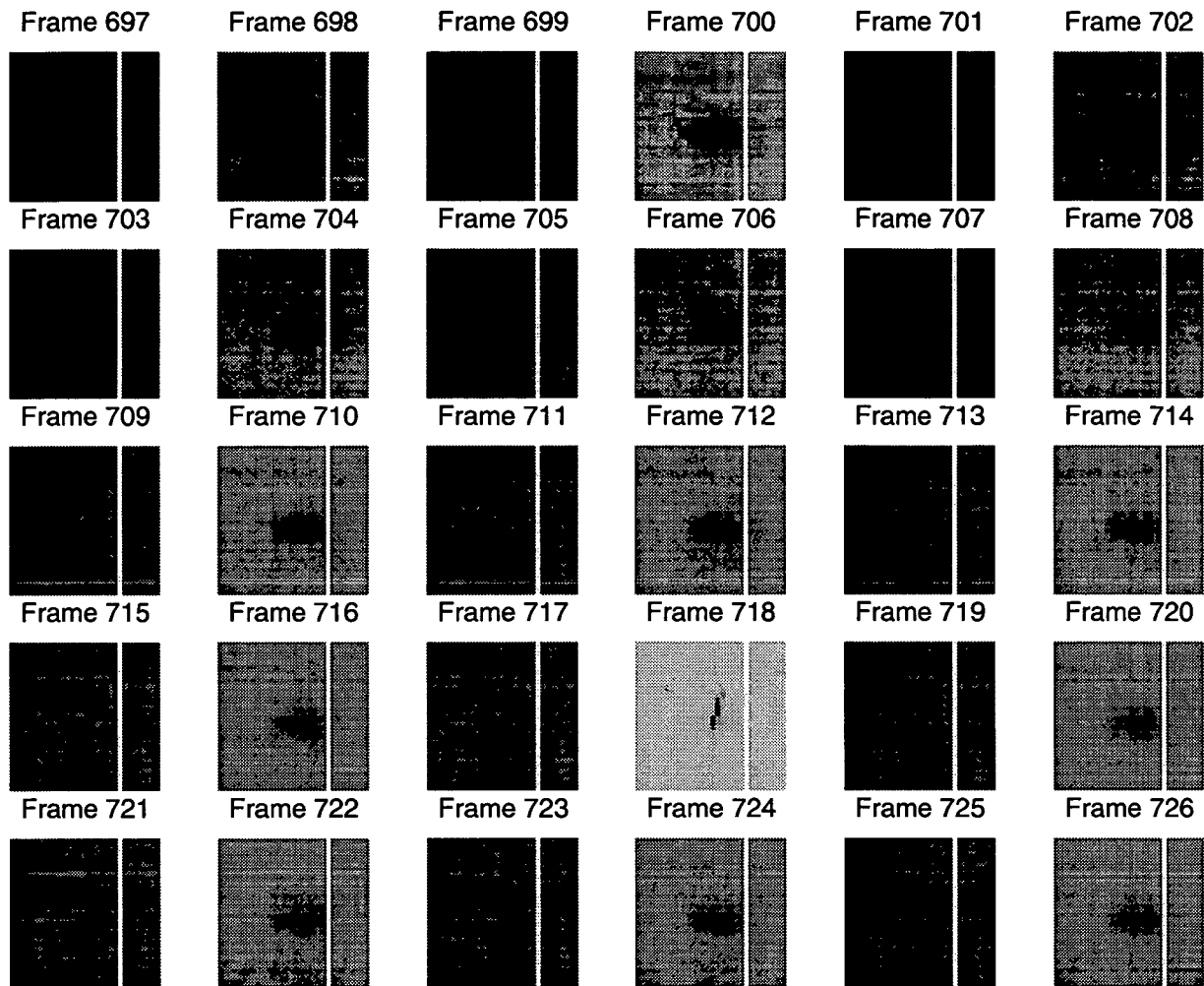


Figure 4.14. Selected ISOCAM raw images sequence (30 images) during NGC 1808 observation at $6.7\mu\text{m}$

while pixel values, for both original image and JPEG2000 reconstructed image, are depicted on the the Y-axis. It is shown in this figure the approximation error due to the EBCOT quantization.

For further assessment, the lossless codecs ZIP and RAR are run over the NGC 1808 raw images and compared to JPEG 2000 results in terms of compression ratio, processing time and memory usage.

ZIP's implosion algorithm finds duplicated strings in the input data. The second occurrence of a string is replaced by a pointer to the previous string, in the form of a pair (distance, length). Afterward, distances and lengths are themselves compressed using Shannon-Fano encoding [49], which is somewhat similar to Huffman coding [49]: frequent values are encoded on fewer bits than unlikely values.

RAR is a compressed archive format developed by Eugene Roshal that uses several encod-

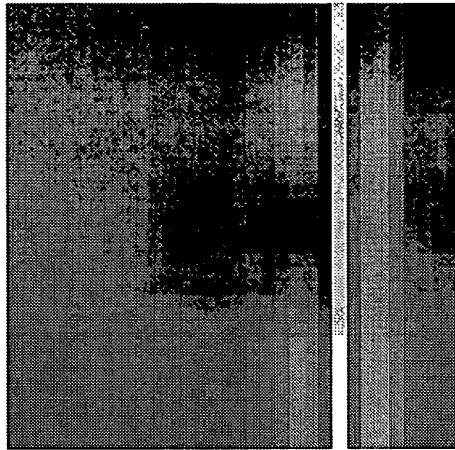


Figure 4.15. Resulting NGC 1808 image after JPEG 2000 compression (Kakadu method) for a compression ratio of 6

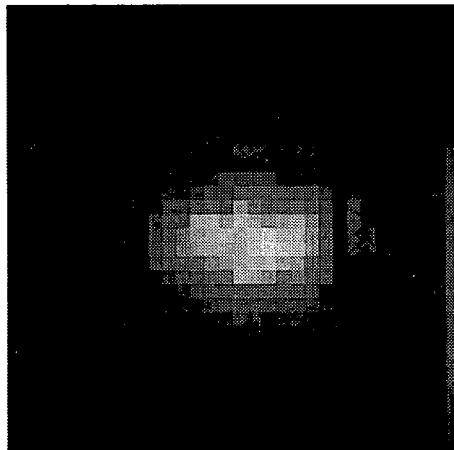


Figure 4.16: Resulting NGC 1808 image after OBP for a compression ratio of 15

ing algorithms mainly Huffman-like [49] to support several compressed formats.

Compression results using the above listed generic methods are reported in Table 4.2 for comparison purpose. The results for the proposed method "OBP" is also reported in this table. All methods have been run on a 450 MHz Pentium PC with Windows Nt 4. It is noted the highest compression ratio for faster processing time, and lower memory space needed by OBP for the reduction of NGC1808 raw images compared to the generic compression methods. The OBP approach makes use of the IR astronomy signal characteristics and the limited resources for a better of fit the compression needs to the available resources. Note also that the resulted NGC 1808 image using OBP approach is equivalent to the original image in Figure 4.13. An evaluation of OBP on a IR data from a large database from PACS detector test is made in Chapter 6.

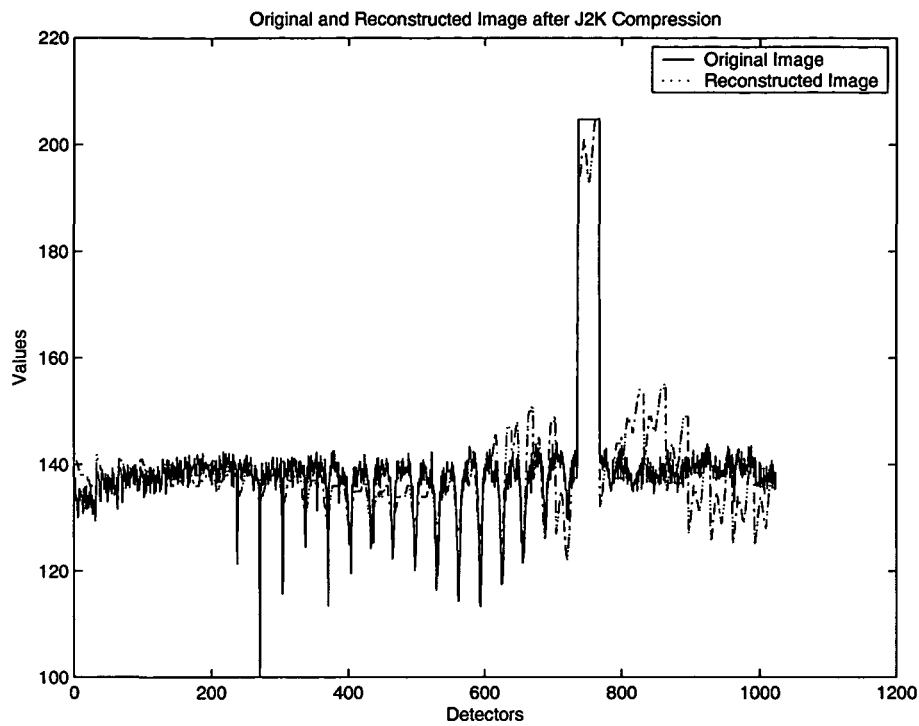


Figure 4.17: Illustration of the original and JPEG2000 compressed image on a 1-D plot

Method	CR	Processing Time (msec.)	Memory Usage (KB)	PSNR	PIL (%)
ZIP	1.39	24285	37240	INF	0
RAR	1.40	34500	18912	INF	0
JPEG 2000	6.38	158600	4128	54	3.34
OBP	15.44	120	1900	97	0.08

Table 4.2. Comparison of compression performances on NGC 1808 raw IR images(1032 frames) between JPEG 2000, ZIP, RAR and the proposed approach (OBP)

Chapter 5

Complexity Related Aspects

This chapter intends to estimate the complexity of the OBP concept for an assessment of the feasibility of this approach for IR space observatories. Indeed, IR space observatories usually have limited budget and therefore, limited resources. Thus, an evaluation of the complexity of OBP for the available processing resources is mandatory to validate the realisability of this concept. First of all, the criteria to assess the complexity of an algorithm are investigated for the case of **Digital Signal Processors (DSP)**, which are the common processing platform in space applications. Then, a formulation for a quantitative estimation of the complexity of a compression algorithm is made. It is then used to measure OBP complexity on a DSP.

This chapter can be subdivided into 2 parts: complexity analysis and OBP complexity measure. In the first part, a methodology for complexity analysis of a compression algorithm is given. Using arithmetic and memory operations, a complexity measure for a given algorithm can be performed by choosing appropriate weights that depend on the platform architecture. The resulting approach is used to measure the OBP complexity on the Analog device DSP – ADSP 21020 – in the second part of this chapter. The final complexity is the sum of the contribution of all OBP modules to given input data with size "N".

5.1 Complexity Definition and Measures

The complexity of an algorithm can be described as the number of steps required for this given algorithm to solve a computational problem. The level in difficulty in solving mathematically posed problems are measured by the time, number of steps or arithmetic operations, or memory space required, respectively called, time complexity, computational complexity, and space complexity. The interesting aspect is usually how complexity scales with the size of the input, where the size of the input is described by some number "N". Thus an algorithm may have computational complexity $O(f(N))$, where "f" is the complexity function that is proportional to the number of required steps.

Complexity is a very important parameter for data compression theory and applications. The reason is that it is often desired that the algorithm works in a transparent manner to the user. Thus, its execution should require minimum resources and be executed as fast as possible.

The complexity of a given algorithm can be analyzed in two ways: qualitatively and quantitatively [97]. Qualitative analysis usually means determining the complexity of the algorithm relative to other algorithms. Such analysis does not usually allow to quantify the difference in complexities between algorithms. Quantitative analysis methods assess the complexity of a given algorithm in absolute terms, and often provide a numerical estimate of the complexity. Therefore, using quantitative analysis, it is also possible to state, for example, that algorithm A is three times less complex than algorithm B. Measuring the complexity of a given algorithm is along and difficult process. Currently, very few methods exist to measure the complexity of entire signal processing algorithms. In the case of simple algorithms, such as the DCT, the number of arithmetic operations can give a good estimate of the algorithm complexity. However this is not sufficient for more complex schemes such as image compression algorithms. In the following subsections, both complexity analysis techniques are detailed.

5.1.1 Qualitative Complexity

The first approach taken to understand and optimize the complexity of signal processing algorithms is based on an intuitive understanding of the complexity. For instance let say that it is possible to find two algorithms realizing the same task. Suppose, the first one is based on integer arithmetic, whereas the second one uses floating-point arithmetic. It is known that even with the most modern computer architectures, floating-point operations are more complex than their integer equivalents. However, it is difficult to quantify this difference without considering a specific hardware architecture [97].

Let us propose another example, in which it is well known that two algorithms differ in complexity because of the amounts of memory they require. However, the relationship between the size of the memory and the complexity is not defined. Therefore, the difference in complexity is not quantifiable. Nowadays, the wavelet transform, or more precisely, the Discrete Wavelet Transform (DWT), is one of the most commonly used signal processing tool. It is very demanding in terms of arithmetic and memory operations. A good example is the comparison between the DCT-based codec JPEG and the DWT-based codec JPEG 2000 [145], which shows that JPEG2000 is computationally more demanding than its predecessor. There exist fast wavelet-transform algorithms based on filter banks [79, 131], and the lifting scheme [125, 26]. The latter technique allows to compute an integer version of the DWT, called the Integer Wavelet Transform (IWT). Evidently, the IWT has lower complexity than the original DWT. It can also be used to speed-up the wavelet-transform based algorithms for lossless image compression.

5.1.2 Quantitative Complexity

While qualitative analysis only gives an intuitive understanding of the algorithm complexity, it is more interesting to be able to quantify the reduction in complexity as a result of some optimization. A measure of the complexity is also needed to compare different algorithms realizing the same task.

Image compression is a typical example. Several algorithms can compress a given image with approximately the same efficiency. However, it is useful to evaluate them using the complexity criterion. How can these algorithms be compared? The nature of the algorithms and the

reasons for their compression-efficiency may be based on very different principles. Moreover, the algorithms cannot be characterized purely in terms of arithmetic operations. This makes it difficult to use common measures of the complexity. This leads to consider new methodologies to measure the complexity for these algorithms. Such a measure should not only incorporate notions linked to the number of arithmetic operations, but also the number of memory operations. Another aspect that should also be taken into consideration is the number of logical tests, or branches. A realistic measure should incorporate all those aspects. In practice, it is very difficult to apply such a comprehensive complexity-measure to an entire algorithm as a unit. However, most algorithms can be broken down into smaller components. For instance, compression algorithms are often based on a block transform followed by a quantization step, and finally an entropy coding scheme. Many compression algorithms use the same transform and the same quantization procedures. Therefore, the complexity of these blocks needs to be computed only once.

Finally, as mentioned before, a quantitative measure of complexity can also be used to compare algorithms. This is especially appropriate for comparing compression algorithms which vary greatly in nature, and therefore cannot be easily compared in qualitative terms. Furthermore, quantitative complexity-analysis can be effectively used to design rate-complexity or distortion-complexity functions for compression algorithms. This is a logical extension of the common rate-distortion approach used in these algorithms. Reichel [97] has investigated a general-purpose approach for quantitative measure of the complexity for the DWT-based codecs, based on the classification of the operations into categories. He has then, verified this approach to Pentium I and Pentium III by choosing appropriate weights for each category.

5.2 Software Complexity

One way to measure the complexity of signal processing algorithms is to look at their resulting software implementations. The complexity of the software can be, then, measured. This gives information concerning the original algorithm. This solution is only an approximation as the notion of complexity is often very different between the programming and the signal processing worlds. In fact, the most commonly used complexity measure of signal processing algorithms is the execution time on a given implementation. A review of many software complexity measures can be found in [139]. The different methods are compared, pointing out the aspects they can handle and the ones they fail to incorporate. However, it is possible to select a subset of measures that are similar to the aspects relevant to the application at hand.

5.3 Implementation Complexity

One of the major approaches to the construction of correct concurrent programs is successive refinement: start with a high-level specification, and construct a series of programs, each of which "refines" the previous one in some way. In the realm of shared-memory concurrent programs, this refinement usually takes the form of reducing the grain of atomicity of the operations used for interprocess communication and synchronization. For example, a high-level design might

assume that the entire global state can be read and updated in a single atomic transition, whilst a low-level implementation would be restricted to the operations typically available in hardware: atomic reads and writes of registers, test-and-set of a single bit, load-linked/store-conditional, compare-and-swap, etc. Each of the successive refinements is considered correct if and only if it conforms to the specification. The notions of conformance to a specification leads to the implementability concept or, in other terms, how challenging is the software implementation.

5.4 State-of-the art Complexity Measurements and Optimizations

The estimation of the complexity of signal processing algorithms is a very old problem. Some signal processing algorithms have already been studied in terms of complexity. Often, only the pure arithmetic complexity (additions, multiplications) was studied. Moreover, the studied algorithms correspond generally to the transform parts of the codec and are thus mostly arithmetic based. One of the pioneers in the domain is Winograd, who studied the multiplicative complexity of many basic signal processing tools. He started with Finite Impulse Response (FIR) filter analysis in [136]. He then analyzed the Discrete Fourier Transform (DFT) [137] and the DCT [35]. Most of the time, the analysis is followed by an optimization of the scheme according to the measured features. All the studied algorithms are perfectly deterministic and the complexity is independent from the input data.

Another signal processing tool that has been often studied is the Fast Fourier Transform (FFT). In [47] different FFT algorithms are compared in terms of computational speed, memory requirements, implementation complexity, ease of testing and accuracy. However, FFT is rarely used in data compression, because it introduces complex numbers. Its real version, i.e. DCT is generally used instead. Fast algorithms have been designed where the number of multiplications is minimized [34]. DWT was also studied in terms of arithmetic operations in [58]. However the analysis of the transform is very rudimentary. A better comparison of many implementations of the transform can be found in [101].

In the framework of the JPEG algorithm, many data dependent complexity measurements and optimizations have been performed. Each time, only the DCT part of the algorithm has been studied. Variable complexity inverse DCT algorithms were proposed in [40] and [66]. In both cases, the algorithm uses the fact that DCT coefficients are mostly zero because of the quantization. The same type of optimization was also proposed for the forward DCT [67] and the inverse DWT [36]. The complexity is measured using arithmetic operations, branches and memory accesses. The number of operations are summed after having been multiplied by the following weights: 1 for additions and shift, 3 for multiplications, 5-6 for tests and 1 for each memory access. All those algorithms lead to the same output as the conventional version of the transform. There is only vague information about how those weights were determined.

Another approach to complexity optimization is to trade complexity for the accuracy of the transform: the complexity can be reduced if the algorithm is allowed to give only an approximation of the correct transform. This strategy has been used for the DCT transform in [68].

This simplified inverse DCT sets some coefficients to zero in order to reduce the number of operations. The images are compressed using the JPEG codec at different bitrates. The total distortion, due to the approximate DCT and to the compression, is measured as a function of the number of multiplications. This allows plotting the complexity/distortion curve of the algorithm. Varying the size of the block can also be used to modify the relationship between the complexity and the performance of the transform. Let us recall that the DCT is conventionally performed on blocks of 8×8 . In [44], the block size of the transform is varying in order to find a R-D optimum. The number of multiplications is used to measure the complexity. The rate and the distortion are predicted analytically using a first order regressive model and a Laplacian distribution. Even if the primary aim of the author is to find a R-D optimum, a 3-D plot of the complexity/distortion/rate function is provided.

Much less research was done concerning memory utilization. However, JPEG is already relatively memory efficient because of the block structure of the DCT. On the other hand, DWT based algorithms do not naturally use a block structure. This has encouraged algorithms minimizing the overall memory demands. The memory bandwidth of an optimized DWT codec was studied in [89]. This algorithm corresponds to one mode of JPEG2000.

Again, most of the previously cited works concentrated on the transform part of the algorithm. To my knowledge, only Nielsen [85] and Reichel [97] have tried to measure the complexity of a full compression system. Nielsen developed a model for the complexity and applied it to voice coding algorithms. Sadly, the paper is incomplete and this approach was not followed in other papers. The measure was based on arithmetic and memory complexity (reads and writes), "smartness of the programmer", parallelism and architecture considerations. A simple example of FIR filtering is used to demonstrate the technique. The following articles on the subject did not further investigate the problem and only use execution time as a measure of the complexity [84]. Reichel [97] studied the complexity related aspects for image compression algorithms. He presents a general framework for measuring the algorithmic complexity using the arithmetic and memory operations. In this chapter, an extension of Reichel's work is performed for DSP-based applications and the OBP concept is particularly evaluated.

5.5 Measuring the Complexity

The concept of arithmetic complexity is the most commonly used type of complexity. It is also very intuitive. Obviously an algorithm doing two additions is more complex than an algorithm doing only one addition. But what about an algorithm performing an addition and a multiplication. Which one is more complex? From a mathematical point of view the two operations are equivalent, they both have the same properties. From a software point of view, the multiplication is a much more complex operation as it generally needs more CPU cycles to be computed. Some researchers have stated that in modern architectures the two operations are equivalent and that the arithmetic complexity is simply the total number of operations [97]. A more general approach will be taken in Section 5.5.1, where weights are applied to each operation. Changing the definition of the arithmetic complexity will then simply correspond to a modification of the weights.

The branches complexity corresponds to the act of taking a decision. Algorithms that are very regular, where the same paths are always taken, will be less complex than others where multiple choices must be made. This refers to two aspects of the branches complexity. The presence of a test will increase the complexity of a scheme, but the cost of the operation will also depend on the behavior of the branch. This principle will be explained in more details in Section 5.5.1.

The idea of memory complexity is much less intuitive. In fact it can be divided into two types of complexity [97]: The memory stock and the memory bandwidth. The memory stock corresponds to the amount of memory needed to execute the algorithm. An algorithm based on local information, such as a block of pixels, is less complex than an algorithm working on global information, which needs to access the entire data. The other memory related complexity is the bandwidth complexity. Basically, this term refers to the number of Digital Signal Processor (DSP) times the data must be accessed to perform the algorithm. An algorithm that needs to access each input only once is less complex than one that will need multiple accesses. Those two memory related complexities will be studied in more detail in Section 5.5.2.

A measure is proposed, which allows the comparison of the memory and the arithmetic complexity. Once the measures are defined, they should be applied to data or image compression algorithms, like OBP. In fact most algorithms can be subdivided in small processing blocks. For instance, transform based codecs can be divided in a transform, a quantization and an entropy coder block. In many cases, different algorithms use the same blocks. Thus the computation of the complexity can be highly reduced since parts of the algorithm were already analyzed. In other words, it is highly desirable to decompose an algorithm into sub-blocks of known complexity. The final complexity would simply be the sum of the contribution of each block.

5.5.1 Arithmetic Complexity

There are many types of arithmetic operations. The complexity of each operation depends on the hardware architecture. Historically, the multiplication was considered as the most demanding operation [97] and many algorithms were optimized according to this feature. In the proposed approach all operations will be considered. Finally, the overall arithmetic complexity is the weighted sum of all operations. In the rest of this section, the term complexity will always refer to the arithmetic complexity unless stated otherwise. However, it is not sufficient to define the relevant operations for the analysis of the arithmetic complexity. It is also necessary to define a counting methodology, which can be applied on algorithms of different nature. The methodology developed in this section is based on the execution time. Thus, automatic and semi-automatic methods can be, then, developed to compute the arithmetic complexity of the whole scheme.

The Counters

There are different types of arithmetic operations. It is very confusing to "count" each one of them separately. In order to simplify the computation of the complexity, the operations can be grouped into categories. All operations in a given category have similar complexity. This approach is mainly focused on software implementations. Using a-priori knowledge on the DSP architecture, we propose to divide the operations into four distinct categories. It will be shown in the next section that they correspond to different execution times, and thus complexity. A counter is associated with each categories. It corresponds to the number of occurrences of operations from the category. The following categories were used [97]:

- Basic bit and logical operations (C_l): Bits-shifts, logical operations, bit manipulation, etc.
- Basic arithmetic operations (C_a): Additions, subtractions, comparisons, etc.
- Semi-complex arithmetic operation (C_m): Multiplications, etc.
- Complex arithmetic operation (C_c): Divisions, etc.

To these arithmetic operations, two more groups will be added. The first is the use of look-up tables. As this can replace complex arithmetic operations, it is taken in consideration using the counter C_t . The second corresponds to branches and tests (if, for, while, etc.) and is represented by C_b . This branch counter corresponds to the act of taking a decision and not to the assembler understanding of the branch.

For each group the total number of operations should be computed. The influence on the final measure of complexity depends on the architecture. Thus the overall arithmetic complexity C_{AR} can be computed using the following formula:

$$C_{AR} = w_l C_l + w_a C_a + w_m C_m + w_c C_c + w_t C_t + w_b C_b \quad (5.1)$$

where the weights depend on the architecture on which the algorithm will be implemented. The concept behind this model can be validated using a simple CPU architecture for software implementation. Operations are executed in a sequential manner. Each arithmetic operation takes a given number of cycles to execute, which is independent of the operations preceding and/or following. The total execution time is then the sum of all individual contributions. This does not take into account memory operations directly. Most modern CPU architectures have multiple arithmetic units. Moreover, the processing time of each operation depends on the surrounding ones. In this case, the hypotheses of the model are no longer valid. It will be shown in the following sections that the model allows a fair prediction of the execution time of different kind of algorithm even for the complex processors of embedded systems.

The Weights

In order to evaluate the arithmetic complexity of an algorithm, the counters must be summed according to Eq. 5.1. As stated in the previous section, the weights are dependent on the architecture where the algorithm is implemented. In this section, the weights are estimated for the DSP architecture (more precisely the Analog Device ADSP 21000 family) [140] and for the

Celeron architecture from Intel [142]. The estimation is based on the principle that the complexity is proportional to the execution time of the algorithm. However, we are interested in the execution time of a given operation in a real software environment and not in the theoretical number of cycles given by Analog Device or Intel. To do so, basic programs were implemented, each of them performing one type of operation inside a loop. The complexity of the operation is then evaluated using the difference of execution time between the loop with and without the operation to measure. In order to improve the precision of the measure, up to five operations of the same type can be made inside the loop. By hypothesis, the complexities are additive, thus, the relationship between the execution time and the number of operations is linear. The slope of the time for one iteration-loop as a function of the number of operations per iteration, gives a fair estimate of the execution time for the operation. This allows a good estimation of operation complexity in a real software environment.

One of the difficulties of such an approach is that we would like to measure only the complexity of the operation without the different memory access times. To solve this problem, we make sure that the number of variables accessed during the loop stays constant, with and without the operation to measure. An example of a loop is presented in Table 5.1 by means of the ANSI C language, where C1 and C2 are two declared variables and initialized to 1.

Reference	One Addition	Two Addition
for(i=0;i<1000;i++) C1=C2;	for(i=0;i<1000;i++) C1=C1+C2;	for(i=0;i<1000;i++) C1=C1+C2+5;

Table 5.1: Basic example of a loop for measuring the execution time of the addition

The execution times have been tested on two different computers with ADSP 21020 processors (33 MHz clock speed) [141] and on Celeron processor [142] with clock speed of 500 MHz. Moreover many loop sizes have been tested. In order to compare the results obtained on the different computers, they are normalized with regards to the processor speed. The measure is expressed in terms of number of cycles needed to compute the operation. A rough estimate of the processing time of the loop is subtracted from the measured data.

Simple Operations– To access the complexity of the category represented by C_l four different operations were used: the logical "or" and "and" and the left and right bit shifts. The results of the simulations on the two platforms are presented in Figure 5.1. A linear fit of the data is also included in order to determine the slope of time vs. the number of operations.

It can be observed that the processing time of the operations is fairly constant. Each logical operation needs approximately 0.89 to 1.2 cycles to be computed on the Celeron and ADSP respectively. The ADSP processor seems to need less extra time compared to the Intel Celeron processor. The ADSP processor has instruction cache possibility for faster computational processing.

The complexity of the category C_a is computed in a similar manner in Figure 5.1(b). The

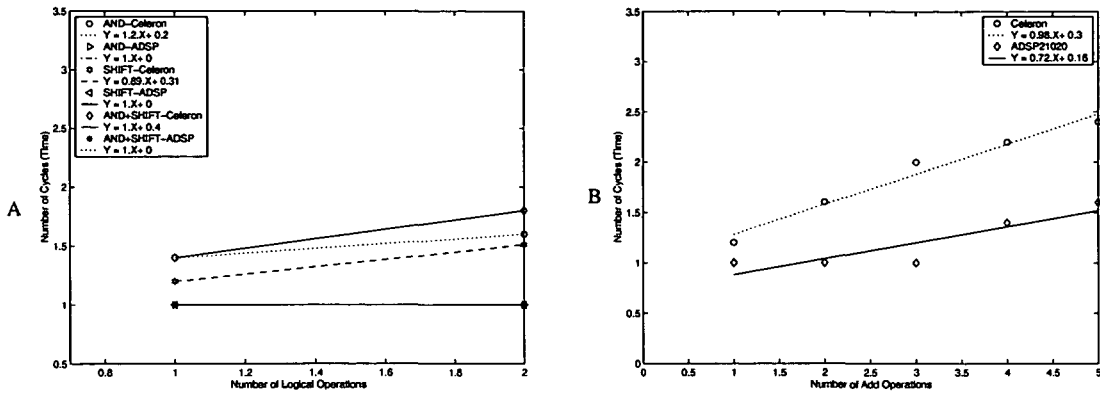


Figure 5.1. Required time to compute 1,2 or 3 operations in computer cycles. (A) Two logical operations (AND, OR) and a SHIFT have been tested for the Celeron and ADSP 21020. (B) Complexity of the addition on the ADSP 21020 and the Intel Celeron

slope of the curves is approximately 0.72 and 0.98 for respectively the ADSP 21020 and the Celeron processors.

Complex Operations– The two categories C_m and C_c behave differently from the two previous ones. In this case, very different execution times can be observed if the two operands are variable or if one of them is constant. The results for the multiplication and the division are presented respectively in Figure 5.2-A and Figure 5.2-B.

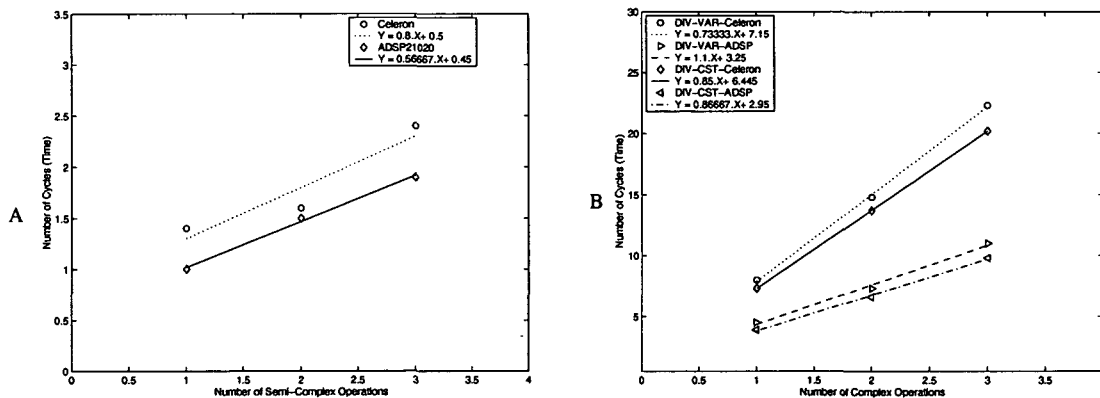


Figure 5.2. Required time to compute 1,2 or 3 operations in computer cycle on two different processor architectures ADSP 21020 and Intel Celeron. (A) multiplications (B) Divisions

Branches– The branches are special operations, in the sense that for many architectures their complexity is not constant. Most modern processors use the notion of pipelining to speed up the computation process. This means that the operations are processed in some sort of parallel manner. For instance the first part of the pipeline can take care of the instruction

decoding, while the second one execute the instruction itself. Modern architectures can have up to 16 levels of pipeline. When a branch has to be executed, two solutions are possible. Either the pipeline is stopped until the decision concerning the branch has been made, or the system tries to predict the result of the branch and carries the most probable operations. If the prediction was correct, then the gain over the first solution is large. But if a wrong decision was taken, the whole content of the pipeline must be discarded and all variables must be returned to their original values. It is obvious that this is a very costly operation. Future architectures will use the notion of predicate. In this case both paths of the branch are executed simultaneously. Once the result of the branch is known, only the values corresponding to the correct path are kept.

In the case of The ADSP-21000 family, processing the instructions is performed in three clock cycles:

- In the **fetch cycle**, the DSP reads the instruction from either the internal instruction cache or program memory.
- During the **decode cycle**, the instruction is decoded, generating conditions that control instruction execution.
- In the **execute cycle**, the ADSP-21020 executes the instruction; the operations specified by the instruction are completed.

These cycles are overlapping, or pipelined, as shown in Table 5.2. In a sequential program flow, when one instruction is being fetched, the instruction fetched in the previous cycle is being decoded, and the instruction fetched two cycles before is being executed. Thus, the throughput is one instruction per cycle, and thus, complexity is reduced.

Time (cycles)	Fetch	Decode	Execute
1	0x08		
2	0x09	0x08	
3	0x0A	0x09	0x08
4	0x0B	0x0A	0x09
5	0x0C	0x0B	0x0A

Table 5.2: Pipelined Execution Cycles

The branches in ADSP processor consists of CALL, JUMP, RTS (**ReTurn** from Subroutine) and RTI (**ReTurn** from Interrupt). The CALL instruction initiates a subroutine. Both jumps and calls transfer program flow to another part of program memory, but a call also pushes a return address onto the Program Counter (PC) stack so that it is available when a return from subroutine instruction is later executed. Jumps branch to a new location without allowing return. A return causes the processor to branch to the address stored

at the top of the PC stack. There are two types of returns: RTS and RTI. The difference between the two is that the RTI instruction not only pops the return address off the PC stack but also pops the status stack if status registers have been pushed as a result of an external interrupt. There are several parameters that have to be specified for a branch, for different complexities [140].

For Celeron or Pentium processors, large pipelines are used and the processors have a complex unit in charge of predicting the result of the branches. In this case, if the branch is predicted correctly, its complexity will be quit low. On the other hand, if the prediction is wrong, the complexity will be much larger. In order to simplify the measure, the complexity of branches can be divided in three groups. The first one corresponds to branches that are taken with only small or large probabilities. A typical example are loops, where the same decisions are taken most of the time. In this case, the complexity of this operation is minimal. The second group is the branches that cannot be predicted, like a test on the sign of uniformly distributed data. This leads to the maximum complexity of the operation. The last group is the branches with known probability [97].

Summary- The time needed to perform each type of operation is summarized in Table 5.3. The complexity weights are derived from the execution time. The execution times are normalized according to the fastest operation and rounded to the nearest half integer. For each category, the execution speed is indicated together with the approximate weight. It can be observed that if the absolute time needed to perform an operation is different from the Celeron to ADSP21020 processor, their relative weights are approximately constant. The fact that some operations were measured to take less than one cycle is due to the measurement errors.

	w_l	w_a	w_m Var.	w_c Const.	w_c Var.	w_t	$w_b(P_b)$
Celeron	1	1	1	7	8	1	$(\min(6.5, 13.P_b+1))$ [97]
ADSP-21020	1	1	1	5	6	1	$4.P_b+1$

Table 5.3. Complexity weights. The time necessary to compute each type of operation is expressed in cycles per operation. The weight w_t depends on the size of the data. Only the minimum weight is indicated in this table. The weights are computed by normalizing the execution times in regards to the fastest operation and a rounding to the nearest half integer

From this table, there is evidence of non-constant complexity. In this case, special care must be taken during the analysis. If different types of operations are present, then the category should be subdivided into sub-groups of equivalent complexity. The most complicated category is the branches. Thus, in many analyses these counters will be presented in a separate table, together with the probability p_b . Finally, the weights w_t can be considered as a pure memory operation. For this reason, its complexity is equal to one read operation (see next Section).

5.5.2 Memory Complexity

The meaning of memory complexity is even less clear than the arithmetic one. As stated in the definition, the simplest notion is to say that an algorithm is more complex if it needs more memory for its execution. This type of complexity refers to the amount or the quantity of memory. It is called the storage complexity. Another aspect that should also be taken into consideration is the number of memory accesses. An algorithm could need only a small size of storage, but access it many times. Does it mean that its memory complexity is larger than another one accessing the same storage but only once? This second type of memory complexity is called the bandwidth complexity. An algorithm accessing the memory frequently is said to have a high bandwidth complexity.

Once the two memory complexities have been defined, it is interesting to understand their relationship. How can the two complexities be compared/combined? Even more, how can they be compared to the arithmetic complexity?

To answer these two questions, weights have been given to the different types of memory operations [97]. The value of these weights depend on the size of the storage. This way the two types of memory complexity are highly linked. The determination of the weights is based, in this study, on the execution time. This is the same approach that was taken in Section 5.5.1 to weight the different arithmetic operations.

Amount

As presented before, the storage complexity can be measured using the amount of memory necessary to execute the algorithm. This amount is easily derived from the description of the algorithm and its size will be called s_a . For instance, a block-based algorithm like Digital Signal Processor (DSP) has to store only the block in memory. Its complexity is proportional to the size of the block. On the contrary, algorithms that are not block based generally have a complexity proportional to the size of the input data. This is the case of most wavelet-based algorithm. The difficulty is to quantify this difference.

The simplest case is when the algorithm has to be implemented in a dedicated architecture. Then, the storage complexity is directly proportional to the size of the memory needed to execute the algorithm. However, if the algorithm is implemented in an existing platform, the complexity becomes dependent of the existing memory architecture.

Most modern architectures are based on M levels of memory [97]. Where the size s_m of the memory Mem_m increases and its access speed r_m (or w_m for writing) decreases with m . Data are stored in the smallest memory Mem_m , which can fully hold them. When data are needed by the processing unit, the portion that needs to be accessed is transferred to Mem_{m-1} . This procedure is repeated until Mem_1 is reached. This way, neighboring data are already stored in fast memories. This transfer from one memory to another is generally done outside the processor. This means that many memory operations can be conducted without increasing the computing time. With this architecture in mind, two algorithms holding in memory Mem_m have the same complexity in terms of amount of memory.

Bandwidth

Determining the bandwidth complexity of an algorithm is a much more complicated problem than measuring its memory needs. Like the arithmetic complexity, the bandwidth is dependent on the algorithm but also on the implementation. It also depends on internal parameters of the algorithm, such as the size of the bitstream, and the nature of the input data. The fact that the bandwidth is sensitive to the same parameters as the arithmetic complexity is a motivation for using the same methodology.

Only two types of memory operations are possible when bandwidth is concerned. Data can only be read from or written to memory. However, due to the structure of the memory, the time depends on the way the data are accessed. In the following, a distinction is made between data accessed sequentially or in a pseudo-random order. If the information is read in a sequential order, then the data have a high probability to be found in the cache memory with the fastest speed. In case of random access, this probability is much smaller and depends on the size of the data set. The complexity counters linked to the memory operations are:

- C_r : Number of read operations from the memory.
- C_w : Number of write operations to the memory.
- C_{MB} : Complexity relative to the memory bandwidth.

In most algorithms, only one sub-type of memory access is performed. All memory accesses are either done on local data or on pseudo-random order. The final memory complexity is computed by summing the memory counters according to their relative complexity, i.e.:

$$C_{MB} = w_r.C_r + w_w.C_w \quad (5.2)$$

where w_r and w_w are the weights for respectively, the Read and Write operations.

The same methodology as the one described in Section 5.5.1 can be used for the two memory categories [97]. The only difference is that the procedure is now simplified by keeping only memory operations. The simplification also uses the fact that CPUs have a given number of registers (or buffers) that are used to store local variables. Thus, variables such as loop counters can be neglected in the bandwidth count.

Weights Calculation

The weights can be derived from the speed of the memory as described in [97] using the following equations:

$$t_r = p_1 t_{r,1} + (1 - p_1)(p_2 t_{r,2} + (1 - p_2)(p_3 t_{r,3} + (1 - p_3)(\dots))) \quad (5.3)$$

where t_r and t_w are the time needed to respectively read and write information from/to memory. For a data size s_a , p_m for random memory access can be expressed as follows:

$$p_m = \max(1, s_m/s_a) \quad (5.4)$$

where s_m is the size of the memory level m . In case of a sequential access of a memory, p_m can be simplified to:

$$p_m = (b_m - b_{m-1})/b_m \quad (5.5)$$

where b_m is the size the data block transferred from MEM_{*m*+1} to MEM_{*m*} and $b_0=1$.

Like in the case of the arithmetic operations or the single memory model, the weights are directly proportional to the memory speed. Thus algorithms working with data of size inferior to Mem₁ will have much smaller complexity than algorithms needing more memory. If a large amount of memory is needed, then great care must be taken in order to ensure that the accesses are not random. It should also be noted that if the most recent processors have a very fast small memory, the largest one is, proportionally to the speed of the processor, very slow. This is explained by the fact that the external memory has its own clock frequency, which is independent of the one of the processor. Fast processors will then see a memory which is slower compared to them [97].

5.5.3 The combination: Arithmetic and Memory Complexity

So far two very different types of complexity have been presented. The arithmetic (including the branches) and the memory complexity. In both cases, weights series have been presented. In this section, the two complexities will be merged in simple examples. Thus it can be verified that the total complexity of a scheme including the two types of complexity corresponds to the sum of each individual contribution.

The first example combines a read operation and a multiplication. The read is performed using sequential access of the memory. The multiplication is performed between two variables: a random number and the value read from memory. The predictions are presented together with the experimental results in Figure 5.3. It can be seen that the total complexity corresponds to the addition of the two types of complexity. Moreover the prediction is very close to the measured data. For low memory demands, most of the complexity comes from the multiplication. When the data do not hold in Mem₁ (L1) anymore, the importance of the multiplication and the memory access is approximately equivalent. But as soon as the RAM (Mem₃) must be used, the memory access becomes the major complexity factor.

Another verification can be performed using sequential access of the memory and the Modulo operator (i.e. return the remainder of an integer division) on a variable. In this case, the complexity cost of this Modulo operation is much larger than the one for the memory access. The results are presented in Figure 5.4.

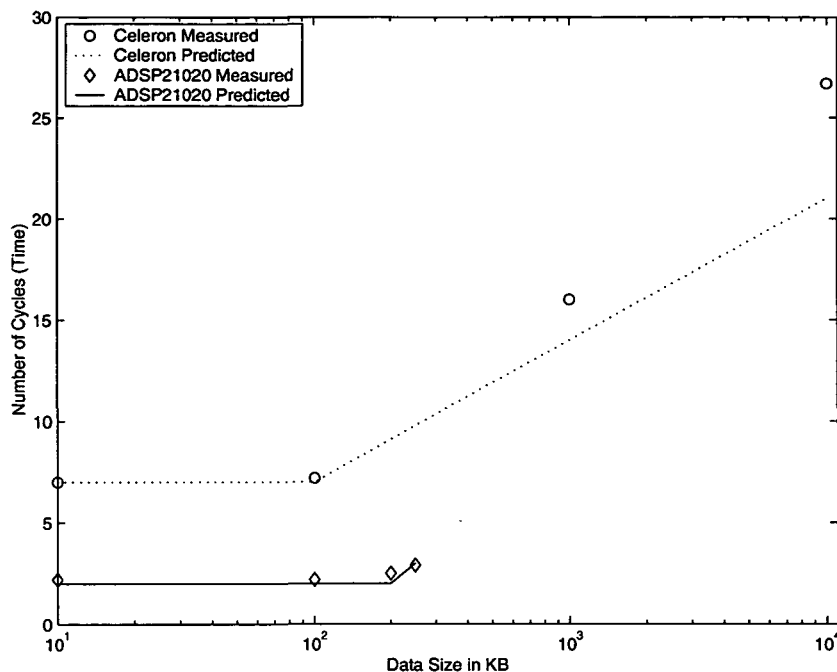


Figure 5.3. Number of cycles needed to read a value from the memory in a sequential manner and multiply it with a number for both Intel Celeron and ADSP 21020 processors. Predicted and measured times are depicted

In the second example, the prediction is adequate for the ADSP21020 but not optimal for the Celeron. It can be observed that in this last case, the measured data correspond approximately to the execution time of the modulo operation. However, the large cost expected by the read in the main memory (RAM) is not observed. It is justified by the fact that in this last generation of processors, there are some cases where operation can be executed in parallel. The model fails to predict such behavior as it is based on the assumption that the level of parallelism between the instruction is independent of the context. However, Reichel's experiments [97] have shown that this case of failure occurs only when one operation is much more complex than the other one. The last example is a merging between a division by a constant, a read and a write operation. But still the overall complexity is once again close to the sum of the complexity of each individual operation.

5.6 Complexity Calculation of the On-Board Processing

In this Section, the complexity of the proposed OBP (Chapter 4) is estimated according to the analysis performed in the previous sections. For an appropriate estimation, OBP modules are represented by flowcharts, that is, the simplest way to visualize algorithms. Then, complexity prediction of every module is performed. Finally, the overall complexity of OBP will be the sum of the individual modules complexity. Please note that complexity measure is related to the size of the input data "N", that is the number of detectors "D" multiplied by the number of

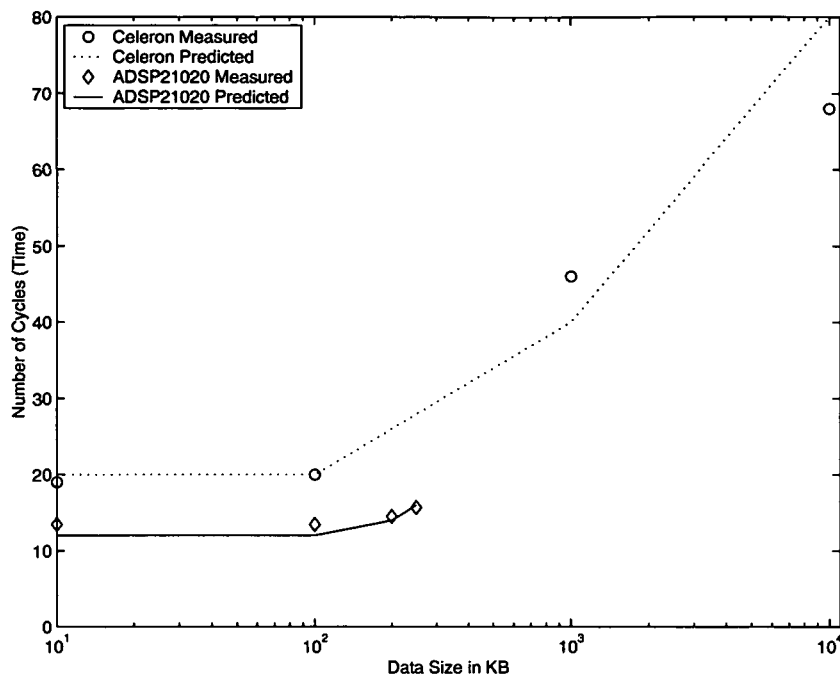


Figure 5.4. Time needed to read a value from the memory in a sequential manner and use Modulo operator (i.e. return the remainder of an integer division) for a random variable, on both Intel Celeron and ADSP 21020 processors. Predicted and measured times are depicted. The measured execution time in case of the Celeron processor corresponds to the execution time of the modulo without the memory access

frames "F": " $N = D \times F$ ". Therefore, the final complexity is estimated according to "N". In the following, flowcharts for the individual modules are given and their complexity is estimated for the ADSP 21020 processor.

5.6.1 Flowchart for the Raw Data Selection Module

As described in Chapter 4, raw data selection mainly consists of the transmission of lossless compressed selected raw data. This has two advantages: the first one is the check for the correctness of the on-board processing, and the second advantage is the easy maintenance of the lossy compression such that if detector signal model or glitch occurrence change, then the oversampling or glitch detection methods have to be adapted for minimal scientific loss and high compression efficiency.

Figure 5.5 depicts a typical flowchart for the raw data selection method. The complexity measure of this algorithm can be performed according to the criteria described in Section 5.5. The resulting complexity C_{RCS} is then:

$$C_{RCS} = 3R_S \cdot F + 1 \quad (5.6)$$

where R_S is the number of selected raw channels.

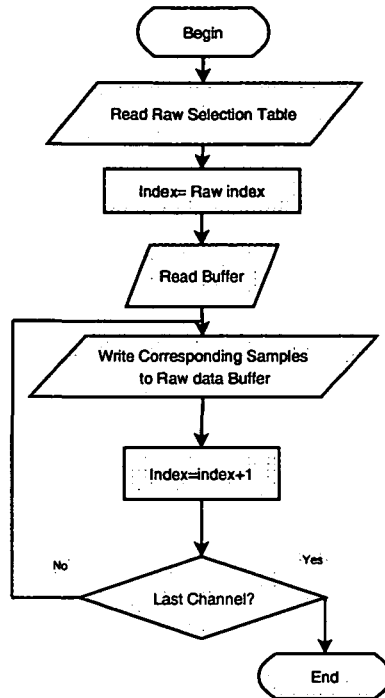


Figure 5.5: Flowchart of the raw data selection module (Case of Herschel-PACS)

5.6.2 Flowchart for the Detector Selection Module

Detector selection is important for the transmission of data (pixels) of interest. It has the advantage of an optimal exploitation of the telemetry bandwidth by discarding dead pixels data or non-relevant information from the bitstream for higher scientific gain.

Figure 5.6 depicts a typical flowchart for detector selection module. The complexity C_{DXS} for this algorithm can be measured as follows:

$$C_{DXS} = D_S.F + D.F + 3D + 1 \quad (5.7)$$

where D_S is the number of selected detectors.

5.6.3 Flowchart for the Preprocessing Module

The preprocessing module has the task of correcting the received signal to a predefined model. This latter is supervised by electronic engineers during the design, manufacturing and testing of the detectors. Different types of correction can be performed on-board, by using simple operations (arithmetics) for calibration, to complex operations (convolution) for filtering. Figure 5.7 illustrates a flowchart for the preprocessing module with simple operations to ease complexity estimation. It represents the case of Herschel-PACS 6 where two imaging types are used "photometry" and "spectroscopy"

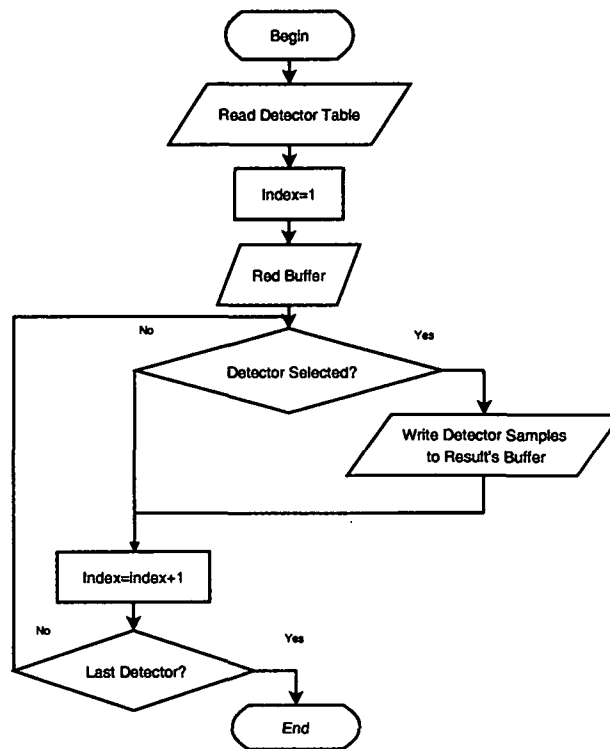


Figure 5.6: Flowchart of the detector selection module (Case of Herschel-PACS)

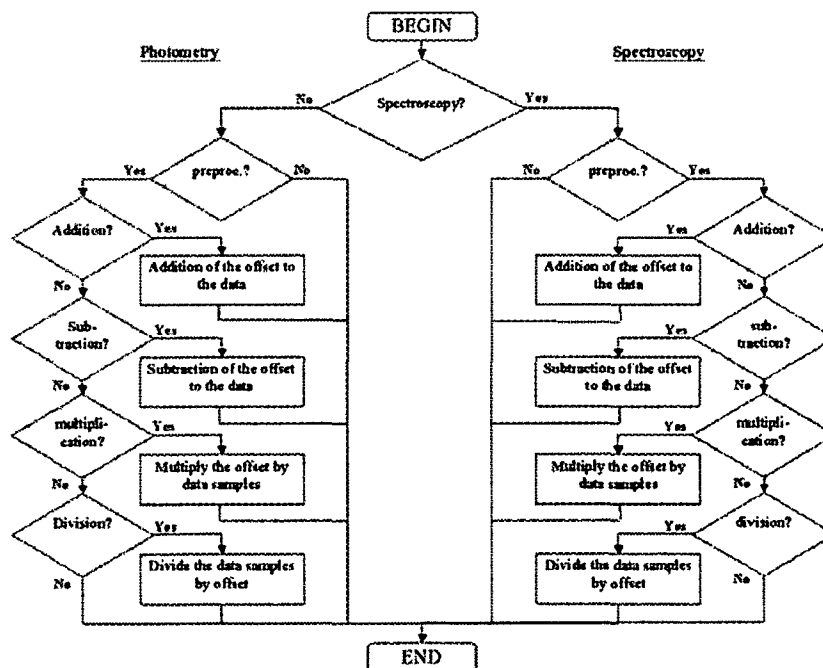


Figure 5.7: Flowchart of a typical preprocessing module (Case of Herschel-PACS)

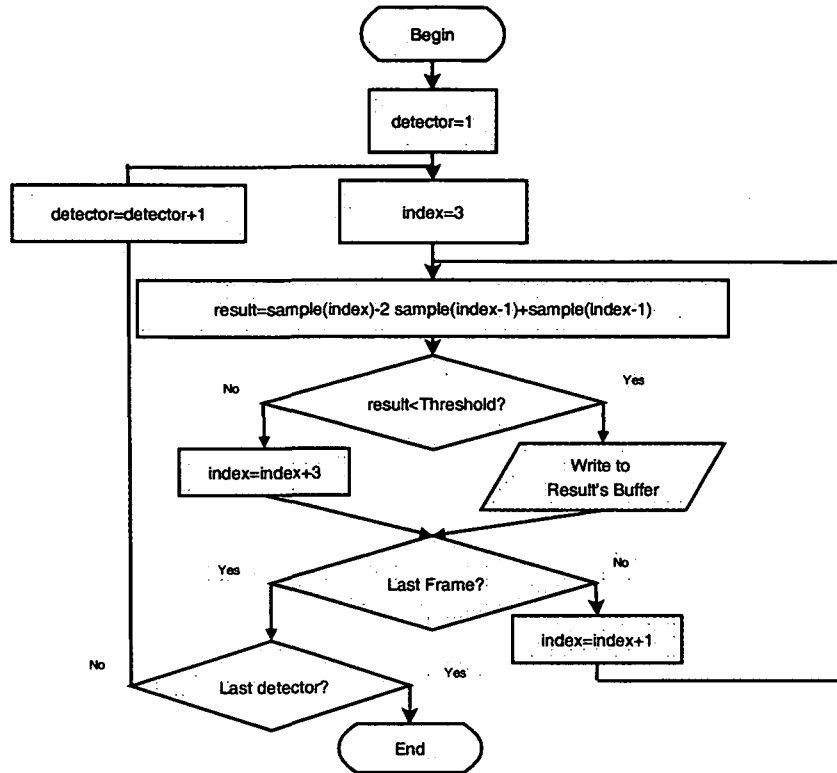


Figure 5.8: Flowchart of a glitch detection module using the SDDM method

The complexity C_{PP} for this algorithm can be measured as follows:

$$C_{PP} = D_S \cdot F + 4 \quad (5.8)$$

It is noticed that the complexity C_{PP} depends on the number of selected detectors.

5.6.4 Flowchart for the Glitch Detection Module

This global goal of this module is to detect and remove outliers (glitches) from the data stream before integration. The flowchart depicted in Figure 5.8 presents a glitch detection algorithm using the SDDM method that is described in Chapter 4.

The complexity C_{GD} for this algorithm is measured as follows:

$$C_{GD} = D_S(9F - 24) + 1 \quad (5.9)$$

The resulting symbolic number of frames after glitch detection and some samples removal is F_G .

5.6.5 Flowchart for the Oversampling Reduction Module

This module aims to reduce the oversampling of typical measurements, introduced by the electronics to improve the astronomical system efficiency. Indeed, the oversampling reduction is

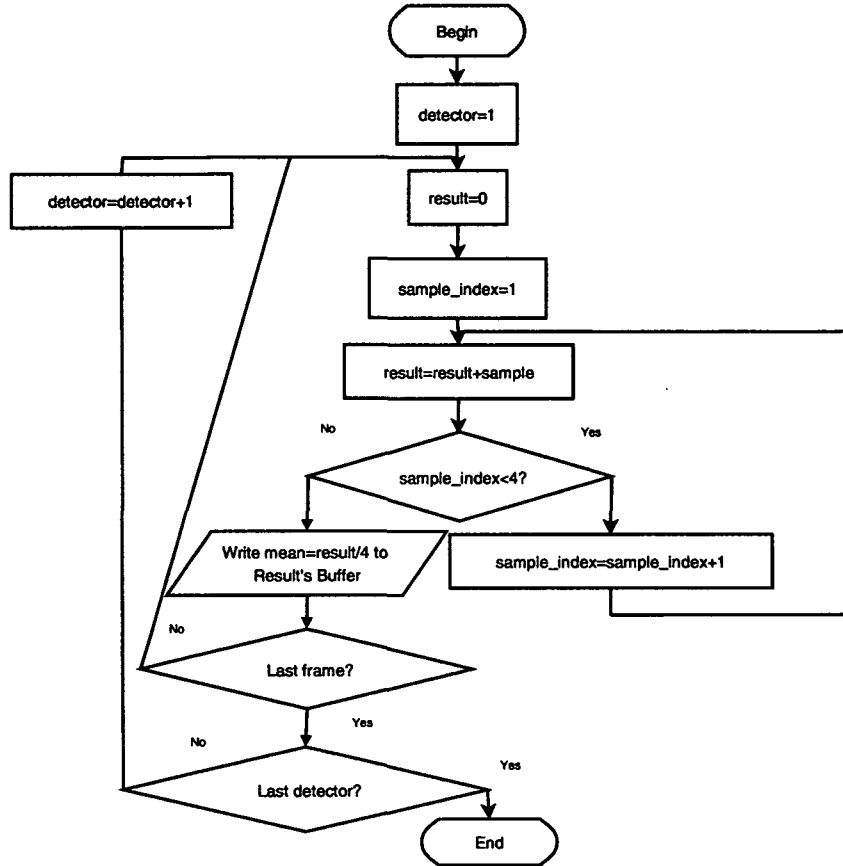


Figure 5.9: Flowchart of a typical oversampling reduction module

a critical part of the OBP as it is a lossy compression and care must be taken to not lose relevant information. Figure 5.9 presents a simple oversampling reduction method using the mean algorithm. That is exactly the simplest method used for the noise reduction (see Section 2.3.3).

The complexity C_{OR} for this algorithm can be measured as follows:

$$C_{OR} = D_S(4F_G + 3) + 1 \quad (5.10)$$

For fast processing the division, that is a complex arithmetic operation, is replaced by an equivalent but simple operation, which is the bit shift operator (shift to the right). Indeed, division by 4 is equivalent to a bit shift of 2. The number of frames after mean calculation is then, $F_A = F_G/4$.

5.6.6 Flowchart for the Integration Module

The complexity calculation of the integration module is similar to the one for oversampling reduction as the mean algorithm is also used. Figure 5.10 gives an overview of the integration algorithm for Herschel-PACS taking into account some instruments configuration like chopper position (observing the same target) and grating position (observing through the same spectral

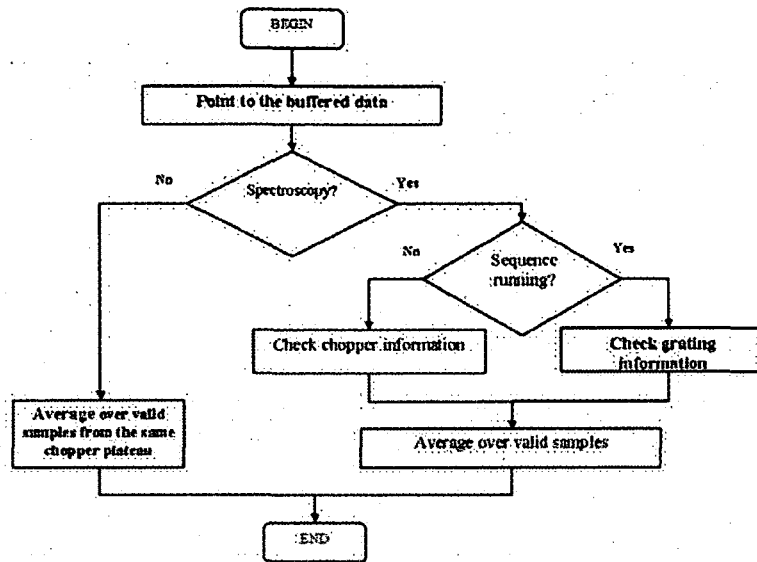


Figure 5.10: Flowchart of the integration module (Case of Herschel-PACS)

bandwidth). Indeed, integration over time is efficient only if several frames from the same source target and frequency band are considered.

The complexity measure C_{IT} for this algorithm is:

$$C_{IT} = D_S(4F_A + 8) + 1 \quad (5.11)$$

The number of frames after integration is then, $F_I = F_A/IT$, where IT is the number of integrated frames.

5.6.7 Flowchart for the Redundancy Reduction Module

In this module, the redundancy in the data stream is forced through a proper sorting method. Afterwards, this redundancy is reduced as a first step for lossless compression. Figure 5.11 presents a typical photoconductor's ramps sorting flowchart while Figure 5.12 depicts the redundancy reduction steps.

Their combined complexity C_{RR} can be computed as follows:

$$C_{RR} = 6D_S.F_A + 6 \quad (5.12)$$

5.6.8 Entropy Encoding Module

As described in Chapter 4, OBP makes use of two entropy encoders namely, the RZIP algorithm and the arithmetic coding. Complexity analysis of the arithmetic coding flowchart has already been performed by Reichel [97] for different platforms. The complexity of the RZIP algorithm can be performed in a similar way. RZIP is a symbol-oriented compression technique, where the *symbols* format is integer for low computational cost. RZIP can be tuned to look for *duplicate*

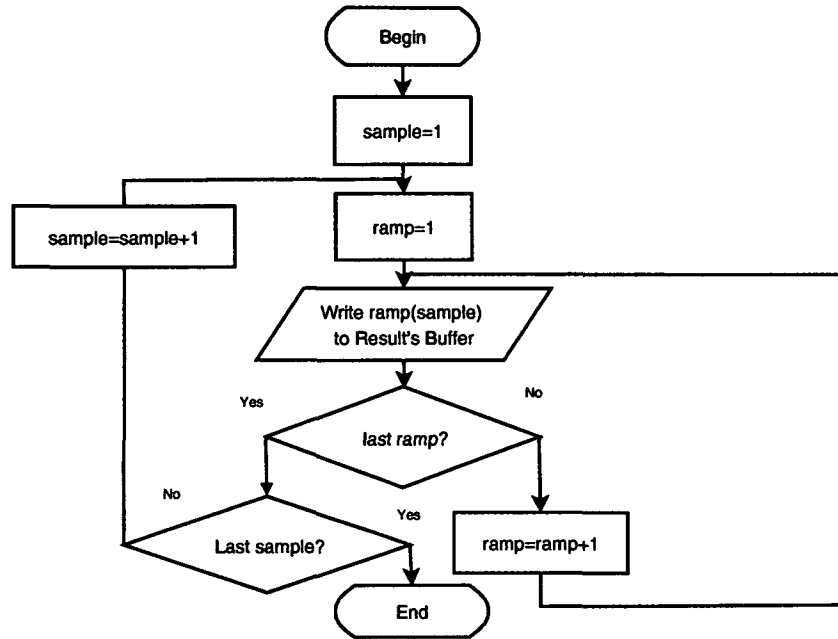


Figure 5.11: Flowchart of the ramp sorting module (Case of Herschel-PACS)

symbols at different distances (2^n) where n belongs to the range $[3,10]$ for realistic coding. RZIP replaces the *duplicate symbol* by a distance.

For instance, for $n=3$ RZIP searches for *duplicate symbols* occurrence at distance limited to 8 integers (32 Bytes). A distance coded in $4(n+1)$ bits replaces each *duplicate symbol*.

The total bitstream is calculated as follows:

$$Code = (32 \cdot symbols + (n+1) \cdot duplicates) \text{ bits} \quad (5.13)$$

Note that only duplicates that are located at the dedicated distance (8 in our case) are taken into account, which makes the task of the data sorting critical. Indeed, this limitation is related to the processing time for lossless compression that has to be acceptable. Indeed, the computational cost is proportional to the distance chosen. The bigger is the distance, the slower is the algorithm.

The computational cost C_{RZ} is:

$$C_{RZ} = K \cdot INT \cdot distance \quad (5.14)$$

where

K : memory access operations (read, write),

INT : the total number of integers (Size of input data) and

$distance$: $2^n - 1$.

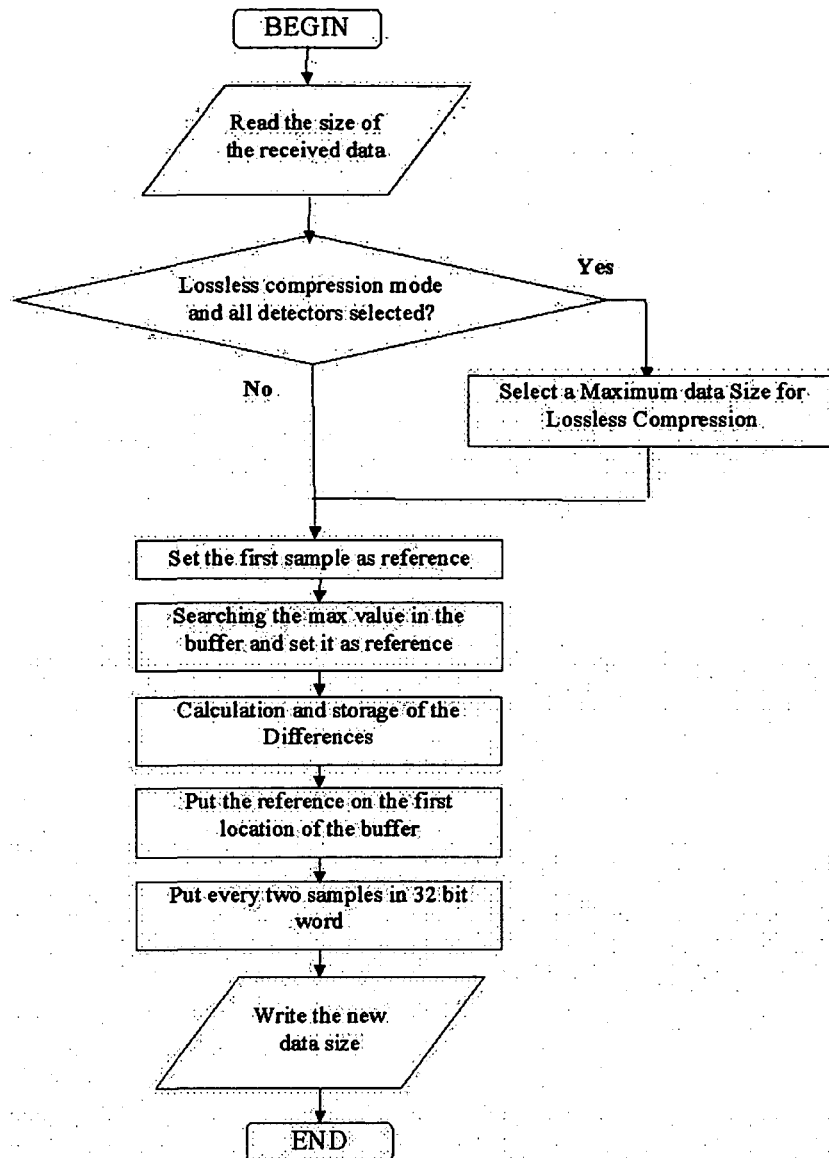


Figure 5.12. Flowchart of the temporal and spatial redundancy reduction module (Case of Herschel-PACS)

Several iterations of RZIP with small distances e.g. 8 (range 3) have to be performed for efficient compression in terms of compression ratio and complexity. Therefore, as RZIP has the property to be fast for well-sorted data, an adequate range, which depends on the block size, can be used to efficiently code the sorted data.

Chapter 6

Case Study: HERSCHEL-PACS Infrared Camera

In this chapter, the Herschel-PACS mission from the European Space Observatory is detailed. The scientific specifications of PACS, relevant for our investigation goals, are also presented including the compression challenges. Typical PACS data from the detector test (year of 2003 and 2004) are also given in this chapter. Experimental analysis and results are presented for the on-board processing approach.

6.1 The Herschel Mission

The Herschel Space Telescope (HSO) (formerly "Far InfraRed and Submillimetre Telescope" (FIRST)) will perform photometry and spectroscopy in the 57-670 μm range. It will have a radiatively cooled telescope and carry a science payload complement of three instruments housed inside a superfluid helium cryostat. It will be operated as an observatory for a minimum of three years following launch and transit into an orbit around the Lagrangian point L2 in the year 2007. The Lagrangian point L2 (see Figure 6.1) is 1.5 million Km far from the Earth away from the sun. It is a very good position for exploring the Universe, avoiding the undesirable emission of heat radiation from the Earth, the Moon and the Sun, which would cause too much interference in the measurements.

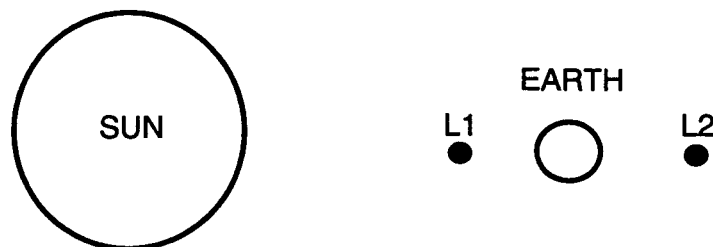


Figure 6.1: Illustration of the Lagrangian points L1 and L2 (not to scale)

Figure 6.2 depicts an illustration of the HSO as imagined by an artist. Herschel is CornerStone number 4 (CS4) in the European Space Agency (ESA) "Horizon 2000" science plan. It will be the largest space telescope of its kind when launched. Herschel's 3.5-metre diameter mirror will collect long-wavelength infrared radiation from some of the coolest and most distant objects in the Universe. Herschel will be the only space observatory to cover the range from far-infrared to submillimetre. The scientific objectives of Herschel are exploring the formation of stars and galaxies. HSO will solve the mystery of how stars and galaxies were born. The Herschel satellite is approximately 7 metres high and 4.3 metres wide, with a launch mass of around 3.25 tonnes. It will be launched with another mission, Planck - a mission to study the cosmic microwave background radiation. The two spacecrafts will separate soon after launch and will operate independently. The HSO will travel to the L2 orbit for an operational lifetime of three years minimum and will potentially offer about 7000 hours of science time per year. The HSO is a multiuser observatory accessible to astronomers from all over the world.

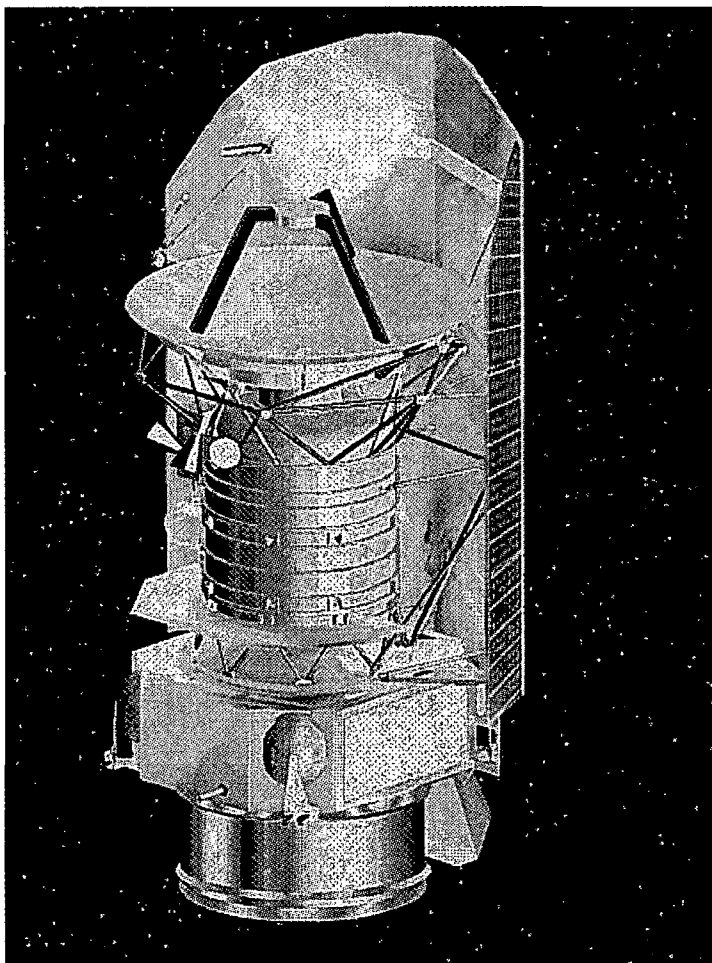


Figure 6.2: Artist's impression of Herschel (~1998)

The HSO [149] will carry the infrared telescope and will house three scientific instruments inside its superfluid Helium cryostat that are, **Photodetector Array Camera and Spectrometer (PACS)**, **Heterodyne Instrument for the Far Infrared (HIFI)** and **Spectral Photometer Imaging REceiver (SPIRE)**. These three instruments are built by different European consortia with international cooperation (see Table 6.1). PACS and SPIRE are cameras that will allow Herschel to

Instrument	Principal Investigator (PI) location	spectral range
PACS	MPE Garching, Germany	57-210 μm
HIFI	SRON Groningen, The Netherlands	480-1910 GHz
SPIRE	Univ. of Wales/Cardiff, UK	200-670 μm

Table 6.1: The scientific payload of the Herschel Space Observatory.

take pictures in six different "colors" in the far-infrared. HIFI is a spectrometer with extremely high resolution. The scientific payload complement was approved by the ESA in February 1999.

The case-study for the thesis investigation is the PACS instrument [150]. The evaluation of the OBP concept is performed on PACS data. In the following section, PACS and its objectives will be described further.

6.2 The PACS Instrument Description

PACS [94] employs two Ge:Ga photoconductor arrays (stressed/unstressed), and two bolometer arrays to, respectively, perform imaging line spectroscopy and imaging photometry in the 60 - 210 μm wavelength band (Figure 6.3).

In photometry mode, it will simultaneously image two bands, 60 - 90 μm or 90 - 130 μm and 130 - 210 μm , over fields of view of 1.75 x 3.5 arcmin with full beam sampling in each band. In spectroscopy mode, it will image a field of about 50 x 50 arcsec, resolved into 5 x 5 pixels, with an instantaneous spectral coverage of about 1500 km/s and a spectral resolution of about 175 km/s. In both modes background-noise limited performance is expected, with sensitivities (5 sigma in 1h) of 3 mJy or $2.5 \times 10^{-18} \text{ W/m}^2$, respectively.

PACS will contribute to track the energy released during the formation of stars and galaxies in IR range, since dust layers prevent the escape of radiation at shorter wavelengths. While the formation of stars can be observed in our galactic neighborhood, the observation of forming galaxies allows a look in the very distant and therefore very young universe. Together with SPIRE, deep multi-band photometric surveys will be used, searching for far IR-luminous galaxies at high z . Afterwards, spectroscopy imaging is used to follow-up the power sources (Active Galactic Nuclei (AGN)/starburst), and investigate how they evolve. Figure 6.4 and Fig-

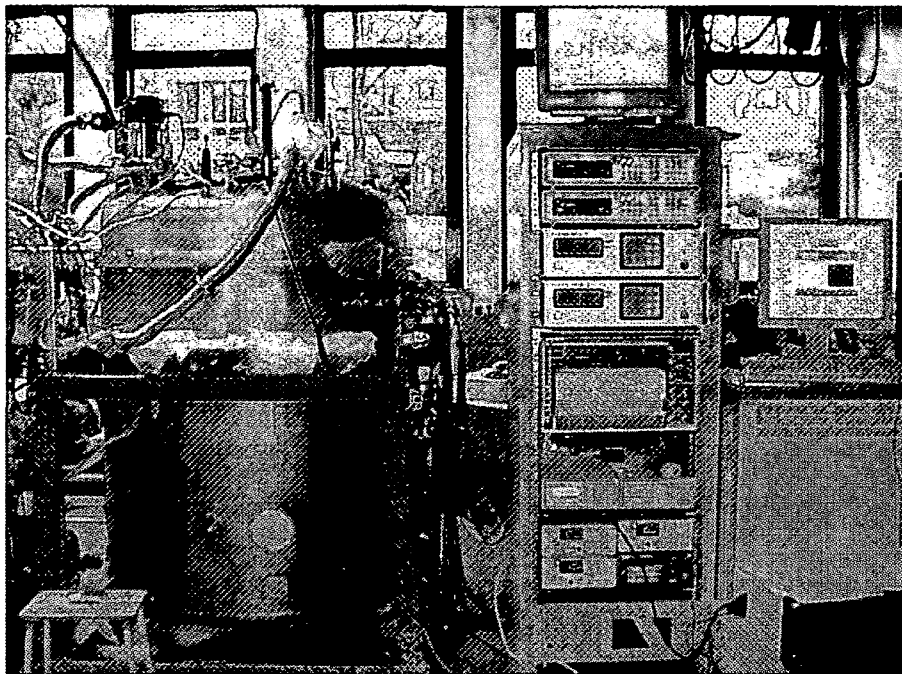


Figure 6.3: PACS instrument in-development (July 2004)

Figure 6.5 illustrate an example of respectively photometry and spectroscopy observation using PACS [150].

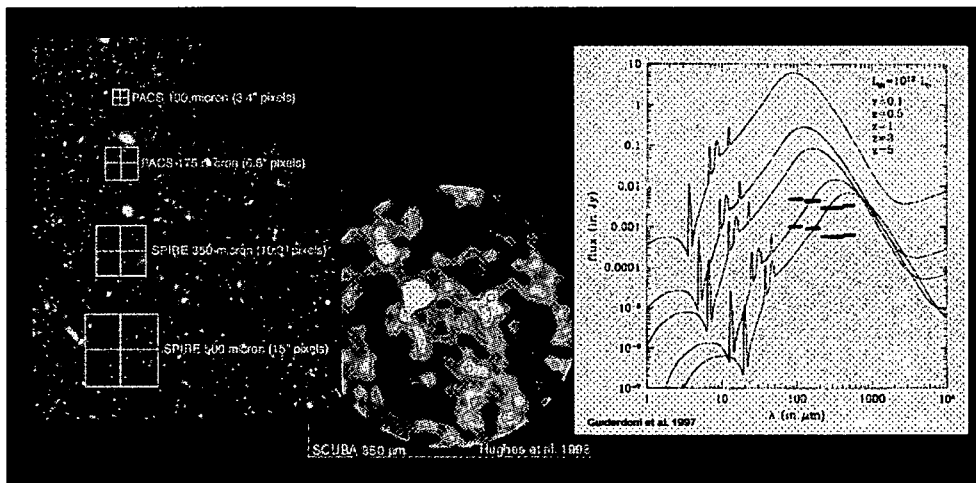


Figure 6.4: Photometry surveys using PACS and SPIRE

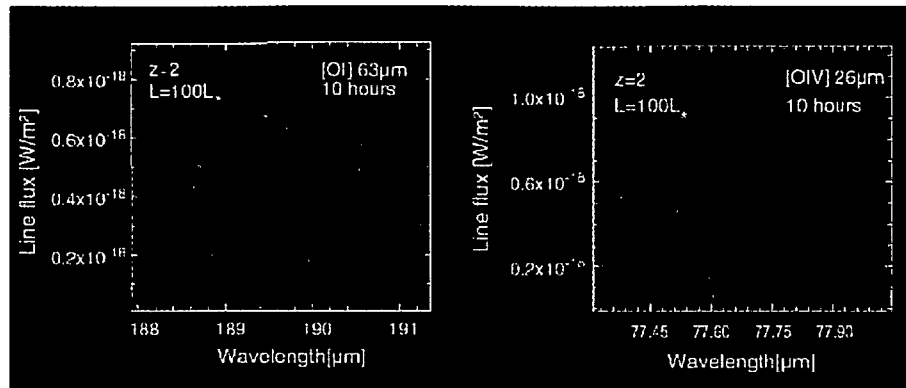


Figure 6.5: Follow-up spectroscopy using PACS

6.2.1 Design Concept

A. Photometry: Imaging photometry is performed in two bands simultaneously (60 – 90 μm or 90 – 130 μm and 130 – 210 μm) using a dichroic beam splitter. Two filled silicon bolometer arrays will be used in photometry:

- Blue bolometer: 64 x 32 pixels with a field of view of 3.5 arcmin x 1.75 arcmin at wavelength range: 60 – 130 μm
- Red bolometer: 32 x 16 pixels with field of view: 3.5 arcmin x 1.75 arcmin at wavelength range: 130 – 210 μm

Figure 6.6 shows the focal plane footprint in photometry. It shows the projection of the blue or red bolometer arrays on the field of view. Figure 6.7 represents typical bolometer arrays for PACS. It depicts a single pixel structure and whole detector matrix as well.

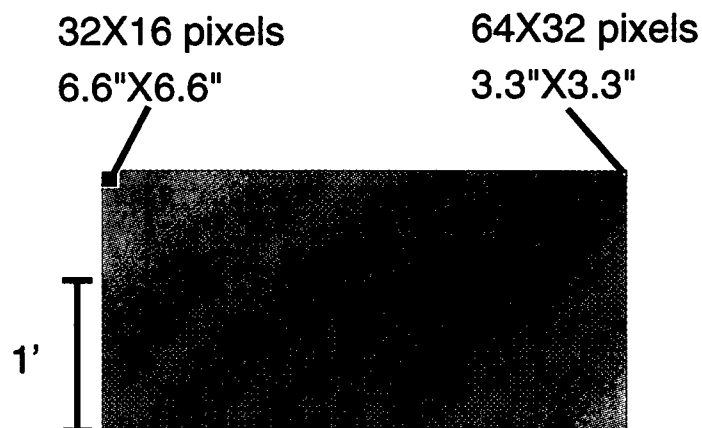


Figure 6.6: The focal plane foot print in photometry

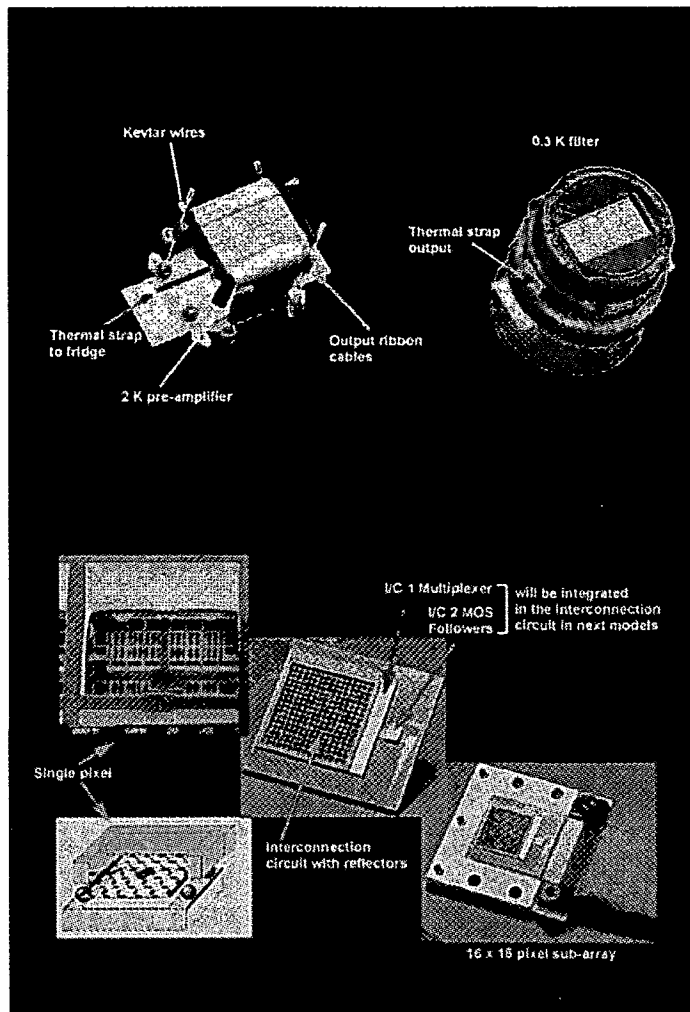


Figure 6.7. Upper figure: typical bolometer focal plane design. Bottom figure: a single pixel (left side) and a 16 x 16 pixel subarray (right side)

The bolometer performance mainly depends on the readout scheme used at the multiplexer stage. Figure 6.8 shows the readout concept of the bolometer arrays. It consists of a modulation stage where the measurement is stored in a cold buffer and of an amplification stage where a resulting differential signal (between off-light and on-light pixels) is amplified, integrated and injected into the multiplexer stage. The resulting signal is afterwards oversampled while converted from analog to digital. That are the resulting science data that consist of the photometric observation, which have to be transmitted to ground.

The measured noise spectrum from the above described readout scheme is depicted in figure 6.9. The red line indicates the required noise to reach the expected Noise Equivalent Power (NEP). Except for low frequencies the measured noise is equal to or below the required noise. This makes the observation reconstruction at low frequency challenging

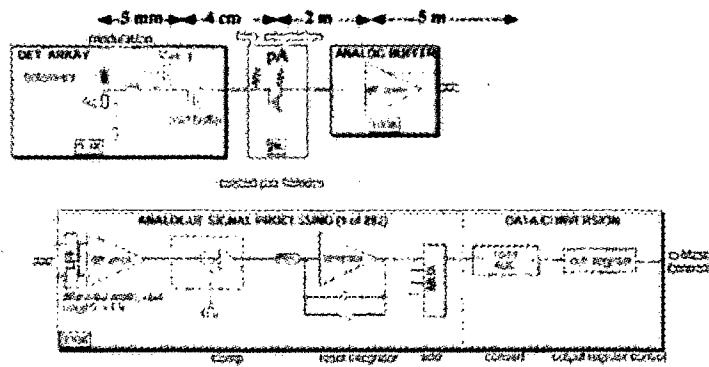


Figure 6.8: Readout scheme of the bolometer arrays

and thus, the efficient data transmission for high compression ratio would need proper attention.

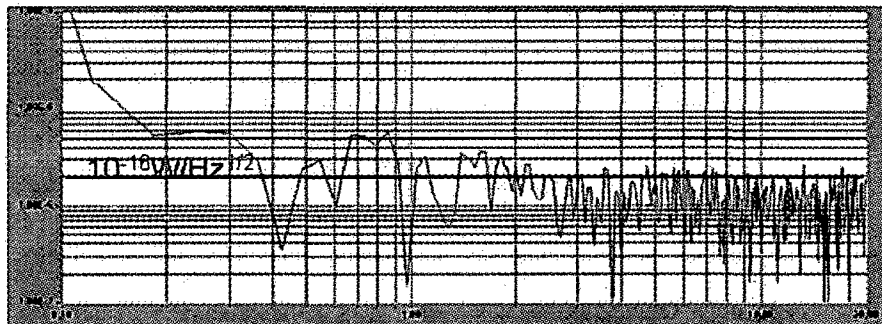


Figure 6.9: Measured noise spectrum in photometry

B. Spectroscopy: Integral field line spectroscopy is used at wavelength range 57 – 210 μm . An optical image slicer rearranges 2D field of view (5 x 5 pixels) along 1D slit (1 x 25 pixels). Figure 6.10 shows the projection of the focal plane onto the detector arrays.

A long-slit grating spectrograph ($R \sim 1500$)(see Figure 6.11) disperses light while used in 3 orders:

- 1st order (red detector) 105 – 210 micron
- 2nd order (blue detector) 72 – 105 micron

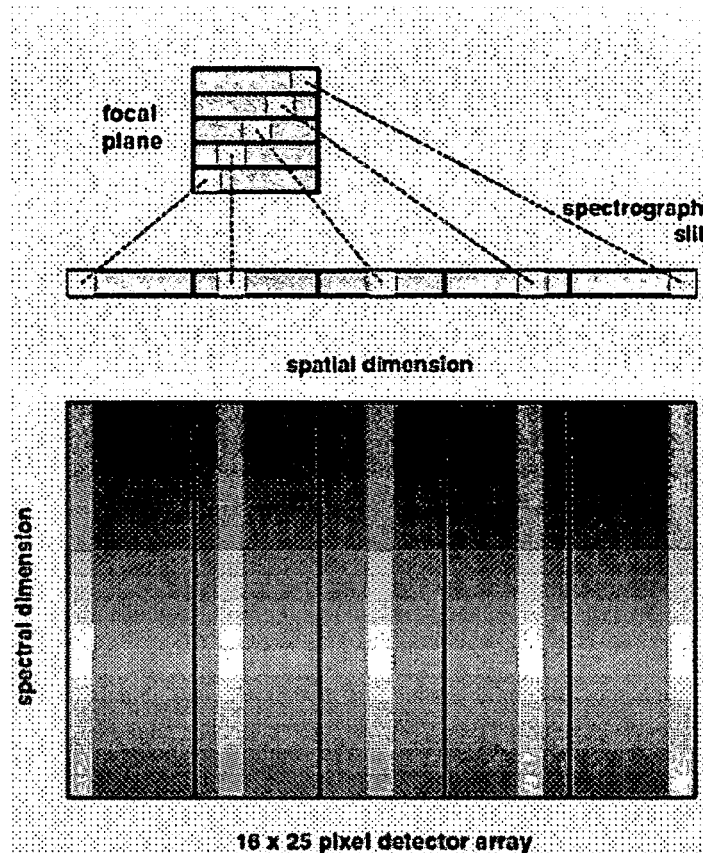


Figure 6.10: Projection of the focal plane onto the detector arrays (spectroscopy mode)

- 3rd order (blue detector) 57 – 72 micron.

The grating efficiency in each wavelength range is given in Figure 6.12.

The dispersed slit image is projected on two 16 x 25 pixel filled arrays of Ge:Ga photoconductors (see Figure 6.13). They are unstressed for the wavelength range 40 – 120 μm and stressed for the range 120 – 210 μm . Furthermore, there are also two test channels for each row, for calibration and validation purposes.

There are 25 linear modules for integrated **Cryogenic Readout Electronics (CRE)**. The schematic CRE system is presented in Figure 6.14. It consists of a **Capacitive feedback TransImpedance Amplifier (CTIA)** for each pixel, based on AC-coupled inverter or DC-coupled differential amplifier stage in silicon CMOS technology. There are 16 CTIAs multiplexed on each CRE chip for each linear detector module. Figure 6.15 shows CRE chips integrated in detector module. Furthermore, for design simplification, there is an additional empty module in warm electronics, which results in a total of data channels of 18 x 26.

The spectral channels are simultaneously recorded for each spatial element. The mea-

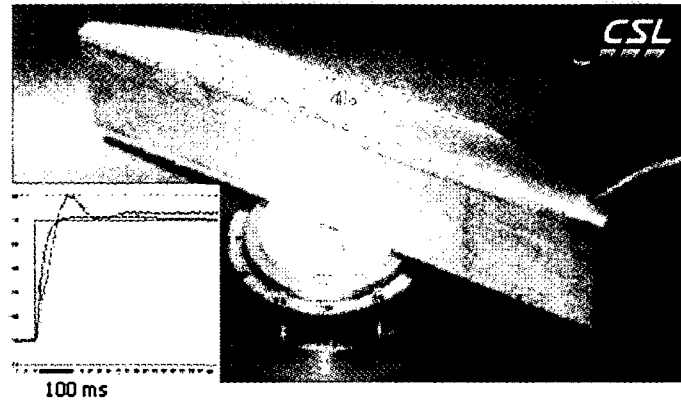


Figure 6.11. Image of the grating that is developed by Centre Spatial de Liege (CSL) in Belgium

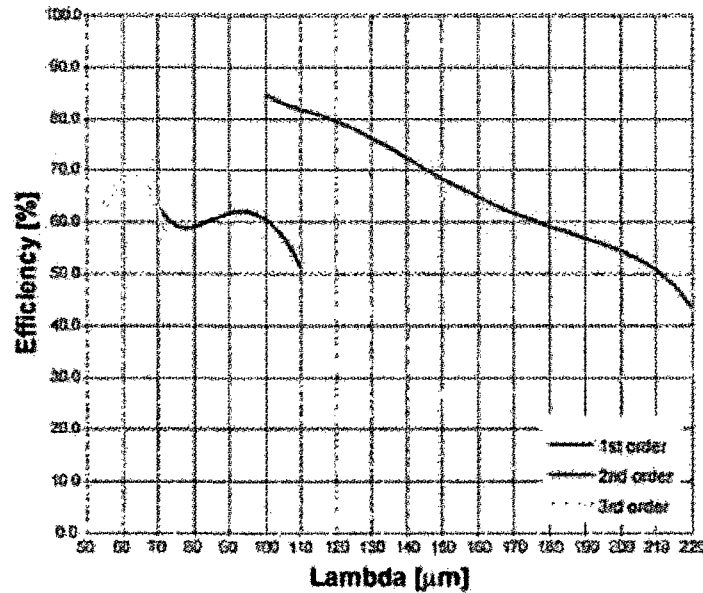


Figure 6.12: Grating efficiency respective to the wavelength ranges

sured responsivities for two light levels and detector modules temperatures are shown in Figure 6.16. The responsivity is defined as the signal current

$$I_{out} = \frac{U_{out}}{R_{fb}} \quad (6.1)$$

through the detector per incoming photon power P_{ph} :

$$R = \frac{I_{out}}{P_{ph}} \quad (6.2)$$

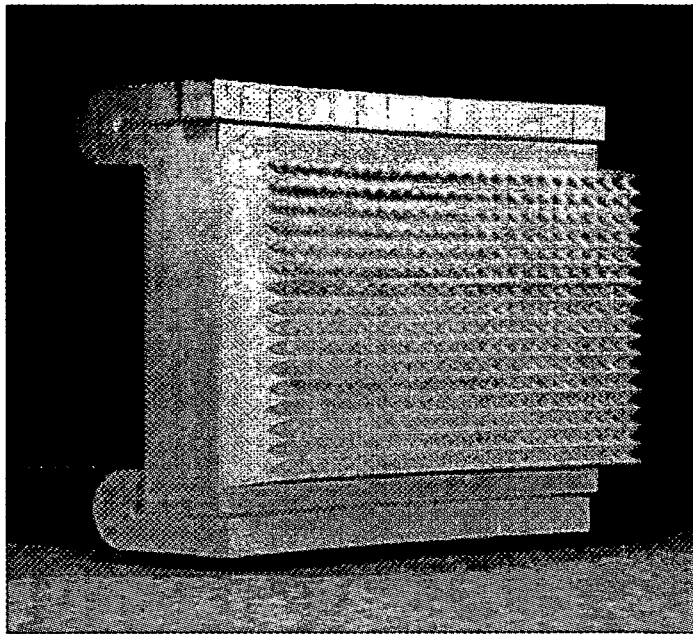


Figure 6.13: PACS photoconductors array

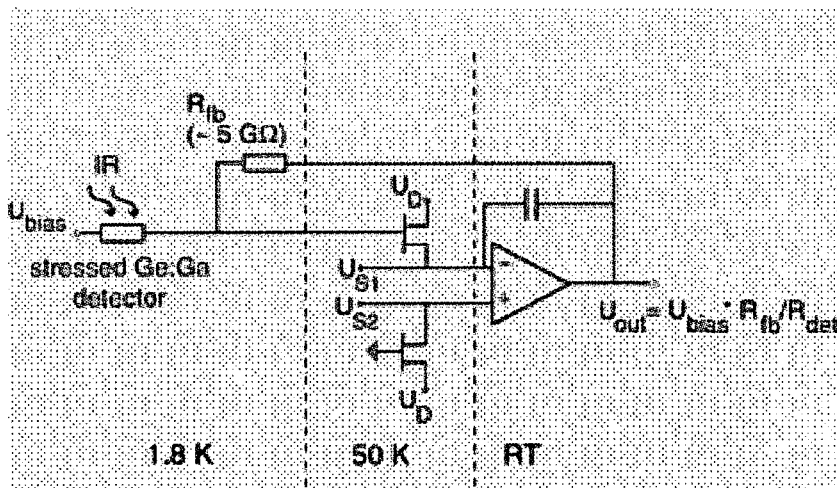


Figure 6.14: Cryogenic Readout Electronics (CRE)

where R_{fb} is the feedback resistance. The responsivities show the well-known non-linear dependence of the applied bias voltage. Indeed, the output signal is given by the bias voltage U_{bias} times the ratio of the resistances of R_{fb} and the detector R_{det} . While U_{bias} and R_{fb} remains constant, the detector resistance changes with the intensity of the absorbed light. Therefore, the output signal is a direct measure of the absorbed photon power. As in previous measurements, the pixels can be grouped into a type of high and

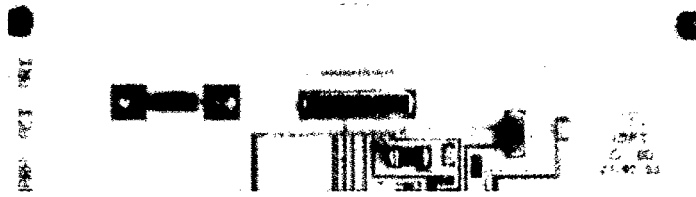


Figure 6.15: Integrated (CRE) after manufacturing

low responsivity.

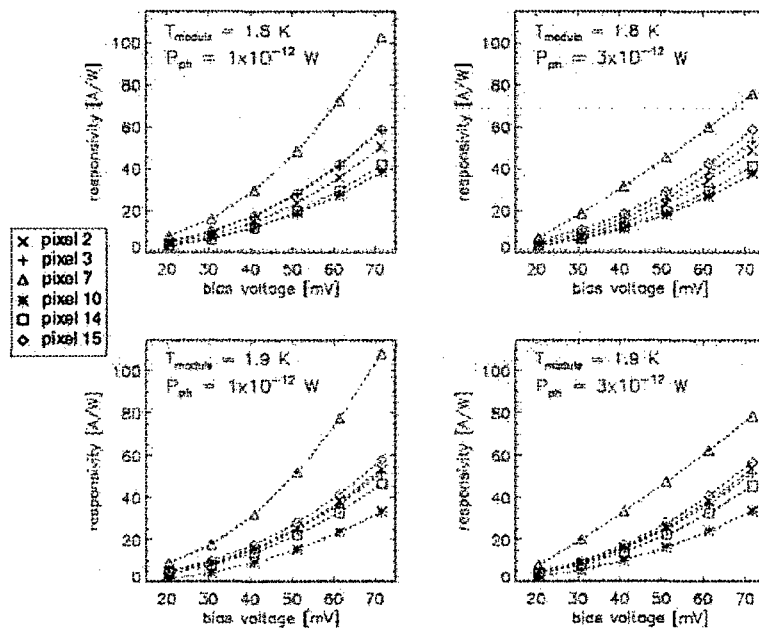


Figure 6.16: The measured responsivities for two light levels

Measured NEP at two light levels and detector module temperatures is presented in Figure 6.17. The NEP can be calculated from the measured noise voltage U_N and responsivity:

$$NEP = \frac{U_N}{R_{fb} * R} \quad (6.3)$$

The NEP is a very important figure of merit since it is inversely proportional to the signal-to-noise ratio of a measurement, which actually determines the sensitivity of the instrument.

At bias voltages below 30 mV the measured NEP is still dominated by the noise of the

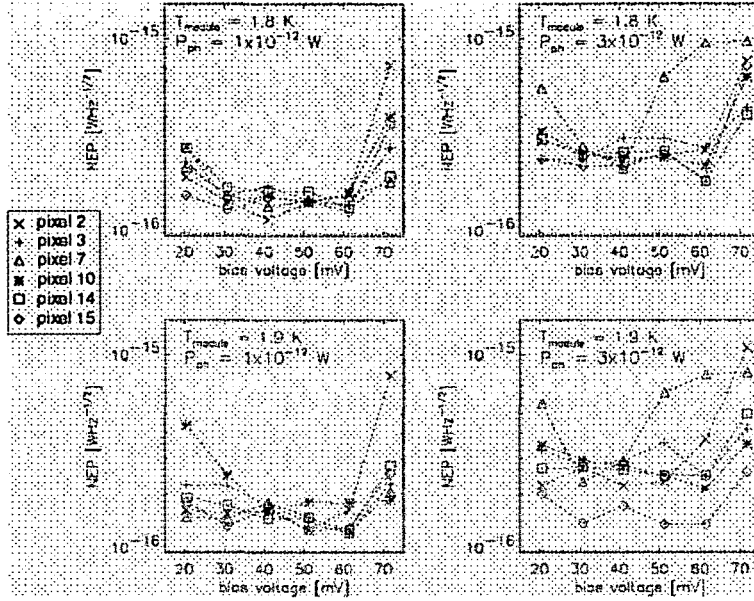


Figure 6.17: The measured NEP for the photoconductors

readout electronics, whereas at bias voltages exceeding 60 mV the noise is rising steeply because of the avalanche effect. At intermediate bias voltages the NEP is independent of the bias voltage. In that range, the NEP is limited by the noise of the photon background. At the higher flux level, the NEP shows more scatter and the avalanche effect starts to dominate the noise at lower bias voltages.

The derived quantum efficiency at two light levels and detector module temperatures is presented in Figure 6.18. The quantum efficiency is the probability of a photon which hits the detector to produce a charge carrier. If the NEP is limited by the noise of the photon background, the quantum efficiency Q is calculated as follows:

$$Q = \frac{4 * E_{ph} * P_{ph} * B}{NEP^2} \quad (6.4)$$

where

$$B = \frac{1}{1 - \exp(-E_{ph}/kT_{BB})} \quad (6.5)$$

E_{ph} and P_{ph} are the energy of single photon and the total received photon power, respectively.

Since the quantum efficiency is proportional to $1/NEP^2$, each fluctuation in the NEP translates to larger fluctuations of the calculated quantum efficiency. Especially for the

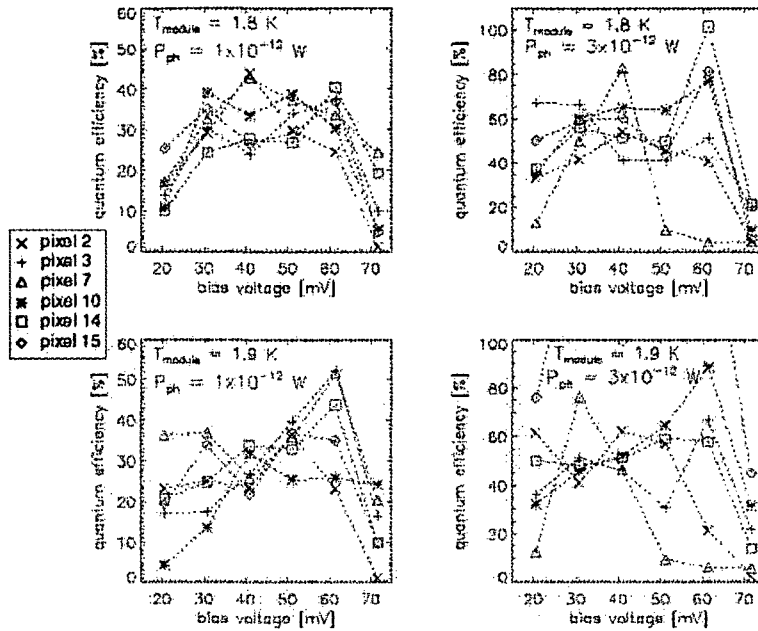


Figure 6.18: The measured quantum efficiency for the photoconductors

higher flux level the calculated quantum efficiency varies between 0 and 100%. We therefore put more emphasis on the measurements at the lower flux level.

In the background limited regime (bias voltages between 30 and 60 mV) the quantum efficiency varies between 20 and 50% with a mean value of about 33%. This is somewhat above the requirement of 30%. Although the scatter for the higher flux level is large, these measurements seem to suggest a mean value above 40%.

6.2.2 The PACS Instrument Units

A. The Optical System: The light from the telescope or one of the internal calibration sources is directed into the spectrometer and photometer section of the instrument. In the spectrometer, the optical image slicer re-arranges the 5×5 pixel field of view along a slit of 1×25 pixel which is dispersed by the grating. A dichroic beamsplitter separates the two spectroscopic bands before the light reaches the Ge:Ga photoconductors.

In the photometer the light is separated in the two photometric bands and imaged on the blue and red bolometers. Figure 6.19 illustrates the optical flow to and within PACS.

B. The Chopper: The chopper will be used for spatial modulation and for observation of internal calibration sources. Electromagnetic linear drive with magnetoresistive position sensors are used for this purpose. Figure 6.20 depicts an image of the chopper that is developed by Max-Planck Institute for Astronomy (MPIA) in Germany.

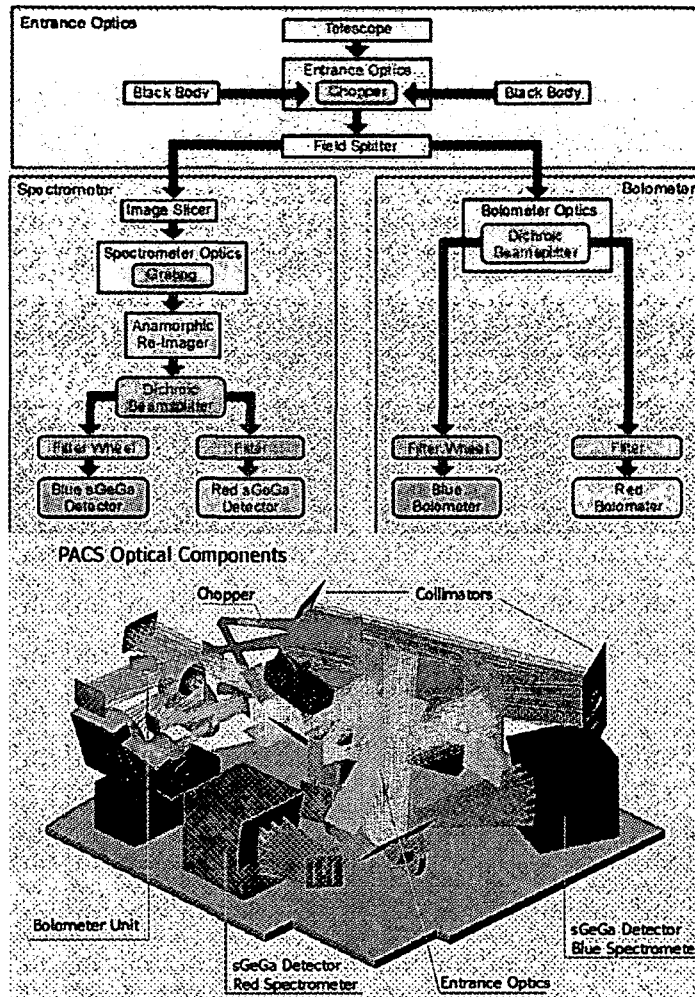


Figure 6.19. The optical flow for PACS imaging in flowchart (top figure) and in simulation (bottom figure)

C. The Instrument Units: The PACS instrument consists mainly of two parts that are mounted on different locations on the spacecraft. One part is located inside the cryostat in the focal plane on the **Optical Bench (OB)** at cryogenic temperatures. This part is the instrument **Focal Plane Unit (FPU)**. The other part of the instrument is located on the **Service Module (SVM)** and includes the instrument **Warm Electronics (WE) Units** and the **Warm Interconnecting Harness (WIH)**. The instrument block diagram in Figure 6.21 illustrates the electrical and configuration aspects (the manufacturer of the respective unit is also indicated).

The red boxes consists of the **Signal Processing Unit (SPU)**, that is responsible for data reduction for efficient transmission on the limited telemetry bandwidth. The SPU is the unit where the proposed OBP approach is implemented. The following sections contain the quantitative summary of the compression challenges for PACS. An evaluation of the

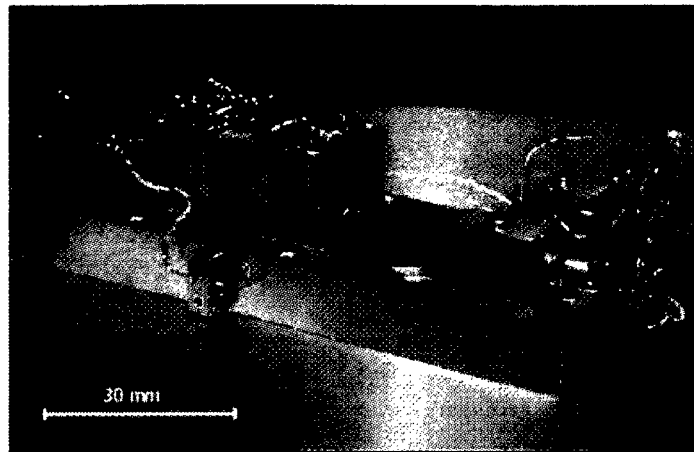


Figure 6.20: Image of the chopper

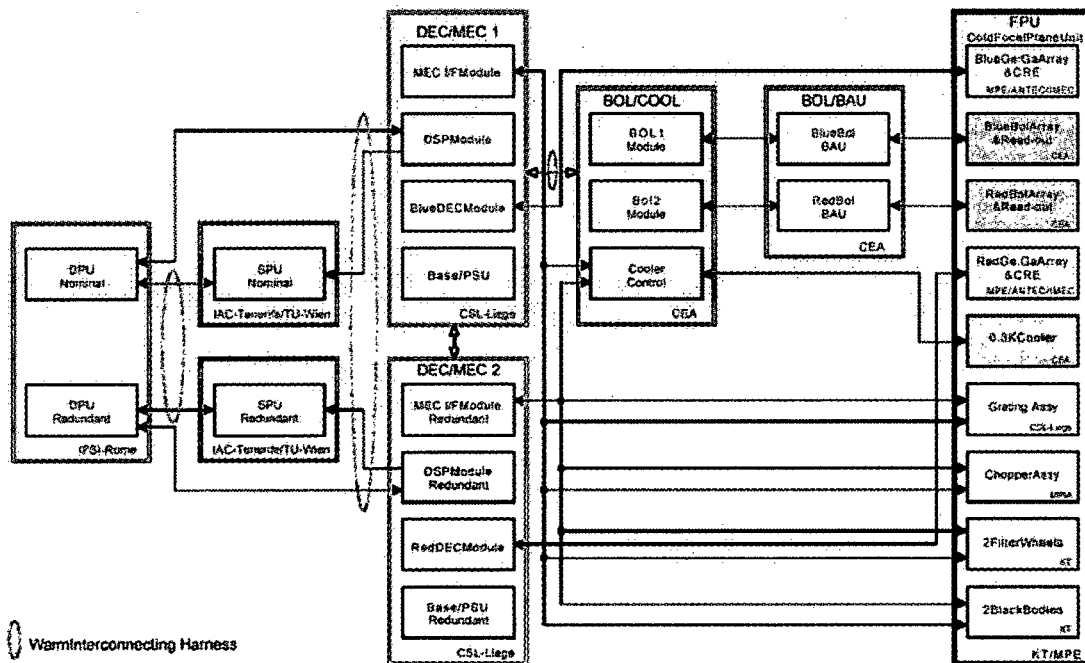


Figure 6.21: Scheme of PACS instrument units

OBP approach is performed on PACS data in terms of result quality and complexity.

6.3 PACS Constraints

In this section, the relevant PACS specifications for the **On-Board Processing (OBP)** framework are presented. The main challenge is the high data rate of the instrument for the limited telemetry bandwidth. The maximum raw data stream of 4000 Kbits/s has to be downlinked within a dedicated telemetry rate in the order of 118 Kbits/s. Therefore, a compression ratio of 34 is required in this case for an adequate transmission. In addition to that, the detectors data mostly consist of the telescope background, on which the source signal of interest is merged for a signal-to-noise ratio of the order of 1000. Furthermore, the detectors are continuously exposed to high energy cosmic particles inducing a disturbance (glitches) of the readout voltage which decrease the signal to-noise ratio and hence the data accuracy level. In the sequel, PACS signal specifications and transmission constraints are detailed.

6.3.1 PACS Signal Description

This section contains the scientific performance of the in-development PACS instrument (status from July 2004). This information needs to be verified by test, analysis or a combination of the two and shall serve the purpose of demonstrating that the instrument will operate as intended for the particular mission. The following specifications are reported for the PACS instrument interface design document [33] from July 2004.

Background and system noise levels in spectroscopy and photometry modes are given below in Table 6.2. The sensitivity of the photometer critically depends on the knowledge of the IR background from telescope and other sources, which couple into beam. An increase in background flux would affect the sensitivity figures: approximately proportionally to the square root of the background level while a decrease of the background could lead to slight improvements in sensitivity. Other parameters that determine the system sensitivity are the telescope main beam efficiency, pixel geometric efficiency, detective QE, transmission of filters and optics, and spectral bandwidth. Some of these parameters have been measured, others are the results of modeling and will be updated in a later stage of the PACS development.

Mode	λ [micron]	R (Resolu.)	Telescope Efficiency	Background Signal [W]	η	Coupling Correction	System NEP [W.Hz ^{-1/2}]
Phot.	60-85	2.9	0.64	2.4×10^{-12}	0.16	56	9.2×10^{-15}
Phot.	85-130	2.4	0.73	2.7×10^{-12}	0.11	34	5.9×10^{-15}
Phot.	130-210	2.2	0.77	6.3×10^{-12}	0.18	18	3.0×10^{-15}
Spec.	60	2650	0.55	3.3×10^{-14}	1	26	1.2×10^{-16}
Spec.	90	2400	0.69	2.0×10^{-14}	1	23	6.2×10^{-16}
Spec.	130	1100	0.74	2.7×10^{-14}	0.64	22	5.2×10^{-16}
Spec.	180	1650	0.77	7.1×10^{-15}	0.35	37	4.5×10^{-16}

Table 6.2: PACS instrument sensitivity

In Table 6.2, the assumed detector NEP , in addition to background photon noise is 10^{-16} $W/Hz_{1/2}$ in photometry and 5×10^{-18} $W/Hz_{1/2}$ in spectroscopy. Furthermore, the point source detection limit for 1 hour and 5σ is in the range of [1.9 - 4.4] mJy in photometry while it is in the range of [3.1×10^{-18} - 7.8×10^{-18}] Wm^{-2} in spectroscopy depending on the observation wavelength.

6.3.2 PACS Signal-to-Noise Ratio

In this section the calculations of the ratio between the telescope signal and the source signal are performed. These numbers are computed according to the signal specifications given in the previous section. The background and the system noise level in spectroscopy and photometry modes are described below.

Photometry

The bolometer signal is injected to the 16-bits Analog to Digital Converter (ADC) with a dynamic range of 3.3V. However, the real dynamic range per sample is 15 bits (significant) because a reserve of 1V for the signal is foreseen. The data are buffered on an output register before the processing.

The estimated SNR on the received background – if such a total power measurement could be done, which of course is not possible with the bolometers – would be ~ 7000 in 1/40 s (40 Hz readout rate). The dynamic range in the subtracted signal should be $\sim 10\%$ of the total power, caused by variation in the pixel responsivity or thermistor tolerances. Thus, 10 bits (1024 levels) are sufficient to represent the signal. With 15 effective bits in the ADC, this leaves 5 bits for noise sampling, which will be reduced to the proper ~ 4 bits at the data processing level. For bright sources, a SNR of ~ 10000 is expected, which leaves only 2 bits for the noise, but this is not a problem as the SNR is so high that a small amount of quantization noise can be tolerated.

The SNR for PACS bolometers can be estimated according to the information provided in Table 6.2. The Coupling Correction "CC" is a factor taking the telescope and pixel efficiencies into account. Since, the total NEP ($TOTNEP$) is required for the calculation of the SNR , the coupling correction is used to retain the values of all NEP contributing sources ($SYSNEP$):

$$TOTNEP_{\lambda} = SYSNEP_{\lambda}/CC_{\lambda} \quad (6.6)$$

Then, the SNR for 1 second integration, can be calculated using the relation:

$$SNR_{\lambda} = BG_{\lambda}\sqrt{2}/TOTNEP_{\lambda} \quad (6.7)$$

where BG_{λ} is the background signal for a dedicated wavelength " λ ".

For 4 samples averaging (oversampling reduction), the sampling rate is reduced from 40 Hz to 10 Hz. Therefore, the SNR can be calculated for an integration interval of 1/10s:

$$SNR_{\lambda}@10Hz = SNR_{\lambda}/\sqrt{10} \quad (6.8)$$

By calculating the SNR for a particular wavelength, the number of bits allocated to the noise (containing the source signal) is finally:

$$bits = Round[\log_2(2^{16}/SNR_\lambda)] + 1(signbit) \quad (6.9)$$

where "Round" is the rounding to the upper value and \log_2 denotes the dual logarithm $\log_2(x) = \ln(x)/\ln(2)$.

Using Equation 6.9, the $bits$ allocated to the noise are calculated for the different wavelength and represented in Table 6.3.

λ [microns]	SNR_λ	$SNR_\lambda@10Hz$	$bits$
60-85	21200	6700	4.3
85-130	22500	7120	4.3
130-210	55700	17610	2.9

Table 6.3: PACS SNR in photometry

Based on this estimation, redundancy reduction step of the OBP should reduce the signal dynamic range to an average number of 5 $bits$ (4.3 $bits$) before its encoding to 4 $bits$ by the RZIP and arithmetic coders.

Spectroscopy

The SNR in spectroscopy is estimated using the same methodology as for photometry. The only difference is that the calculated SNR concerns ramp slopes and not sample averages.

For 8-sample slopes, the sampling rate is reduced from 256 Hz to 32 Hz. Therefore, the SNR is calculated for an integration interval of 1/32s:

$$SNR_\lambda@32Hz = SNR_\lambda/\sqrt{32} \quad (6.10)$$

Using Equation 6.9, the $bits$ allocated to the noise are calculated for the different wavelength and represented in Table 6.4.

λ [microns]	SNR_λ	$SNR_\lambda@32Hz$	$bits$
60	10200	1800	6.2
90	1090	193	9.4
130	1600	283	8.8
180	836	148	9.8

Table 6.4: PACS SNR in spectroscopy

Based on this estimation, redundancy reduction step of the OBP should reduce the signal dynamic range to an average number of 10 *bits* (9.8 *bits*) before its encoding by the RZIP and arithmetic coders.

6.3.3 PACS Telemetry Rates

For transmission of science data, three modes are foreseen: prime, burst and parallel modes. In the PACS prime mode, the maximum 24 hours average telemetry rate is limited to 118 Kbit/s for the science data. In the burst mode, it is limited to 300 Kbit/s for a maximum total duration of 30 minutes per 24 hour period. During "parallel" observations (PACS and SPIRE instruments together), the spacecraft shall be capable of receiving data from PACS at a maximum 24 hr average rate of 42 kbit/s for the science data. Please note, there is 3 hours daily telecommunication period between the spacecraft and the ground station in Perth (Australia) for the transmission of the instruments data.

Therefore for the prime mode, the nominal transmission mode, a typical compression ratio of 34 is required¹.

6.3.4 Summary of PACS Constraints for Data Processing

In what follows, PACS constraints, that are relevant for the OBP, are summarized for photometry (Table 6.5) and spectroscopy (Table 6.6).

Signal/Noise ratio	≈ 6700 – 17600
Glitch rate	10s/pixel
Glitch tails	< 0.3s
Detector output	16bit
Significant bits	15bit
Data rate	1700 Kbits/s
Typical compression ratio	16

Table 6.5: Assumed photometry characteristics

The OBP is implemented on the SPU sub-system for the reduction of the science data to fit the telemetry bandwidth. This task is achieved by the Application SoftWare (ASW) and related programs, implemented on the SPU DSPs. Furthermore, the SPU has to control the communication functionality with neighboring sub-units, the DEtector Controller/MEchanical Controller (DEC/MEC) and Data Processing Unit (DPU), for optimal data flow between the detector and the spacecraft.

¹This is for the PACS prime spectroscopy mode, in what follows will only consider this mode, because PACS will operate on this mode for 95% of the mission. Furthermore, for the other modes the requirements for the compression are less demanding

Signal/Noise ratio	$\approx 140 - 1800$
Glitch rate	10s/pixel
Glitch tails	$< 0.5s$
Detector output	16bit
Significant bits	16bit
Data rate	4000 Kbits/s
Typical compression ratio	34

Table 6.6: Assumed spectroscopy characteristics

The target hardware where OBP is implemented has the following specifications/ constraints:

- TSC21020F IEEE 32/40 bits Floating Point Digital Signal Processing at up to 18 MHz and 54 MFLOPs
- 256k x 48 bits EEPROM program bank ((Error Detection And Correction) (EDAC protected) i.e. 1.5 MBytes
- 512k x 48 bits Program RAM (EDAC protected) i.e. 3 MBytes
- 512k x 32 bits Data RAM and 512k x 40 bits Expansion RAM (both banks EDAC protected) i.e. 2 MBytes.
- Communication links: 3 bi-directional IEEE-1355 controlled by SMCS332 capable of 100 Mbps data rates.

Therefore, under these circumstances (18 MHz CPU, 54 MFlops and 4 MB data memory), OBP has to reduce the 4000 Kbits/s by a factor of about 34 to fit the telemetry bandwidth.

6.4 Illustration of PACS Data

The signals presented in this section represent engineering data from PACS detector test on July 2004. As the signal is out of specifications (ESA and contractors), detectors tuning still has to be performed to reach the dedicated PACS instrument performance. Figure 6.22 depicts a sequence of 1D signals from PACS bolometers (photometry) for different chopper plateaus. Figure 6.23 shows a 1D signal from 8 different PACS photoconductors (spectroscopy) for 64-sample ramps.

These are different ramp shapes in spectroscopy while the photometry data seem to have stable signal. Please note that these data are free from glitches and that the real signal might look different at L2 likely with high cosmic radiation.

6. Case Study: HERSCHEL-PACS Infrared Camera

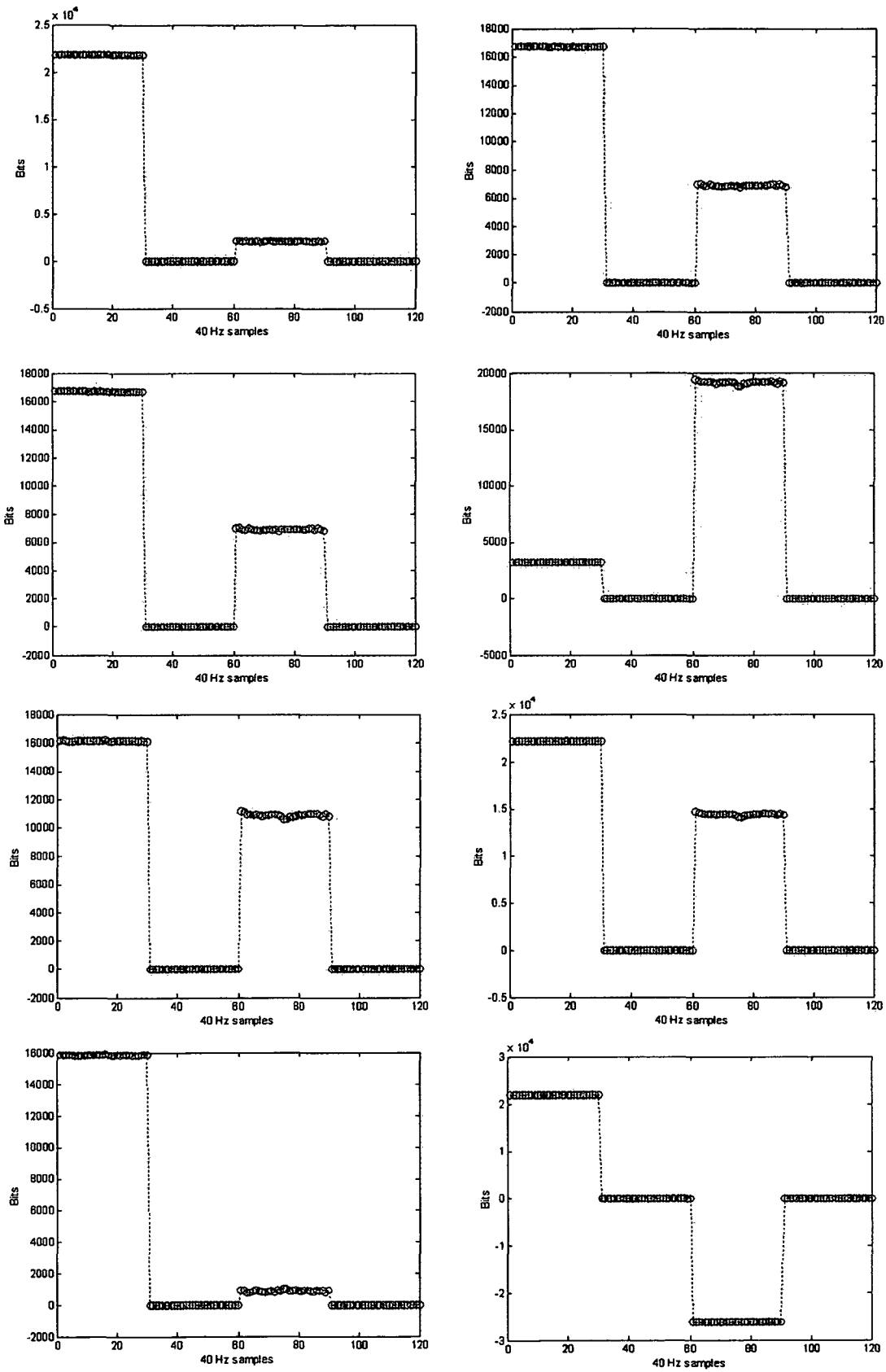


Figure 6.22: PACS photometry data from selected detectors

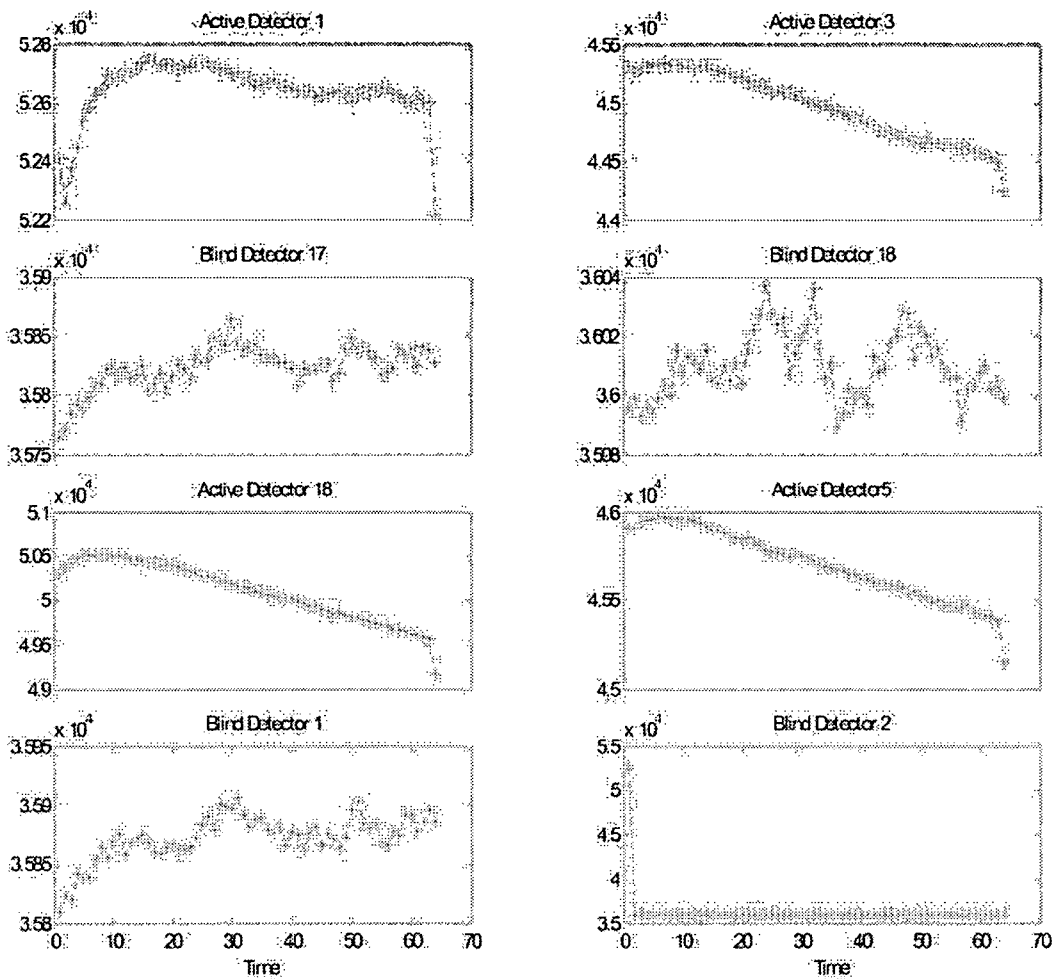


Figure 6.23: PACS spectroscopy data from selected detectors with 64-sample ramps

6.5 PACS Data Analysis

In this section, analysis for spectroscopy ramps is performed to investigate the best processing strategy. Spectroscopy is chosen for the high demanding compression (CR=34) and the high data rate (4000 Kbits/s). This analysis can easily be extended to photometry data.

For the best processing strategy, ramp models [10] have been considered while observing test data from the PACS database (Six-Pack data). Therefore, an Atlas of PACS ramps [1] has been built for the classification of the different models. These ramp models can be exploited in by the preprocessing and the oversampling reduction processing step. The preprocessing module can use this information for correcting the detector measurements to one of those ramp model depending on the detector setting. Also, the oversampling reduction method can be cho-

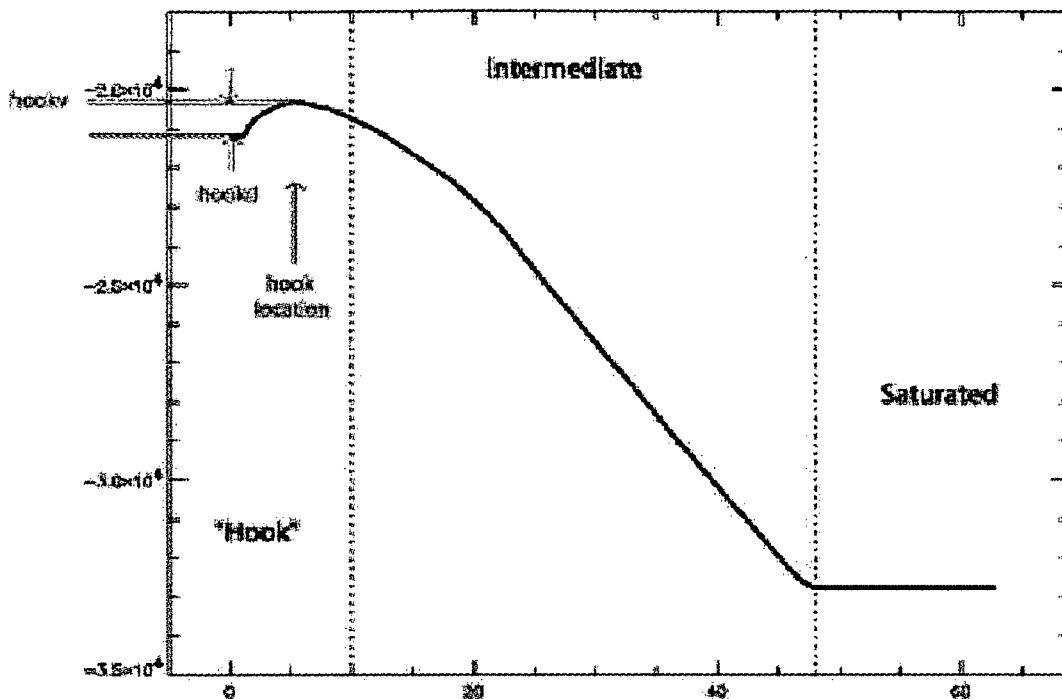


Figure 6.24: Typical spectroscopy ramp model

sen accordingly to the ramp characteristics. For instance, for curved ramps, adequate sub-ramp length has to be chosen by the user for best non-linear approximation and acceptable complexity. The user can use the input from the raw data selection module to adapt the oversampling reduction method to the estimated ramp model.

In the following sections, these ramp models are detailed.

6.5.1 PACS Input Data

The relevant test parameters for the generation of PACS data are summarized below:

- Number of detector modules (CREs): 6
- Module temperature: 1.8 K
- Black body temperatures: 33 and 50 K
- Integrating capacitors: 0.1, 0.3, 1.0, and 3.0 pF.
- Bias levels: 30, 40, 50, and 60 mV
- 64-sample ramps are considered

Currently, the input data, also called "Six-Pack data", have been generated from April - July 2003. There are 33 files in total. Each file contains data on all 18 channels for all 6 modules. For each test setup and each module and each channel, there is an averaged ramp. All subsequent analyses are carried out on these averaged ramps. Thus, the total number of ramps are:

$$33 \text{ Files} \times 6 \text{ Modules} \times 18 \text{ Channels} = 3,564 \text{ averaged ramps}$$

6.5.2 Ramp Morphology

Figure 6.24 [1] shows one example (averaged) data ramp on which distinct morphological regions and features are labeled. All ramps are characterized using these regions and features. They are described as follows:

A. Hook: The curved part at the beginning of the ramp resembling a hook. This does not exist for all ramps. The hook section begins at the first readout and ends at readout number $2P_m$. P_m is the readout that contains the maximum value of the ramp.

"hookv" is the signal level at hook maximum, P_m . "hookd" is the depth of the hook. It is defined as the difference between the second readout and the hook maximum readout (P_m).

B. Intermediate: It is the middle section of the ramp, although when the ramp is not saturated this section continues until the end of the ramp. The intermediate section begins at $2P_m$, where the hook section ends. It stops at either when the ramp ends or where saturation is detected.

C. Saturated: If it exists, this is the end part of the ramp and begins where the intermediate part ends. When the ramp slope is consistently found to be 0 or near 0 towards the end, there is, then, evidence for saturation.

First, it is assumed that the saturated part of the ramp is in the second half of all readouts. Second, slopes are obtained by calculating the differences between subsequent readouts. Third, the set of slopes that are above the average slope are examined for the entire data set and compared to the set of slopes with values below the average slope. If the difference/distance between the two averages is found to be significant (given the dispersion in the high- and low- averaged slopes), it is declared that a saturated region exists. This method is, unfortunately, not 100% accurate, but the error in determining the saturated component does not significantly change any of the conclusions.

6.5.3 Ramp Types

After visual inspection of all ramps, five distinct morphological shapes for the ramps are found in the test setup considered here. A typical example of each type is shown in Figure 6.25 and discussed below.

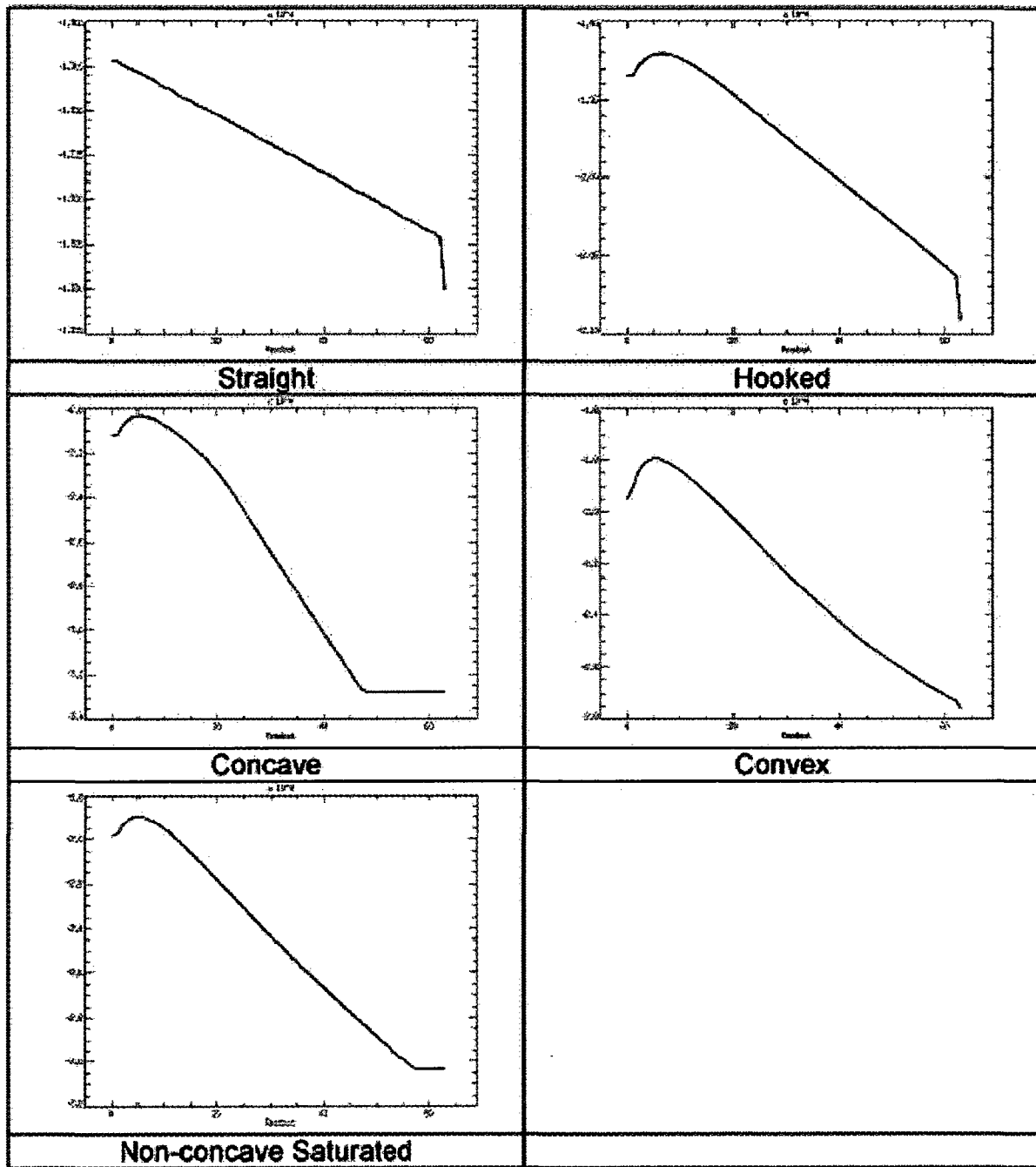


Figure 6.25: PACS spectroscopy Atlas

A. Straight Ramps: These ramps show no hook region nor saturation, and the intermediate section is best approximated by a straight line. By definition, the location of the hook is the maximum value of the ramp. All ramps where the maximum value is in the first or second readout are considered straight ramps.

B. Hooked Ramps: These ramps show a clear hook region, are otherwise straight and without saturation. Extending the definition just given above, ramps in which the ramp maximum is located after the 2nd readout are considered hooked .

C. Concave Ramps: These ramps are hooked ramps but with a non-linear intermediate section and a saturated end section. The non-linearity is identified by fitting the intermediate section of the ramp with a second order polynomial function. The fit is not meant to suggest that second order polynomials describe the non-linearity adequately. Rather, the fit is used to identify those ramps that have a significant non-linear coefficient. That is, if the second order polynomial is written as:

$$y(x) = A_0 + A_1x + A_2x^2 \quad (6.11)$$

Then, ramps with non-linear intermediate sections have significant/non-zero values for A_2 . When the coefficient A_2 is negative, these ramps are termed "concave" resembling optical surfaces with similarly directed curvature.

D. Convex Ramps: Similar to concave ramps, these ramps are hooked ramps with a nonlinear intermediate section. For convex ramps, however, the coefficient A_2 has positive value. The last few readouts of the ramps are not saturated in this case.

E. Non-concave Saturated Ramps: These are convex or straight ramps but with a saturated section at the end.

6.5.4 Analytical Ramp Model

So far, ramp models from observed detector data have been derived. In this section, the mathematical model of the ramp is presented, as formulated by Poglitsch [94], that is resulting from the detector design.

The key idea is to represent a ramp by 8 parameters and, therefore, achieving a CR of 8. The physical ramp model "y" is described as follows:

$$y(x) = P_0 \left(\sqrt{\frac{P_1}{((P_1/P_2^2 + P_3) \exp((2P_1t)/P_4) - P_3)}} - P_2 \right) + P_5 + P_6(1 - \exp(-x/P_7)) \quad (6.12)$$

where x is the number of readouts per ramp,

t is the time = $x/256$ expressed in seconds and

$P_0...P_7$ are the 8 required parameters to solve this mathematical equation.

... Original
... Fit

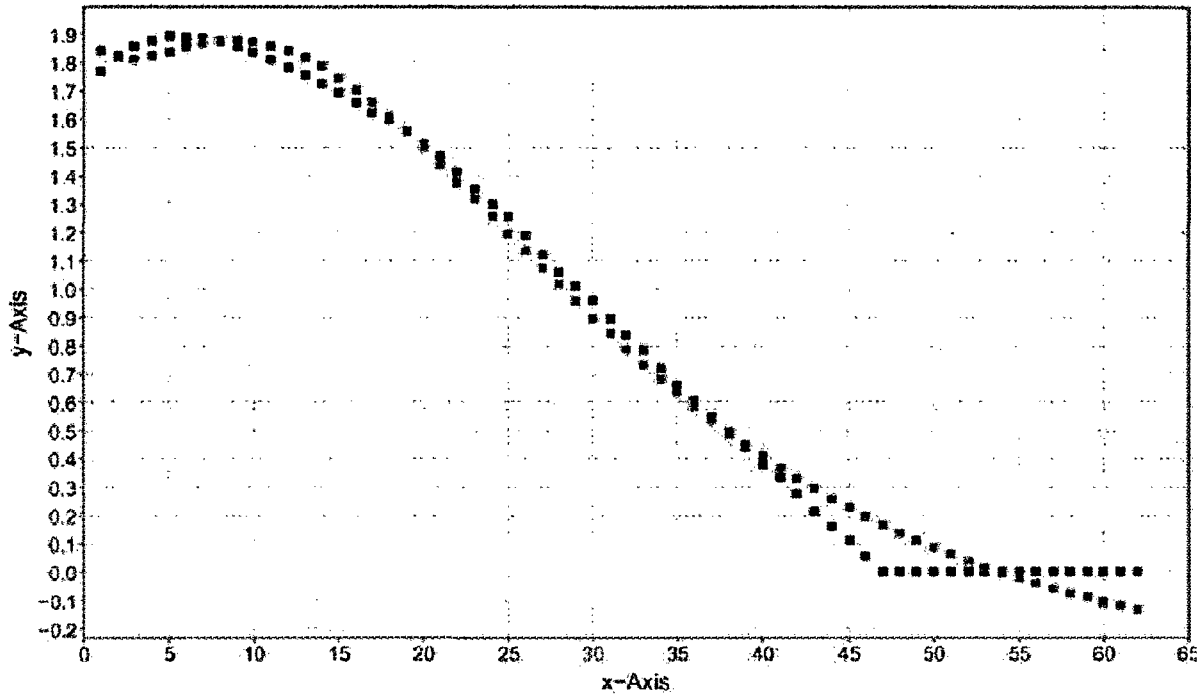


Figure 6.26: Ramp analytical model vs. measurement

The estimation of the eight parameters is a challenging problem. The implementation of this model in Fortran and in Java failed to exactly fit all ramps from the "Six-Pack" data. Furthermore, this fitting method is computationally expensive to deal with real time processing. Figure 6.26 depicts the fitting result using this analytical model respective to the ramp result from detector measurements. Therefore, a combination between the mathematical model and the measurements (modelled ramps) is a good compromise to find the best approximation of the detector signal, such that the measurements can be used to correct the mathematical model.

6.6 Tests and Evaluation of the On-board Processing

In this section, the evaluation of the OBP concept on PACS is performed. The key concepts i.e. glitch detection and oversampling reduction are considered.

As the spectroscopy case is the most critical and demanding in terms of CR and processing power, the case of photoconductors where the detector output is of the form of ramps is considered. The maximum possible compression rate we could obtain by a lossless compression (i.e., the original measurements can be recovered) can be computed as follows: A compression

ratio of 16/10 (see Section 6.3.2) is obtained by eliminating non-significant bits via redundancy reduction. An additional compression factor of 4 is obtained by calculating the slope/subslopes of the ramp, which has to be given at least with the accuracy of the SNR . Therefore, 16 bit for the slope are sufficient. A further lossless compression of the signal is not possible because it basically contains the noise of the telescope, which is by definition, incompressible. This noise cannot be eliminated because the astronomical science signal can be lost. Therefore, a lossless CR of 6.4 is achieved and an additional CR of 5.4 has to be obtained in order to fit detector data into the telemetry rate. Since lossless compression is not feasible for such rate we have to perform on-board integration. Either, we have to integrate over 6 slopes², or to fit for larger subslope length (≥ 16).

The important issue to consider is the potential loss of scientific data depending on the integration time and on glitch detection efficiency. This loss is already quantified in Section 4.3.3 where its results are used during this evaluation.

6.6.1 Oversampling Reduction Results

Table 6.7 summarizes the test results for the oversampling reduction methods on PACS spectroscopy data.

From the table results, it is noted that the least squares method combined with SDE glitch detection offers the best adequate results in terms of computing time and robustness to outliers.

RANSAC seems to be prohibitive for DSP applications due to its high computational complexity.

6.6.2 Compression Results

The on-board processing concept has been tested on a benchmark of 24 hours observations spread out over 6 months data. The data includes additive simulated glitches. This is the summary of the test parameters:

- Number of detector modules (CRE): 6.
- Module temperature: 1.8 K
- Black body temperature: 33 and 50 K
- Integrating capacitors: 0.1, 0.3, 1.0, and 3.0 pF
- Bias levels: 30, 40, 50 and 60 mV
- Number of samples per ramp: 64, 256 and 512
- Number of simulated glitches per second: 20

²In fact, integration over 5 slopes should be sufficient because due to the decrease in signal to noise ratio we could gain the rest by temporal and spatial redundancy reduction

Method	sample/ ramps	Processing Time [%]	Performance Evaluation	Glitch Detection
Least Squares	64	31	Not recommended for cumulative process Better for subramp	Not Suited
	4	37		
	8	39		
RANSAC	64	>100	Slow. Recommended for cumulative process	Good for electrical outliers detection
	4	>100		
	8	>100		
RANSAC+ Least Squares	64	>100	Slow. Recommended for cumulative process	Good for electrical outliers
	4	>100		
	8	>100		
SDE_REG_APP1	64	12	Fast. Robust to non-linearity and saturation	best suited for glitch detection
	4	17		
	8	18		
SDE_OVL_APP1	64	5	Fast. Robust to non-linearity and saturation	best suited for glitch detection
	4	9		
	8	10		
SDE_REG_APP2	64	7	Fast. Robust to non-linearity and saturation	best suited for glitch detection
	4	11		
	8	11.5		
SDE_REG_APP3	64	4	Fast. Robust to non-linearity and saturation	best suited for glitch detection
	4	6.7		
	8	7.5		

Table 6.7: Test results of the oversampling reduction methods on PACS 64-sample ramps

- Glitch tail: < 0.5 s
- Number of tested files: 660
- Number of ramps: 660 Files X 6 Modules X 18 Channels X 1100 Ramps

The used glitch detection method is SDDM (SDE_REG_APP2) while least squares fit was used for subramps fitting. Table 6.8 depicts the quantitative results for the test of OBP on these data.

The compression performance is evaluated by calculating *PIL*, *RMSE*, *SNR*, *PSNR* and CR for ramp length between 64 to 512 samples. The errors are computed between the original and the reconstructed ramps from sub-slopes. Three subramp lengths (4, 8 and 16 samples) are considered for the calculation of subslopes (slopes over parts of the ramp). The results are also made for different integrations between subsequent slopes: 1 (for no integration), 2 and 4.

As a first remark, CR is inversely proportional to the ramp length. Indeed, the lossless compression is more efficient the more the ramps are available, as it exploits the redundancy between subsequent ramps. As the maximum number of samples to store in buffer is fixed to

Samples per Ramp	Samples per Subramp	Slopes per Integration	CR	PIL in [%]	RMSE	SNR	PSNR
64	4	1	20.3	0.5859	22.7155	85.1347	31.6397
	4	2	34.2	0.9045	39.5735	81.9164	30.9459
	4	4	50.1	1.5934	67.2158	73.2973	30.3768
	8	1	35.6	0.9495	40.6454	83.3543	31.0973
	8	2	53.8	1.7102	70.3416	75.8434	30.2223
	16	1	58.2	1.7220	68.2575	75.7197	30.3019
128	4	1	18.4	0.4195	20.6589	87.4799	33.3454
	4	2	29.4	0.8104	35.3481	84.2544	32.9818
	4	4	47.9	1.3304	62.2487	73.9230	32.9748
	8	1	32.3	0.8159	35.3415	84.1694	33.0001
	8	2	50.1	1.3910	63.4834	79.9998	32.0478
	16	1	54.5	1.5111	64.3269	77.9972	32.0039
256	4	1	11.9	0.3559	18.8654	90.6587	35.4648
	4	2	26.7	0.7950	33.7613	85.3187	33.4858
	4	4	42.6	1.3045	60.0023	81.2876	33.0718
	8	1	30.5	0.8004	34.9897	84.5484	33.2354
	8	2	45.2	1.3159	61.1604	79.2348	32.9926
	16	1	50.3	1.4208	63.7325	78.1734	32.9736
512	4	1	8.1	0.3443	17.5986	95.1874	38.1944
	4	2	23.6	0.7501	30.0186	91.2743	36.1875
	4	4	36.2	1.1094	56.3482	84.3445	34.8448
	8	1	26.0	0.7854	33.9720	90.4513	36.1057
	8	2	40.1	1.1972	59.3458	85.5364	34.4428
	16	1	44.9	1.3008	60.0046	84.0029	34.1484

Table 6.8: Test results of the on-board processing on different PACS ramp lengths

512, 1 ramp per detector is considered in case of 512-sample ramps while 8 ramps per detector are considered in case of 64-sample ramps. Therefore, the smaller the ramp length is, the more redundancy is in the buffered data.

It is noted also that CR and *PIL* are proportional to the subramp length, the bigger the subramp length is, the more compression and data loss is obtained. In the same manner, the number of integrations is proportional to the *PIL* and CR. The other metrics (*RMSE*, *SNR*, *PSNR*) seem not to give a consistent behavior respective to the change of the subramp length such that a significant change in subramp length may not cause a significant change in the error. Therefore, the following conclusions are based on *PIL* metric.

For 64-sample ramps, it is noted that 4-sample subramps including 2 integrations or 8-sample subramps without integration are sufficient to fit the PACS telemetry bandwidth ($CR > 34$). Though, the first alternative is likely appreciated due to the smaller *PIL* (0.90).

In case of 128-sample ramps, one can clearly see that the option with 4-sample subramps without integration is the best regarding the smaller PIL , although the CR is slightly below the requirement. Other alternatives are 4-sample subramps including 4 integrations or 16-sample subramps.

The case of 256-sample ramps is similar to the previous one, where 8-sample subramps without integration can be appreciated due to the attractive PIL .

In the last case (512-sample ramps), the option with 4-sample subramps including 4 integrations seems to be the best for the required CR and an acceptable PIL .

It is noted in all cases, that options with $PIL < 1\%$ are very common and attractive using this OBP scheme for smaller ramp length while other cases are also acceptable as, in all cases, $PIL < 3\%$ (The science requirement).



Figure 6.27. Souvenir image after the success of the first light from PACS with detectors cooled down to "0.27 K" (22 July 2004)

Chapter 7

Conclusion and Perspectives

This thesis presents a novel work for efficient transmission of infrared images from limited budget infrared observatories. The framework "On-Board Processing" (OBP) has been introduced for optimal exploitation of the telemetry bandwidth and the processing resources to feed the infrared observatory needs. The processing concept makes use of the infrared detectors signal characteristics knowledge to reach the best achievable compression ratio, that cannot be attained by generic compression methods (e.g. JPEG 2000).

In the following subsections, the summary of the thesis is presented. Furthermore, the main contributions and innovations of this work to the scientific community are listed. Possible extensions of this work and further investigations are also proposed.

7.1 Summary

In this work, a solution has been presented to infrared space astronomy for efficient data transmission and better exploitation of the telemetry bandwidth and the available processing resources. Figure 7.1 summarizes the thesis work.

Chapter 1 outlines the motivation for the need of a novel general framework for efficient data transmission from space observatories. Infrared detectors - an increasingly important technology in astronomy - served as an example to demonstrate that the novel compression approach can deal with high entropy data and limited processing resource budget. Furthermore, compression challenges for space applications are pointed out. The need for recognition of optimal processing tool within infrared astronomy constraints is stressed. The contribution of this work to the scientific research is also summarized in this chapter.

In Chapter 2, infrared astronomy aspects, relevant for the dissertation goals, are presented. A brief description of infrared space technology is given. Then, signal characteristics of infrared detectors are investigated. Afterwards, the light detection mechanism using infrared sensors is detailed and the resulting signal models for diverse types of detectors are illustrated. Finally, typical images from infrared astronomy are illustrated and the astronomical efficiency of a system is summarized.

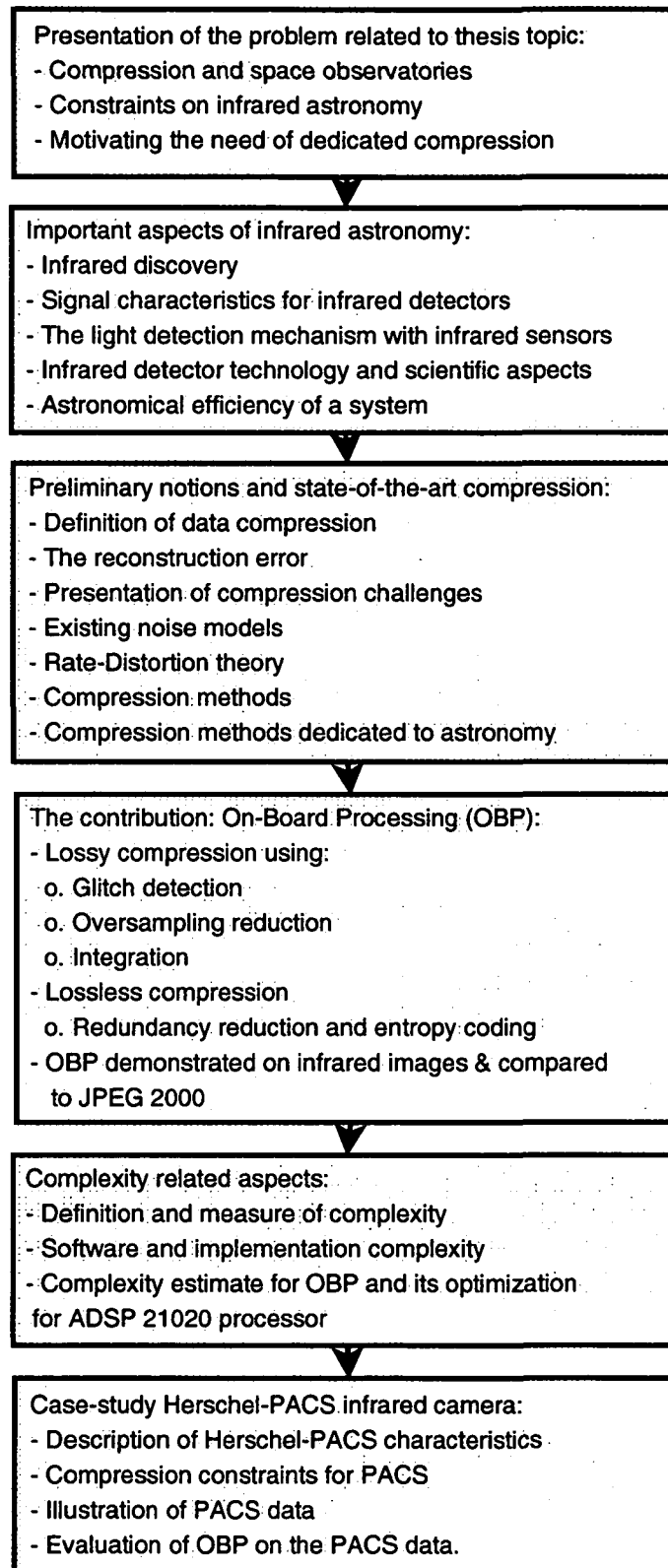


Figure 7.1: Thesis summary

In Chapter 3, preliminary notions that are necessary to follow the dissertation work are introduced. The formal definition of data compression is presented. Also, the conventional evaluation criteria for the validation of processing results like signal-to-noise ratio are reported. A new criterion **Potential Information Loss (PIL)** is introduced for an objective quantitative evaluation. Also, the existing noise models with respect to their statistics are presented. Then, Rate-Distortion theory is briefly given. Furthermore, this chapter contains state-of-the-art compression methods, that are relevant for the thesis investigation. Recent image compression techniques make use of wavelet-based approaches for specific performances. Indeed, wavelets have the advantage to be multiresolution, localized and achieving the critical sampling. Therefore, it is embedded in the image compression standard "JPEG 2000". Finally, techniques that were dedicated to astronomical image compression have been also outlined and compression challenges are summarized.

Chapter 4 presents the contribution of this work to science, that is, the processing of astronomical data from infrared observatories. This novel framework is dedicated for efficient infrared data compression, on-board space observatories. It deals with limited-budget space observatories constrained with limited telemetry, processing resources and large data volume. The individual modules of the proposed framework **On-Board Processing (OBP)** are detailed with special emphasize to the glitch detection, oversampling reduction and integration steps. This latter modules are the lossy part of the compression concept, that drive the result quality and the efficiency of the compression. It was demonstrated with a simple example that OBP outperforms the generic compression method "JPEG2000" on infrared image compression.

Additionally to compression performance and quality, the importance of algorithm complexity for the design of a compression method is stressed in Chapter 5. Indeed, the complexity of an algorithm defines the feasibility and the applicability of the method. Therefore, existing methods for computing algorithm complexity were briefly introduced. Following that, two approaches for complexity-analysis were presented. The first one analyzes and optimizes the complexity in an intuitive manner. The second approach proposes a methodology for measuring and quantifying the complexity. Furthermore, the complexity measurements and optimizations for DSP are given. Then, an evaluation of OBP complexity on **Digital Signal Processor (DSP)** based applications (case of ADSP21020) is performed.

Chapter 6 presents the case-study, Herschel-PACS [150], for the validation of the proposed framework feasibility on IR astronomy. First, the Herschel-PACS mission is summarized. Then, compression constraints for PACS observation are detailed. Examples of PACS detector data are depicted for illustration of the problem. Afterwards, an analysis of the PACS most demanding mode "spectroscopy" is performed, by comparing the analytical models to the observations. An Atlas of models has been built, based on observed morphologies in the data. Finally, an evaluation of OBP on PACS data is performed and the processing results are given. The evaluation is performed using the criteria described in Chapter 3.

7.2 Main Achievements

This section summarizes the main contributions of the work presented in this thesis for further development of science (signal/image processing) and enhancement of the understanding of the field "Compression".

- The statement of the problem is presented for space observatories where the readout rate largely exceeds the available downlink bandwidth. The description of the constraints is related to image processing for space applications.
- The proposition of the novel general framework **On Board Processing (OBP)** is given, which consists of data reduction on the remote satellite for efficient data transmission, that is required to fit the telemetry.
- Evaluation of the proposed framework is performed using standard metrics. Furthermore, a new quality measure (PIL) has been proposed, that presents an objective quantitative evaluation of the framework feasibility.
- The constraints of the OBP approach are investigated for high compression efficiency and acceptable image quality. They are related to noise and complexity aspects.
- The problem was illustrated on infrared astronomy with a complex detector technology, in which the resulting detector signal presents high entropy, and different noise models for diverse types of sensors and readout modes.
- Investigation on the infrared astronomical signal has been performed, by a detailed study of the light detection mechanism and noise behavior has been presented for different acquisition techniques.
- State-of-the-art Rate-Distortion theory has been summarized and the different mathematical methods that contribute to the formulation of the R-D problem have been presented.
- OBP approach has been presented in details with individual processing steps, with special emphasise on the glitch detection and the oversampling reduction steps.
- Feasibility of the OBP for IR astronomy has been investigated by studying the complexity issues, as space astronomy is most likely constrained with the limited processing resources.
- Qualitative and quantitative measures of the complexity are presented. Complexity aspects of the OBP approach have been formulated for embedded DSP, that is the usual platform dedicated for space applications.
- The case-study Herschel-PACS [150] has been used for the validation of the investigation results. The feasibility of the OBP approach on real astronomical applications has been demonstrated on this infrared instrument (PACS).
- An Atlas has been built for PACS spectroscopy. Based on observational data, the ramps (spectroscopy data) have been classified into five categories depending on their morphology.

- The developed compression framework is integrated on the PACS instrument [4] for efficient transmission of astronomical images in the wavelength range of 57-210 μm .

7.3 Future Work

The work presented in this dissertation can be extended in several ways. This section proposes a list of topics, which might be interesting for further investigation.

- Feasibility measure of the proposed framework for other applications, like medical imaging (X-rays) or optical imaging.
- Investigation of data reconstruction at the user level for data loss while compression due to cosmic particles (glitches).
- Analysis of the data reconstruction respective to the transmission loss. Reconstruction rate vs. telemetry loss.
- Assessment of other methods than wavelets, like curvelet [17] or contourlet [28] transforms, for on-ground data reduction in order to reconstruct faint sources.
- Investigation on entropy coders for optimal infrared astronomical data lossless compression.
- Extension of the complexity measures for other architectures than the DSPs.
- ... For any other ideas, please mail me at nabil@prip.tuwien.ac.at...

Bibliography

- [1] B. Ali and B. Schulz. Atlas of PACS Ge:Ga Test Ramps. *NASA Herschel Research Center, Technical Report October, 2003*
- [2] D.A. Allen et al. IRIS: an IR Imager and Spectrometer for the Anglo-Australian Telescope. *Proc. Astron. Soc. Australia, 10, 298, 1993*
- [3] P. N. Appleton, P. R. Siqueira and J. P. Basart. Morphological Filter for Removing 'Cirrus-like' Emission from Far-IR Extragalactic IRAS Fields. *Astro. J. 106, 1664-1678, 1993*
- [4] A.N. Belbachir, H. Bischof, R. Ottensamer, H. Feuchtgruber, C. Reimers and F. Kerschbaum. On-board Data Processing to Lower Bandwidth Requirements on an Infrared Astronomy Satellite: the Case of the Herschel-PACS Camera. *EURASIP Journal of Applied Signal Processing, To appear on 2005.*
- [5] A.N. Belbachir, H. Bischof and F. Kerschbaum. A Data Compression Concept for Space Applications. *DSP-SPE'00, IEEE Digital Signal Processing Workshop in Hunt, TX, USA, October 2000.*
- [6] A.N. Belbachir and H. Bischof. On-Board Data Compression: Noise and Complexity Related Aspects. *Technical Report Number 75, PRIP, TU Vienna, 2003.*
- [7] A.N. Belbachir and P.M. Goebel. A Sparse Image Representation Using Contourlets. *10th Computer Vision Winter Workshop, Zell an der Pram, Austria, February 2005.*
- [8] A.N. Belbachir, T. Chilton, M. Dunn, M. Nunkesser, S. Sidhom and G. Szajnowski. Image Compression using Hartley Transform. *Technical Report Number 87 at PRIP, TU Vienna, 2003.*
- [9] A.N. Belbachir, P.M. Goebel. The Contourlet Transform for Image Compression. *Physics in Signal and Image Processing Conference PSIP05, Toulouse, France, January 2005.*
- [10] A.N. Belbachir, B. Schulz. Discussion on the On-board Reduction/Compression Concept for PACS Spectroscopy Data. *Technical Report, PACS Document Tree Leuven, Belgium, July, 2003.*
- [11] A. Bijaoui. Généralisation de la Transformation d'Anscombe. *Technical Report, 1994.*
- [12] H. Bischof, A.N. Belbachir, D.C. Hoenigmann, and F. Kerschbaum. A data reduction concept for FIRST/PACS. In *J. B. Breckinridge and P. Jakobsen, editors, UV, Optical, and IR Space Telescopes and Instruments VI. SPIE, Munich, Germany, March 2000.*
- [13] J. Blommaert et al. CAM - The ISO Camera. *ISO Handbook Volume III, V2, June 2003.*
- [14] R. Bracewell. The Fourier Transform and its Applications. *McGraw-Hill, 2nd edition, 1986.*
- [15] R. Buccigrossi and E. Simoncelli. Image Compression via Joint Statistical Characterization in the Wavelet Domain. *Internet Manuscript, 1997.*
- [16] G. Buttmann. Wilhelm Herschel. *Wissenschaftl. Verl.-Ges., 1961.*

- [17] E.J. Candes and D.L. Donoho. Curvelets - A Surprisingly Effective Non-Adaptive Representation for Objects with Edges. *in Curve and Surface Fitting*, A. Cohen, C. Rabut, and L.L. Schumaker, Eds. Saint Malo: Vanderbilt University, 1999.
- [18] E. J. Candes and D. L. Donoho. Ridgelets: a Key to Higher-Dimensional Intermittency? *Phil. Trans. R. Soc. Lond. A.*, pp. 2495-2509, 1999.
- [19] E. J. Candes and D. L. Donoho. New Tight Frames of Curvelets and Optimal Representations of Objects with Smooth Singularities. *Department of Statistics, Stanford University, Tech. Rep.*, 2002.
- [20] T.H. Chao and H. Zhou. Electro-Optic Imaging Fourier Transform Spectrometer. *4th Annual Earth Science Technology Conference, USA*, 2004.
- [21] C. Chrysafis and A. Ortega. Line Based, Reduced Memory, Wavelet Image Compression. *in IEEE Trans. on Image Processing*, 2000.
- [22] L.M. Close and D.W. Mc Carthy Jr.. High Resolution Imaging With a Tip-Tilt Cassegrain Secondary. *PASP*, 106,77,1994.
- [23] Consultative Committee for Space Data Systems. Telemetry Synchronization and Channel Coding. *Blue Book, NASA Press, September 2003*.
- [24] M. Datcu and G. Schwarz. Advanced Image Compression: Specific Topics for Space Applications. *DSP'98, International Workshop on DSP techniques for Space Applications 1998*
- [25] I. Daubechies. Orthonormal Bases of Compactly Supported Wavelets. *Communication on Pure and Applied Mathematics*, vol. XLI, pp. 909-996, 1988
- [26] I. Daubechies and W. Sweldens. Factoring Wavelet Transforms into Lifting Steps. *J. Fourier Anal. Appl.*, vol.4, no.3, pp.245-267, 1998
- [27] S.R. Deans. The Radon Transform and Some of Its Applications. *New York: Wiley*, 1983
- [28] M.N. Do and M. Vetterli. The Contourlet Transform: An Efficient Directional Multiresolution Image Representation. *IEEE Transactions on Image Processing*, Oct. 2003.
- [29] M.N. Do and M. Vetterli. Orthonormal Finite Ridgelet Transform for Image Compression. *ICIP'2000, Vancouver, Canada, September 2000*.
- [30] M.N. Do and M. Vetterli. The Finite Ridgelet Transform For Image Representation. *IEEE Transactions on Image Processing*, Jan. 2003.
- [31] D.L. Donoho. Denoising by Soft-thresholding. *IEEE Trans. on Information Theory*, Vol.41, pp.613-627, 1995
- [32] D.L. Donoho and M. Duncan. Digital Curvelet Transform: Strategy, Implementation, and Experiments. *in Proc. Aerosense 2000, Wavelet Applications VII, SPIE*, 4056, 2000.
- [33] G. Doubrovik. Herschel-Planck Instrument Interface Document Part B(PACS). *Alcatel Space for ESA*, July 2004.
- [34] P. Duhamel and H. H'mida. New 2^n DCT Algorithms suitable for VLSI Implementation. *IEEE ICASSP 87, NY, USA*, pp.1805-1808, 1987.
- [35] E. Feig and S. Winograd. On the Multiplicative Complexity of the Discrete Cosine Transform. *IEEE Trans. on Information Theory*, vol. 38, pp. 1387-1397, Jul. 1992.
- [36] P. Fernandez and A. Ortega. An Input dependent Algorithm for the Inverse DWT. *36th Conf. on Sig., Sys and Computers, Asilomar'98*, vol.1, pp. 472-476, Nov. 1998.
- [37] M.A. Fischler and R.C. Bolles. Random Sample Consensus: A Paradigm for Model Fitting with Applications to Image Analysis and Automated Cartography. *Communications ACM* 24, pp.381-395, June 1981.

-
- [38] A.M. Fowler and I. Gatley. Demonstration of an Algorithm for Read-Noise Reduction in IR Arrays. *Astrophys. J.* 353:L33-L34, 1990
- [39] P. Frick, R. Beck, E.M. Berkhuijsen, and I. Patrickeyev. Scaling and Correlation Analysis of Galactic Images. *MNRAS* 327, 1145, Blackwell Publishing, September 2001
- [40] K. Froitzheim and H. Wolf. Knowledge- Based Approach to JPEG Acceleration. *SPIE, the Int. Soc. for Optical Engin., vol 2419, USA pp.318-328, 1995*
- [41] R.Q. Fugate and W.J. Wild. Untwinkling the Stars. *Sky and Telescope*, 87, No.5, 25, 1994
- [42] J.D. Garnett and W.J. Forrest. Multiply Sampled Read-Limited and Background-Limited Noise Performance. *Proc. SPIE Vol. 1946, IR Detectors and Instrumentation, p.395, 1993.*
- [43] I.S. Glass. Handbook of Infrared Astronomy. *Cambridge University Press, Oct.1999.*
- [44] M.J. Gormish. Source Coding with Channel, Distortion and Complexity Constraints. *PhD Thesis, Stanford University, 1994.*
- [45] G. Grimmett and D. Stirzaker. Probability and Random Processes. 2nd ed. *Oxford, England: Oxford University Press, 1992.*
- [46] N.M. Haegel. Numerical Modeling of Transient Behavior in Far-Infrared Photoconductors. *Far IR, Sub-MM and MM Detector Technology Workshop, USA, April 2002.*
- [47] H.Hakimmashhadi. Discrete Fourier Transform and FFT. *Chap.4, 77-118, NY, USA: Marcel Dekker, 1988.*
- [48] F.R. Hampel, E.M. Ronchetti, P.J. Rousseeuw, and W.A. Stahel. Robust Statistics - The Approach Based on Influence Functions. *John Wiley & Sons, 1986.*
- [49] G. Held. Data and Image Compression. *Wiley 1996.*
- [50] N. Henbest M. Marten. The New Astronomy. *Second Edition, Cambridge University Press, 1996.*
- [51] M. Holschneider, R. Kronland-Martinnet, J. Morlet and P. Tchamitchian. The Algorithme à Trous. *Publication CPT-88/P.2115, Marseille, 1988.*
- [52] F.N. Hooge. 1/f Noise is No Surface Effect. *Physics Letters, Vol.29A, Nr.3, pp. 139-194, April 1969.*
- [53] F.N. Hooge. 1/f Noise Sources. *IEEE Transactions on Electron Devices, Vol.41, Nr.11, pp.1926-1935, Nov. 1994.*
- [54] Z. Ivesic et al. Infrared Classification of Galactic Objects. *ApJ, USA, May 2000.*
- [55] H. Izumiura et al. A detached dust shell surrounding the J-type carbon star Y Canum Venaticorum. *A and A* 315, L221-L224, October 1996.
- [56] L. Kazovsky, S. Benedetto, and A. Willner. Optical Fiber Communication Systems. *Artech House, 1996.*
- [57] F. Kerschbaum, H. Bischof, A.N. Belbachir, D. C. Hoenigmann, and T. Lebzelter. Evaluation of FIRST/PACS data compression on ISO data. In J. B. Breckinridge and P. Jakobsen, editors, *UV, Optical, and IR Space Telescopes and Instruments VI. SPIE, Munich, Germany, March 2000.*
- [58] C.K. Koc, G. Chen and C.K. Chui. Complexity Analysis of Wavelet Signal Decomposition and Reconstruction. *IEEE Trans. on Aerospace and Electronic Systems, vol.30, pp 910-918, Jul.1994.*
- [59] F. Kordes, R. Hogendoorn, and J. Marchand. Handbook of Data Compression Algorithms. *Spacecraft Control and Data Systems Division, ESA TM-06, 1990.*
- [60] L.J. Kozlowski. Low Noise Capacitive Transimpedance Amplifier Performance vs. Alternative IR Detector Interface Schemes in Submicron CMOS. *Proc. SPIE, 2745, 1996.*

- [61] W.G. Kropatsch. Benchmarking Graph Matching Algorithms -A Complementary View. *Pattern Recognition Letters*, vol. 24(8), 2003.
- [62] G.G. Langdon. An Introduction to Arithmetic Coding. *IBM Journal of Research and Development*, March 1984.
- [63] C. Lawson and R. Hanson. Solving Least Squares Problems. *Englewood Cliffs, NJ: Prentice-Hall*, 1974.
- [64] J. Lee. Optimised Quad-tree for Karhunen-Loeve Transform in Multispectral Image Coding. *IEEE Trans. on Image Processing*, April 1999.
- [65] K. Leech et al. SWS-the Short Wavelength Spectrometer. *ISO Handbook Volume V, Version 2.01*, June 2003.
- [66] K. Lengwehasatit and A. Ortega. DCT Computation with Minimal Average Number of Operations. *Vis. Com. and IP, VCIP97, USA, Feb. 1997*.
- [67] K. Lengwehasatit and A. Ortega. DCT Computation Based on Variable Complexity Fast Approximation. *ICIP'98, USA, pp.95-99, Oct. 1998*.
- [68] K. Lengwehasatit and A. Ortega. Distortion/Decoding Time Tradeoffs in Software DCT-Based Image Coding. *IEEE ICASSP'97, Munich, Germany, 1997*.
- [69] M. Livny, V. Ratnakar. Quality-controlled compression of sets of images. *International Workshop on Multi-Media Database Management Systems, NY, USA, Aug. 1996*.
- [70] R.L. Libbey. Signal and Image Processing Sourcebook. *Multiscience Press, USA, 1994*.
- [71] M. Lloyd-Hart et al.. First Astronomical Images Sharpened with Adaptive Optics using a Sodium Laser Guide Star. *Astrophys. J.*, 493, 950, 1998.
- [72] M. Louys, J.-L. Starck, S. Mei and F. Murtagh. Astronomical Image Compression. *Astronomy and Astrophysics*, page 579-590, May 1999.
- [73] F.J. Low. Low-Temperature Germanium Bolometer. *Journal of the Optical Society of America*, 51, 1300-4, 1961.
- [74] N.Y. Lu et al. An ISOPHOT Study of the Disk of Galaxy NGC6946: 60 m IR and Radio Continuum Correlation. *A and A 315, L153-L156, September 1996*.
- [75] Y. Lu and M. Do. CRISP-Contourlet: A Critically Sampled Directional Multiresolution Image Representation. *SPIE Conf. on Wavelets X, San Diego, Aug. 2003*.
- [76] C. Lucas et al. Development of Gallium-Doped Silicon 128X192 Element Arrays for 8-14 μm Observation. *Proc. SPIE Orlando, 2475, pp.50-55, 1995*.
- [77] C.B. Luginbuhl, A.A. Henden, F.J. Vrba and H.H. Guetter. Photometric Characterization of the U.S. Naval Observatory HgCdTe IR camera. *In Infrared Detectors and Instrumentation for Astronomy, Proc. SPIE, 1995*.
- [78] E. Magli, G. Olmo. Integrated Compression and Linear Feature Detection in the Wavelet Domain. *ICIP' 2000, Canada, September 2000*.
- [79] S. Mallat. A Wavelet Tour of Signal Processing. *2nd ed. Academic Press, 1999*.
- [80] J. Marchadier and W.G. Kropatsch. Functional Modeling of Structured Images. *4th IAPR-TC15 Workshop on Graph-Based Representation in Pattern Recognition pages 35-46, York, UK, 2003*.
- [81] S. Matsuura et al. Current Status of the Detector Development for the Far-IR Surveyor (FIS) on Astro-F. *Far IR, Sub-MM and MM Detector Technology Workshop, USA, April 2002*.
- [82] P. McNerney. The Communication of Images from New Generation Astronomical Telescopes. *Astronomical Data Analysis Software and Systems Conference, San Francisco, USA, 2000*.

-
- [83] H. Moseley. Large Format Bolometer Arrays for Far Infrared, Submillimeter, and Millimeter Wavelength Astronomy. *Far IR, Sub-mm and mm detector Technology Workshop, CA, USA, April 2002.*
- [84] J. Natvig. Evaluation of Six Medium Bitrate Coders for the Pan-European Digital Mobile Radio System. *IEEE Journal on Selected Areas in Communications, vol. 6, pp. 324-331, Feb. 1988.*
- [85] H. Nielsen. Complexity Evaluation of Signal Processing Algorithms. *EUSIPCO'88, Sig. Proc.IV: Theory and Applications, Netherlands, 1988.*
- [86] J. Odegard et al. Wavelet-Based SAR Speckle Reduction and Image Compression. *Proc. SPIE, Vol.2487, pp.259-271, 1995.*
- [87] S.I. Olsen. Estimation of Noise in Images: an Evaluation. *CVGIP: Graphical Models and Image Processing, 55(4), 319-323, 1993.*
- [88] A. Omont et al. ISOGAL: A Deep Survey of the Obscured Inner Milky Way with ISO at $7\ \mu\text{m}$ and $15\ \mu\text{m}$ and with DENIS in the Near-IR. *A&A 403, 975-992, April 2003.*
- [89] E. Ordentlich, D. Taubman, M. Weinberger, G. Seroussi, and M. Marcellin. Memory Efficient Scalable Line-Based Image Coding. *IEEE Data Compression Conference, (Snowbird, USA), pp. 218-227, Mar. 1999.*
- [90] S. Ott. Innovative Cosmic Ray Rejection in ISOCAM Data. *ADASS IX, ASP Conference Series, Vol. 216, 2000.*
- [91] R. Ottensamer, A.N. Belbachir, H. Bischof, H. Feuchtgruber, F. Kerschbaum, C. Reimers and E. Wiewprecht. The HERSCHEL-PACS On-Board Software Data Processing Scheme. *Astronomical Data Analysis Software and Systems Conference, Victoria, Canada, September 2001.*
- [92] R. Ottensamer, F. Kerschbaum, C. Reimers, A.N. Belbachir and H. Bischof. The Austrian HERSCHEL-PACS On-Board Reduction Work Package. *Hvar Observatory Bulletin, vol. 26, no. 1, p. 77-80, Hungary, 2002.*
- [93] R. Ottensamer, A.N. Belbachir, H. Bischof, H. Feuchtgruber, F. Kerschbaum, A. Poglitsch and C. Reimers. HERSCHEL/PACS On-Board Reduction/Compression Software Implementation. *SPIE International Symposium on Astronomical Telescopes, Glasgow, Scotland, UK, June 2004.*
- [94] A. Poglitsch et al. The Photodetector Array Camera and Spectrometer (PACS) for the Herschel Space Observatory. *Journal of the American Astronomical Society, (2004AAS...204.9302P), May 2004.*
- [95] W. Press. Wavelet-Based Compression Software for FITS Images. *in Astronomical Data Analysis Software and Systems I, A.S.P. Conf. Ser., Vol. 25, eds. D.M. Worrall, C. Biemesderfer and J. Barnes, 1992.*
- [96] K. R. Rao and P. Yip. Discrete Cosine Transform: Algorithms, Advantages, Applications. *Academic Press, Boston, 1990.*
- [97] J. Reichel. Complexity Related Aspects of Image Compression. *PhD Thesis, EPFL, Switzerland, 2003.*
- [98] C. Reimers, A.N. Belbachir, H. Bischof, R. Ottensamer, H. Feuchtgruber, F. Kerschbaum and A. Poglitsch. Feasibility of the On-Board Reduction/Compression Concept for Infrared Camera. *7th International Conference on Pattern Recognition, Cambridge, UK, August 2004.*
- [99] S.T. Ridgway and J.W. Brault. Astronomical Fourier Transform Spectroscopy Revisited. *Ann. Rev. A and A, 22, 291-318, 1984.*

- [100] G.H. Rieke. Detection of Light: From the Ultraviolet to the Submillimeter. *Cambridge University Press, Cambridge, UK, 1994.*
- [101] O.Rioul and P. Duhamel. Fast Algorithms for Discrete and Continuous Wavelet Transforms. *IEEE Trans. Inf. Theory, vol. 38, Mar. 1992.*
- [102] N.A. Romero. Johnson Noise. *Junior Physics Laboratory, MIT of Cambridge, MA 02139, USA, November 1998.*
- [103] D. Rosenthal et al. Stressed Ge:Ga Detector Arrays for PACS And FIFI LS. *Far IR, Sub-mm and mm detector Technology Workshop, CA, USA, April 2002.*
- [104] P.J. Rousseuw and A.M. Leroy. Robust Regression and Outlier Detection. *Wiley, New York, 1987.*
- [105] S.S. Ruth and P.J. Kreutzer. Data compression for large business files. *Datamation 18, 62-66, Sept. 1972.*
- [106] A. Said and W. Pearlman. A New, Fast, and Efficient Image Codec Based on Set Partitioning in Hierarchical Trees. *IEEE Trans. on Circuits and Systems for Video Technology, Vol.6, pp.243-250, 1996.*
- [107] J. Sanchez and M.P. Canton. Space Image Processing. *CRC Press, 1999.*
- [108] M. Sauvage et al. ISOCAM Mapping of the Whirlpool Galaxy (M51). *A and A 315, L82L92, September 1996.*
- [109] K. Sayood. Introduction to Data Compression. *Second Edition, Morgan Kaufmann, 2000.*
- [110] W. R. Schwartz, M. P. Smylie and N. M. Haegel. Transient Modeling and Measurements for Ge:Ga Photoconductors. *Far IR, Sub-MM and MM Detector Technology Workshop, USA, April 2002.*
- [111] J. Serra. Image Analysis and Mathematical Morphology. *Academic Press, New York, 1982.*
- [112] C.E. Shannon. Technical Journal. *Bell Systems, 1948.*
- [113] J. Shapiro. Embedded Image Coding Using Zerotrees of Wavelet Coefficients. *IEEE Trans. On Signal Processing, Vol.41, pp. 3445-3465, 1993.*
- [114] D. Shaw and P. Hodge. Cosmic Ray Rejection in STIS. *Instrument Science Report STIS 98-22, 1998.*
- [115] R. Siebenmorgen, E. Kruegel, and R.J. Laureijs. The Infrared Continuum Radiation of NGC1808 : A PAH and Polarisation Study. *A and A astro-ph/0107098, July 2001.*
- [116] M.G. Stapelbroeck, D.H. Seib, J.E. Huffman and R.A. Florence. Large-Format Blocked Impurity-Band Focal Plane Arrays for Long Wavelength IR Astronomy. *Proc. SPIE, 2475, 41, 1995.*
- [117] J.L. Starck, F. Murtagh and A. Bijaoui. Image Processing and Data Analysis: the Multi-scale Approach. *Cambridge University Press, 1998.*
- [118] J.L. Starck and F. Murtagh. Astronomical Image and Data Analysis. *Springer-Verlag, 2002.*
- [119] J.L. Starck, D.L. Donoho and E.J. Candes. The Curvelet Transform for Image Denoising. *IEEE Trans. On Image Processing, Vol.11, No.6, June 2002.*
- [120] J.L. Starck, M.K. Nguyen and F. Murtagh. Wavelets and Curvelets for Image Deconvolution: a Combined Approach. *Trans. on Signal Processing, 83, 10, pp- 2279-2283, 2003.*
- [121] J.L. Starck, D.L. Donoho and E.J. Candes. Astronomical Image Representation by the Curvelet Transform. *Astronomy and Astrophysics 398, 785-800, 2003.*

-
- [122] C. Sterken and M. de Groot. The Impact of Long-Term Monitoring on Variable Star Research. *Proceeding of the NATO Advanced Research Workshop, Belgium, 1993.*
- [123] G. Strang and T. Nguyen. Wavelets and Filter Banks. *Wellesley Cambridge Press, 1996.*
- [124] E. Sturm et al. ISO-SWS Spectroscopy of ARP 220, A Highly Obscured Starburst Galaxy. *A and A 315, L133L136, October 1996.*
- [125] W. Sweldens. The Lifting Scheme: A Custom-Design Construction of Biorthogonal Wavelets. *Appl. Comput. Harmon. Anal., vol.3, no.2, pp. 186-200, 1996.*
- [126] D. Taubman. Kakadu Survey Documentation. *June 2003.*
- [127] D. Taubman. High Performance Scalable Image Compression with EBCOT. *IEEE Transactions on Image Processing, volume 9 (number 7), pages 1151-1170, July 2000.*
- [128] D. Taubman, E. Ordentlich, M. Weinberger and G. Seroussi. Embedded Block Coding in JPEG 2000. *Signal Processing Image Communication, volume 17 (number 1), pages 49-727, January 2002.*
- [129] N.P. Topiwala. Wavelet Image and Video Compression. *Boston, Kluwer 1998.*
- [130] E. Tuncel and K. Rose. Computation and Analysis of the N-Layer Scalable Rate-Distortion Function. *IEEE Trans. on Information Theory, Vol.49, No.5, May 2003.*
- [131] M. Vetterli and J. Kovacevic. Wavelets and Subband Coding. *Prentice Hall, NJ, USA, 1995.*
- [132] L. Vigroux et al. ISOCAM Observations of the Antennae Galaxies. *A and A 315, L93L96, September 1996.*
- [133] R.J. Wainscoat and L.L. Cowie. A Filter for Deep Near-IR Imaging. *Astron. J.,103,332, 1992.*
- [134] White R.. Digitized Optical Sky Surveys. *Mc Gillivray and Thompson Eds., Kluwer, p.167, 1992.*
- [135] W. Wijmans and P. Armbruster. Data Compression techniques for Space Applications. *DASIA'96, Rome, Italy, May 1996.*
- [136] S. Winograd. On the Complexity of Symmetric Filters. *Proc. of IEEE Int. Symp. Cir. Sys., NY, USA, pp.262-265, 1979.*
- [137] S. Winograd. Signal Processing and Complexity of Computation. *IEEE ICASSP 80, vol.24, NY, USA, pp. 94-101, 1980.*
- [138] E. Young, G. Rieke, and J. Davis. Development of Advanced Far-Infrared Photoconductor Arrays. *Far IR, Sub-mm and mm detector Technology Workshop, CA, USA, April 2002.*
- [139] H. Zuse. Software Complexity. *NY, USA: Walter de Gruyter, 1991.*
- [140] Analog Device. ADSP-21000 Family "ADSP-21020" User's Manual. *Analog device Inc., 1995.*
- [141] <http://www.analog.com>
- [142] Intel Corporation. Mobile Intel Celeron Processor. *Technical Report, Document Number 245421-041, November 2004.*
- [143] http://coolcosmos.ipac.caltech.edu/cosmic_classroom/ir_tutorial/
- [144] <http://www.datacompression.info>
- [145] JPEG 2000 Image Coding System" at <http://www.jpeg.com/JPEG2000.html>, 2000
- [146] <http://www.ccsds.org/>
- [147] <http://www.iso.vilspa.esa.es>
- [148] <http://irsa.ipac.caltech.edu/IRASdocs/iras.html>
- [149] <http://www.mpe.mpg.de/projects.html#first>

- [150] <http://pacs.mpe.mpg.de>
- [151] <http://hubble.nasa.gov>
- [152] http://hubblesite.org/sci.d.tech/nuts_and_bolts/instruments/nicmos/
- [153] http://coolcosmos.ipac.caltech.edu/resources/paper_products/index.html
- [154] <http://sirtf.caltech.edu/>
- [155] <http://vathena.arc.nasa.gov/curric/space/lfs/kao.html>
- [156] <http://www.rarlab.com>
- [157] <http://www.winzip.com>

CURRICULUM VITAE

Ahmed Nabil Belbachir

December 06, 2004



PERSONAL INFORMATION

- Born: 1973, March 24th in Oran, Algeria
- Citizenship: Algerian
- Marital Status: Single
- Home Address: 20, Brigittenauer Laende 164-168/Stg.3/Top 29 Vienna, Austria
- Office Address: PRIP, 4, Favoritenstr. 9-11/4/183-2 Vienna, Austria
- Office Phone: +43 (1) 58801 18366
- Fax: +43 (1) 58801 18392
- Mobile Phone: +43 (0) 699 11096020
- Email: nabil@prip.tuwien.ac.at
- URL: <http://www.prip.tuwien.ac.at/~nabil>

CURRENT POSITION

- Since January 2000, Research Assistant involved in the astronomical project "Data Compression for ESA HERSCHEL/PACS Project".
- Since March 2000, PhD student at PRIP, Institute of Computer Aided Automation. The topic is On Board Data Compression: Distortion and Complexity Related Aspects
- Since October 2003, Student Assistant "Tutor" for Digital Image Processing, at PRIP

EDUCATION

- **03/2000 -** PhD student at Vienna University of Technology in the field of computer science. The topic of the Dissertation is "On-Board data Compression: Distortion and Complexity Related Aspects"
- **11/2000** Training at the Company Eonic System, Belgium on the virtual operating system for DSP 'VIRTUOSO'
- **05/2000** Intensive program course at INSA, Lyon, France, in the field of Image Processing "Still Image Compression Using Hartley Transform"
- **04/2000** Awarded Masters degree in Signal Processing, University of Oran, Algeria
- **11/1999** Internship for Research on Digital Filter Implementation at the Polytechnic University, Barcelona, Spain
- **09-10/1999** Internship for Research on Digital Filter Design at the University of Cagliari, Italy
- **1996** Awarded degree in electronic engineering, University of Oran, Algeria

- 1990 High school graduation, focus on mathematics – Al Hayat school, Oran, Algeria
- 1987 Middle school accomplishment, - Montesquieu school- Oran, Algeria.
- 1983 Primary school accomplishment, -Ben Boulaid school- Oran, Algeria.

WORK EXPERIENCE

- **Since 2000** Work on the ESA Project “Herschel Telescope”, for the Design, Development and Implementation of the On-Board Compression Software for the Photodetector Camera “PACS”
- **01-09/1999** Lecturer at the Institute of Computer Science, University of Oran, Algeria
- **04-12/1996** Work in a Private Company, Algeria for the Maintenance of TV Sets
- **01-12/1995** Technical Engineer at a private factory ‘Papeterie Oranaise’, Algeria to monitor the Automation Process

VISITS

- **11/2004** Attending the Workshop on Multiscale Geometric Methods for Astronomical Data Analysis at the Institute for Pure and Applied Mathematics (IPAM) in UCLA, California, USA.
Organizers: Dr. J-L Starck and Dr. V. Martinez
- **7/2004** Visit to Max-Planck Institute for Extraterrestrial physic (MPE), Garching, Germany, in the frame of the ESA-HERSCHEL Project. Topic of the Visit is: **SPU HLSW CQM Test - Phase 3-**
Host Person: Dr. H.Feuchtgruber
- **3/2004** Visit to Max-Planck Institute for Extraterrestrial physic (MPE), Garching, Germany, in the frame of the ESA-HERSCHEL Project. Topic of the Visit is: **SPU HLSW CQM Test - Phase 2-**
Host Person: Dr. H.Feuchtgruber
- **2/2004** Visit to Max-Planck Institute for Extraterrestrial physic (MPE), Garching, Germany, in the frame of the ESA-HERSCHEL Project. Topic of the Visit is: **SPU HLSW CQM Test - Phase 1-**
Host Person: Dr. H.Feuchtgruber
- **11/2003** Visit to Max-Planck Institute for Extraterrestrial physic (MPE), Garching, Germany, in the frame of the ESA-HERSCHEL Project. Topic of the Visit is: **ESA Review of PACS Instrument Hardware Design Review - SPU HLSW Presentation -**
Host Person: European Space Agency
- **7/2003** Visit to University of Cagliari, Department of electrical and electronic engineering, Italy. Topic of the Visit is: **Agro-alimentary Quality Control.**
Host Person: Prof. A. Fanni
- **6-7/2003** Visit to Max-Planck Institute for Extraterrestrial physic (MPE), Garching, Germany, in the frame of the ESA-HERSCHEL Project. Topic of the Visit is: **Improvement of Data Compression for HERSCHEL/PACS**
Host Person: Dr. H.Feuchtgruber

- **1-3/2003** Visit to Max-Planck Institute for Extraterrestrial physic (MPE), Garching, Germany, in the frame of the ESA-HERSCHEL Project. Topic of the Visit is: **Development, Test and Debugging of the SPU HLSW**
Host Person: Dr. H.Feuchtgruber
- **12/2002** Visit to Max-Planck Institute for Extraterrestrial physic (MPE), Garching, Germany, in the frame of the ESA-HERSCHEL Project. Topic of the Visit is: **Development, Test and Debugging of the SPU HLSW**
Host Person: Dr. H.Feuchtgruber
- **9/2002** Visit to Max-Planck Institute for Extraterrestrial physic (MPE), Garching, Germany, in the frame of the ESA-HERSCHEL Project. Topic of the Visit is: **AVM test for PACS**
Host Person: Dr. H.Feuchtgruber
- **6-8/2002** Visit to Canaries Institute for Astrophysics in Tenerife (IAC), Spain, in the frame of the ESA-HERSCHEL Project. Topic of the Visit is: **Development, Test and Debugging of the SPU HLSW**
Host Person: Dr. J.M. Herreros
- **4/2002** Visit to Canaries Institute for Astrophysics in Tenerife (IAC), Spain, in the frame of the ESA-HERSCHEL Project. Topic of the Visit is: **Development, Test and Debugging of the SPU HLSW**
Host Person: Dr. J.M. Herreros
- **2/2002** Visit to Max-Planck Institute for Extraterrestrial physic (MPE), Garching, Germany, in the frame of the ESA-HERSCHEL Project. Topic of the Visit is: **ESA Review of PACS Instrument Baseline Design Review - SPU HLSW Presentation -**
Host Person: European Space Agency
- **7/2001** Visit to University of Cagliari, Department of electrical and electronic engineering, Italy. Topic of the Visit is: **Development of Neural Network Techniques for Agronomical and Industrial Applications.**
Host Person: Prof. A. Fanni
- **6/2001** Visit to the University of Hanover, department of Electrical Engineering, Germany. Topic of the Visit is: **DSP Implementation for Video Coding.**
Host Person: Prof. H.G. Musmann
- **3/2001** Visit to Max-Planck Institute for Extraterrestrial physic (MPE), Garching, Germany, in the frame of the ESA-HERSCHEL Project. Topic of the Visit is: **ESA Review of PACS Instrument Intermediate Design Review - SPU HLSW Presentation -**
Host Person: European Space Agency
- **11/2000** Visit to Max-Planck Institute for Extraterrestrial physic (MPE), Garching, Germany, in the frame of the ESA-HERSCHEL Project. Topic of the Visit is: **Concept for the SPU HLSW**
Host Person: Dr. H.Feuchtgruber
- **7/2000** Visit to Max-Planck Institute for Extraterrestrial physic (MPE), Garching, Germany, in the frame of the ESA-HERSCHEL Project. Topic of the Visit is: **Discussion on the PACS Operating and Observing Modes**
Host Person: Dr. H.Feuchtgruber
- **5/2000** ERASMUS Intensive Program at INSA-Lyon (MPE), France.

Host Person: Prof. J.M. Jolion

- **11/1999** Visit to Catalan Polytechnic University in Barcelona, Spain. Topic of the Visit is: **Digital Filter Implementation in the Discrete Space**
Host Person: Prof. J.S. Alvarez
- **9-10/1999** Visit to University of Cagliari, Department of electrical and electronic engineering, Italy. Topic of the Visit is: **Digital Filter Design in the Discrete Space.**
Host Person: Prof. M. Marchesi

TEACHING ACTIVITIES

- Since 10/2003, Tutor for Digital Image Processing, at PRIP
- Lecture and practical course on Computer Architecture. University of Science and Technology Oran, 1998-1999.

ORGANIZATIONAL

- **4/2004** Organization of the Meeting between PRIP, IfA, MPE , ESA and CAPTEC in Vienna (at PRIP).
- **1/2002** Organization of the Meeting between PRIP, IfA and Joanneum in Graz.
- **5/2001** Organization of the Meeting between PRIP, IfA and MPE at PRIP (Vienna).

MEMBERSHIP AND REVIEWING

- Reviewer for Elsevier Journal for Digital Signal Processing and for the IEEE Transactions of Signal Processing Journal.
- Member of the European Association of Signal processing "EURASIP"
- Member of the International Association for Pattern Recognition (IAPR)
- Member of the Technical Committee 13 "Pattern Recognition for Astronomy and Astrophysics" - IAPR-TC13 -
- Member of the Austrian Association for Pattern Recognition (IAPR)
- Member of the Austrian Association for Astronomy and Astrophysics (OeGAA)
- Former General Secretary of the Algerian Association for Researchers "Baheth"

QUALIFICATIONS

- Arabic (native) French (excellent) English (very good), German (good) Spanish (good) Italian (conversation)
 - Organizational abilities, teaching experience, flexible, team-oriented
 - Background in economics and geography
 - Computer knowledge: Pascal, Fortran, Matlab, Assembly language, ANSI C, and Spice
 - Oriental music study (Andalous)
 - Latin dance: Salsa, Merengue, Pachata
 - Former football player of the university football team in Algeria
-

PUBLICATIONS

Journal Papers

- 1- **Ahmed Nabil BELBACHIR**, Horst BISCHOF,, Roland OTTENSAMER, Franz KERSCHBAUM and Christian REIMERS, "On-board Data Processing to Lower Bandwidth Requirements on an Infrared Astronomy Satellite: Case of Herschel-PACS Camera," EURASIP Journal for Applied Signal Processing, to appear on March 2005.
- 2- Roland OTTENSAMER, Franz KERSCHBAUM, Christian REIMERS, **Ahmed Nabil BELBACHIR** and Horst BISCHOF, "The Austrian HERSCHEL/PACS On-Board Reduction Work Package," Hvar Observatory Bulletin, vol. 26, no. 1, p. 77-80, Hungary, 2002.

Referred Conferences

- 1- **Ahmed Nabil BELBACHIR**, Alessandra FANNI, Mario LERA and Augusto MONTISCI, "An Automatic Optical Inspection System for the Diagnosis of Printed Circuits Based on Neural Networks," 40th IEEE-Industry Applications Society 2005 Annual Meeting, Hong-Kong, China, October, 2005(submitted).
- 2- Christian W. DAWSON, Linda SEE, Robert J. ABRAHART, Robert L. WILBY, Asaad Y. SHAMSELDIN, François ANCTIL, **Ahmed Nabil BELBACHIR**, G. BOWDEN, Graeme DANDY, Nicolas LAUZON and Holger MAIER, "A Comparative Study of Artificial Neural Network Techniques for River Stage Forecasting," International Joint Conference on Neural Networks 2005 IJCNN'05, Montreal, Canada , August, 2005 (submitted).
- 3- **Ahmed Nabil BELBACHIR**, Peter GOEBEL, "A Sparse Image Representation Using Contourlets ," in the 10th Computer Vision Winter Workshop, Zell an der Pram, Austria, February, 2005..
- 4- **Ahmed Nabil BELBACHIR**, Peter GOEBEL, "The Contourlet Transform for Image Compression," in the IEEE Conference on Physics in Signal and Image Processing (PSIP'2005), Toulouse, France, Jan./Feb. 2005.
- 5- Benamouer BOULERIAL, Mohamed Faouzi BELBACHIR and **Ahmed Nabil BELBACHIR**, "Reduced Search Space for the Optimal Design of Linear Phase FIR Filter," 12th European Signal Processing Conference EUSIPCO'04, Vienna, Austria, September 2004.
- 6- Christian REIMERS, **Ahmed Nabil BELBACHIR**, Horst BISCHOF, Roland OTTENSAMER, Helmut FEUCHTGRUBER, Franz KERSCHBAUM, and Albrecht POGLITSCH, "A Feasibility Study of On-Board Data Compression for Infrared Cameras of Space Observatories," 7th International Conference on Pattern Recognition, Cambridge, UK, August 2004.
- 7- Roland OTTENSAMER, **Ahmed Nabil BELBACHIR**, Horst BISCHOF, Helmut FEUCHTGRUBER, Franz KERSCHBAUM, Albrecht POGLITSCH and Christian REIMERS, "Herschel-PACS On-Board Reduction/Compression Software Implementation," SPIE International Symposium on Astronomical Telescopes, Glasgow, Scotland, UK, June 2004.
- 8- Roland Ottensamer, **Ahmed Nabil BELBACHIR**, Horst BISCHOF, Helmut FEUCHTGRUBER, Franz KERSCHBAUM, Christian REIMERS, Ekki WIEPRECHT, "The HERSCHEL/PACS On-

- Board Software Data Processing Scheme”, Astronomical Data Analysis Software & Systems Conference, Victoria, Canada, September 2001.
- 9- **Ahmed Nabil BELBACHIR**, Sergio BIBBO, Alessandra FANNI, Benaoumer BOULERIAL, Mohamed Faouzi BELBACHIR, " Evaluation of the Iterative Least Square Method in Digital Filter Design, " the Seventh LASTED International Conference, Signal and Image Processing (SIP2000) Las Vegas, Nevada, USA, November 2000.
 - 10- **Ahmed Nabil BELBACHIR**, Horst BISCHOF, Franz KERSCHBAUM, "A Data Compression Concept for Space Application, " DSP-SPE'00, IEEE Digital Signal Processing Workshop in Hunt, Texas, USA, October 2000.
 - 11- **Ahmed Nabil BELBACHIR**, Benaoumer BOULERIAL, Mohamed Faouzi BELBACHIR, "A New Approach to Finite Wordlength Coefficient FIR Digital Filter Design Using the Branch and Bound Technique," EUSIPCO'00, Tampere - Finland, September 2000.
 - 12- **Ahmed Nabil BELBACHIR**, Mohamed Faouzi BELBACHIR, Alessandra FANNI, "A New Approach to Digital Filter Design Using the Tabu Search," IEEE NORDic SIGNAL Processing, NORSIG'00, Sweden, June 2000.
 - 13- **Ahmed Nabil BELBACHIR**, Benaoumer BOULERIAL, Mohamed Faouzi BELBACHIR, "A Sequential Robust Method to Finite Wordlength Coefficient FIR Digital Filter Design," IEEE NORDic SIGNAL Processing, NORSIG'00, Sweden, June 2000.
 - 14- Horst BISCHOF, **Ahmed Nabil BELBACHIR**, Dieter Claus HOENIGMANN, and Franz KERSCHBAUM, "A data reduction concept for FIRST/PACS," In J. B. Breckinridge and P. Jakobsen, editors, UV, Optical, and IR Space Telescopes and Instruments VI. SPIE, Munich, Germany, March 2000.
 - 15- Franz KERSCHBAUM, Horst BISCHOF, **Ahmed Nabil BELBACHIR**, Dieter Claus HOENIGMANN, and Thomas LEBZELTER, "Evaluation of FIRST/PACS data compression on ISO data," In J. B. Breckinridge and P. Jakobsen, editors, UV, Optical, and IR Space Telescopes and Instruments VI. SPIE, Munich, Germany, March 2000.
 - 16- **Ahmed Nabil BELBACHIR**, Benaoumer BOULERIAL, Mohamed Faouzi BELBACHIR, "Une Approche Itérative pour la Conception de Filtres Numériques RIF à Phase Linéaire dans l'Espace Discret des Coefficients," Conférence Maghrébine en Génie Electrique, CMGE'99, Constantine, Algeria, December 1999.
 - 17- **Ahmed Nabil BELBACHIR**, Benaoumer BOULERIAL, Mohamed Faouzi BELBACHIR, "Synthèse de Filtres Numériques RIF à Phase Linéaire dans un Espace Discret de Mot Machine de Longueur Finie," Séminaire National sur l'Automation et le Signal, SNAS'99, Annaba, Algeria, November 1999.
 - 18- **Ahmed Nabil BELBACHIR**, Benaoumer BOULERIAL, Mohamed Faouzi BELBACHIR, "Synthèse de Filtres Numériques," Journée d'Electronique, JE'99, Oran, Algeria, June 1999.

Technical Reports

- 1- **Ahmed Nabil BELBACHIR** Florian SCHMITZBERGER and Walter KROPATSCH, "On-Board Data Compression for Herschel-PACS Control Data," Technical Report Number 90 at PRIP, TU Vienna, December 2004.

- 2- Ernst HIRZ, **Ahmed Nabil BELBACHIR** and Robert SABLATNIG, "On-Ground Astronomical Data Processing. "A Software Tool for HERSCHEL/PACS Data Decompression and Analysis," Technical Report Number 88 at PRIP, TU Vienna, April 2004.
- 3- **Ahmed Nabil BELBACHIR**, Ted CHILTON, Mark DUNN, Marc NUNKESSER, Sahbi SIDHOM and Georges SZAJNOWSKI, "Image Compression using Hartley Transform," Technical Report Number 78 at PRIP, TU Vienna, December 2003.
- 4- **Ahmed Nabil BELBACHIR** and Horst BISCHOF, "On-Board Data Compression: Noise and Complexity Related Aspects," Technical Report Number 75 at PRIP, TU Vienna, October 2003.
- 5- **Ahmed Nabil BELBACHIR**, "Quality Control of Agro-alimentary products," Technical Report at the University of Cagliari, Italy, July 2003.
- 6- **Ahmed Nabil BELBACHIR** and Mohammed Faouzi BELBACHIR, "Development of Neural Network Techniques for Agronomical and Industrial Applications," Technical Report at the University of Cagliari, Italy, July 2001.
- 7- **Ahmed Nabil BELBACHIR**, Mohamed Faouzi BELBACHIR, "Information Processing," Technical Report at the University of Cagliari, Italy, October 1999.

Theses

- 1- **Ahmed Nabil BELBACHIR**, " Digital Filter Design in the Discrete Space," Master Thesis, 2000. Advisor: Mohamed Faouzi BELBACHIR
- 2- **Ahmed Nabil BELBACHIR** and Hassane Baghdad KICHOU, "Signal Reconstruction from its Spectral Phase: Noise Study," Engineer Thesis, June 1996. Advisor: Mohamed Faouzi BELBACHIR.